UNIVERSITÀ
DEGLI STUDI
DI TRIESTE

UNIVERSITÀ DEGLI STUDI DI TRIESTE

XXXVII CICLO DEL DOTTORATO DI RICERCA IN

CHIMICA

DIPARTIMENTO DI SCIENZE CHIMICHE E FARMACEUTICHE – UNIVERSITÀ DEGLI STUDI DI TRIESTE

EXPLORING THE SOLID FORM LANDSCAPE OF ANTIPARASITIC DRUG COMBINATIONS

Settore scientifico-disciplinare: **CHEM08-A Farmaceutico Tecnologico Applicativo**

DOTTORANDA
ILENIA D'ABBRUNZO

COORDINATORE
PROF. ENZO ALESSIO

SUPERVISORE DI TESI
PROF. BEATRICE PERISSUTTI

CO-SUPERVISORE DI TESI
PROF. DRITAN HASA

ANNO ACCADEMICO 2023/2024

"I am among those who think that science has great beauty.

A scientist in his laboratory is not only a technician:

he is also a child placed before natural phenomena

which impress him like a fairy tale"

Marie Curie

Contents

List of abbreviations

ACT	Acetone
ACN	Acetonitrile
AIM	Atoms in Molecules
API	Active Pharmaceutical Ingredient
ASDs	Amorphous solid dispersions
ASU	Asymmetric unit
AUC	Area under the curve
BCS	Biopharmaceutic Classification System
BENZOH	Benzyl alcohol
1-ButOH	1-butanol
CCDC	Cambridge Crystallographic Data Centre
CHF	Chloroform
C_{max}	Maximum plasma concentration
CSD	Cambridge Structural Database
CyHXN	Cyclohexanone
DAC mixing	Dual asymmetric centrifugal mixing
DFT	Density functional theory
DMA	Dimethylacetamide
DMSO	Dimethyl sulfoxide
DoE	Design of Experiments
DSC	Differential scanning calorimetry
DVS	Dynamic vapor sorption
EA	Ethyl acetate
EDA	Energy decomposition analysis
EDD	Electron density difference
Eq.	Equivalents
EtOH	Ethanol
XGBoost	eXtreme Gradient Boosting
FaSSGF	Fasted state simulated gastric fluid
FaSSIF	Fasted state simulated intestinal fluid
FDA	Food and Drug administration
FE-SEM	Field-emission scanning electron microscopy

FT-IR	Fourier-transform Infrared Spectroscopy
FT-IR-ATR	Fourier-transform Attenuated Total Reflectance Infrared Spectroscopy
GRAS	Generally Recognized as Safe
H_2O	Water
H-bonds	Hydrogen bonds
HEC	Hydroxyethyl cellulose
HS-ATR-MIR	Hot-stage attenuated total reflectance mid-infrared spectroscopy
HSM	Hot-stage microscopy
HXN	Hexane
IDR	Intrinsic dissolution rate
ILAG	Ionic liquid-assisted grinding
ILs	Ionic liquids
iPOH	Isopropanol
IUPAC	International Union of Pure and Applied Chemistry
MBZ	Mebendazole
MCR-ALS	Multivariate curve resolution and alternating least squares
MeOH	Methanol
MEPS	Molecular electrostatic potential surfaces
MOFs	Metal-organic frameworks
MTDSC	Modulated differential scanning calorimetry
4-MTHP	4-methyltetrahydropyran
NCM	Niclosamide
NG	Neat grinding
NTS	Newly Transformed Schistosomula
LAG	Liquid-assisted grinding
PEG	Polyethylene glycol
PM	Physical mixture
POLAG	Polymer-assisted grinding
2-PrOH	2-propanol
2-pyr	2-pyrrolidone
PVDF	Polyvinylidene fluoride
PXRD	Powder X-ray diffraction
PZQ	Praziquantel
RAM	Resonant acoustic mixing

RCS	Refrigerated cooling system
RESS	Rapid expansion of supercritical solution
RH	Relative humidity
$scCO_2$	Supercritical CO_2
SCF	Simulated colonic fluid
SE	Solvent evaporation
SEM	Scanning electron microscopy
SGF	Simulated gastric fluid
SHG	Second harmonic generation
SI	Saturation index
SIF	Simulated intestinal fluid
S. *mansoni*	Schistosoma *mansoni*
SMILES	Simplified molecular input line entry system
SPE	Single pulse excitation
SSNMR	Solid -state nuclear magnetic resonance spectroscopy
STM	Saturation temperature measurements
SXRD	Single-crystal X-ray diffraction
TEA	Triethylamine
TEG	Triethylene glycol
T_g	Glass transition temperature
TGA	Thermogravimetric analysis
THF	Tetrahydrofuran
T_{max}	Time to reach maximum concentration
TMS	Tetramethylsilane
TPPM	Two-pulse phase modulation
VALAG	Variable amount liquid-assisted grinding
VATEG	Variable-temperature grinding
VT-XRD	Variable-temperature X-ray diffraction
WBR	Worm burden reduction
WHO	World Health Organization
XRD	X-ray diffraction

1. Introduction

1.1 Mechanochemistry

Mechanochemistry is an important branch of chemistry that focuses on promoting and accelerating chemical reactions through the application of mechanical energy. Unlike other methods that often rely on solvents or liquid-phase reagents, mechanochemistry uses techniques such as grinding, milling, and friction to induce chemical transformations. This approach not only significantly reduces the use of solvents, thus aligning with the principles of green and sustainable chemistry [1,2], but also facilitates the discovery of new materials and solid forms that are otherwise inaccessible through conventional methods [3–7].

Mechanochemical processes have gained considerable attention in pharmaceutical chemistry as a powerful tool for developing novel drug formulations and drug combinations, which can improve therapeutic efficacy and patient compliance, as well as the modification of the physicochemical properties of active pharmaceutical ingredients (APIs). Particularly, the use of mechanochemical methods has proven effective in stabilizing APIs in their metastable forms, which are often more soluble but less stable than their thermodynamically favored counterparts [8,9]. Additionally, mechanochemistry enables the creation of pharmaceutical salts, cocrystals, hydrates/solvates and coamorphous, which can simultaneously translate into improved properties of a drug, such as solubility, dissolution rate, and permeability, offering new pathways for drug development and delivery [10–15].

Given its advantages, mechanochemistry represents a promising frontier in the pharmaceutical sciences, with the potential to revolutionize the discovery and manufacture of pharmaceutical solid forms. Its application in drug development not only aligns with current demands for greener and more sustainable practices but also provides innovative solutions to long-standing formulation challenges, positioning mechanochemistry as a key technology for the future of pharmaceutical innovation.

1.1.1 Definition, origins and mechanistic models

Mechanochemistry is the discipline focused on obtaining solid forms through the sole application of mechanical energy. James et al. define mechanochemical reactions as "*Reactions, normally of solids, induced by the input of mechanical energy, such as by grinding in ball mills"* [3].

Historically, mechanochemistry can be divided into four distinct periods (Figure 1):

- "Involuntary" Mechanochemistry: this initial phase encompasses the use of friction to generate fire and the grinding of herbs with mortars, practices that were not yet recognized as chemical processes mediated by mechanical force.
- Recognition of Mechanochemical Processes (19th Century Onwards): during this period, there was a growing acknowledgment that such practices involved mechanochemical principles. This era marked the beginning of understanding mechanochemistry as a distinct discipline, capable of facilitating a variety of chemical reactions through mechanical energy.
- Development of Mechanochemistry with Potential Pharmaceutical Applications: This phase saw the exploration of mechanochemistry in pharmaceutical contexts, revealing its potential to enhance the synthesis and formulation of APIs and other drug-related compounds.
- Application and Continuous Advancement in Pharmaceutical Mechanochemistry: the most recent phase is characterized by the active application of mechanochemical techniques in drug development and their continuous refinement to optimize pharmaceutical processes and outcomes. In the pharmaceutical field, one of the most widely used mechanochemical techniques is grinding, wherein reagents, with or without the presence of minimum amount of liquid, are milled for a specified time within a milling apparatus [16].

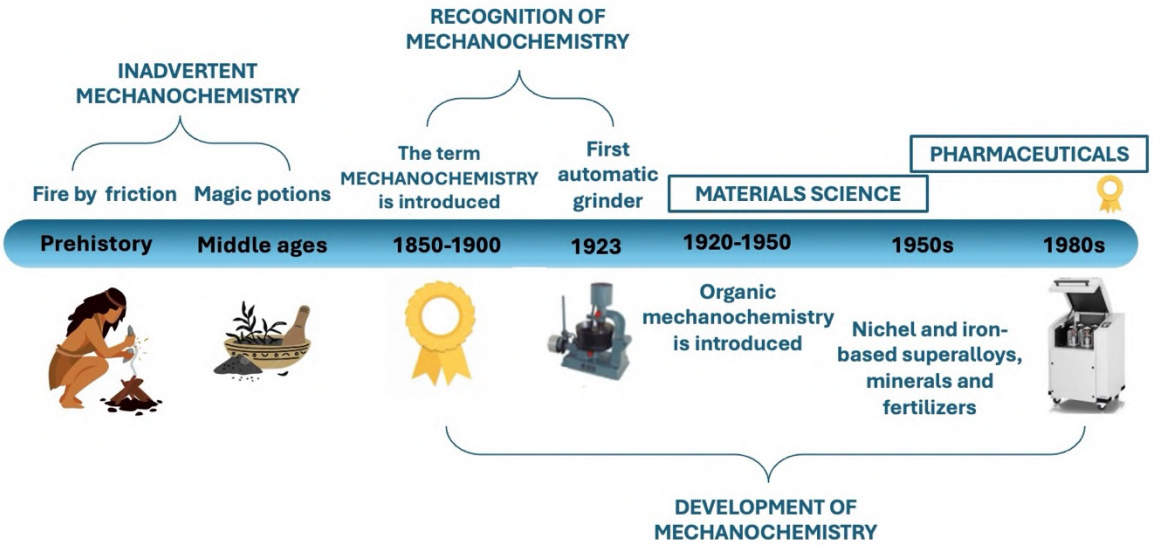

Figure 1. Schematic representation of mechanochemistry history. Adapted from reference [17].

Over the past three decades, the field has expanded significantly and is currently considered one of the most effective techniques for the synthesis and screening of solid forms (i.e., polymorphs, salts, cocrystals and hydrates/solvates) [4,14,18].

To explain the behavior of organic compounds in mechanochemical processes, three mechanistic models have been proposed:

- The Molecular Diffusion Hypothesis: this model suggests that molecules in solids possess sufficient mobility to migrate across the crystal surface, particularly when the compounds have high vapor pressures in the solid state.
- The Eutectic Intermediate Hypothesis: this theory suggests the formation of a eutectic intermediate that subsequently nucleates to form a crystal, which occurs especially in liquid-assisted crystallization processes, where a transient liquid interface forms between two solid substances.
- The Amorphous Phase Formation Hypothesis: This hypothesis suggests that the temporary formation of amorphous phases occurs in all compounds that exhibit dense H-bonding patterns and limited molecular mobility.

The common feature of these three mechanisms is the formation of an intermediate phase—whether gaseous, liquid, or solid—possessing higher energy or mobility than the initial compound [19].

Until recently, understanding the real-time dynamics of these reactions has been challenging due to the lack of suitable monitoring techniques. However, recent breakthroughs in '*in situ monitoring techniques*' have opened new possibilities for understanding and optimizing these reactions, making them more accessible and controllable for a broader range of chemists.

The ability to monitor mechanochemical reactions in real-time is revolutionary because it allows chemists to map reaction pathways, uncover previously unknown intermediates, and determine the exact conditions that lead to the formation of desired products. Prior to these advancements, mechanochemical reactions were often seen as "black box" processes, where the inputs and outputs were known but the exact mechanisms were difficult to trace. With *in situ* techniques, this opacity is lifted, leading to better control over reaction conditions, faster optimization, and the possibility to scale up processes for industrial use.

Specifically, the application of *in situ* Synchrotron X-ray diffraction (XRD) and Raman spectroscopy allow chemists to observe chemical transformations as they occur during mechanical processing (Figure 2).

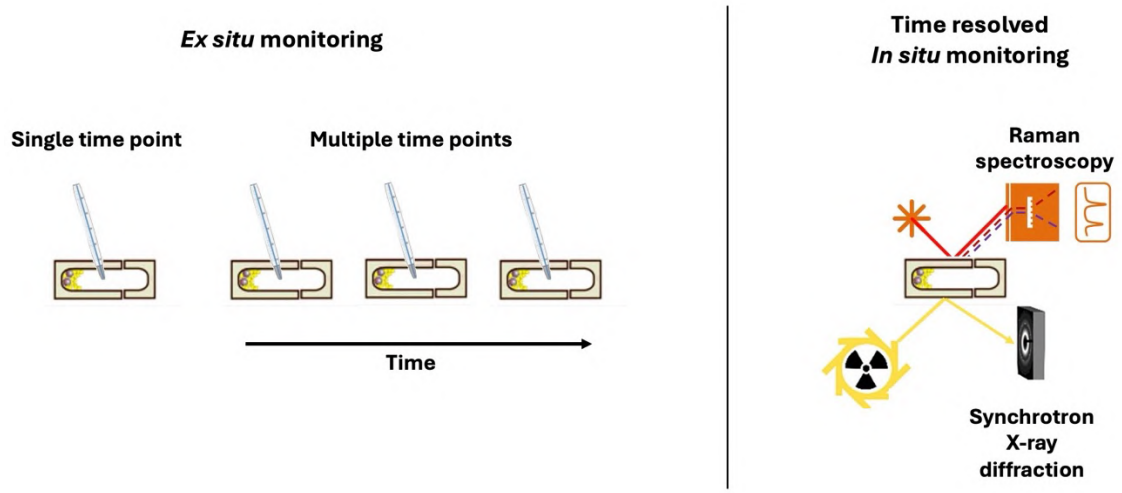

Figure 2. Schematic representation of *ex situ* and recent *in situ* monitoring techniques. Adapted from reference [20].

These techniques provide real-time insights into the kinetics and structural changes occurring during the reaction, revealing the formation of intermediates, phase transitions, and product formation without having to pause or interfere with the reaction itself. *In situ* XRD allows researchers to observe the crystalline phase evolution during milling or grinding, offering precise data on how the crystal structure changes as the reaction progresses. Raman spectroscopy, on the other hand, provides molecular-level information on the vibrational modes of the reactants, intermediates, and products, giving insight into bond formation, breakage, and changes in the molecular environment [21–26].
These techniques were first used to monitor the synthesis of porous metal-organic frameworks (MOFs) from ZnO [22,27]. Considering the importance of mechanochemistry for the screening and synthesis of pharmaceutical solids [28–30], in 2013 Halasz et al. proposed the first *in situ* XRD study of mechanochemical transformations of organic pharmaceutically relevant solids. They selected carbamazepine-saccharin cocrystal as a suitable first model for the application of real-time Synchrotron XRD analysis [25]. Since then, few examples of pharmaceutically relevant mechanochemical reactions monitored in real-time have been reported in literature [31,32].

1.1.2 Devices and main process variables

Regarding the mechanochemical preparation of pharmaceutical solids, the most frequent mechanochemical operation is represented by grinding, usually by means of mills of different types and with various equipment [4,5,14,17].
The manual grinding of materials using mortars and pestles has been a traditional method for centuries. However, the process was characterized by several challenges, primarily due to the

variability introduced by human operators. Studies have shown that manual grinding is often inefficient, resulting in a lower yield and inconsistent particle size distribution, which is critical for various applications, particularly in pharmaceutical and food industries. The dependence on the operator's skill, strength, and endurance made difficult to standardize the grinding process.
Moreover, when grinding was conducted in open environments, the evaporation of liquids used to facilitate the process was a common problem, further affecting the final product's quality.

As a response to these challenges, the invention of automated mills marked a significant advancement. These machines enabled a consistent, operator-independent grinding process, which could be controlled and scaled according to specific requirements, thereby significantly improving productivity and product uniformity. The first “automatic mortar and pestle” was developed by the company Retsch in 1923 [16].
Ball mills are among the most effective devices for rapidly imparting large quantities of mechanical energy to materials. Their design enables the continuous and uniform collision of milling media with the loaded material, resulting in efficient energy transfer. This process facilitates the breakdown of particles, promotes chemical reactions, and accelerates phase transformations, all within a relatively short time frame [33]. The three main categories of ball mills used are vibrational mills and, at larger scales, attritor and planetary mills (Figure 3).

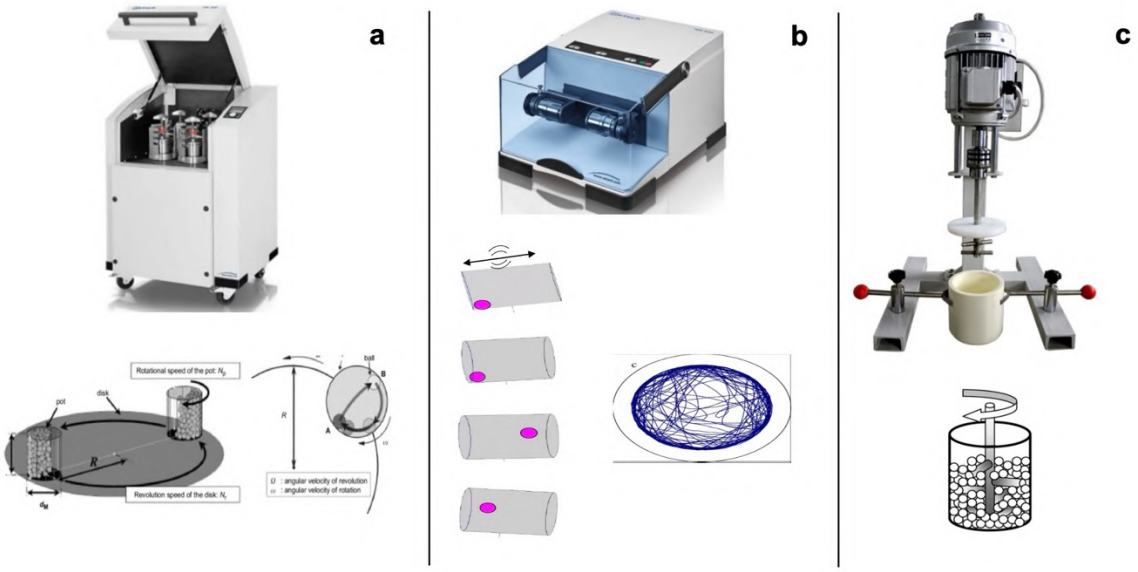

Figure 3. (a) Planetary mill (top left) and schematic representation of the operation and involved motions (bottom left); (b) Vibrational mill (top centre) and schematic representation of the operation and involved motions (bottom centre); (c) Attritor mill (top right) and schematic representation of the operation and involved motions (bottom right). Adapted from reference [33].

1.1.2.1 Planetary mills

A planetary mill operates by rotating around its own central axis, while simultaneously, multiple jars fixed on a rotating plate move either clockwise or counterclockwise relative to the base (Figure 3a). This dual rotation creates a complex motion within each jar, where the grinding media and the loaded material are subjected to intense and continuous collisions. These collisions, occurring on the walls of the jars, induce high shear and compressive forces that result in mechanochemical activation [17,18,33,34].

While planetary mills are frequently used for synthesizing crystalline inorganic materials [35], their main use in the pharmaceutical industry is due to their high effectiveness in reducing particle size and promoting drug amorphization at the laboratory scale [36,37].

1.1.2.2 Vibrational mills

Vibrational mills, as the name suggests, operate through a vibrational mechanism. The system consists of a vibrating clamp that is horizontally connected to two jars (frequently of steel), which oscillate at frequencies ranging from 3 to 25 Hz (Figure 3b). This rapid shaking motion causes the grinding media (usually spheres) inside the jars to collide continuously with one another, with the walls of the jars, and with the sample material. These frequent impacts result in the efficient transfer of mechanical energy, leading to the fragmentation of particles and the initiation of chemical reactions.

In addition to steel, a range of jars and grinding materials is commercially available for these devices, including alumina, tungsten carbide, zirconia, agate, plastic, and methacrylate. The volumes of the grinding jars can vary from 1 to 50 mL, while the diameter of the grinding balls ranges from 1 millimiter to several centimeters.

Vibrational mills are particularly useful for applications requiring fine grinding and the uniform dispersion of materials, as the vibrational motion ensures consistent energy distribution throughout the process [18,38].

1.1.2.3 Process variables

By optimizing factors such as milling speed, ball size, material loading, etc. (Figure 4), ball mills can achieve high levels of mechanical activation, making them essential tools in both research and industrial applications for mechanochemical synthesis and processing. Thus, process variables cannot be underestimated when talking about grinding.

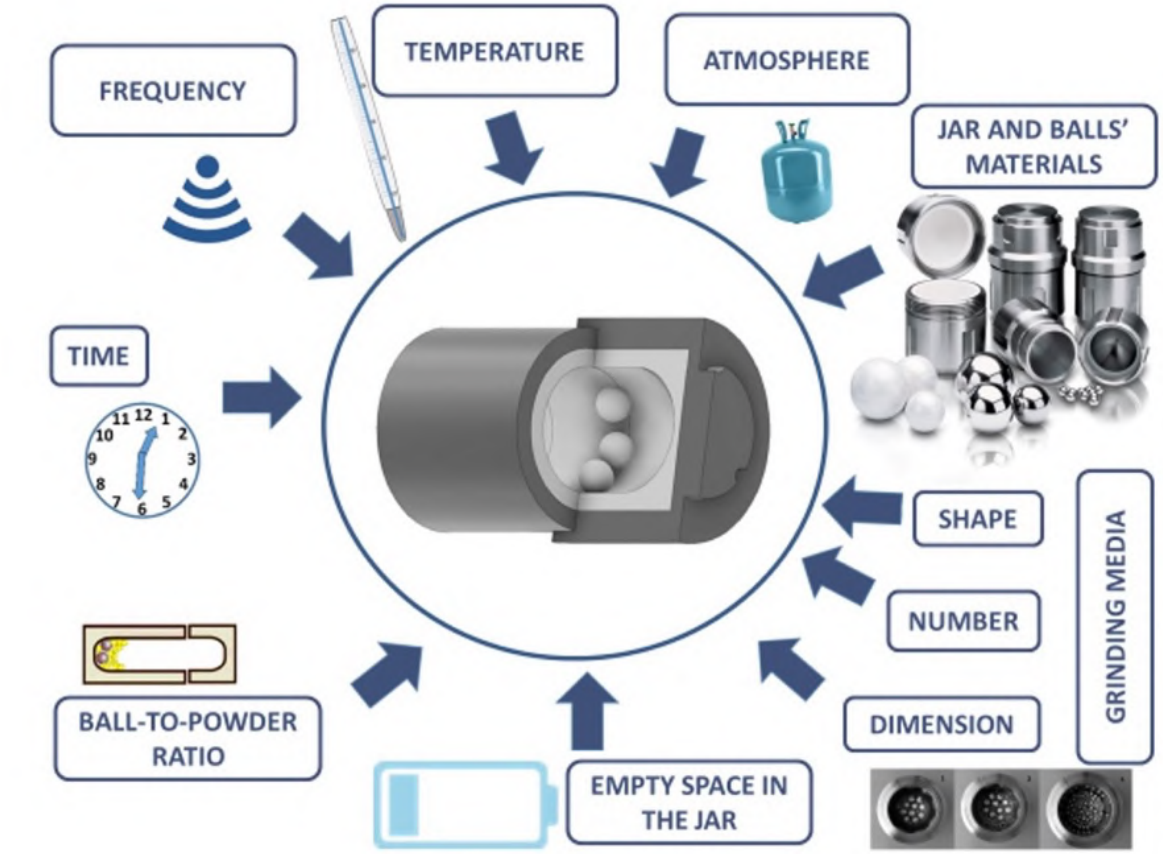

Figure 4. Main process variables involved in mechanochemistry. Adapted from references [33, 36, 39–42].

1.1.2.3.1 Material of jars and grinding media

The selection of jar and grinding media materials is crucial in mechanochemical processes. Stainless steel is a common choice for both jars and balls due to its durability and hardness. However, stainless steel has the drawback of potentially contaminating the final product, which can be problematic in applications requiring high purity. To mitigate this issue, alternative materials such as zirconia, methacrylate, or other plastics are often employed, especially when contamination must be minimized [39].

When choosing grinding media, three key factors must be considered:

- Shape: spherical grinding media are generally preferred, as their shape provides a larger surface area for impact, leading to more efficient energy transfer to the powder.
- Number: the quantity of grinding media directly affects the energy intensity of the milling process and should be adjusted based on the specific material being processed.
- Size: the size of the grinding balls can range from 1 millimiter to several centimeters, and it should be selected according to the desired particle size reduction and the nature of the material being milled [40].

Additionally, the capacity of the jars used in these processes can vary from as small as 1 mL to as large as 50 mL, depending on the scale of the milling operation.
An idea of the great variety of grinding media can be seen in Figure 5.

Figure 5. Examples of grinding media in planetary mills (left) and vibrational mills (right) [41].

1.1.2.3.2 Empty space in the jars

Another important parameter is the volume of empty space in the jars, which influences both energy transfer and mixing efficiency. The trajectories and collisions of the grinding balls are dependent on the volume of the jar and the degree of filling. The optimal filling volume will vary based on the type of mill and the specific requirements of the reaction, as different mills and reactions require different conditions to achieve efficient mechanochemical processing [33].

1.1.2.3.3 Ball-to-powder ratio

The ball-to-powder ratio is a critical factor that can significantly affect the efficiency and outcome of the milling process. A higher proportion of grinding media generally leads to a more energetic milling process, which can reduce reaction time. However, an excessively high ratio may also cause degradation of the powder, resulting in an undesirable outcome. Thus, careful optimization of this ratio is necessary to balance the need for sufficient energy input with the risk of over-milling [33].

1.1.2.3.4 Grinding time

The duration of the milling process is another key variable that primarily affects the progression of the reaction. As grinding time increases, the mechanical activation of the starting materials also increases, which can lead to the formation of amorphous phases. This is often the desired outcome in mechanochemical synthesis, as demonstrated in studies that aim to enhance the solubility of poorly soluble drugs, such as vinpocetine, by inducing amorphization through co-grinding [36].

1.1.2.3.5 Temperature

The temperature control is one of the more complex variables in mechanochemical processes, as it is inherently linked to the milling action itself. The collisions between the grinding balls and the jar contents generate heat, which can influence the reaction. Specialized mills, such as cryomills, which use jars cooled with liquid nitrogen, are designed to control temperature and prevent overheating [42]. In most cases, however, temperature remains uncontrolled, and traditional mills typically operate at room temperature.

1.1.2.3.6 Frequency

Finally, frequency is a relatively simple parameter to adjust, as most mills are equipped with frequency control settings. Increasing the frequency directly raises the kinetic energy of the grinding balls, which enhances the milling intensity. Frequencies around 25 Hz are most used, although higher frequencies, such as 30 Hz, can be employed depending on the specific needs of the process [33].

By carefully controlling these variables, it is possible to optimize mechanochemical reactions to achieve the desired outcomes efficiently and effectively.

1.1.3 Several techniques applicable to the same instrument

There are various milling techniques that can be selected depending on the desired final product characteristics. These most common mechanochemical applications are neat grinding (NG), liquid-assisted grinding (LAG), variable amount of liquid-assisted grinding (VALAG) and polymer-assisted grinding (POLAG). There are also more specific methods which are less often used such as variable-temperature grinding (VATEG) and ion liquid-assisted grinding (ILAG) [17].
Each approach offers specific advantages and is tailored to optimize different aspects of the mechanochemical process, such as particle size, crystallinity, solubility, or chemical reactivity, to achieve the targeted material properties.

1.1.3.1 Neat grinding (NG)

This milling process relies solely on the transfer of mechanical energy to achieve the desired solid form, making it a solvent-free and environmentally friendly technique. This approach is particularly advantageous for producing new solid-state compounds, such as polymorphic forms, amorphous or coamorphous solids, polymeric amorphous dispersions, and inclusion complexes [11,12,43–45].

A range of variables can influence mechanochemical processes. In NG, these variables can be broadly classified into grinding conditions within the jar (such as speed, ball size, and ball-to-powder ratio), conditions external to the jar (like temperature and atmosphere), the nature of the starting materials, and the specific type of milling device used.

Compared to liquid-assisted grinding (LAG) (presented below), NG tends to produce a product with a lower degree of crystallinity when starting from the same solid material. This makes NG more suitable for obtaining amorphous forms, as it provides conditions that more readily disrupt the crystalline structure [46–48].

However, the energy input in NG may sometimes be insufficient to induce complete mechanochemical activation [5]. In such cases, the addition of a small amount of solvent (LAG) may be necessary to facilitate the desired chemical transformation or structural change.

1.1.3.2 Liquid-assisted grinding (LAG)

LAG is a technique that involves milling in the presence of small quantities of a liquid, which acts under catalytic conditions to enhance the grinding process. While LAG is more complex than NG, it offers significant advantages by accelerating reaction kinetics and enhancing the crystallinity of the product. This is particularly beneficial in cases where NG may not provide enough energy to achieve full mechanochemical activation, especially when dealing with multicomponent crystalline systems such as cocrystals, solvates/hydrates, and salts [17,49,50].

Compared to traditional solution-based crystallization methods, LAG provides a valuable alternative that facilitates direct interactions (often H-bonds) between the different components in the system, rather than between the components and the solvent [3]. This results in a final product that can be easily dried, eliminating the need for extensive solvent removal and reducing the risk of residual solvent contamination.

The exact mechanism behind the effectiveness of LAG remains partially understood. It is hypothesized that the solvent primarily plays a physical role, enhancing the diffusion of molecules and enabling closer contact between reactants. However, the choice of solvent can be crucial in some cases, particularly for the formation of multicomponent systems like cocrystals, and for controlling polymorphism and solvate formation [19].

A critical step in LAG is determining the optimal amount of solvent to add, which can greatly influence the efficiency and outcome of the mechanochemical reaction. To guide this process, Friščić introduced the empirical parameter η, which serves as a practical tool for selecting the appropriate solvent quantity to achieve desired reaction conditions [51].

The parameter η is defined as the ratio of the volume of the added solvent (in μL) to the mass of the sample (in mg), as shown in equation 1:

$$\eta = \frac{V\ (liquid,\ \mu L)}{\mathrm{m\ (sample, mg)}} \quad \textbf{(1)}$$

This parameter helps categorize different milling environments based on the solvent-to-solid ratio, thereby assisting in the optimization of mechanochemical processes.

Depending on the value of η, several techniques can be identified:

- η = 0 corresponds to NG, where no solvent is used.
- 0 < η < 2 represents LAG, where small amounts of liquid catalyze the process without dissolving the solid components.
- < η < 12 describes slurry methods, where more liquid is added to create a thick slurry that facilitates mixing and grinding.
- η > 12 indicates solution synthesis, in which the components are fully dissolved in a solvent to achieve complete mixing and reaction.

For LAG, η values typically range between 0 and 2 μL/mg, a range that defines the catalytic conditions of the liquid. Within this range, the solvent does not dissolve the solid components appreciably but instead acts to enhance the mobility of the reactants, improving the frequency and efficiency of their collisions [5].

A schematic representation of LAG is shown in Figure 6.

Figure 6. Addition of solvent in LAG.

Friščić's parameter η provides a straightforward yet powerful framework for selecting liquid quantities that optimize the balance between solid-state reactivity and liquid-phase catalysis. By adjusting η, researchers can fine-tune the milling environment to target specific outcomes, such as increased reaction rates, enhanced crystallinity, or the selective formation of desired multicomponent

systems [51]. This makes η an invaluable tool in the growing field of mechanochemistry, enabling a more systematic approach to optimizing complex reactions that were previously governed by trial and error.

1.1.3.3 Variable amount of liquid-assisted grinding (VALAG)

Grinding with a variable amount of liquid has emerged as an advanced technique in the field of mechanochemistry, representing an evolution of LAG. This approach involves systematically adding varying amounts of a liquid tailored to the specific requirements of the system being studied. The primary goal of this method is to determine the optimal liquid quantity needed to drive the mechanochemical reaction to completion efficiently.

Recently, it has been discovered that, by carefully adjusting the amount of liquid, this technique not only improves reaction kinetics and yields but also enables access to different polymorphic forms of the target compound. For example, using different liquid volumes can favor the formation of a more/less stable polymorph, an amorphous form with enhanced solubility, or even enable the selective synthesis of less common crystalline forms that may not be accessible under standard conditions [17,51–53].

1.1.3.4 Polymer-assisted grinding (POLAG)

POLAG is a mechanochemical technique where polymers are added during the grinding process to influence the reaction environment, modulate the energy transfer, and guide the formation of desired solid products. In POLAG, the polymers act as grinding aids, facilitating the transformation of reactants into new solid phases, such as polymorphs, amorphous phases, cocrystals, or other multicomponent systems [54–56] (Figure 7). The polymers can affect the reaction in several ways: by improving the mixing of reactants, providing additional kinetic energy, and stabilizing specific intermediates or products. The length and molecular weight of the polymer chains play a crucial role in determining the outcomes of the mechanochemical process, as they influence the energy transfer and the nature of the interactions with the reactants [17,57,58].

POLAG is characterized by a parameter known as δ, defined as the ratio of polymer additive (in mg) to reactant mass (in mg), which is used to quantify the effect of the polymer on the reaction process. This parameter represents the ability of the polymer to interact with the reactants and modulate the energy landscape of the system. A higher δ value typically indicates stronger polymer-reactant interactions, which can enhance the grinding efficiency or promote the formation of specific solid phases [57]. In this context, the polymer is more effective at reducing the energy barrier for the

reaction or stabilizing intermediate states, leading to faster or more complete transformations. The choice of polymer type, molecular weight, and concentration are critical factors that influence δ and, consequently, the outcome of the grinding process. For instance, shorter polymer chains may enhance mixing and reduce agglomeration of reactants, while longer chains may provide more substantial steric effects or participate in specific interactions that guide product formation [17].

Polymers have shown to be crucial in dehydrating hydrated systems, as the polymer may help to remove water molecules from the crystalline lattice by disrupting H-bonding networks [59,60].

Recent developments have demonstrated that POLAG can go beyond its traditional role as a catalytic aid in mechanochemical reactions. It has been discovered that in some cases, polymers can become an integral part of the newly formed solid-state systems, resulting in the formation of novel polymeric cocrystals (Figure 7). In these instances, the polymer is not just facilitating the reaction but is actively incorporated into the crystal lattice, creating new materials with potentially unique structural and functional properties and, thus, expanding POLAG applications in pharmaceuticals, material science, and sustainable chemistry [61].

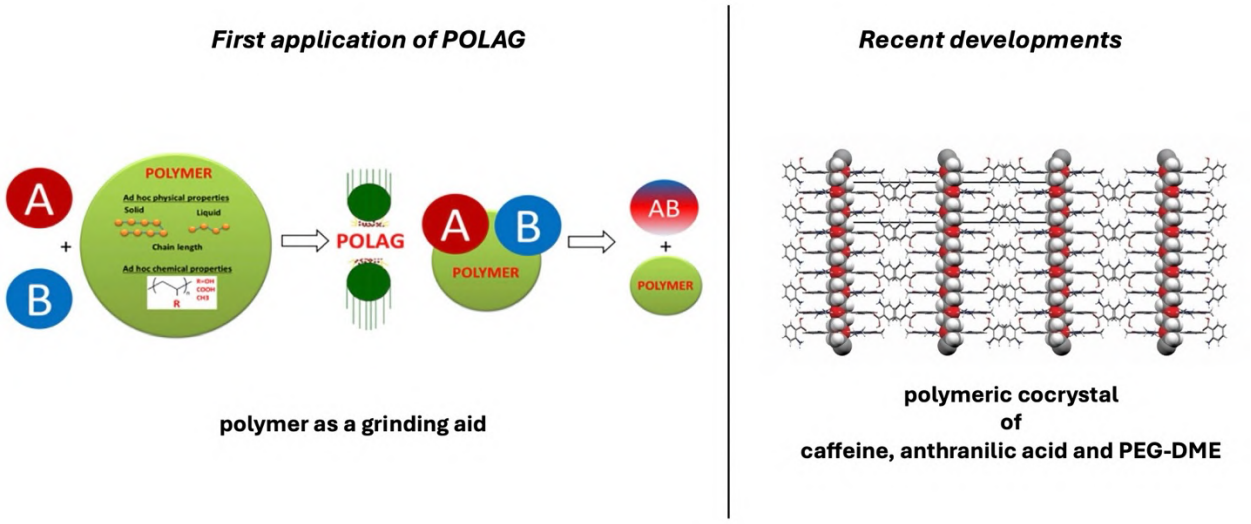

Figure 7. First application of POLAG (left) and recent advancements (right). Adapted from references [17,61].

1.1.3.5 Variable-temperature grinding (VATEG)

VATEG is a mechanochemical technique where the temperature is deliberately controlled and varied during the grinding process to influence reaction pathways, kinetics, and product formation. By adjusting the temperature of the grinding environment, VATEG allows researchers to precisely modulate the energy input and thermal environment of the reaction, thus affecting the formation and stability of different solid phases, such as polymorphs, amorphous phases, or cocrystals. VATEG

provides an additional degree of control over mechanochemical processes, enabling the synthesis of target materials that may not be accessible under ambient conditions.

For instance, grinding at temperatures below the glass transition temperature (T_g) of a material may facilitate the formation of amorphous phases, as suggested by Willart and Descamps [37]. In contrast, grinding above the T_g but below the melting point can promote the formation of specific polymorphic forms or stabilize metastable phases.

Recent studies have used VATEG to synthesize pharmaceutical cocrystals, where temperature control was shown to influence the stability and crystallinity of the resulting compounds [62]. VATEG has also been used to investigate the thermodynamics and kinetics of solid-state reactions, providing insights into the role of temperature in driving phase transitions, solvate formation, and decomposition processes [4].

1.1.3.6 Ion liquid-assisted grinding (ILAG)

ILAG is a mechanochemical technique where small quantities of ionic liquids (ILs) are added during the grinding process to act as reaction facilitators or catalysts [63]. ILs are salts that are liquid at relatively low temperatures (typically below 100 °C) and consist of a large organic cation and a small inorganic or organic anion [64]. Their unique properties, such as low volatility, high thermal stability, tunable polarity, and strong solvation ability, make them particularly suitable for enhancing mechanochemical processes. In ILAG, ILs are employed to improve the efficiency and selectivity of the grinding process by modulating the reaction environment, enhancing molecular diffusion, and stabilizing intermediates or products.

ILAG has been used to synthesize a variety of solid-state materials, including cocrystals, salts, solvates, and MOFs [15,58,63–66]. The addition of ILs can facilitate the formation of desired solid forms by acting as both a solvent and a template for the reactions, promoting the association between different molecules and enhancing the mechanochemical activation of reactants. In fact, ILAG has shown promising results in various applications, particularly in the synthesis of pharmaceutical cocrystals, where it has been demonstrated that ILs can provide a pathway to achieve desired cocrystal forms that are challenging to synthesize using traditional methods. Additionally, ILAG has been used to control polymorphism, enhance the solubility of poorly soluble drugs, and stabilize reactive intermediates during grinding processes [17,22,64–66].

1.1.4 Recent advances in mechanochemistry: speed mixing and resonant acoustic mixing (RAM)

Speed mixing and resonant acoustic mixing (RAM) are relatively recent advancements in the field of mechanochemistry, having gained attention in the last decade as novel methods for inducing and accelerating solid-state reactions. These techniques offer alternative ways to apply mechanical energy to materials, allowing for the efficient preparation of various pharmaceutical compounds, including cocrystals, amorphous dispersions, and other solid-state forms.

While speed mixing relies primarily on high-speed rotation and shear forces to achieve mixing [67–69], RAM leverages acoustic energy to accomplish similar goals. Both methods share the common objective of enhancing the energy transfer between particles, leading to improved mixing efficiency and faster reaction kinetics [70–73]. They can also be combined to achieve complementary effects; for example, using RAM to initially disperse and mix components and speed mixing to achieve a finer, homogeneous mixture [74].

1.1.4.1 Speed mixing

Speed mixing, also known as high-speed or dual asymmetric centrifugal (DAC) mixing, was developed to combine high rotational speeds with rapid mixing. This method involves the simultaneous rotation of a mixing vessel around two axes, creating a combination of centrifugal and shear forces. The dual-axis rotation creates complex flow patterns and high shear rates that promote intimate mixing and enhanced contact between reactant particles, leading to accelerated reaction rates. Speed mixing is particularly effective for producing homogeneous mixtures in a short amount of time, making it an ideal choice for mechanochemical processes that require precise control over reactant distribution [67–69,75].

1.1.4.2 Resonant acoustic mixing (RAM)

RAM was developed around the early 2000s and is a technique that uses low-frequency acoustic waves to induce vibrations in a mixing vessel, typically at frequencies between 50-100 Hz. The vibrations create high-acceleration movements that efficiently transfer mechanical energy to the reactant particles, causing collisions and friction that can trigger solid-state reactions. The term "resonant" refers to the mixing vessel being tuned to a resonant frequency, which maximizes energy transfer efficiency and minimizes energy loss [5,70–73,76,77].

RAM technique offers a significant advantage over traditional ball milling and other mechanical grinding methods by eliminating the need for direct contact between grinding media and the reactants.

This innovative approach allows for a more controlled and efficient mixing process, where mechanical energy is transferred acoustically rather than through physical collisions. As a result, RAM minimizes issues like excessive heat generation, which can lead to the degradation of heat-sensitive materials, and significantly reduces the risk of contamination. By maintaining the integrity of delicate compounds while still promoting mechanochemical reactions, RAM represents a cutting-edge solution in the field, particularly beneficial for applications requiring high precision and material stability. RAM has been shown to be effective for processing highly viscous materials, powders, and even composite materials with varying densities [71,72,77–79].

1.1.4.3 Pharmaceutical applications of speed mixing and RAM

These innovative mixing techniques have found applications in the pharmaceutical field, where they offer advantages in terms of improved process efficiency, scalability, and product quality. For instance, in literature there are few examples of their application for:

- Cocrystals: they have been used to synthesize pharmaceutical cocrystals by enhancing the contact between APIs and coformers, reducing the time needed to achieve the desired solid-state form [32,79–81].
- MOFs synthesis: both speed mixing and RAM have been successfully applied in the synthesis of MOFs, which are highly porous crystalline materials with significant potential in drug delivery, gas storage, and catalysis [78,82].
- Amorphous solid dispersions (ASDs): RAM has been employed in the preparation of ASDs, where APIs are dispersed within a polymeric matrix to improve solubility and stability. The gentle yet efficient mixing provided by RAM ensures that the API is uniformly distributed in the polymer, minimizing the risk of recrystallization and maintaining the amorphous state, which is critical for enhancing dissolution rates [83,84].
- Blend uniformity in tablet formulations: RAM is also being explored for ensuring uniformity in tablet formulations. The resonant acoustic waves can effectively mix powders of different particle sizes and densities, resulting in more consistent dosage forms and reducing the risk of content uniformity issues that can arise during conventional mixing methods [73,85].

This section has already been published.

1.2 Praziquantel

In recent years, the focus on developing innovative and affordable pharmacological solutions for neglected tropical diseases, such as Schistosomiasis, has grown significantly. The need for such treatments is accentuated by the fact that approximately 240 million people currently suffer from Schistosomiasis, and over 251 million required preventive treatments in 2021, according to the World Health Organization (WHO) [86]. Schistosomiasis is a parasitic disease, both acute and chronic, caused by blood flukes (trematode worms) of the genus Schistosoma. It is particularly prevalent in areas lacking adequate sanitation and clean water [87–89]. Infection primarily occurs when individuals encounter contaminated water, where larval forms of the parasite penetrate the skin [90]. Once inside the body, immature parasites develop into adult schistosomes, which release eggs into various tissues, leading to severe complications such as bladder cancer, kidney failure, liver fibrosis, and intestinal and urinary diseases [91].

Currently, praziquantel (PZQ) is the treatment of choice for all forms of Schistosomiasis [92,93]. It is included in the WHO Model List of Essential Medicines for both adults and children [94,95]. The recommended therapeutic regimen consists of a dose of 20 mg/kg administered three times per day at intervals of 4 to 6h, or a single dose of 40 mg/kg as preventive chemotherapy [91,96]. The relatively high dosage is due to PZQ classification as a Biopharmaceutics Classification System (BCS) class II drug, which indicates high permeability but low solubility (0.40 mg/mL in water (H_2O) at 25 °C) and bioavailability [97–100]. Additionally, PZQ undergoes extensive first-pass metabolism within 1-3h, forming mono- and di-hydroxy derivatives as its main metabolites [88,92,101]. Despite these challenges, PZQ is well-tolerated, safe, and cost-effective [102].

PZQ is administered orally (under the trade name Biltricide® [103]) as a racemic mixture [i.e., (11bRS)-2-(Cyclohexylcarbonyl)-1,2,3,6,7,11b-hexahydro-4-H-pyrazino[2,1-a]isoquinolin-4-one], although only the (R)-enantiomer is responsible for its therapeutic effects [104–109]. The (S)-enantiomer, on the other hand, contributes to the drug's bitter taste and certain side effects, such as abdominal pain, drowsiness, fever, nausea, and vomiting [110–113].

Due to its poor solubility, PZQ must be administered in relatively high doses, and its side effects, that are attributed to the (S)-enantiomer, highlight the importance of exploring alternative solid forms to enhance its physicochemical and biopharmaceutical properties. Over the past 50 years, significant research has been performed with the aim of improving the properties of PZQ through the development of ASDs with excipients like povidone [102,114–116], sodium starch glycolate [117], mesoporous silica [118], calcium carbonate complexes [119,120], mannitol and gelucire [121], and

clay minerals [122]. Other approaches have included the preparation of PZQ-β-cyclodextrin complexes [123–129], PZQ-liposome systems [130], polymeric and solid lipid nanoparticles [131–134], coground systems [42,45,135,136], fast-dispersing granules [137], melt granulation combined with ultrasonic spray congealing [138] and, more recently, micro- and nanocrystals [139,140].

Currently, alternative strategies are being explored to improve the physicochemical properties of PZQ. These include deracemizing the racemic compound by forming diastereomeric cocrystals, converting it into crystalline polymorphs, and developing multicomponent systems such as solvates, hydrates, and cocrystals.

In Table 1 are reported the different solid forms of PZQ (including enantiomers, polymorphs, solvates/hydrates, and cocrystals) discovered and isolated over the past five decades.

Table 1. Reported solid forms for PZQ.

Acronym	Type of solid form	Stoichiometry	Reference code	References
	Anhydrous polymorphs			
PZQ Form A	polymorph A	N/A[§]	TELCEU	[141]
PZQ Form B	polymorph B	N/A[§]	TELCEU01	[43]
PZQ Form C	polymorph C	N/A[§]	GOYZOM	[142]
PZQ Form D	polymorph D	N/A[§]	Not indexed	[143]
PZQ Form E	polymorph E	N/A[§]	Not indexed	[143]
PZQ Form G	polymorph G	N/A[§]	Not indexed	[144]
PZQ Form H	polymorph H	N/A[§]	Not indexed	[144]

Hydrates				
(S)-PZQ-HH	(S)-praziquantel hemihydrate	1:0.5	SIGBUG	[110]
(R)-PZQ-HH	(R)-praziquantel hemihydrate	1:0.5	SIGBUG01	[111]
(R)-PZQ-MH	(R)-praziquantel monohydrate	1:1	LIVFED	[104]
PZQ-MH	praziquantel monohydrate	1:1	Not indexed	[145]
PZQ-HH	(RS)-praziquantel hemihydrate	1:0.5	WUHQAU	[146]
PZQ-HH	(RS)-praziquantel hemihydrate	1:0.5	Not indexed	[147]
Solvates				
PZQ-2P	praziquantel-2-pyrrolidone	1:1	DAJCAW	[148]
PZQ-AA	praziquantel-acetic acid	1:1	DAJCEA	[148]
PZQ-DMA	praziquantel-dimethylacetamide	1:1	Not indexed	[144]
Cocrystals				
PZQ-OXA	praziquantel-oxalic acid	1:1	TELCOE	[141]
PZQ-MALO	praziquantel-malonic acid	1:1	TELDEV	[141,149]
α-PZQ-SUC	praziquantel-succinic acid Form α	1:1	TELDAR01	[141,150]
β-PZQ-SUC	praziquantel-succinic acid Form β	1:1	TELDAR	[141]
PZQ-MALE	praziquantel-maleic acid	1:1	TELCIJ	[141]

PZQ-FUM	praziquantel-fumaric acid	1:1	TELBUJ	[141]
PZQ-GLU	praziquantel-glutaric acid	1:1	TELDIZ	[141]
PZQ-ADI	praziquantel-adipic acid	2:1	TELCAQ	[141]
PZQ-PIM	praziquantel-pimelic acid	2:1	Not indexed	[141]
(R)-PZQ-GLU	(R)-praziquantel-glutaric acid	1:1	KEQVEL	[151]
(R)-PZQ-SUC	(R)-praziquantel-succinic acid	1:1	KEQVAH	[151]
(R)-PZQ/L-MAL	(R)-praziquantel-(L)-malic acid	1:1	CUZPIY	[152]
(S)-PZQ/L-MAL	(S)-praziquantel-(L)-malic acid	1:1	CUZPEU	[152]
PZQ-MAL	praziquantel-malic acid	1:1	Not indexed	[124]
PZQ-SA	praziquantel-salicylic acid	1:1	Not indexed	[124]
PZQ-TA	praziquantel-tartaric acid	1:1	Not indexed	[124]
PZQ-KAE	praziquantel-kaempferol	2:1	ANAYOG	[153]
PZQ-QUE 1	praziquantel-quercetin 1	2:1	ANAYUM	[153]
PZQ-QUE 2	praziquantel-quercetin 2	1:1	Not indexed	[153]
PZQ-MYR	praziquantel-myricetin	1:1	ANAZAT	[153]
PZQ-1,4-DITFB	praziquantel-1,4-diiodotetrafluorobenzene	1:1	AVEKAQ	[154]
PZQ-4-HA	praziquantel-4-hydroxybenzoic acid	1:1	AVEJIX	[154]
PZQ-3,5-DNA	praziquantel-3,5-dinitrobenzoic acid	1:1	AVEJET	[154]
PZQ-HQ	praziquantel-hydroquinone	1:1	AVEKIJ	[154]
PZQ-VA	praziquantel-vanillic acid	1:1	AVEJAP	[154]

PZQ-VA	praziquantel-vanillic acid	1:2	Not indexed	[154,155]
PZQ-2,5-DHA	praziquantel-2,5-dihydroxybenzoic acid	1:1	AVEHUH	[154]
PZQ-2,4-HA	praziquantel-2,4-dihydroxybenzoic acid	1:1	AVEJUJ	[154]
PZQ-ORC	praziquantel-orcinol	1:1	AVEHOB	[154]
PZQ-SA MH	praziquantel-salicylic acid monohydrate	1:1	AVEHER	[154]
PZQ-4-ASA ACN	praziquantel-4-aminosalicylic acid acetonitrile solvate	1:1:1	AVEJOD	[154]
PZQ-2,5-DHA ACN	praziquantel-2,5-dihydroxybenzoic acid acetonitrile solvate	1:1:1	AVEHIV	[154]
PZQ-3,5-DHA ACN	praziquantel-3,5-dihydroxybenzoic acid acetonitrile solvate	1:1:1	AVEKEU	[154]
PZQ-CA	praziquantel-citric acid	1:1	DAJYUM	[156]
PZQ-PA	praziquantel-phtalic acid	1:1	DAJZIB	[156]
PZQ-3-HA	praziquantel-3-hydroxybenzoic acid	2:1	DAJZEX	[156]
PZQ-4-HA	praziquantel-4-hydroxybenzoic acid	1:1	AVEJIX01	[156]
PZQ-PA	praziquantel-protocathecuic acid	1:1	Not indexed	[157]
PZQ-GA	praziquantel-gallic acid	1:1	Not indexed	[157]
PZQ-FA	praziquantel-ferulic acid	1:1	HIVXIX	[157]
PZQ-PA ACN	praziquantel-protocathecuic acid acetonitrile solvate	1:1:1	HIVXUJ	[157]
PZQ-GA ACN	praziquantel-gallic acid acetonitrile solvate	1:1:1	HIVXOD	[157]
(R)-PZQ/(S)-PZQ/D-MAL/L-MAL	(R)-praziquantel-(S)-praziquantel-(D)-malic acid-(L)-malic acid	1:1:1:x.x	2205816*	[158]

(R)-PZQ/(S)-PZQ/D-TA/L-TA	(R)-praziquantel-(S)-praziquantel-(D)-tartaric acid-(L)-tartaric acid	1:1:1:x.x	2205817*	[158]
PZQ-PU	praziquantel-N-phenyl urea	1:1	VOCRIS	[159]
(S)-PZQ-DMTU	(S)-praziquantel-1,3-dimethylthiourea	1:1	VOCREO	[159]
(R)/(S)-PZQ-DMTU	(R)/(S)-praziquantel-1,3-dimethylthiourea	1:1	VOCROY	[159]
PZQ-CU	praziquantel-curcumin	2:1	GOGSOO	[160]
PZQ-CU EA	praziquantel-curcumin ethyl acetate solvate	2:1:1	GOGVEH	[160]
PZQ-3-HA	praziquantel-3-hydroxybenzoic acid	1:1	ROLMEO	[161]
PZQ-BTC	praziquantel-benzene-1,2,4,5-tetracarboxylic acid	2:1	ROLMIS	[161]
PZQ-5-HIP ACN	praziquantel-5-hydroxyisophtalic acid acetonitrile solvate	1:4:2	ROLMOY	[161]
PZQ-TRI DH	praziquantel-trimesic acid dihydrate	1:2:2	ROLNIT	[161]
PZQ-SUB	praziquantel-3-hydroxybenzoic acid	2:1	ROLMAK	[161]
PZQ-CLA	praziquantel-chloranilic acid	1:1	JORKOU	[162]
(R)/(S)-PZQ-DBTFB	(R)/(S)-praziquantel-1,4-dibromotetrafluorobenzene	1:1	JORKUA	[162]
PZQ-DBTFB	praziquantel-1,4-dibromotetrafluorobenzene	1:1	JORLAH	[162]
PZQ-trans-FA	praziquantel-trans-ferulic acid	1:2	HIVXIX01	[162]
PZQ-2,3-DHA	praziquantel-2,3-dihydroxybenzoic acid	1:1	JORLIP	[162]
PZQ-TFTIB	praziquantel-1,3,5-trifluoro-2,4,6-triiodobenzene	1:1	JORLOV	[162]

§ not applicable for single compound, * reference code not found

1.2.1 (RS)-Praziquantel ((RS)-PZQ) (Form A): the commercial Form

PZQ is a white, crystalline, odorless powder known for its pronounced bitterness [98,163]. Chemically, it is a synthetic tetracyclic tetrahydroisoquinoline derivative with the IUPAC name (11bRS)-2-(Cyclohexylcarbonyl)-1,2,3,6,7,11b-hexahydro-4-H-pyrazino[2,1-a]isoquinolin-4-one, as shown in Figure 8. As depicted, PZQ lacks any H-bond donor groups, while its two amide carbonyl groups can act as H-bond acceptors.

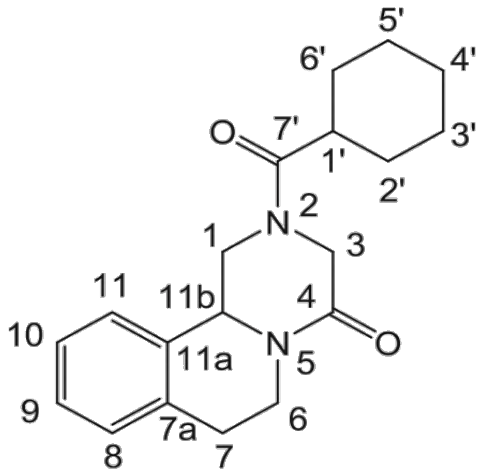

Figure 8. PZQ chemical structure with atom numbering.

PZQ is highly hydrophobic, with a LogP value of 2.7 [164], and is sparingly soluble in H_2O at 25 °C (0.40 mg/mL) across a pH range of 1 to 7.5 [99]. However, it is more soluble in organic solvents, with a solubility of 97 mg/mL in ethanol (EtOH) and 567 mg/mL in chloroform (CHF) [97,98,165]. Recent studies have further explored its solubility in various solvents at different temperatures, reporting results in terms of mole fraction. For instance, at room temperature, the solubility is 2.214 × 10^{-2} in acetone (ACT), 4.336 × 10^{-2} in cyclohexanone (CyHXN), 2.291 × 10^{-2} in n-hexane (n-HXN), 2.012 × 10^{-2} in ethyl acetate (EA), and 2.521 × 10^{-2} in acetonitrile (ACN). As typical of an endothermic process, the solubility of PZQ increases with rising temperature [166,167].
PZQ exhibits an intrinsic dissolution rate (IDR) of 31.2 ± 0.6 µg x cm^{-2} min^{-1} at 37 °C [43] (Figure 9). Its melting point is characterized by a sharp endothermic signal within the range of 136-142 °C, with no indication of concurrent decomposition [98,99] (Figure 9).

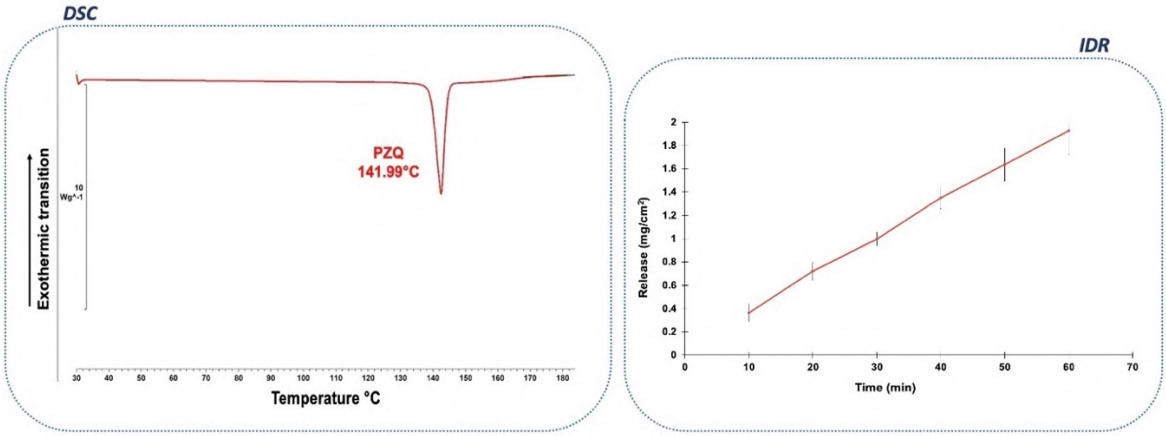

Figure 9. DSC curve (left) and IDR (right) of PZQ Form A.

Needle-like single crystals of suitable size for single-crystal X-ray diffraction (SXRD) analysis were first obtained by Espinosa and colleagues through the slow evaporation of a 1:1 solution of (RS)-PZQ and pimelic acid (PIM) in a solvent mixture of ACT and H_2O [141]. The (RS)-PZQ form, commonly referred to as Form A and indexed as TELCEU in the Cambridge Structural Database (CSD [168]), crystallizes in the triclinic space group *P*-1, featuring four crystallographically independent molecules in the asymmetric unit (ASU).

Among these four independent molecules, two exhibit orientational disorder in the cyclohexyl segment due to the presence of two rotamers, as confirmed by dynamic ^{1}H-NMR measurements [104]. Despite this disorder, all the carbonyl groups of the four PZQ molecules in the unit cell are aligned in the *syn*-conformation, indicating a consistent spatial arrangement [141,169,170].

The crystallographic data, as well as the details of the crystal structure, are illustrated in Figure 10.

Crystal data	(RS)-PZQ
formula	$C_{19}H_{24}N_2O_2$
MW (g/mol)	312.411
T (K)	293
Space group	P-1
a (Å)	10.454(3)
b (Å)	15.112(4)
c (Å)	22.963(6)
a (°)	99.531(5)
b (°)	98.419(5)
g (°)	108.270(5)
V (Å^3)	3320.1(16)
Z	8
m (mm^{-1})	0.081
r_{calcd} (g/cm^{-3})	1.250
R	0.0810
R_w	0.2232

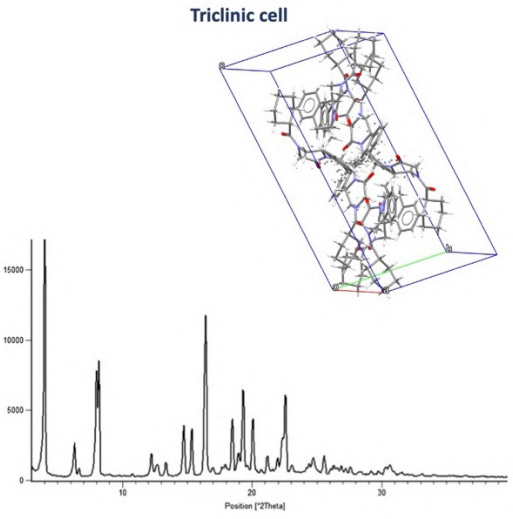

Figure 10. PXRD pattern and crystallographic data of PZQ Form A.

In addition to differential scanning calorimetry (DSC), thermogravimetric analysis (TGA), and powder X-ray diffraction (PXRD), Fourier-transform infrared spectroscopy (FT-IR) and solid-state NMR (SSNMR) are key solid-state techniques used to investigate crystal polymorphism and the interactions between PZQ and coformers in its various multicomponent solid forms. These techniques have been instrumental in characterizing all the polymorphs and new solid forms of PZQ discovered to date.

The FT-IR spectrum of (RS)-PZQ can be seen in Figure 11.

Various FT-IR spectra of (RS)-PZQ have been reported in literature [117,125,133,138,171,172], but some discrepancies were noted in the assignment of certain vibrational bands, particularly those associated with the carbonyl groups. These discrepancies were later refined through calculations based on Density Functional Theory (DFT) using the DMOL3 program [170].

Specifically, (RS)-PZQ exhibits two main characteristic bands in the range of 3028-2852 cm^{-1}, attributed to the stretching vibrations ν(CH) of CH and CH_2 groups, with the aromatic CH bonds appearing at higher frequencies than the aliphatic ones. The ν(C=O) bands are observed between 1736-1627 cm^{-1}; however, initial studies failed to differentiate between the two carbonyl groups of PZQ (i.e., the heterocyclic carbonyl and the cyclohexyl carbonyl). This difficulty arises from the fact that both carbonyl groups share a similar local environment, making it challenging to assign specific bands to each group [117,125,133,138,170,171].

In a subsequent study, Borrego et al. were able to distinguish the two ν(C=O) bands through additional computational calculations. They suggested that the stretching of the C-C=O plane, twisted for the heterocyclic carbonyl group, appears at higher frequencies, while the cyclohexyl carbonyl group, where the carbonyl is coplanar with the ring, resonates at lower frequencies [169].

Other researchers have also reported bands corresponding to C-H bond deformation or bending δ(CH) and stretching vibrations of the C-N bonds ν(CN) in the range of 1450-1200 cm^{-1} [125,133], which are slightly lower than those predicted by Borrego and coauthors [170]. Simulations comparing the DFT-calculated spectra for both the *anti*- and *syn*-conformation of (RS)-PZQ with experimental data revealed that in the *syn*-conformation, both carbonyl groups are oriented toward the $COCH_2N$ group, creating a stronger local dipole effect than in the *anti*. Consequently, the frequency difference in ν(C=O) between the two carbonyl groups is greater in the *syn*-conformation [170]. In a later study, the authors concluded that the *anti*-conformation is less polar and therefore more stable in an apolar environment, whereas the *syn*-conformation is more polar [169].

A comparison of the two calculated conformations with experimentally observed carbonyl group frequencies (bands at 1647 and 1624 cm^{-1}) confirmed that (RS)-PZQ Form A adopts the *syn*-conformation, as evidenced by its molecular packing in the crystal structure [43,45,141,169,170].

The ^{13}C and ^{15}N CPMAS SSNMR spectra of (RS)-PZQ have been detailed by Arrúa, Costa and Zanolla et al. [43,116,127]. The ^{13}C CPMAS spectrum is characterized by the splitting of all signals, most prominently seen in the resonance around 164 ppm, which corresponds to the carbonyl C4 (refer to Figure 8 for atom numbering). This signal splitting confirms the presence of four crystallographically independent molecules in the unit cell, consistent with the known crystal structure. The spectrum can be divided into three distinct regions: the aliphatic carbon region (20-60 ppm), the aromatic carbon region (120-135 ppm) and the carbonyl region (160-175 ppm).
In the ^{15}N CPMAS spectrum, resonances for the nitrogen atoms N2 and N5 are clearly distinguishable with chemical shifts at 82.4 and 97.2 ppm, respectively.
The Table in Figure 11 provides the experimental ^{13}C and ^{15}N chemical shifts (in ppm) with their corresponding assignments for each atom. Figure 11 illustrates the ^{13}C and ^{15}N spectra of (RS)-PZQ, providing further clarity on the molecular structure and its solid-state behavior.

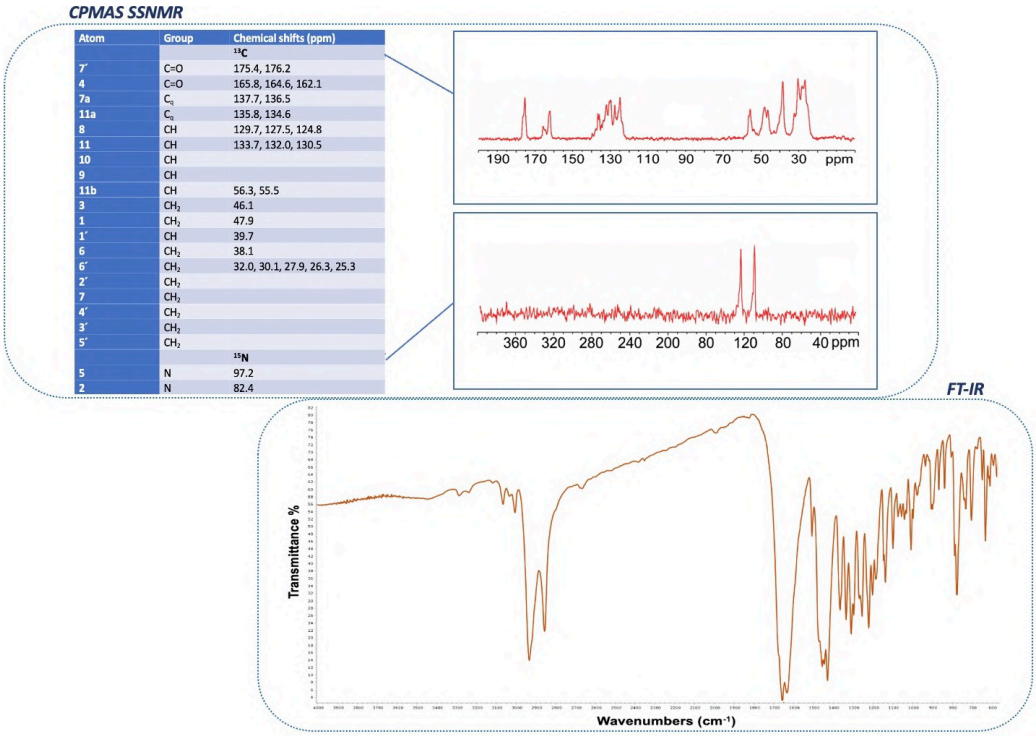

Figure 11. FT-IR spectrum and chemical shifts assignments and ^{13}C and ^{15}N SSNMR spectrum of PZQ Form A. Adapted from references [43,141].

1.2.2 PZQ enantiomers

As highlighted before, PZQ is administered as a racemic mixture ((RS)-PZQ), even though its schistosomicidal activity is solely attributed to the (R)-enantiomer. In contrast, the (S)-enantiomer is primarily responsible for its bitter taste and undesirable side effects [108,109,113]. Studies have shown that administering the pure (R)-eutomer can potentially reduce adverse effects and lower the required dosage [173].

Enantiomerically pure (S)-(+)-PZQ and (R)-(-)-PZQ were first isolated as hemihydrates ((S)-PZQ-HH [110] and (R)-PZQ-HH [111]) through an integrated approach combining chromatography for enantioenrichment and subsequent crystallization from a methanol/water ($MeOH/H_2O$) mixture. These two hydrated forms provided the first crystal structures of the pure enantiomers, indexed in the CSD as SIGBUG and SIGBUG01, respectively. Both enantiomers crystallize in the monoclinic space group *C*2, featuring four molecules in the unit cell connected via hydrogen bonds (H-bonds) and one independent molecule in the ASU. Notably, these enantiomers adopt an *anti*-conformation, in contrast to the *syn*-conformation observed for racemic (RS)-PZQ. This difference is due to water molecules forming bridging H-bonds between the carbonyl groups of different molecules [119,169,170]. The melting points of these enantiomers (~110 °C) suggest improved solubility compared to racemic (RS)-PZQ [165,172].

In 2013, Cedillo et al. [174] isolated an enantiomerically pure PZQ derivative, (S)-(+)-cis-4-benzyloxy-PZQ, using praziquanamine as an intermediate for synthesizing (S)-(+)-cis-4-hydroxy-PZQ, a key PZQ metabolite [101]. The crystal structure of this derivative was indexed as RIMBIA in the CSD. A year later, the same group used an alternative approach to isolate the (R)-eutomer by forming diastereoisomers derived from (S)-(+)-naproxen (i.e., (R)-(-)-PZQ-(S)-naproxen and (S)-(+)-PZQ-(S)-naproxen). These diastereoisomers were separated via flash column chromatography, followed by acid hydrolysis and acylation of the desired diastereoisomer (R)-(-)-PZQ-(S)-naproxen, indexed as LIVDOL in the CSD, to yield enantiomerically pure (R)-PZQ as a monohydrate ((R)-PZQ-MH) [104]. Through a four-step synthetic sequence starting from (R)-PZQ-MH, they also produced enantiomerically pure (R)-PZQ derivatives, such as (R)-(-)-trans-4-hydroxy-PZQ-MH and (R)-(-)-cis-4-benzyloxy-PZQ, with their respective crystal structures indexed as LIVFED, LIVFIH, LIVDUR, and LIVFAZ. Interestingly, (R)-PZQ-MH exhibited the same *anti*-conformation as the previously described hemihydrates (SIGBUG and SIGBUG01), unlike the *syn*-conformation seen in racemic (RS)-PZQ.

In 2015, researchers resolved (RS)-PZQ by forming diastereomeric cocrystals with enantiomerically pure L-malic acid (L-MAL) as a coformer [152]. Using LAG with AcT, they obtained a novel phase

that, upon further analysis, was revealed to be a mixture of diastereomeric cocrystals (R)-PZQ/L-MAL and (S)-PZQ/L-MAL, indexed as CUZPIY and CUZPEU in the CSD. Both cocrystals displayed similar unit cell parameters and space group ($P2_1$) and exhibited the *anti*-conformation of the PZQ carbonyl groups. However, (R)-PZQ/L-MAL exhibited stronger intermolecular interactions and a higher melting point, as confirmed by DSC. Solubility experiments showed notable differences between the two cocrystals, which enabled the chiral resolution of racemic (RS)-PZQ via fractional crystallization. Moreover, IDR analysis showed that (R)-PZQ/L-MAL exhibited significantly higher dissolution rates than both (R)-PZQ-HH and (RS)-PZQ.

In 2021, Valenti et al. developed an innovative deracemization technique by coupling incompatible racemization and crystallization processes [175]. By screening 30 crystalline derivatives, they identified a derivative (PZQ + pivaloyl derivative) that crystallizes as a conglomerate, which enabled racemization. Using a palladium on carbon (Pd/C) packed column at 130 °C, they achieved racemization, while deracemization was accomplished by alternating crystal growth and dissolution steps through temperature cycling. This approach achieved complete deracemization of the solid phase, yielding the desired (R)-enantiomer.

1.2.3 PZQ crystalline polymorphs

Structural and crystal polymorphism are well-known phenomena in the solid-state. According to the International Union of Pure and Applied Chemistry (IUPAC), a polymorph is defined as a solid crystalline phase that shares the same chemical composition as another phase but exhibits a different crystal structure [176]. These polymorphs possess distinct intermolecular and/or interatomic distances, resulting in structural variations that can significantly impact the physical and chemical properties of a drug [177–179]. As a result, polymorphism has gained attention as a viable strategy for enhancing certain physicochemical properties of pharmaceutical solids, without introducing exogenous atoms or molecules in the API structure.

Although investigations on PZQ began over fifty years ago, with the drug receiving approval for human Schistosomiasis treatment in 1980 [87,180,181], the first polymorphic form of the racemic compound, referred to as Form B, did not appear in literature until 2018. Multiple attempts to crystallize new polymorphs of PZQ through slow evaporation using various solvents such as H_2O, EtOH, MeOH, 2-propanol (2-PrOH), 1,2-ethanediol, and dimethyl sulfoxide (DMSO), only resulted in the formation of the known Form A [182].

Table 2 provides a schematic overview of all known polymorphs of PZQ, along with the methods by which they were discovered.

Table 2. Overview of known PZQ polymorphs and respective discovery methods.

polymorphic form	method	reference code	reference
A	commercial	TELCEU	Espinosa-Lara et al., 2013[141]
B	neat grinding, 4h, 20 Hz	TELCEU01	Zanolla et al., 2018[43]
C	neat grinding, 4h, 23 Hz	GOYZOM	Zanolla et al., 2019[142]
D	neat grinding, 5h, 25 Hz	Not indexed	Saikia et al., 2021[143]
E	liquid-assisted grinding (10 μL THF), 1h, 25 Hz	Not indexed	Saikia et al., 2021[143]
G	desolvation of PZQ-DMA monosolvate	Not indexed	Guedes Fernandes de Moraes et al., 2023[144]
H	cooling crystallization, without agitation	Not indexed	Guedes Fernandes de Moraes et al., 2023[144]

Zanolla et al. succeeded in isolating polymorph B by milling commercial Form A using NG conditions at 20 Hz for 4h [43]. This new polymorph exhibited distinct physical properties and improved biopharmaceutical characteristics, which will be discussed below.

Scanning electron microscopy (SEM) revealed that the crystals of Form B had a markedly different morphology compared to the needle-like crystals of Form A. Form B appeared as aggregates of long, thin whiskers (see Figure 13 below). DSC and TGA indicated that Form B is anhydrous, with the DSC curve showing a single endothermic peak at 112.10 °C, corresponding to its melting point and confirming the absence of any dehydration events. PXRD analysis further confirmed that Form B was structurally distinct from Form A. The crystal structure of Form B, solved using Synchrotron XRD, revealed that it crystallizes in the centrosymmetric monoclinic space group *C*2/*c*, with eight molecules per unit cell and one independent molecule in the ASU (Figure 12).

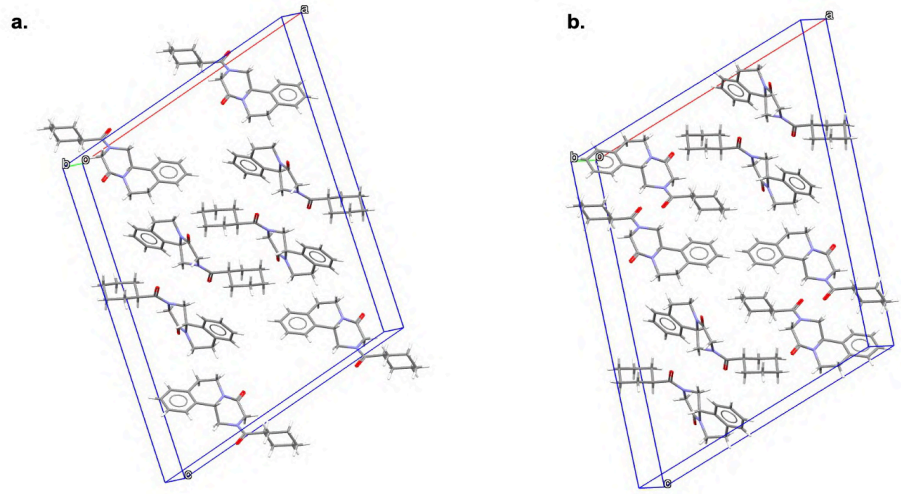

Figure 12. Crystal structures of (**a**) polymorph B and (**b**) polymorph C of PZQ.

The ^{13}C CPMAS spectrum of Form B displayed a single set of resonances, unlike Form A, which showed signal splitting due to the presence of four crystallographically independent molecules. Both the ^{13}C and ^{15}N SSNMR spectra exhibited sharp peaks, shifted slightly from those of Form A, confirming the formation of a new crystalline phase. FT-IR spectroscopy also revealed subtle differences between the two polymorphs. In Form A, two distinct signals at 1647 cm^{-1} and 1624 cm^{-1} correspond to the stretching vibrations of the heterocyclic and cyclohexyl carbonyl groups, respectively [43,45,141,169]. In Form B, these signals nearly overlapped, reducing the frequency difference in carbonyl vibrations, consistent with the *anti*-conformation of PZQ, as supported by theoretical calculations [119,170].

In terms of biopharmaceutical properties, Form B displayed significantly improved solubility and IDR compared to Form A. Specifically, Form B exhibited a water solubility of 281.31 ± 8.32 mg/L at 20 °C, nearly double that of Form A (140.30 ± 9.26 mg/L), and an IDR of 62.2 ± 1.3 µg x cm^{-2} min^{-1} at 37 °C, also approximately double that of Form A (31.2 ± 0.6 µg x cm^{-2} min^{-1}). Furthermore, *in vitro* tests of antischistosomal activity against Schistosoma *mansoni* (S. *mansoni*) demonstrated that Form B had an IC_{50} of 0.07 µg/mL, closely matching the value for Form A (0.05 µg/mL). *In vivo* studies on infected mice revealed that both polymorphs significantly reduced the overall worm burden (WBR) when administered orally, with a WBR of 89% for Form B and 87% for Form A at the highest tested dose of 300 mg/kg [183].

Stability studies indicated that Form B remains physically stable under dry conditions at room temperature for at least 12 months. Additional methods for producing polymorph B were later developed. For instance, Zanolla et al. discovered that Form B could be obtained from PZQ

hemihydrate (PZQ-HH) by subjecting it to various conditions. After four months of monitoring the stability of PZQ-HH, they observed its conversion to Form B, which was initially misidentified as Form A. Form B could also be generated by heating PZQ-HH at 50 °C under vacuum (35 mmHg) overnight, or by milling the hemihydrate for 60 min at 25 Hz [146].

Another study identified other conditions leading to the formation of polymorph B during cooling crystallization in the presence of triethylamine (TEA). When the crystallization process was performed without filtration or agitation, Form B emerged [144]. In contrast, cooling crystallization with TEA in the presence of agitation or filtration led to the formation of Form A or a solvated form of PZQ, depending on the solvent. This demonstrates the significant role of process parameters in determining the polymorphic outcome.

By systematically exploring the experimental design space for polymorph B formation as a function of two key milling parameters—frequency and milling time—using a rotated Doehlert matrix [184] , Zanolla et al. discovered a third polymorph, designated Form C [142].

SEM revealed that Form C consists of clustered particles (see Figure 13), distinct from the needle-shaped crystals of Form A and the thin whiskers of Form B. Thermal analysis showed that Form C exhibits a single melting peak at 106.84 °C, with no dehydration or other thermal events, as confirmed by TGA. Form C (indexed as GOYZOM in the CSD) crystallizes in the centrosymmetric monoclinic space group *I*2/*c*, with eight molecules per unit cell and one independent molecule in the ASU (see see Figure 12 above), as corroborated by ^{13}C CPMAS SSNMR spectroscopy. Polarimetric analysis also confirmed its racemic nature, with an optical rotation of $[\alpha] = 0.0144 \pm 0.0295$ (n=3).

The FT-IR spectrum of Form C closely resembled that of Form B, further indicating a structural relationship between the two polymorphs and their difference from the commercial Form A. The characteristic carbonyl stretching bands of Form A at 1647 and 1624 cm^{-1}, indicative of its *syn*-conformation, were shifted in Form C to 1642 and 1631 cm^{-1}, suggesting a conformational change in the *anti* PZQ coformer, as seen in polymorph B [119].

Further characterization of Form C revealed significant differences in its physicochemical properties. The new polymorph exhibited the highest water solubility among the three forms, at 382.69 ± 9.26 mg/L at 20 °C, compared to 281.31 ± 8.32 mg/L for Form B and 140.30 ± 9.26 mg/L for Form A. This trend aligns with the relative melting points, where Form C has the lowest melting temperature, followed by Forms B and A. In terms of *in vitro* antischistosomal activity against S. *mansoni*, Form C demonstrated an IC_{50} of 0.21464 μM after 72h, comparable to the literature-reported IC_{50} of 0.1 μM for Form A [185]. However, in contrast to the high stability of Form B, which remained stable

for over a year, Form C exhibited significantly lower physical stability, maintaining its form for only two months. This reduced stability aligns with its lower melting point and higher water solubility.
Like Form B, subsequent research uncovered alternative methods for producing Form C. Saikia et al. reported the formation of Form C with trace amounts of Form A by performing LAG using 5 μL of tetrahydrofuran (THF) [143]. Additionally, Guedes Fernandes de Moraes et al. successfully obtained Form C via both fast and slow cooling crystallization in TEA, regardless of the initial concentration of PZQ Form A [144].

In 2021, Saikia and colleagues identified two new polymorphic forms of PZQ, designated Form D and Form E, through mechanochemical methods [143]. Form D was specifically obtained by NG of PZQ Form A for 5h at a frequency of 25 Hz. DSC revealed a melting point of 133.3 °C for this novel polymorph. Further confirmation of the formation of Form D came through FT-IR spectroscopy, which showed shifts in key frequencies.
LAG with the addition of 10 μL of THF or ACT led to the formation of a different polymorph, named Form E. DSC analysis of this new form indicated a melting point at 135.5 °C, suggesting a distinct solid-state structure. This was further supported by PXRD, which displayed a pattern significantly different from that of Form A, including the disappearance of the characteristic peak at 6.7° 2θ and the emergence of a very intense peak at 21.8° 2θ. SSNMR spectroscopy of Form E further confirmed its uniqueness by showing chemical shifts of the two carbonyl groups at 175.3/173.0 ppm and 162.2 ppm, as opposed to the shifts reported for Form A (175.4/176.2 ppm and 165.8/164.6/162.1 ppm).
Unfortunately, attempts to obtain suitable single crystals of Forms D and E for SXRD analysis were unsuccessful, leaving their precise crystal structures unsolved. Nevertheless, the discovery of these polymorphs further expands the polymorphic landscape of PZQ and underscores the versatility of mechanochemistry in generating new solid forms.

More recently, two additional polymorphic forms of PZQ have been discovered, named Form G and Form H [144]. Starting with Form G, Guedes Fernandes de Moraes et al. first detected its presence while characterizing the PZQ-dimethylacetamide (PZQ-DMA) solvate through thermal analysis. The DSC curve revealed a new endothermic peak at 132.57 °C, positioned between the desolvation event and the melting point of Form A. Upon studying the physical stability of the PZQ-DMA solvate at ambient conditions, it was observed that after 20 days, the solvate transformed into a mixture of Form A and a previously unidentified form, confirmed by new peaks in PXRD analysis. The authors were able to isolate pure Form G by exposing PZQ-DMA to a water-vapor-induced atmosphere overnight. This newly identified form exhibited an endothermic event at 132.57 °C, attributed to its melting

point, as no mass loss was detected in concurrent TGA experiments, ruling out desolvation. Furthermore, Form G displayed a distinct habitus compared to the lath-shaped PZQ-DMA crystals, presenting smaller rod-like crystals (Figure 13). However, no further characterization of Form G has been conducted so far.

The other polymorph, Form H, emerged from studies investigating the influence of two process parameters on the cooling crystallization of (RS)-PZQ in the presence of TEA. Specifically, when the prepared solution was filtered before cooling and agitation was avoided, a new metastable polymorph, Form H, was formed. DSC analysis identified a unique endothermic peak at 79.59 °C, which did not correspond to any weight loss in the TGA, confirming it as a melting event. This established Form H as the most thermally unstable anhydrous polymorph of PZQ. SEM images revealed small platy crystals for Form H (Figure 13). However, no additional solid-state properties of this polymorph have been reported to date [144].

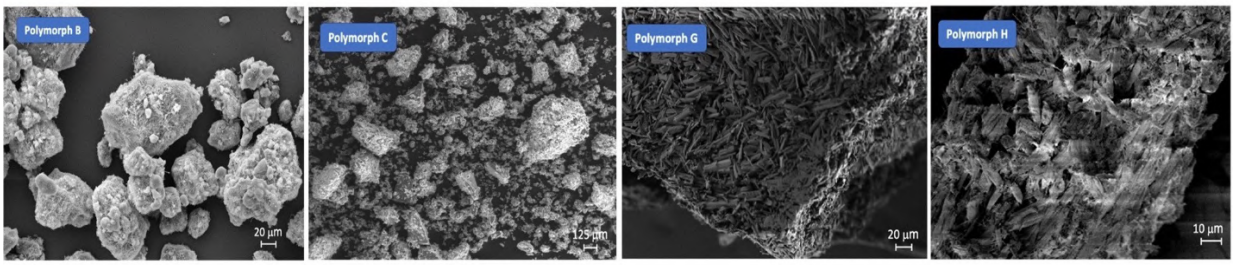

Figure 13. SEM images of polymorph B (1000x), polymorph C (50x), polymorph G (295x) and polymorph H (775x). Adapted from references [43,142,144].

1.2.4 PZQ amorphous forms

Literature provides limited information regarding the amorphous forms of PZQ.

Most studies highlight the formation of ASDs of PZQ in the presence of a secondary compound, such as polymers, to enhance amorphization and stability [45,102,114,119,121,122,135,139,140,186,187]. However, in 2018, Zanolla et al. demonstrated that it was possible to obtain amorphous PZQ without any secondary substances by employing a melt-quenching method [42]. Specifically, amorphous PZQ was obtained by heating the compound from 25 °C to 160 °C at 10 K/min, cooling it down to 0 °C at 20 K/min, and subsequently re-heating to 100 °C at 20 K/min. The T_g of amorphous PZQ was determined through modulated differential scanning calorimetry (MTDSC) and was identified as an inflection point at 37.70 °C, closely matching the theoretically predicted value [188].

In the same study, the authors also achieved amorphous PZQ with residual crystallinity by conducting cryogenic NG at low temperatures, using liquid nitrogen as a cryogenic medium.

In a subsequent study on the mechanochemical conditions for PZQ polymorph C formation, Zanolla and colleagues also observed the formation of amorphous-nanocrystalline PZQ when lower mechanochemical energy (lower frequency and extended milling time) was applied [142]. Notably, PZQ did not degrade when milled alone, unlike in cases where amorphous dispersions were formed. In those cases, diminished drug recovery was often observed, with degradation highly dependent on the type and percentage of the excipient used [42,45,118].

A later study introduced a novel approach to amorphizing PZQ by grinding polymorph E for 1h without solvents. This amorphous state was stable under ambient conditions for two weeks, after which it recrystallized into polymorph B following a heating cycle to 135 °C and cooling back to room temperature [143].

In 2020, Salazar-Rojas et al. presented another method for obtaining amorphous PZQ, like that proposed by Costa et al. [116]. Going into more details, Form A was placed in a vacuum oven at 150 °C under 60 mmHg for 30 min, then transferred to a desiccator and stored below 30 °C. Confirmation of the amorphous state was provided by optical microscopy, which showed the absence of crystalline habitus, and further supported by classical solid-state characterization techniques. No melting point was detected via DSC, although no T_g value was reported. The amorphous form displayed typical PXRD halo patterns and signal broadening in SSNMR. Moreover, the IDR of amorphous PZQ was significantly higher, at 9.0 mg x cm^{-2} h^{-1}, compared to 1.6 mg x cm^{-2} h^{-1} for Form A [145].

Most recently, in 2023, Guedes Fernandes de Moraes et al. achieved amorphous PZQ via fast cooling crystallization using MeOH/H_2O mixtures with 50% v/v H_2O content, although further characterization of this form was not conducted [144].

1.2.5 PZQ multicomponent solid forms

1.2.5.1 PZQ Hydrates

The study of hydrated forms of drugs is crucial because water is commonly present in various preformulation studies and throughout multiple stages of drug manufacturing. Water molecules, with their donor and acceptor hydrogen groups, can form H-bonds with other compounds. This ability to create H-bonds can significantly affect the properties of the drug. Specifically, the formation of hydrates often alters several physicochemical characteristics of the drug, including its solubility. Hydrates typically exhibit lower solubility compared to their anhydrous counterparts, which in turn can influence their biopharmaceutical properties [189]. Therefore, a thorough investigation of the hydrated forms of a drug is often essential.

In the case of the anthelmintic drug (RS)-PZQ, three distinct hydrated forms have been documented in literature.

The first hydrated form of PZQ, identified as PZQ monohydrate (PZQ-MH), was reported by Salazar-Rojas and colleagues. This form appeared as a distinctive pink solid. To obtain PZQ-MH, PZQ Form A was melted in a vacuum oven at 150 °C under 60 mmHg for 30 min. The molten PZQ was then transferred to a humidity-controlled chamber, rapidly cooled to 20 °C with liquid nitrogen, and exposed to 70% relative humidity (RH %). After cooling, the solid was stored in a freezer at -20 °C overnight and subsequently kept below 30 °C in a closed flask for further analysis [145].
Thermal analysis of the new form revealed two distinct endothermic transitions: the first, a broad endothermic event starting at approximately 78 °C and ending at 130 °C, was attributed to dehydration, while the second peak at 144 °C corresponded to the melting point of PZQ Form A. TGA analysis confirmed a gradual weight loss between 80-120 °C, totaling 5.4%, which aligns with the theoretical value for a PZQ monohydrate. The water content of PZQ-MH confirmed the 1:1 stoichiometry.
Crystallinity of PZQ-MH was confirmed by PXRD, which displayed sharp peaks distinctly different from those of Form A. Spectroscopic analysis revealed an intense peak at 3417 cm^{-1} in the FT-IR spectrum, indicating the presence of water within the crystal structure. In the region related to carbonyl stretching vibrations, PZQ-MH exhibited a single shifted carbonyl signal at 1626 cm^{-1}, compared to the double peak at 1647 and 1624 cm^{-1} observed for anhydrous Form A. This shift suggests interactions between the carbonyl group and water, as also indicated by the deshielding of carbonyl carbon atoms in the SSNMR spectra.
^{1}H-NMR spectroscopy further confirmed the presence of water, with a distinct resonance at 1.63 ppm. The integral of this signal was compared to the doublets in the 4.6-3.7 ppm region to verify the 1:1 stoichiometry.
Interestingly, PZQ-MH demonstrated a slightly higher dissolution rate (2.2 mg x cm^{-2} h^{-1}) compared to Form A (1.6 mg x cm^{-2} h^{-1}), which is contrary to the usual expectation that hydrates have lower dissolution rates [189]. Despite the extensive characterization, the crystal structure of PZQ-MH has not yet been solved or deposited in the CSD.

Zanolla and colleagues identified a new racemic PZQ hemihydrate (PZQ-HH) through mechanochemical processes [146]. They described several methods for synthesizing this hydrated form: PZQ-HH could be obtained by a two-step mechanochemical treatment comprising 30 min of NG, which involves the formation of an amorphous intermediate, followed by 1h of LAG with water. Alternatively, PZQ-HH was also successfully synthesized in a one-step 1h LAG process using Form

B as the starting material. Furthermore, slurry experiments with PZQ Form B over three days resulted in the formation of PZQ-HH, whereas Form A did not convert to PZQ-HH under similar conditions. PZQ-HH could also be formed by grinding PZQ Form A with a small amount of preformed PZQ-HH seeds (95:5 or 90:10 w/w) in a 1h LAG process with water. This method demonstrated that even a few seeds of PZQ-HH could promote the complete transformation of Form A into PZQ-HH, allowing for a one-step procedure rather than the previously mentioned two-step treatment.

The new hydrated form was extensively characterized. PZQ-HH appeared as a white powder composed of large, porous plate-like agglomerates with a broad specific surface area (see Figure 15 below). Thermal analysis of PZQ-HH revealed a sharp endothermic event at approximately 68 °C, indicative of dehydration, followed by two additional endothermic transitions at 109.05 °C and 133.95 °C, corresponding to the melting points of polymorph B and Form A, respectively. These transitions were corroborated by hot-stage microscopy (HSM). TGA analysis showed a weight loss of 2.19%, consistent with the theoretical value for a hemihydrate.

The PXRD pattern of PZQ-HH exhibited unique sharp reflections, distinct from those of known PZQ forms, including Form A, B, and C, as well as enantiomeric hemihydrates. The crystal structure of PZQ-HH was solved from the capillary PXRD pattern and indexed as WUHQAU in the CSD (Figure 14). PZQ-HH crystallizes in the triclinic space group *P*-1 (like Form A) but contains only one independent molecule per ASU, unlike the four in TELCEU. Each H_2O molecule in the crystal structure is H-bonded to two PZQ molecules (one (R)- and one (S)-), confirming the 1:0.5 stoichiometry. The carbonyl groups in PZQ-HH exhibit the *anti*-conformation, like Forms B and C, but different from the *syn*-conformation in Form A.

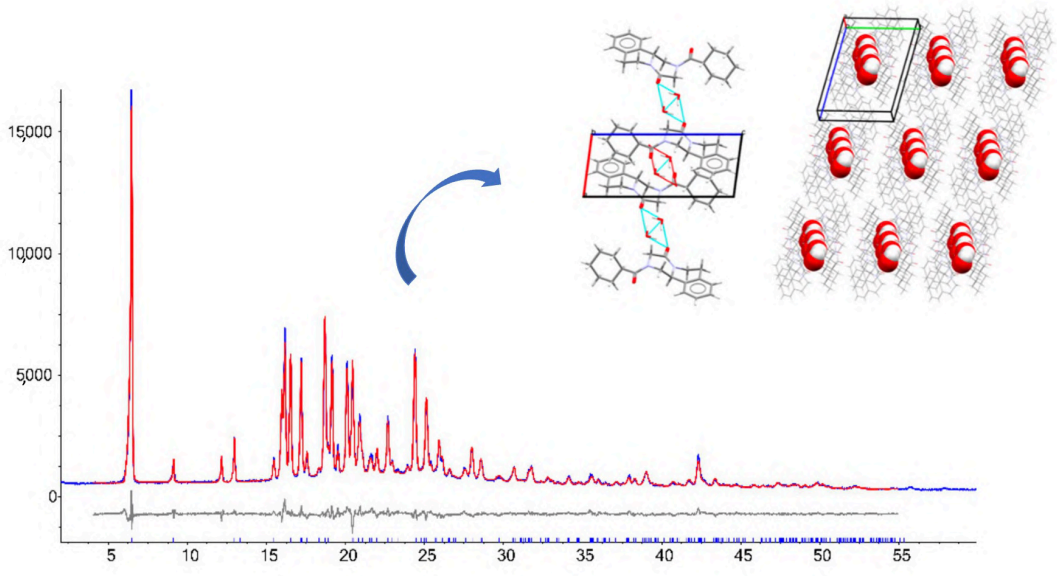

Figure 14. Rietveld refinement from the experimental pattern and crystal structure with packing and H-bonds motifs of PZQ-HH. Adapted from reference [146].

^{13}C CPMAS SSNMR spectra supported the formation of a new pure phase and confirmed the presence of only one molecule per ASU, aligning with crystallographic data. SSNMR analysis indicated significant similarities between PZQ-HH and Form B, but notable differences from Form A.

FT-IR spectroscopy revealed a sharp band at 3543 cm^{-1}, confirming the presence of water, and a broad band at 1629 cm^{-1} for the carbonyl stretching, shifting from the typical doublet at 1647 and 1624 cm^{-1} in Form A. This shift indicates intermolecular interactions between PZQ carbonyl groups and water.

Regarding biopharmaceutical properties, PZQ-HH demonstrated improved water solubility, measured at 310.89 ± 3.07 mg/L, compared to 217 ± 10.33 mg/L for Form A. The IDR of PZQ-HH was 0.0618 ± 0.0051 mg x cm^{-2} h^{-1}, comparable to Form B and about twice that of Form A (0.0299 ± 0.031 mg x cm^{-2} h^{-1}). In *in vitro* tests against S. *mansoni*, PZQ-HH exhibited an IC_{50} of 0.15 μM, like the IC_{50} of 0.1 μM for Form A [185].

PZQ-HH demonstrated physical stability at ambient temperature for 3 months before gradually converting to Form B.

Notably, other researchers have found that PZQ-HH can also be obtained by exposing PZQ monosolvate with acetic acid (PZQ-AA) to a water-vapor atmosphere, resulting in the desolvation of AA and subsequent hydration [144].

In a study by Salazar-Rojas et al., both PZQ-MH and PZQ-HH were subjected to thermal stress and monitored using hot-stage attenuated total reflectance mid-infrared spectroscopy (HS-ATR-MIR) combined with multivariate curve resolution and alternating least squares (MCR-ALS), alongside DSC analysis [190]. The monitoring setup involved heating the samples at a rate of 5 °C/min (30-145 °C) while collecting MIR spectra (3500-600 cm^{-1}) every minute. MCR-ALS was employed to solve the spectral overlap between the different solid-state forms.

For PZQ-HH, prior DSC analysis indicated that dehydration leads first to polymorph B, followed by the appearance of Form A [146]. The HS-ATR analysis confirmed that PZQ-HH fully converted to Form B at around 90 °C, followed by a second transformation at 107 °C, yielding Form A at approximately 115 °C. Finally, Form A underwent complete fusion at 136 °C. MIR spectra captured during this process revealed a key transformation: the disappearance of the ν(OH) band at 3485 cm^{-1}, signaling water loss as PZQ-HH converted to Form B. Additionally, the carbonyl stretching band (ν(C=O)) of the amide group at 1634 cm^{-1} split into two peaks at 1643 and 1631 cm^{-1}, which shifted

during the transformation to Form B, reflecting increased bond rigidity. As Form B converted to Form A, the ν(C=O) peaks shifted further to 1645 and 1620 cm^{-1}, confirming the transformation.

In the case of PZQ-MH, the dehydration was observed as a single-step transformation directly to Form A [145]. Under HS-ATR thermal treatment, dehydration began at approximately 70 °C, with maximum conversion to Form A (around 90%) occurring at 90 °C. Melting of Form A became evident after 125 °C. These events aligned perfectly with DSC observations. Similarly to PZQ-HH, the initial MIR spectral change for PZQ-MH was the disappearance of the ν(OH) band at 3481 cm^{-1}, marking water loss during conversion to Form A. The carbonyl stretching band at 1624 cm^{-1} split into two vibrations, shifting to 1645 and 1620 cm^{-1}, consistent with Form A.

Salazar-Rojas et al. also investigated the impact of thermal stress on the dissolution behavior of PZQ-HH and PZQ-MH. For this, PZQ-HH was heated to 84 and 124 °C for 20 min (referred to as HH84 and HH124, respectively), and PZQ-MH was heated to 124 °C for 20 min (MH124). DSC and PXRD analyses confirmed the HS-ATR-MIR findings: HH84 showed the presence of Form B with a small amount of amorphous material (indicated by a baseline shift in PXRD), while both HH124 and MH124 contained predominantly Form A with traces of amorphous content.

Regarding dissolution, HH84 exhibited a faster initial dissolution rate and increased drug release at early time points (10 min) compared to unheated PZQ-HH, likely due to the presence of Form B. In contrast, HH124 and MH124, containing Form A and some amorphous content, showed faster early dissolution due to the amorphous fraction, but overall had a lower dissolution rate compared to HH84, driven by the predominance of Form A.

A subsequent study reported a new hydrated form of PZQ discovered through supercritical CO_2 ($scCO_2$) processing. MacEachern and colleagues used rapid expansion of supercritical solution (RESS) as the $scCO_2$ processing method to obtain the new solid form [147]. In their experiment, PZQ was placed in a Kimwipe and inserted into a 100 mL high-pressure vessel, which was maintained at 40 °C and 17.9 MPa for 22.5h. Following this, the vessel was purged with CO_2 for 20 min at a flow rate of 4-5 L/min before being depressurized, allowing the solubilized solids to be collected. The solid remaining in the Kimwipe was simply exposed to high-pressure conditions for the duration of the experiment.

SEM analysis revealed that the new form had a distinct needle-like morphology with larger particle sizes than those seen in anhydrous PZQ Form A (Figure 15). In terms of its thermal properties, DSC indicated a complex thermal profile: an initial endotherm with an onset at 83.11 °C (peak at 92.5 °C) corresponded to dehydration, producing a novel dehydrate. This dehydrate subsequently melted and recrystallized into Form A, with the final endotherm occurring at 139 °C, consistent with the melting

point of Form A. TGA showed a mass loss of 3.38% corresponding to the first endothermic event, which, together with KF titration revealing a water content of 3.24%, confirmed the hydrate nature of the new solid, containing approximately 0.6 equivalents (eq.) of water. The slight excess of water (0.1 eq.) was attributed to the hygroscopicity of the material, thus classifying it as a hemihydrate.

PXRD pattern of this new form was indexed using PDXL2 software, identifying a monoclinic space group of *P*2/*m* with a unit cell volume of 2332.09 Å^3 (a = 14.128 Å, b = 13.536 Å, c = 13.187 Å; α = γ = 90°, β = 112.368°) and a value of five formula units per unit cell (Z=5). Despite this, the $scCO_2$ process did not yield single crystals, so no full crystal structure solution was deposited in the CSD.

IR analysis of the new hydrate revealed a band at 3586 cm^{-1}, absent in anhydrous Form A, and like a peak at 3543 cm^{-1} reported by Zanolla et al. for a different hemihydrate [146], which was attributed to an O-H stretching typical of hydrates. Shifts in the carbonyl stretching bands at 1624-1649 cm^{-1} were also observed, resembling those of PZQ polymorphs B and C, indicating a potential shift from a *syn* to an *anti*-conformation of PZQ molecules.

The new hydrate demonstrated notable physical stability, remaining stable for at least 7.5 weeks under stressed conditions (40 °C and 75% RH). Additionally, it exhibited improved solubility in biorelevant media, such as fasted state simulated gastric fluid (FaSSGF) (pH 1.6) and fasted state simulated intestinal fluid (FaSSIF) (pH 6.5), as well as in water, showing a 13-20% higher solubility compared to unprocessed PZQ Form A. In a later study, this same PZQ-HH, obtained through the $scCO_2$ process, was also found to form during fast cooling crystallization in mixtures of MeOH/H_2O (30-40% v/v H_2O) and EtOH/H_2O (40-50% v/v H_2O) [144].

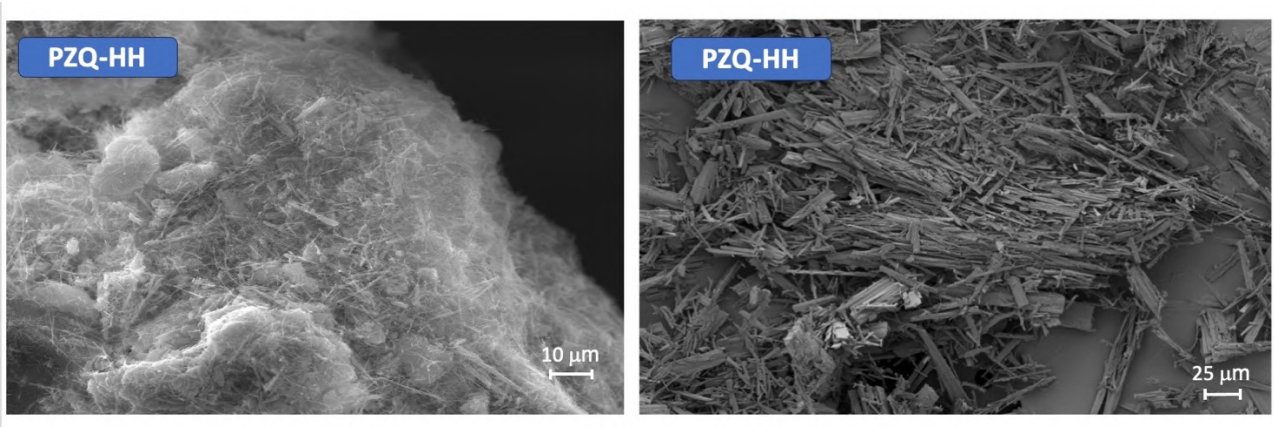

Figure 15. SEM images of PZQ-HH (1000x) (left) and PZQ-HH from CO_2 supercritical (500x) (right). Adapted from references [146,147].

1.2.5.2 PZQ Solvates

It is well-known from literature that solvates are often discovered either serendipitously during specific manufacturing processes or through systematic polymorph screening programs, which include techniques such as solution crystallization, slurry methods, and more recently, mechanochemistry [191]. To date, only a few PZQ solvates have been identified, primarily through cooling crystallization and mechanochemical approaches (see Figure 19 below).

The first two PZQ solvates were obtained via mechanochemical screening using different liquids [148]. Specifically, 2-pyrrolidone (2-pyr) and acetic acid (AA) were identified as suitable solvents to form PZQ solvates (PZQ-2-pyr and PZQ-AA, respectively) with a 1:1 stoichiometry. This was achieved by grinding the drug in the presence of each solvent, regardless of the quantity added (with tested η values in the range 0.05–0.5 μL [51]) for 30 min at 25 Hz. The same result was observed when starting from PZQ polymorph B.

Moreover, PZQ-2-pyr and PZQ-AA could also be obtained via slurry experiments by suspending an excess of PZQ Form A in 2-pyr and AA. SEM images revealed distinct morphologies: PZQ-AA appeared as layered blocks with flat particles and rough surfaces showing some holes, while PZQ-2-pyr exhibited flat agglomerates with very thin needle-like formations on the surface (see Figure 17 below).

PXRD patterns for both solvates revealed sharp reflections, distinct from PZQ Form A and other known PZQ forms, suggesting isostructurality between the two new solvates. This was confirmed through Synchrotron XRD, which solved their crystal structures, showing that both solvates crystallize in the triclinic *P*-1 space group (Figure 16). Each PZQ molecule is linked via strong H-bonds to one molecule of solvent in the ASU. FT-IR and SSNMR analyses confirmed the intermolecular interactions and the stoichiometry.

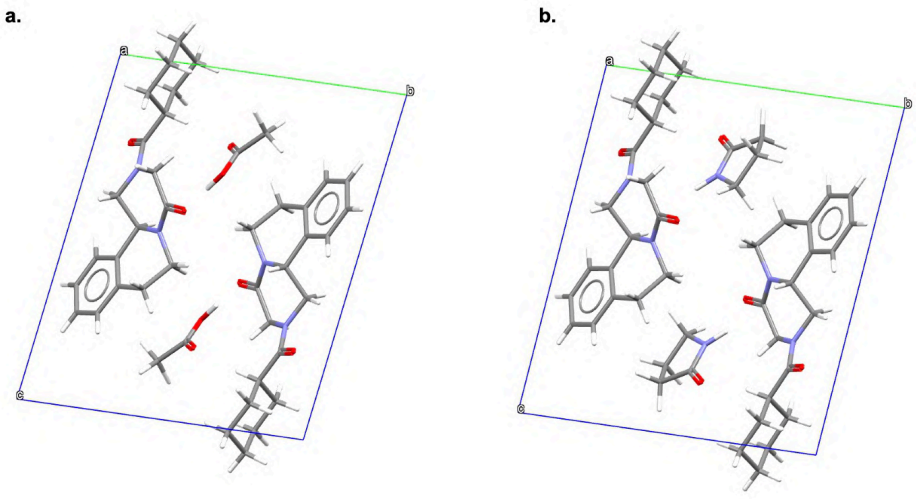

Figure 16. Crystal structures of (**a**) PZQ-AA and (**b**) PZQ-2-pyr solvates.

In FT-IR, PZQ-2-pyr and PZQ-AA both exhibited a shift in the stretching vibration of the heterocyclic carbonyl group (which appears at 1647 cm^{-1} in Form A) to 1638 cm^{-1}, confirming the presence of an *anti*-conformation. Additionally, the N-H stretching band of 2-pyr (originally at 3488–3474 cm^{-1}) was shifted down to 3243 cm^{-1} in PZQ-2P, confirming both the presence of 2-pyr in the structure and the intermolecular interactions between the two components. In the case of PZQ-AA, two characteristic bands at 2600 cm^{-1} confirmed the presence of AA in the structure.

SSNMR spectra further verified the presence of solvent molecules in both solvates. PZQ-AA displayed peaks at 172.1 ppm (COOH) and 19.7 ppm (CH_3), while PZQ-2-pyr exhibited signals at 177.5 ppm (C=O) and 19.4, 28.9, and 40.4 ppm (CH_2). In PZQ-AA, one carbonyl signal overlapped with the COOH signal of AA (172.1 ppm), while in PZQ-2P, this signal remained distinguishable. In both spectra, the number of signals was consistent with the 1:1 stoichiometry. PZQ-2-pyr and PZQ-AA were indexed in the CSD under refcodes DAJCAW and DAJCEA, respectively.

Thermally, PZQ-2-pyr and PZQ-AA exhibited a single endothermic event corresponding to desolvation, occurring at 85.69 °C and 72.26 °C, respectively. In terms of biopharmaceutical performance, both solvates demonstrated superior water solubility and IDR, approximately double that of the anhydrous (RS)-PZQ.

These monosolvates also exhibited remarkable physical stability. When stored at room temperature in sealed vials, they remained stable for at least 18 months. Additionally, even after prolonged mechanical treatment (25 Hz for 200 min), no transformation was observed.

Notably, PZQ-AA monosolvate was later reproduced via fast and slow cooling crystallization, regardless of the initial concentration of (RS)-PZQ [144].

Guedes Fernandes de Moraes et al. reported the discovery of a dimethylacetamide solvate of PZQ (PZQ-DMA) [144]. This solvate was obtained through a fast-cooling crystallization process of PZQ Form A. The study explored two variables: the initial concentration of PZQ (low and high) and the cooling rate (slow at 0.2 °C/min and fast at 5 °C/min). The PZQ-DMA solvate formed under both low and high concentrations of PZQ, but only when fast cooling crystallization was applied. In contrast, the slow cooling method consistently resulted in the recovery of the starting Form A.

The newly obtained solvate was characterized by a PXRD pattern with diffraction peaks that were distinctly different from those of TELCEU and all previously reported PZQ solid forms. However, thermal analysis was critical in confirming that the new form was indeed a solvate. The DSC curve revealed an endothermic event at 58 °C, corresponding to the desolvation of PZQ-DMA solvate, followed by two melting events. These melting points were attributed to Form G and Form A,

respectively. The desolvation was further confirmed through TGA, which showed a weight loss of approximately 20%, consistent with the theoretical value for a monosolvate.

SEM imaging revealed lath-shaped crystals for the PZQ-DMA solvate (Figure 17), which were noticeably different from the smaller, acicular crystals typical of Form A. Although solid-state characterization confirmed the formation of a new phase, no crystal structure for PZQ-DMA was solved or deposited in the CSD.

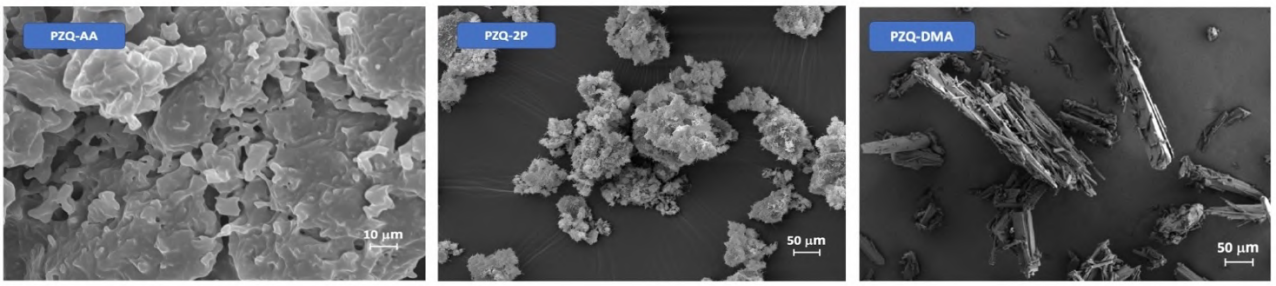

Figure 17. SEM images of PZQ-AA (1500x) (left) and PZQ-2-pyr (370x) (centre) and PZQ-DMA (160x) (right) monosolvates. Adapted from references [144,148].

1.2.5.3 PZQ Cocrystals

Cocrystallization has emerged as a promising strategy in pharmaceutical science to develop new crystal forms with enhanced properties [192]. Pharmaceutical cocrystals, consisting of an API and one or more cocrystal formers, are particularly valuable due to their ability to improve various physicochemical properties such as solubility, bioavailability, mechanical, humidity, and thermal stability, as well as compressibility. Additionally, they play a crucial role in separation technologies, especially for chiral molecules [29,44,49,193–198].

Given that PZQ lacks traditional salt-forming functional groups, possessing only two carbonyl groups capable of acting as H-bond acceptors, the drug presents an intriguing potential for cocrystal formation. This characteristic, combined with the possibility of creating diastereomeric cocrystal pairs for chiral resolution, has recently drawn significant attention to PZQ as a candidate for cocrystallization studies.

Espinosa-Lara and coworkers were the first to investigate the cocrystallization potential of (RS)-PZQ with aliphatic dicarboxylic acids, hypothesizing that dimeric heterosynthons could induce cocrystallization through LAG [141]. The study involved combining PZQ with oxalic acid (OXA), malonic acid (MALO), succinic acid (SUC), maleic acid (MALE), fumaric acid (FUM), glutaric acid (GLU), adipic acid (ADI), pimelic acid (PIM), suberic acid (SUB), azelaic acid (AZE), and sebacic acid (SEB) in molar ratios of 2:1, 1:1, and 1:2, using either ACT or ACN as solvents. Of these, nine new cocrystals were discovered, while no cocrystallization occurred with SUB, AZE, or SEB.

PXRD analysis confirmed that OXA, MALO, SUC, MALE, FUM, and GLU formed 1:1 cocrystals (i.e., PZQ-OXA, PZQ-MALO, α-PZQ-SUC, PZQ-MALE, PZQ-FUM, and PZQ-GLU), whereas ADI and PIM produced 2:1 cocrystals (PZQ-ADI and PZQ-PIM). FT-IR spectra analysis demonstrated notable shifts in PZQ's carbonyl stretching vibrations, suggesting diverse H-bonding patterns and weaker interactions in the cocrystals. These C=O stretching vibrations, initially ranging from 1658 to 1704 cm^{-1} in the starting materials, shifted to higher wavenumbers in the cocrystals, indicative of weaker C-H···O and O-H···O bonds.

To obtain single crystals suitable for SXRD, PZQ and each coformer were dissolved in different molar ratios (2:1, 1:1, 1:2, 1:3, and 1:4) in hot ACT or ACN with mechanochemically preformed cocrystals acting as seeds. This approach succeeded in isolating single crystals of PZQ-OXA, PZQ-MALO, PZQ-MALE, PZQ-FUM, PZQ-GLU, and PZQ-ADI, but not for PZQ-PIM (Figure 18). Notably, solution crystallization of PZQ and SUC yielded a new polymorph, β-PZQ-SUC (Figure 18), distinguishable from α-PZQ-SUC by PXRD and FT-IR, suggesting polymorphic behavior.

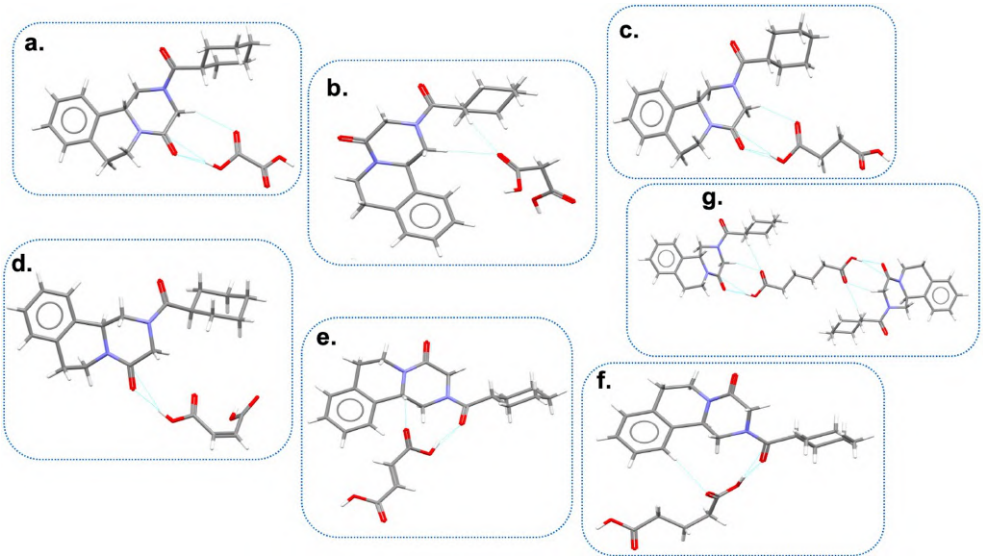

Figure 18. H-bonds motifs and ASUs of first seven cocrystals discovered: (**a**) PZQ-OXA; (**b**) PZQ-MALO; (**c**) β-PZQ-SUC; (**d**) PZQ-MALE; (**e**) PZQ-FUM; (**f**); PZQ-GLU; (**g**) PZQ-ADI.

Structural analysis revealed that PZQ-OXA, β-PZQ-SUC, and PZQ-GLU (indexed as TELCOE, TELDAR, and TELDIZ, respectively, in the CSD) crystallized in the space group *P*-1 with similar unit cell edge lengths, indicating commonality in their supramolecular arrangements. Each cocrystal featured a 1:1 stoichiometry, with PZQ molecules adopting an *anti*-conformation. PZQ molecules in SUC and GLU cocrystals formed homodimeric motifs, while PZQ-OXA and PZQ-FUM (CSD refcode TELBUJ) displayed double-bridged heterodimeric motifs.

PZQ-MALE (CSD refcode TELCIJ) crystallized in the orthorhombic space group *P*na2_1 and showed connectivity like PZQ-SUC, with additional C-H···O contacts between MALE molecules. In contrast, PZQ-MALO (TELDEV in the CSD) crystallized in *P*2_1/*c* and was the only cocrystal exhibiting the *syn*-conformation of PZQ Form A. This unique configuration enabled the formation of 26-membered cyclic [2+2] aggregates due to MALO disorder over two positions, facilitating additional stability via interconnections. Recently, this cocrystal was also obtained by MacEachern and coauthors through $scCO_2$ in the presence of MeOH as cosolvent: varying the operating conditions, applying a pressure of 30 MPa, a monomodal particle size distribution with an average particle size of 600 nm was obtained [149].

PZQ-ADI (CSD refcode TELCAQ) crystallized in *P*-1 with a 2:1 stoichiometry, where excess PZQ facilitated the formation of homodimeric motifs, creating double chains linked to the coformer. Additionally, a low-temperature crystal structure (CSD refcode TELCAQ01) confirmed the compactness of the PZQ-ADI crystal structure.

In all analyzed cocrystals, heterodimeric O-H···O H-bonding motifs dominated, involving both C=O groups of PZQ. Most cocrystals exhibited an *anti*-conformation for PZQ, except for PZQ-MALO,

which maintained the *syn*-conformation of PZQ Form A. PZQ-MALO was also the only system featuring double-bridged H-bonding contacts between coformer molecules.

Recent work by Wang et al. provided further insight into the α-PZQ-SUC polymorph. Using seeded cooling crystallization, they obtained single crystals of α-PZQ-SUC (CSD refcode TELDAR01), revealing that it crystallized in the orthorhombic space group *Pbca* (Z=8). Compared to β-PZQ-SUC, the α form exhibited higher stability, with a monotropic relationship and a higher melting point and enthalpy of fusion. Despite similar intermolecular interactions, the two polymorphs differed in packing: α-PZQ-SUC formed wavy molecular layers, while β-PZQ-SUC showed nearly planar layers. Hirshfeld analysis suggested that α-PZQ-SUC was more stable based on pairwise interaction energy. Cocrystallization improved PZQ solubility (from 0.26 mg/mL to 0.43 mg/mL in α-PZQ-SUC and 0.50 mg/mL in β-PZQ-SUC), with significant improvements in IDRs, especially for β-PZQ-SUC, which demonstrated a 5.70-fold increase compared to pure PZQ.

Wasim et al. conducted a comprehensive investigation into the physicochemical properties—such as thermal and spectroscopic behavior, solubility, and dissolution—as well as the oral bioavailability and pharmacokinetic parameters of several PZQ cocrystals [199]. Their study aimed to elucidate the relationship between these properties and pharmacokinetic parameters (Cmax, Tmax, and AUC) in relation to the chain lengths (n) of selected dicarboxylic acid coformers: OXA (n=0), MALO (n=1), SUC (n=2), GLU (n=3), and ADI (n=4). They also explored the impact of the polymer hydroxypropyl cellulose (HPC) on cocrystal formation.

The cocrystals were synthesized using the slurry crystallization method, and their nature was assessed by comparing their PXRD patterns with those in the CSD. FT-IR analysis revealed that the spectra of PZQ cocrystals differed from those of the starting materials. Specifically, the carbonyl amidic groups of pure PZQ appeared at 1645 and 1622 cm^{-1}, consistent with previous reports. In the cocrystals, the carbonyl stretching ranged from 1593 to 1630 cm^{-1}, indicating changes in H-bonding. The C=O stretching vibrations of the dicarboxylic acid coformers ranged from 1664 to 1697 cm^{-1}, whereas in the cocrystals, they shifted to 1712-1742 cm^{-1}. This shift suggests weaker intermolecular interactions. Thermal analyses using DSC and TGA showed that none of the cocrystals underwent dehydration and exhibited different melting points from the starting materials. The melting points were observed at 159.9, 147.7, 141.2, 126.2, and 122.9 °C for PZQ-OXA, PZQ-MALO, PZQ-SUC, PZQ-GLU, and PZQ-ADI, respectively, reflecting a trend where a higher number of carbon atoms in the coformer resulted in a lower melting point. TGA results indicated that PZQ-OXA, PZQ-MALO, and PZQ-SUC cocrystals began to dissociate at approximately 163, 147, and 167 °C, respectively. In contrast, PZQ-GLU and PZQ-ADI were thermally more stable, starting to decay at 199 and 208 °C, respectively.

From a biopharmaceutical perspective, solubility studies demonstrated a significant improvement in the aqueous solubility of PZQ cocrystals compared to pure PZQ, which had a solubility of 0.392 ± 0.1 mg/mL. The solubility of PZQ cocrystals ranged from 3.7 ± 1.08 to 10.5 ± 1.7 mg/mL. Dissolution profiles at 90 min showed a trend of improved dissolution: PZQ-SUC (68%), PZQ-ADI (57.96%), PZQ-GLU (54.05%), PZQ-OXA (51%), and PZQ-MALO (46.05%).

Pharmacokinetic studies in rabbits revealed enhanced oral bioavailability for all cocrystals compared to pure PZQ, which had an AUC of 10.06 ± 2.51 μg h/mL. PZQ-SUC exhibited the highest oral bioavailability (33.84 ± 6.05 μg h/mL), while PZQ-MALO had the lowest (15.40 ± 3.65 μg h/mL). The cocrystals generally achieved higher Cmax within 1 hour compared to pure PZQ, except for PZQ-OXA and PZQ-MALO.

The improvements in solubility, dissolution, and oral bioavailability were consistent, indicating that enhanced solubility led to better dissolution and bioavailability. However, the effects of the spacer groups on biopharmaceutical properties and pharmacokinetics were not consistently observed. Lastly, when HPC polymer was included during the slurry preparation, it did not inhibit cocrystal formation, except for PZQ-SUC, where PXRD analysis revealed residual pure PZQ.

Recently, Salas-Zúñiga and colleagues explored the potential of enhancing the solubility and dissolution of PZQ cocrystals by confining them within mesoporous silica (SB-15) with nanopores approximately 5.6 nm in size [186]. Among seven cocrystals previously synthesized, PZQ-GLU cocrystal was selected due to its favorable characteristics: (i) it had a smaller unit cell volume compared to racemic PZQ, (ii) it melted at a lower temperature than raw (RS)-PZQ (ΔT = -15.8 °C), facilitating the melt loading method for confinement, and (iii) upon recrystallization, it consistently produced the original cocrystal and exhibited a distinct IR fingerprint, making it easily identifiable.

Four different SBA-15/cocrystal weight ratios were prepared, and similar experiments were conducted with pristine PZQ in the same silica material for comparison. The nanoconfined materials were characterized using N_2 adsorption-desorption analysis, PXRD, IR spectroscopy, ^{13}C SSNMR, DSC, and field-emission SEM (FE-SEM). These analyses compared the properties of the nanoconfined materials with SB-15, raw PZQ, and pure PZQ-GLU cocrystal.

N_2 adsorption-desorption analysis indicated complete filling of the SB-15 channels at a 50:50 w/w ratio, leading to the selection of the SBA-15/PZQ and SBA-15/PZQ-GLU composites at this ratio for further studies. FE-SEM images revealed a rod-like morphology for SBA-15/PZQ-GLU, in contrast to the smooth surface of micrometer-sized PZQ-GLU crystals. PXRD analysis showed a broad halo for SB-15/PZQ-GLU, indicative of amorphous SBA-15, with low-intensity diffraction peaks overlapping with PZQ-GLU cocrystal. In contrast, SBA-15/PZQ displayed a typical halo diffusion for amorphous materials, with no visible peaks for crystalline PZQ.

FT-IR results demonstrated that the two C=O stretching vibrations of the GLU coformer at 1612 and 1715 cm^{-1} were present in SBA-15/PZQ-GLU, confirming that the cocrystal remained in the nanoconfined state. For SBA-15/PZQ, the C=O bands of raw PZQ (1647 and 1624 cm^{-1}) merged into a broad band at 1645 cm^{-1}, a behavior also observed by Perissutti et al. in ASDs [45]. ^{13}C CPMAS and SPE (Single Pulse Excitation) analysis revealed that SBA-15/PZQ-GLU consisted of a mixture of a cocrystalline bulk solid (outside the mesopores) and a more mobile phase (inside the mesopores), with the latter more evident in composites with lower PZQ-GLU ratios.

Thermal analysis showed that SBA-15/PZQ did not exhibit a distinct melting transition, confirming its amorphous state. SBA-15/PZQ-GLU displayed two broad endothermic transitions at 63.0 and 117.2 °C, indicating the presence of two phases: a cocrystalline bulk solid outside the mesopores, melting at 117.2 °C (like pure PZQ-GLU at 123.0 °C), and a more mobile phase inside the mesopores, melting at 63.0 °C. This suggests that nanoconfined drugs often exhibit significant melting point depression [200–202].

Overall, characterization techniques demonstrated that PZQ was primarily loaded in an amorphous form, while PZQ-GLU showed a more mobile/solid-like phase within SBA-15. This contrasting behavior is attributed to the stronger $O\text{-}H_{GLU}\cdots O{=}C_{PZQ}$ H-bonds in the cocrystal compared to the $C\text{-}H\cdots O{=}C_{PZQ}$ interactions in (RS)-PZQ, as well as a larger crystal lattice volume of PZQ compared to PZQ-GLU (3320.1 vs. 1167.9 $Å^3$).

Dissolution studies in two experimental settings further assessed the impact of the confined cocrystals. Under non-sink conditions with a saturation index (SI) of 0.014 for PZQ and 0.02 for PZQ-GLU, in the presence of a precipitation inhibitor polymer (Methocel 60 HG), SBA-15/PZQ-GLU showed sustained solubilization, increasing the AUC0-90min up to 5.1-fold compared to pristine PZQ, like SBA-15/PZQ. In another setting with a SI of 1.99 for both PZQ and PZQ-GLU in aqueous HCl pH 1.2 at 37 °C, the nanoconfined composites resulted in immediate drug release. These findings confirm that nanoconfinement combined with cocrystallization is an effective strategy to enhance the properties of poorly soluble drugs like PZQ.

Focusing again on PZQ-GLU and PZQ-SUC cocrystals, Salas-Zúñiga and colleagues recently reported the synthesis of two novel cocrystals through LAG using the enantiomerically pure (R)-PZQ in a 1:1 molar ratio with the aforementioned coformers [151]. The newly obtained cocrystals, designated as (R)-PZQ-GLU and (R)-PZQ-SUC, were thoroughly characterized and compared with previously reported analogous cocrystals made from racemic PZQ, hereafter referred to as (RS)-PZQ-GLU and (RS)-PZQ-SUC. The study also compared these with the pure (R)-PZQ hemihydrate (i.e., (R)-PZQ-HH) and pristine (RS)-PZQ.

PXRD patterns of the new cocrystals distinctly differed from both the starting materials and the analogous cocrystals made with racemic PZQ. Single crystals suitable for SXRD were obtained via classical solution crystallization, and the simulated PXRD patterns matched the experimental data. Both (R)-PZQ-GLU and (R)-PZQ-SUC (indexed as KEQVEL and KEQVAH in the CSD, respectively) crystallized in the chiral space group $P2_1$, confirming the enantiomerically pure nature of (R)-PZQ. Structural analysis revealed that the dominant supramolecular interactions in these new crystals were quite similar. Both cocrystals featured amide functions of (R)-PZQ engaged in heterosynthons with O-$H_{coformer}$···O=C_{PZQ} H-bonds involving the COOH groups of the dicarboxylic acids. Additionally, complementary (N)C-H_{PZQ}···O=$C_{coformer}$ interactions formed slightly different eight- and nine-membered cyclic double-bridged heterodimeric synthons.

In IR spectra, the characteristic band for H_2O molecules at around 3500 cm^{-1}, present in (R)-PZQ-HH, was absent in (R)-PZQ-GLU and (R)-PZQ-SUC, indicating their anhydrous nature. Moreover, C=O stretching vibrations of PZQ were shifted to lower wavenumbers, while the C=O bands of the coformers shifted to higher wavenumbers. These shifts suggest that the H-bonding interactions in the cocrystals were stronger than those between water molecules and (R)-PZQ in the hemihydrate, and stronger than the interactions between dicarboxylic acid dimers.

The thermal behavior of the two cocrystals differed slightly. (R)-PZQ-SUC had a melting point of 130.2 °C, which was intermediate between the melting points of its starting materials (112.9 °C for (R)-PZQ-HH and 184.9 °C for SUC). In contrast, (R)-PZQ-GLU exhibited a melting temperature of 81.0 °C, lower than the individual components (112.9 °C for (R)-PZQ-HH and 102.9 °C for GLU). This difference in melting points could be attributed to variations in stability, solubility, and dissolution rates of the cocrystals.

In dissolution studies, the two enantiomerically pure cocrystals were compared to their racemic counterparts and the pure (R)-PZQ-HH in a simulated gastric dissolution medium (HCl, pH 1.2, 37 °C), where dicarboxylic acids are fully protonated. IDR results showed that all four cocrystals (both enantiomerically pure and racemic) demonstrated superior dissolution compared to (RS)-PZQ and (R)-PZQ-HH, with improvements ranging from 2 to 5 times greater relative to (R)-PZQ-HH. The IDR ranking was (R)-PZQ-GLU > (RS)-PZQ-SUC ≈ (RS)-PZQ-GLU > (R)-PZQ-SUC. Notably, the IDR curves for the cocrystals exhibited a significant change in slope between 30 and 60 min, likely due to a phase transformation into (R)-PZQ-HH and (RS)-PZQ-HH, as confirmed by IR and PXRD analysis of the IDR tablets.

Powder dissolution tests were conducted under non-sink conditions by adding dissolution medium to excess cocrystal solid to assess the supersaturation potential. (R)-PZQ-GLU, (RS)-PZQ-GLU, and (RS)-PZQ-SUC exhibited increased solubility compared to (RS)-PZQ and (R)-PZQ-HH, with

maximum concentrations reaching 4.6 mM, 3.8 mM, and 2.7 mM, respectively, within the first 5 min. Conversely, (R)-PZQ-SUC displayed a dissolution profile like that of (R)-PZQ-HH, indicating no supersaturation. After approximately 5 min, the concentrations of the three cocrystals declined to levels comparable to (RS)-PZQ and (R)-PZQ-HH, suggesting rapid reprecipitation. PXRD analysis of the recovered samples indicated a conversion of the cocrystals back to the parent compounds, as observed in the IDR studies.

Returning to the cocrystallization strategy, three years after the initial discovery of PZQ cocrystals with dicarboxylic acids [141], Sánchez-Guadarrama et al. applied cocrystallization for the chiral resolution of racemic PZQ [152]. They achieved this by forming a diastereomeric cocrystal pair with L-MAL, as detailed in paragraph 1.2.2. Specifically, the authors employed LAG with 10 µL of ACT, using a 1:1 stoichiometric mixture of (RS)-PZQ and L-MAL as coformer. The grinding was conducted for 30 min at 25 Hz, resulting in the formation of two enantiomerically pure cocrystals: (R)-PZQ/L-MAL and (S)-PZQ/L-MAL. The structures of these cocrystals were solved and deposited in the CSD [152].

Similarly, Cugovčan and colleagues reported the successful formation of PZQ cocrystals with citric acid (CA), malic acid (MAL), salicylic acid (SA), and tartaric acid (TA) using LAG [124]. In their study, PZQ was milled with each coformer in a 1:1 molar ratio for 30 min at 25 Hz, with or without 15 µL of absolute EtOH. LAG proved to be the most effective technique for cocrystal formation.
PXRD patterns of PZQ-CA, PZQ-MAL, PZQ-TA, and PZQ-SA revealed the presence of new peaks and the absence of residual peaks from the starting materials, confirming the successful formation of cocrystals in a 1:1 molar ratio. DSC analyses showed a new endothermic peak at 51.07 °C for PZQ-CA and at 150.81 °C for PZQ-TA. However, DSC did not provide conclusive information about melting events for PZQ-MAL and PZQ-SA.
Further insights into cocrystal formation were obtained through FT-IR analysis. The typical carbonyl stretching vibrations of PZQ Form A, observed at 1647 and 1624 cm^{-1}, were shifted to lower wavenumbers, and only one broader band was detected at 1612 cm^{-1} for PZQ-MAL, 1593 cm^{-1} for PZQ-SA, and 1606 cm^{-1} for PZQ-TA. These shifts suggest the involvement of both carbonyl groups in H-bonding with the coformer acids. Specifically, the C=O of PZQ H-bonded the alcoholic group of SA. For MAL, differences in band intensities at 3438 and 1683 cm^{-1}, attributed to the -OH and C=O groups of MAL, suggest that the hydroxyl group of MAL likely participated in H-bonding with PZQ carbonyl groups. In the case of TA, the bands at 3402 and 3330 cm^{-1}, corresponding to the

alcoholic group of TA, shifted in PZQ-TA, with a new band emerging around 3480 cm^{-1}, indicating interaction with PZQ carbonyl groups through the alcoholic group of TA.
Notably, in the case of PZQ-CA, FT-IR spectra did not show shifts in PZQ characteristic bands. However, a shift in the C=O groups of CA from 1751, 1745, and 1699 cm^{-1} to 1753, 1726, and 1691 cm^{-1} was observed, suggesting the formation of a new solid form.
All prepared cocrystals exhibited pH-dependent solubility, with the highest saturation solubility observed at pH 4.5, where the ionizable groups of the coformers were fully ionized, as indicated by their pKa values [203,204]. Among the four cocrystals, PZQ-MAL showed the highest solubility. In dissolution studies, all cocrystals demonstrated significantly improved dissolution properties compared to the pure drug. However, it was noted that the PZQ-MAL cocrystal was chemically unstable and promoted PZQ photodegradation. Despite these findings, no new crystal structures were solved and reported in the CSD.

Subsequently, Yang et al. published a study in which they employed theoretical calculations to predict the formation of PZQ cocrystals with three flavonols: kaempferol (KAE), quercetin (QUE), and myricetin (MYR) [153]. They used DFT to analyze the conformations of PZQ and the flavonols, focusing on molecular electrostatic potential surfaces (MEPS) to predict intermolecular interactions and potential cocrystal formation [205]. By determining the conformations of the flavonols and PZQ Form A and their Boltzmann distributions at 300 K, they calculated MEPS to estimate interaction site pairing energies (ΔE). The smaller the ΔE value, the higher the likelihood of cocrystal formation.
KAE, QUE, and MYR exhibited two main conformations. For KAE and MYR, the difference between the two conformations was minimal, whereas QUE displayed more significant variation between its conformations due to the asymmetric distribution of hydroxyl groups. According to the CSD database, conformation 1 (QUE C1) represents approximately 75% of QUE, while conformation 2 (QUE C2) accounts for about 25%. PZQ, on the other hand, showed four primary conformations resulting from the rotation of the cyclohexylcarbonyl group: two *anti*-conformations (C1 and C2) and two *syn*-conformations (C3 and C4). CSD data indicated a predominance of conformations C1 and C3 for PZQ.
ΔE values, which considered the number of H-bond acceptors and donors in PZQ and the flavonols, predicted four potential cocrystals: PZQ-KAE, PZQ-QUE 1, PZQ-QUE 2, and PZQ-MYR. For KAE, the MEPS maxima were found on the hydroxyl groups, which could form H-bonds with the minima on PZQ C1, suggesting a 2:1 stoichiometric ratio. For QUE, C1 had two maxima on hydroxyl groups interacting with PZQ minima, while C2 had maxima that could interact only with PZQ C3. Similarly, MYR was predicted to interact with PZQ C3.

All four predicted cocrystals were successfully synthesized via the suspension-stirring method (Figure 19) and characterized by PXRD. The PZQ-KAE cocrystal was obtained in a 2:1 stoichiometric ratio. For QUE, two distinct cocrystals were identified by PXRD: one with a 2:1 stoichiometry (PZQ-QUE 1) and another with a 1:1 ratio (PZQ-QUE 2), though no single crystal was obtained for the latter. The PZQ-MYR cocrystal was achieved in a 1:1 ratio and single crystals were obtained.

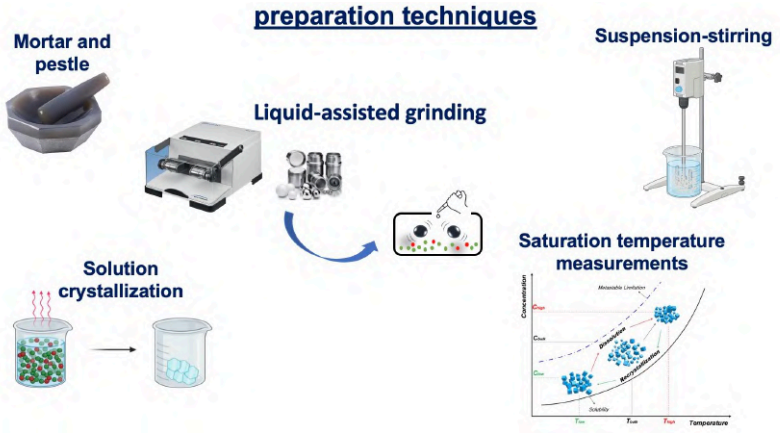

Figure 19. Main preparation techniques used for PZQ multicomponent systems. Adapted from references[153,156,206,207].

SXRD analysis revealed the following structures: PZQ-KAE (indexed as ANAYOG) crystallizes in the monoclinic space group $P2_1/a$ with four formula units per unit cell (Z=4), featuring PZQ in conformation C1 (*anti*). PZQ-QUE 1 (CSD refcode ANAYUM) crystallizes in the triclinic space group *P*-1 with two formula units per unit cell (Z=2), containing both PZQ conformations C1 and C3 (*anti* and *syn*). PZQ-MYR (indexed as ANAZAT) crystallizes in the monoclinic space group $P2_1/c$ with four formula units per unit cell (Z=4), featuring PZQ in conformation C3 (*syn*). These SXRD results corroborated the predicted interactions.

DSC and FT-IR spectroscopy further characterized the cocrystals. DSC curves showed a single melting peak for each cocrystal, situated between the melting points of the starting materials, with PZQ-KAE < PZQ-QUE 1 < PZQ-QUE 2 < PZQ-MYR. FT-IR analysis revealed that the characteristic peaks around 3000 cm^{-1}, associated with crystal water in the raw flavonols, were diminished in the cocrystals, indicating the absence of crystal water due to H-bonding between the hydroxyl groups of the flavonols and the carbonyl groups of PZQ.

Given that both flavonols and PZQ belong to BCS class II, with flavonols being less soluble than PZQ, solubility studies showed that while the solubility of PZQ decreased upon cocrystal formation, the solubility of the flavonols increased approximately threefold.

Building on the knowledge from the previous PZQ cocrystal structures deposited in the CSD, Devogelaer and colleagues employed a network-based link-prediction algorithm [208,209] to forecast 30 new coformer candidates for PZQ [154]. This list included five aliphatic dicarboxylic acids (four of which were previously explored by Espinosa-Lara et al.), derivatives of benzoic acid, and aromatic compounds featuring hydroxyl, amine, and nitro groups. Notably, the list also included salicylic acid and an enantiomer of tartaric acid, which had been mentioned earlier but lacked solved crystal structures [124]. Among the predicted coformers was 1,4-diiodotetrafluorobenzene (1,4-DIFTB), an unusual candidate given its structural divergence from the other coformers.

Of the 30 predicted coformers, 17 were experimentally tested for cocrystal formation. Out of these, 12 were successfully crystallized and analyzed using SXRD. Specifically, eight of these were binary cocrystals: PZQ-1,4-diiodotetrafluorobenzene (PZQ-1,4-DITFB), PZQ-4-hydroxybenzoic acid (PZQ-4-HA), PZQ-3,5-dinitrobenzoic acid (PZQ-3,5-DNA), PZQ-hydroquinone (PZQ-HQ), PZQ-vanillic acid (PZQ-VA), PZQ-2,5-dihydroxybenzoic acid (PZQ-2,5-DHA), PZQ-2,4-hydroxybenzoic acid (PZQ-2,4-HA), and PZQ-orcinol (PZQ-ORC). The remaining four were cocrystal hydrates/solvates: PZQ-salicylic acid monohydrate (PZQ-SA MH), PZQ-4-aminosalicylic acid acetonitrile solvate (PZQ-4-ASA ACN), PZQ-2,5-dihydroxybenzoic acid acetonitrile solvate (PZQ-2,5-DHA ACN), and PZQ-3,5-dihydroxybenzoic acid acetonitrile solvate (PZQ-3,5-DHA ACN).

In all 12 crystal structures, PZQ molecules adopted the *anti*-conformation, with carbonyl groups oriented in opposite directions and, in some cases, a 90° rotation of the cyclohexyl ring. All structures were centrosymmetric, including both the (R)- and (S)-enantiomers of PZQ. The cocrystal structures were classified into four distinct classes based on their intermolecular interaction patterns and enantiomer packing:

- Class 1: This class includes PZQ-2,5-DHA, PZQ-2,5-DHA ACN, PZQ-4-HA, and PZQ-4-ASA ACN (refcodes CSD: AVEHUH, AVEHIV, AVEJIX, AVEJOD, respectively). These cocrystals are characterized by one-dimensional enantiopure chains where both carbonyl groups of PZQ engage in H-bonding with the coformer. The centrosymmetric nature of these crystals means they also contain chains of opposite chirality. The solvates in this class were isostructural with enantiopure chains aligned along the same crystallographic direction.
- Class 2: PZQ-HQ, PZQ-2,4-HA, and PZQ-3,5-DHA ACN (refcodes: AVEKIJ, AVEJUJ, AVEKEU, respectively) belong to this class. Here, H-bonding patterns lead to chains containing both enantiomers of PZQ in a 1:1 molar ratio, with each carbonyl group of alternating PZQ enantiomers participating in H-bonding with the coformer.

- Class 3: PZQ-VA, PZQ-3,5-DNA, and PZQ-SA MH (refcodes: AVEJAP, AVEJET, AVEHER, respectively) are categorized as racemic pair cocrystals, where (R)- and (S)-enantiomers of PZQ interact via H-bonds like those in PZQ polymorph B.
- Class 4: PZQ-1,4-DITFB (indexed as AVEKAQ in the CSD) is unique in this class, where H-bonding is not present. Instead, halogen bonds and π-π interactions are observed. Specifically, alternating PZQ enantiomers form carbonyl-iodide interactions with the coformer, while fluorine atoms in the coformer interact with hydrogen atoms on the aromatic and cyclohexyl rings of PZQ.

This comprehensive approach of predicting and experimentally verifying cocrystal structures significantly expands the understanding of PZQ crystallization behavior and its interactions with a diverse range of coformers.

In a subsequent study, the same research group conducted an in-depth comparison of three cocrystal screening methods: LAG, solvent evaporation (SE), and saturation temperature measurements (STM), evaluating their respective advantages and drawbacks in cocrystal preparation [210]. These methods identified 17 cocrystals in total, with 14 demonstrating stability and 12 having new crystal structures solved.

For the LAG experiments, a 1:1 molar ratio of PZQ and each coformer was ground in the presence of various solvents (MeOH, EtOH, isopropanol (iPOH), ACT, and EA), and the outcomes were assessed via PXRD. Of the 30 tested coformers, 11 (3,5-DNA, SA, 1,4-DITFB, 4-HA, 4-ASA, HQ, VA, 2,5-DHA, 2,4-DHA, and ORC) produced new PXRD patterns, indicating successful cocrystallization. Notably, most coformers yielded consistent solid phases across multiple solvents, though two—VA and 2,5-DHA—produced different PXRD patterns depending on the solvent used. These LAG experiments identified 13 new systems from the 11 successful coformers. SXRD analysis further clarified the nature of these systems, revealing 12 new cocrystal structures, with 8 forming 1:1 cocrystals with PZQ (including 1,4-DITFB, 4-HA, and ORC). Four of these cocrystals were solvates, with three involving ACN (4-ASA, 2,5-DHA, 3,5-DHA), and one (SA) unexpectedly forming a monohydrate due to ambient humidity. VA remained an exception, producing two distinct phases through LAG, one of which was a 1:1 cocrystal confirmed by SXRD. The other phase produced with ACN was not obtained through single-crystal growth experiments and therefore remained a question mark. Only recently, the same scientific group clarified that the second solid form was a 1:2 PZQ-VA cocrystal, which gave positive second harmonic generation (SHG) result. This analysis was useful to understand that the cocrystal crystallized as a conglomerate, (R)/(S)-PZQ-VA, showing a noncongruent melting. Numerous efforts to grow single crystals of this cocrystal have

been done without any success. A possible explanation could be that this cocrystal behaves as an epitaxial conglomerate, showing disorder which makes the cocrystal solution more complicated. Nevertheless, the cell parameters and the space group have been determined: (R)/(S)-PZQ-VA crystallizes in the chiral space group, $P2_1$, with a volume that is consistent with the presence of two PZQ molecules and four VA molecules in the ASU, indicating the 1:2 stoichiometry [155].

The SE experiments, using the same solvents as LAG for consistency, identified 10 successful coformers, with 12 new PXRD patterns observed. As with LAG, VA and 2,5-DHA produced distinct PXRD patterns depending on the solvent. However, unlike LAG, no single crystals were grown from SE phases. For HQ and 2,4-DHA, the PXRD patterns differed from those obtained through LAG, suggesting possible metastable phases. A new PXRD pattern for PIM was also identified through SE, but without corresponding single crystals. Interestingly, 4-ASA showed no new PXRD pattern in SE, contrary to its LAG results.

In STM, 9 coformers successfully formed cocrystals, yielding 12 new PXRD patterns. While PXRD results were generally consistent with LAG and SE, 2,4-DHA produced a unique pattern in EtOH, suggesting a possible polymorph or solvate, though no single crystal was grown to confirm this. A false positive was observed for benzoic acid in EtOH, which yielded a physical mixture (PM) rather than a true cocrystal.

In summary, 12 new cocrystals were fully characterized via SXRD and deposited in the CSD. LAG was the most effective method, identifying 13 stable cocrystals, including one unique to LAG (ORC). SE identified 12 new systems, 9 of which overlapped with LAG and STM, while PIM, HQ, and 2,4-DHA were specific to SE but considered metastable due to inconsistencies. STM produced 12 new patterns, with 11 overlapping with LAG. A unique cocrystal for 2,4-DHA was discovered in STM using EtOH.

Overall, LAG was found to be the most efficient and reliable method for cocrystallization, followed by STM and then SE.

Liu and colleagues conducted a study aimed at investigating the solubility of four PZQ cocrystals formed with carboxylic acids and exploring their structural features through theoretical calculations of intermolecular interactions [156]. The coformers selected—citric acid (CA), phthalic acid (PA), 3-hydroxybenzoic acid (3-HA), and 4-hydroxybenzoic acid (4-HA)—were chosen for their favorable solubility. The cocrystals (PZQ-CA, PZQ-PA, PZQ-3-HA, and PZQ-4-HA) were synthesized via LAG. PZQ-CA had been previously obtained, though its crystal structure remained unsolved [124], and while PZQ-4-HA crystal structure had been reported, no solubility tests or further

characterization were performed [154]. On the other hand, PZQ-PA and PZQ-3-HA had only been theoretically predicted but never synthesized [154].

The study fully characterized the four cocrystals and analyzed the interactions between PZQ and each coformer using advanced theoretical calculations, such as Atoms in Molecules (AIM) topology analysis, electron density difference (EDD) analysis, and energy decomposition analysis (EDA). PXRD analysis revealed distinct diffraction patterns for all four cocrystals, confirming the successful formation of the new phases. PZQ-CA, PZQ-PA, and PZQ-4-HA formed in a 1:1 stoichiometry, while PZQ-3-HA adopted a 2:1 molar ratio. These stoichiometries were further confirmed by SXRD analysis. The crystallographic data showed that PZQ-CA (refcode DAJYUM) crystallizes in the orthorhombic $P2_12_12_1$ space group, PZQ-PA (indexed as DAJZIB) in the monoclinic $P2_1/c$ space group, and both PZQ-3-HA (CSD refcode DAJZEX) and PZQ-4-HA (indexed as AVEJIX01) in the triclinic *P*-1 space group. In all cases, PZQ carbonyl groups exhibited an *anti*-conformation.

SXRD revealed that H-bonding between PZQ carbonyl groups and the hydroxyl groups of the coformers played a key role in stabilizing the cocrystals, with distinct H-bond interaction modes observed. These interactions were further corroborated by FT-IR spectroscopy, which showed shifts in the -OH stretching bands of the coformers and the C=O stretching bands of PZQ. DSC provided insights into the thermal stability of the cocrystals. PZQ-CA had a melting point of 137.2 °C, lower than both PZQ and CA, indicating reduced thermal stability. Similarly, PZQ-3-HA exhibited a melting point of 109.3 °C. In contrast, PZQ-PA and PZQ-4-HA had melting points of 150.0 °C and 155.0 °C, respectively, indicating enhanced thermal stability compared to pure PZQ.

Theoretical calculations via AIM and EDD confirmed the presence of both classical (O-H···O) and nonclassical (C-H···O) H-bonds, with classical interactions being dominant. EDA identified H-bonding as the primary contributor to cocrystal formation, while dispersion and induction forces, though present, played a lesser role.

Solubility tests were conducted *in vitro* in four media with varying pH values. The results showed that all four cocrystals exhibited improved solubility compared to pure PZQ. After 4h, the cocrystals were approximately four times more soluble in a pH 1.2 medium, twice as soluble in pH 4.5 and H_2O, and 3.3 times more soluble in a pH 6.8 medium. Among the four, PZQ-CA demonstrated the lowest solubility, though still higher than that of pure PZQ.

In 2022, the same research group reported the cocrystallization of PZQ with polyhydroxy phenolic acids, including protocatechuic acid (PA), gallic acid (GA), and ferulic acid (FA) [157]. Five new cocrystals were prepared using LAG and SE methods: PZQ-PA, PZQ-GA, and PZQ-FA were synthesized through LAG by grinding a 1:1 molar ratio of PZQ and each coformer in the presence of

ACN. The SE method, using the same solvent, yielded different results, producing two cocrystal solvates, PZQ-PA ACN and PZQ-GA ACN, along with the same PZQ-FA cocrystal previously obtained via LAG. These cocrystals were extensively characterized in the solid state, with the crystal structures of the two cocrystal solvates and the PZQ-FA cocrystal successfully solved.

DSC revealed unique endothermic peaks for the three LAG-derived cocrystals, with melting points intermediate between PZQ and their respective coformers. The two cocrystal solvates displayed endothermic events at 86.16 °C (PZQ-PA ACN) and 104.88 °C (PZQ-GA ACN), corresponding to desolvation. TGA further confirmed that the crystalline lattice collapsed after ACN was lost, with no additional endothermic events observed post-desolvation.

PXRD showed that all five cocrystals had distinct patterns, different from both PZQ and the coformers. Interestingly, PZQ-PA and PZQ-GA exhibited similar PXRD patterns, which was also observed in their respective ACN solvates. This similarity was attributed to the structural resemblance between PA and GA, differing only by the hydroxyl group at the 5-position.

The SE method enabled single-crystal growth, and three out of the five cocrystals were analyzed by SXRD, with their structures deposited in the CSD. The structures of PZQ-PA ACN, PZQ-GA ACN, and PZQ-FA were assigned CSD refcodes HIVXUJ, HIVXOD and HIVXIX, respectively. Both cocrystal solvates crystallized in the monoclinic space group *I*2/*a* and contained one PZQ molecule, one PA/GA molecule, and one solvent molecule, confirming a 1:1:1 PZQ:coformer:solvent stoichiometry. PZQ-FA, on the other hand, crystallized in the monoclinic space group $P2_1/n$, with an ASU containing one PZQ and one FA molecule. In the cocrystal solvates, the phenolic acid formed H-bonds with both PZQ and the solvent as a monomer, whereas in PZQ-FA, the phenolic acid first dimerized and then bonded with PZQ via H-bonds. In all three cocrystals, the PZQ molecules exhibited an *anti*-conformation of their carbonyl groups.

FT-IR spectroscopy corroborated the H-bond interactions and cocrystal formation, showing a shift in the C=O stretching bands of the carboxylic acid. Specifically, for the cocrystal solvates, the vibration of conjugated carboxylic acid monomers was detected at 1716 cm^{-1}, while the characteristic absorption peaks of conjugated carboxylic acid dimers were observed at 1667 cm^{-1}, 1686 cm^{-1}, and 1686 cm^{-1} for PZQ-PA, PZQ-GA, and PZQ-FA, respectively.

The mechanism of cocrystal formation was further explored through theoretical calculations, including molecular interaction energy, EDD analysis, and MEPS analysis. The interaction energies revealed that PZQ-PA ACN exhibited lower interaction energy compared to PZQ-GA ACN, consistent with the lower desolvation temperature of PZQ-PA ACN. PZQ-FA showed the lowest interaction energy, indicating that the FA dimer provided the most stable and easily generated cocrystal structure. EDD and MEPS analyses also demonstrated a decrease in electron density around

the hydroxyl oxygen atoms of the coformers and an increase around the carbonyl oxygen of PZQ, as well as the cyano nitrogen atoms of ACN in the cocrystal solvates, confirming H-bond formation in all cases.

Biopharmaceutical evaluations were performed on the cocrystals without solvents. Solubility tests were conducted in four different media: aqueous HCl solution (pH 1.2), acetate buffer (pH 4.5), and phosphate buffer (pH 6.8). In all media except for acetate buffer (pH 4.5) in the case of PZQ-PA, the solubility of the three cocrystals was significantly improved compared to PZQ. Due to its superior solubility, PZQ-FA was selected for *in vivo* biological activity testing. Although the Tmax and Cmax values of PZQ and PZQ-FA cocrystal were similar, the absorption of PZQ-FA was notably higher.

Recently, Yang et al. presented a study showcasing the application of artificial intelligence in the screening of cocrystals [211]. Specifically, they developed a data-driven prediction method using the eXtreme Gradient Boosting (XGBoost) machine learning model from the *scikit-learn* package. This model was applied to eight previously reported PZQ cocrystals obtained experimentally [153,156,157]. To train the model, they used cocrystal data from the CSD alongside experimental data where no cocrystal formation occurred. The drug and coformer structures were represented by Simplified Molecular Input Line Entry System (SMILES) strings, and RDKit molecular descriptors, derived from the SMILES strings, were used as features. These descriptors were computed via the ChemDes website [212].

When applied to PZQ cocrystallization, the model successfully predicted cocrystal formation with all eight coformers, which aligned with previous experimental results [153,156,157]. This validation demonstrated the potential of the model as a powerful tool for predicting and designing cocrystals in drug research.

A different approach to cocrystal screening was reported by Cappuccino et al., who focused on investigating the formation of cocrystalline solid solutions of PZQ with enantiomerically pure malic (MAL) and tartaric (TA) acids in scalemic and racemic stoichiometry, rather than exploring new coformers for PZQ [158]. Two new cocrystals were structurally characterized and deposited in the CSD, and three non-stoichiometric mixed crystal forms were identified and isolated. Building on previous work that demonstrated the 1:1 cocrystallization of (RS)-PZQ with enantiomerically pure L-MAL—yielding two diastereomeric cocrystals (R-PZQ/L-MAL and S-PZQ/L-MAL) [152]—the authors explored the crystallization of PZQ with racemic MAL. This led to the formation of a novel four-component cocrystal, (R)-PZQ/(S)-PZQ/D-MAL/L-MAL, whose crystal structure was solved using PXRD due to the lack of single crystals of suitable size (CCDC number 2205816). In this

structure, PZQ and MAL molecules alternate in racemic H-bonded chains along the *b*-axis of an orthorhombic *Pbca* unit cell, with the carboxylic acid group acting as a bridge between two carbonyl groups from different PZQ racemes. The hydroxyl group of MAL forms both intramolecular and intermolecular H-bonds, the latter with neighboring antiparallel chains. PZQ carbonyl groups displayed the common *anti*-conformation.

A similar four-component phase was achieved by grinding PZQ with racemic TA, yielding a cocrystal (R-PZQ/S-PZQ/D-TA/L-TA), whose structure was solved (CCDC number 2205817). Here, chains of (S)-PZQ with L-TA alternate along the *a*-axis of a triclinic *P*-1 unit cell with chains of (R)-PZQ and D-TA. These chains are held together by monodentate interactions between the carboxylic groups of TA and the carbonyl groups of PZQ, with additional intermolecular H-bonds formed between hydroxyl groups, and PZQ again displayed an *anti*-conformation.

In contrast, the structure resulting from mechanochemical crystallization of (RS)-PZQ with D-TA remained undetermined, leaving it unclear whether this system was a three-component system ((R)-PZQ/(S)-PZQ/D-TA) or a mixture of diastereomeric crystals ((R)-PZQ/D-TA and (S)-PZQ/D-TA), as seen with MAL. The authors then explored scalemic mixtures and substitutions between MAL and TA to investigate the formation of (RS)-PZQ solid solutions with varied acid compositions. For instance, milling (RS)-PZQ with scalemic MAL ratios (1.5:1.5:1:2 for (R)-PZQ/(S)-PZQ/D-MAL/L-MAL) did not yield diastereomeric crystals but resulted in a solid solution (R-PZQ/S-PZQ/D-MAL/L-MAL), as confirmed by DSC, which showed a superimposition of peaks for the solid solution and the four-component cocrystal.

A similar result was observed for TA: grinding (RS)-PZQ with D-TA and L-TA in a 3:1:2 ratio also produced the solid solution (R-PZQ/S-PZQ/D-TA/L-TA), supported by DSC analysis. Moreover, LAG of (RS)-PZQ with homochiral D-TA and L-MAL in the same ratio did not yield a solid solution but rather a mixture of (R)-PZQ/L-MAL, (S)-PZQ/L-MAL, and the unknown product with D-TA.

When (RS)-PZQ was milled with a pseudoracemate of L-MAL and L-TA, the unknown product with D-TA was obtained, even when the L-TA content was increased relative to L-MAL, suggesting that a four-component solid solution forms at high TA content. The (R)-PZQ/L-MAL and (S)-PZQ/L-MAL phases only appeared when the L-MAL ratio was high. The authors further demonstrated the potential to obtain five-component solid solutions by partially substituting L-MAL with D-MAL in the unknown D-TA product (forming (R)-PZQ/(S)-PZQ/D-MAL/L-MAL/L-TA) or substituting D-TA with L-MAL in (R)-PZQ/(S)-PZQ/D-TA/L-TA, but attempts to substitute D-MAL with L-TA or achieve a six-component solid solution resulted in PMs.

Solubility tests indicated that the solid solutions exhibited a fourfold solubility improvement over pure PZQ, with a faster dissolution rate, likely due to their metastable nature. Pilot *in vivo* studies on

rats, using minicapsules size M containing the solid solutions, showed faster absorption compared to pure PZQ, with a more consistent steady-state concentration.

Given that numerous racemic PZQ cocrystals have been identified, with only a few examples of conglomerate cocrystals, Rapeenun et al. conducted a screening aimed at discovering new conglomerate cocrystals of PZQ [159]. They selected 20 achiral coformers with diverse functional groups (e.g., hydroxyl, carboxyl, amine, amide, and urea) and found that only N-phenyl urea (PU) and 1,3-dimethylthiourea (DMTU) were able to form new cocrystals with PZQ. The study followed a four-step workflow: first, cocrystals were prepared as powders via LAG; second, the samples underwent SHG analysis to detect noncentrosymmetric crystals [213]; third, those with SHG response were further evaluated for conglomerate cocrystal formation by cocrystallizing enantiopure PZQ with the coformers via LAG; and finally, single-crystal structures were determined by SXRD.
For the PZQ-PU cocrystal, the enantiopure cocrystallization process showed that PZQ forms a racemic cocrystal with PU. This conclusion was supported by PXRD analysis, where the diffraction pattern of R-PZQ ground with PU revealed a PM of the starting materials. Therefore, the SHG signal likely originated from residual PU crystals on the cocrystal surface. SXRD analysis further confirmed the racemic nature of the PZQ-PU cocrystal, as it crystallized in the $P2_1/c$ space group with one PZQ and one PU molecule in the ASU (CSD refcode VOCRIS).
In contrast, the enantiopure cocrystallization of PZQ with DMTU via LAG yielded the same PXRD pattern as the racemic PZQ-DMTU cocrystal, indicating a conglomerate behavior. Single crystals suitable for SXRD were grown using two different cooling methods: fast cooling resulted in a rare epitaxial conglomerate (a disordered racemic twin cocrystal), where alternating domains of nearly pure (R)-PZQ-DMTU and (S)-PZQ-DMTU coexisted within the same crystal. This cocrystal (CSD refcode VOCROY) featured a 1:1 ratio of PZQ and DMTU molecules. However, under slow cooling conditions, the epitaxial formation was suppressed, and only (S)-PZQ-DMTU single crystals grew (CSD refcode VOCREO). Both cocrystals crystallized in the monoclinic $P2_1$ space group.
In all three newly identified cocrystals, PZQ consistently exhibited an *anti*-conformation of its carbonyl groups, underscoring the recurring structural motif across these systems.

Caro Garrido and coauthors explored the potential for cocrystallization of PZQ with the nutraceutical curcumin (CU) [160], leading to the discovery of two novel solid forms: a cocrystal solvate with EA and a non-solvated cocrystal. Initially, LAG with toluene indicated the formation of a new solid form, as confirmed by PXRD analysis. The new pattern differed significantly from the starting materials, although some residual peaks of unreacted CU were present. After performing a series of slurry

experiments, they successfully isolated a 2:1:1 PZQ-CU EA cocrystal solvate. Suitable single crystals for SXRD were obtained via cooling and slow evaporation experiments.

This cocrystal solvate (CSD refcode GOGVEH) crystallizes in the monoclinic space group *C*2/*c*, with four formula units per unit cell. In the structure, PZQ molecules adopt an *anti*-conformation of the carbonyl groups. The PZQ and CU molecules are connected by two H-bonds, forming a PZQ···CU···PZQ molecular assembly. The EA solvent molecules are loosely integrated into the crystal lattice, filling voids with minimal influence on the overall packing arrangement. Due to the weakly bound nature of the solvent molecules, the PZQ-CU EA cocrystal could be desolvated, yielding a non-solvated cocrystal that exhibited the same PXRD pattern initially obtained through LAG experiments with toluene. To obtain single crystals of the anhydrous cocrystal, a single crystal of the solvated form was mounted in a glass capillary and heated gradually from room temperature to 370 K at a rate of 3 °C/min, followed by further heating from 370 K to 390 K at 2 °C/min. The anhydrous cocrystal (CSD refcode GOGSOO) crystallizes in the monoclinic space group $P2_1/n$ with four molecules per unit cell. When comparing the solvated and non-solvated structures, only minor differences in their solid-state arrangement were observed.

Thermal analyses, including DSC and TGA, indicated that the cocrystal solvate was stable up to approximately 100 °C, at which point it transitioned to the non-solvated phase. The anhydrous cocrystal exhibited a melting point at 130 °C, lower than that of the individual components. Variable-temperature X-ray diffraction (VT-XRD) experiments conducted from room temperature to 395 K helped clarify the thermal behavior and phase transition from the 2:1:1 cocrystal solvate to the desolvated 2:1 cocrystal form.

Muresan-Pop et al. recently identified five new cocrystals of PZQ through mechanochemical reactions, using variations in process conditions such as liquid type, amount, and milling time [161]. The newly discovered cocrystals were formed with suberic acid (SUB), 3-hydroxybenzoic acid (3-HA), benzene-1,2,4,5-tetracarboxylic acid (BTC), trimesic acid (TRI), and 5-hydroxyisophthalic acid (5HIP), with their structures solved and deposited in the CSD. Notably, a prior study by Liu et al. reported a 2:1 PZQ-3HA cocrystal in the *P*-1 space group [156], but in this work, Muresan-Pop's group identified a 1:1 anhydrous cocrystal crystallizing in the monoclinic $P2_1/n$ space group with PZQ molecules adopting the common *anti*-conformation of the carbonyl groups (CSD refcode ROLMEO).

The PZQ-BTC cocrystal crystallizes in the triclinic *P*-1 space group, with a 2:1 stoichiometry and PZQ in *anti*-stereochemistry, H-bonded with BTC via COOH···O=C interactions (CSD refcode ROLMIS). For the PZQ-5HIP system, an ACN cocrystal solvate was obtained, crystallizing in the *P*-

1 space group, with one PZQ, four 5HIP, and two ACN molecules per ASU (CSD refcode ROLMOY). In this structure, layers of 5HIP molecules form a hexagonal arrangement stabilized by O-H···O H-bonds, while PZQ molecules adopt the less common *syn*-conformation, stabilized by O-H···O=C H-bonds involving the PZQ carbonyls.

The PZQ-TRI dihydrate cocrystal (PZQ-TRI DH) crystallizes in the monoclinic *C*2/*c* space group with an ASU containing one PZQ, two TRI, and two H_2O molecules (CSD refcode ROLNIT). In this structure, the *anti*-conformation carbonyl groups of PZQ are H-bond acceptors from H_2O molecules, and TRI is similarly H-bonded to H_2O.

The PZQ-SUB cocrystal, crystallizing in the monoclinic *I*2/*a* space group, exhibits a 2:1 host-guest stoichiometry, with eight PZQ molecules in *anti*-conformation and four SUB molecules per unit cell (CSD refcode ROLMAK). This cocrystal underwent a more comprehensive characterization, including DSC analysis, which revealed a single sharp endothermic peak at 104 °C, suggesting lower thermodynamic stability compared to the starting materials and indicating potentially higher solubility. Stability testing at 40 °C and 75% RH confirmed the stability of the system over five months. FT-IR analysis revealed shifts in the C=O and O-H stretching vibrations, confirming cocrystal formation: the carbonyl stretching of PZQ shifted from 1650 cm^{-1} to 1638 cm^{-1}, while SUB's carbonyl vibration moved from 1699 cm^{-1} to 1715 cm^{-1} in the cocrystal. The PZQ-SUB cocrystal also displayed a sheet-like structure, with thin parallelepiped layers measuring 100-300 μm in length.

Solubility tests were performed in ultrapure water, simulated gastric fluid (SGF), simulated intestinal fluid (SIF), and simulated colonic fluid (SCF). Among the new cocrystals, PZQ-5HIP ACN showed the highest solubility in SIF but lower solubility than pure PZQ in SCF. The PZQ-BTC and PZQ-SUB cocrystals emerged as the most promising candidates, demonstrating the highest solubility in water across various media.

The most recent advancements in PZQ cocrystallization research come from de Vries and coauthors, who have identified 11 new coformers suitable for PZQ cocrystallization and solved six new cocrystal structures [162]. Their approach used link prediction methods, which were enhanced using a scoring function known as "multi-steps resource allocation." Further refinement of the prediction models was achieved by analyzing the local network structure to eliminate imperfections, alongside the application of an algorithm originally developed by Devogelaer et al. [154].

The newly identified coformers for PZQ include chloranilic acid (CLA), 1,4-dibromotetrafluorobenzene (DBTFB), trans-ferulic acid (trans-FA), 1,3,5-trifluoro-2,4,6-triiodobenzene (TFTIB), and 2,3-dihydroxybenzoic acid (2,3-DHA). The stoichiometric ratio for the

PZQ-trans-FA cocrystal was found to be 1:2, while the other four coformers yielded a 1:1 ratio. All five cocrystals exhibited centrosymmetric structures in the *P*-1 or $P2_1/c$ space groups. Interestingly, the cocrystallization of DBTFB also led to the discovery of a racemic conglomerate cocrystal, which crystallized in the $P2_1$ space group. One particularly notable finding was the *syn*-conformation of PZQ carbonyl groups in the PZQ-TFTIB cocrystal.

The CSD refcodes for these cocrystals are JORKOU (PZQ-CLA), JORKUA and JORLAH ((R)/(S)-PZQ-1,4-DBTFB and PZQ-1,4-DBTFB, respectively), HIVXIX01 (PZQ-trans-FA), JORLIP (PZQ-2,3-DHA), and JORLOV (PZQ-TFTIB).

1.3 Niclosamide

Niclosamide (NCM), a salycilanilide derivative, was first introduced in the 1950s as an anthelmintic agent for the treatment of human tapeworms and cestodes parasites [214]. Currently, NCM is still considered a second-choice drug in the treatment of Schistosomiasis because of its short spectrum of action [215].

As PZQ, it is also included in the WHO Model List of Essential Medicines for both adults and children [94,95].

NCM has recently emerged as a promising candidate for drug repositioning across a diverse array of therapeutic domains. Originally used for its antiparasitic effects, it has garnered renewed interest due to its potential applications in other fields, including antiviral (e.g., SARS-Cov-2), antibacterial, anticancer, and anti-inflammatory treatments. This broad pharmacological profile underscores the potential of NCM to address various unmet medical needs beyond its initial use in parasitology [214,216,217].

Despite its promising therapeutic potential, the clinical development of NCM has been significantly hindered by its poor water solubility, categorizing it as a BCS Class II drug. Since it is practically insoluble in H_2O at 25 °C (13.32 μg/mL [218]), it is poorly absorbed in the gastrointestinal tract, resulting in reduced bioavailability and the occurrence of various gastrointestinal side effects [219]. In the treatment of intestinal trematodes, the recommended posology is 2g per day in a single dose [220], further underscoring the challenges in optimizing therapeutic efficacy for such conditions.

Additionally, this drug has a complex solid-state behavior. A particularly problematic aspect of NCM solubility profile is its tendency to convert easily into a highly insoluble monohydrate form [218,221]. This conversion severely limits its bioavailability, posing a major obstacle for its therapeutic use [30,218,221–225]. To address these solubility challenges, strategies involving the intentional formation of multicomponent systems (such as salts, cocrystals and solvates) have been explored. These solids can prevent or delay the conversion to the monohydrate form, thereby enhancing the solubility and stability of the drug in various formulations [191]. The formation of new multicomponent systems not only improves the solubility but can also affect the physical properties and stability of the drug, which are crucial for developing effective pharmaceutical formulations [191,226,227].

In Table 3 are reported the different solid forms of NCM (including polymorphs, hydrates, solvates, salts, salt cocrystals and cocrystals) discovered so far.

Table 3. Reported solid forms for NCM.

Acronym	Type of solid form	Stoichiometry	Reference code	References
	Anhydrous polymorphs			
NCM Form A	polymorph A	N/A[§]	HEBFUR	[30]
NCM Form B	polymorph B	N/A[§]	HEBFUR01	[221]
	Hydrates			
NCM-H_B	niclosamide monohydrate	1:1	OBEQAN	[218,228,229]
NCM-H_A	niclosamide monohydrate	1:1	OBEQAN01	[221]
NCM-H_A REF	niclosamide monohydrate (refined)	1:1	OBEQAN02	[224]
	Solvates			
NCM-ACT	niclosamide acetone solvate	1:1	KUKRIT	[221]
NCM-ACN	niclosamide acetonitrile solvate	1:1	KUKROZ	[221]
NCM-MeOH	niclosamide methanol solvate	1:1	GOJLIC	[230,231]
NCM-THF	niclosamide tetrahydrofuran solvate	1:1	OBEQER	[229,231]
NCM-TEG HEMI	niclosamide tetraethylen glycol hemisolvate	1:0.5	OBEQIV	[229,231]
NCM-DE	niclosamide diethyl ether solvate	1:1	Not indexed	[231]
NCM-DMSO	niclosamide dimethyl sulfoxide solvate	1:1	WOXVIS	[231,232]

NCM-DMF	niclosamide dimethylformamide solvate	1:1	WOXVEO	[231,232]
NCM-DMA I	niclosamide dimethylacetamide solvate I	1:1	WOXVOY	[232]
NCM-DMA II	niclosamide dimethylacetamide solvate II	2:2	WOXVOY01	[232]
NCM-DOX I	niclosamide dioxane solvate I	1:0.5	WOXWAL	[232]
NCM-DOX II	niclosamide dioxane solvate II	2:1.5	WOXWEP	[232]
Salts				
NCM-IMI	niclosamide-imidazole	1:1	ELOQIH	[224]
NaNCM-DMSO-H_2O	aqua-(niclosamide)-sodium dimethyl sulfoxide solvate	1:1:1	Not indexed	[222]
NaNCM-DMSO-$2H_2O$	diaqua-(niclosamide)-sodium dimethyl sulfoxide solvate	1:1:2	EKOHUJ	[222]
NCM-ETA	niclosamide-ethanolamine	1:1	Not indexed	[233–235]
NCM-PIP	niclosamide-piperazine	1:1	Not indexed	[235]
Salt Cocrystals				
KNCM-NCM-H_2O	catena-[bis(μ-niclosamide)-aqua-potassium]	1:1:1	EKOJAR	[222]
KNCM-NCM-$3H_2O$	catena-[bis(μ-niclosamide)-triaqua-potassium]	1:1:3	Not indexed	[222]
NaNCM-NCM-$3H_2O$	catena-[bis(μ-niclosamide)-triaqua-sodium]	1:1:3	Not indexed	[222]
NaNCM-NCM-$2H_2O$	catena-[bis(μ-niclosamide)-diaqua-sodium]	1:1:2	Not indexed	[222]

Cocrystals				
NCM-CAF	niclosamide-caffeine	1:1	HEBDUP	[30]
NCM-URE	niclosamide-urea	1:1	HEBFOL	[30,236,237]
NCM-PABA	niclosamide-p-aminobenzoic acid	1:1	HEBFAX	[30]
NCM-THEO	niclosamide-theophylline	1:1	HEBFEB	[30]
NCM-THEO ACN	niclosamide-theophylline acetonitrile solvate	1:1:1	HEBFIF	[30]
NCM-NCT	niclosamide-nicotinamide	1:1	Not indexed	[30]
NCM-INA	niclosamide-isonicotinamide	1:1	Not indexed	[30]
NCM-IMI	niclosamide-imidazole	1:1	Not indexed	[222]
NCM-AT	niclosamide-2-aminothiazole	1:1	ELOPOM	[224]
NCM-BA	niclosamide-benzamide	1:1	Not indexed	[224]
NCM-ISO	niclosamide-isoniazide	1:1	Not indexed	[224]
NCM-ACE I	niclosamide-acetamide I	1:1	ELOPUS01	[224]
NCM-ACE II	niclosamide-acetamide II	1:1	ELOPUS	[224]

§ not applicable for single compound

1.2.1 Niclosamide (NCM) Form A: the commercial Form

NCM is a pale yellow/yellowish-white fine crystalline powder which is photounstable [163]. Its chemical formula is $C_{13}H_8Cl_2N_2O_4$ with a molecular weight of 327.12 g/mol and its IUPAC name is 5-chloro-N-(2-chloro-4-nitrophenyl)-2-hydroxybenzamide (Figure 20). As evident from the chemical structure, unlike PZQ, NCM contains an amide capable of forming salts.

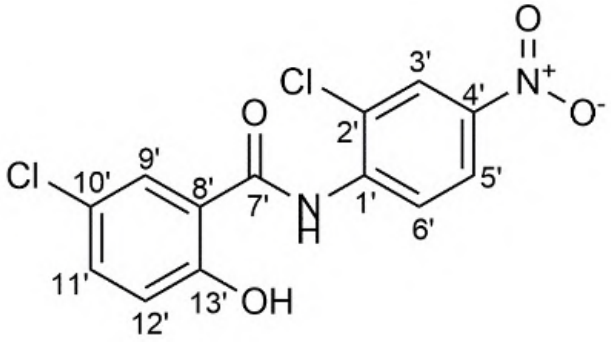

Figure 20. NCM chemical structure with atom numbering.

NCM is highly hydrophobic, with a LogP value of 3.6 [164] and practically insoluble in H_2O at 25 °C (13.32 µg/mL [218]). In contrast, NCM is slightly soluble in ACT and sparingly soluble in EtOH, with its solubility increasing to 43 mg/L in an alcohol/water mixture (40% iPOH) [30].

Bhanushali et al. recently reported the solubility of NCM, expressed as mole fraction, in eight different solvents. At 323.15 K, NCM exhibited its highest mole fraction solubility in polyethylene glycol 400 (PEG400) (1.103×10^{-3}), followed by PEG200 (5.272×10^{-4}), 1-butanol (1-ButOH) (3.047×10^{-4}), 2-PrOH (2.42×10^{-4}), EtOH (1.66×10^{-4}), DMSO (1.52×10^{-4}), MeOH (7.78×10^{-5}), and H_2O (3.27×10^{-7}) [238].

Despite its poor aqueous solubility, NCM exhibits a high affinity for water. It has been reported that the drug tends to rapidly convert to its monohydrate form (NCM H_A, CSD refcode OBEQAN02 [224]), even after a month of simple exposure to ambient humidity. This hydrated form is less soluble than the anhydrous A form and has been described as having a "*cement-like*" behavior due to its extreme insolubility in H_2O [30,239].

Its melting point is characterized by a sharp endothermic signal within the range of 227-232 °C, with no indication of concurrent decomposition [30].

The crystallographic structure of NCM has been solved and deposited in the CSD [168] with refcode HEBFUR [30]. From a crystallographic perspective, NCM exhibits a monoclinic unit cell with space group $P2_1/c$ and one molecule in the ASU ($Z'=1$) (Figure 21).

Crystal data	NCM
formula	$C_{13}H_8N_2O_4$
MW (g/mol)	327.12
T (K)	293
Space group	$P2_1/c$
a (Å)	13.485(2)
b (Å)	7.0669(11)
c (Å)	13.510(2)
a (°)	90
b (°)	98.345(2)
g (°)	90
V (Å³)	1273.83
Z	4
R-Factor (%)	3.49

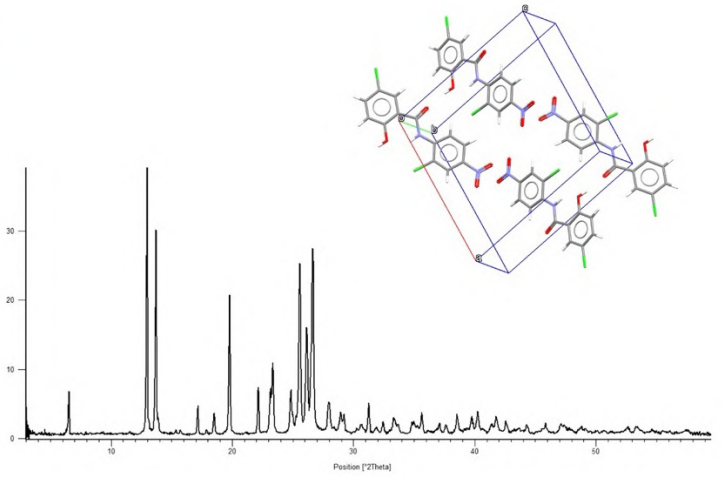

Figure 21. PXRD pattern and crystallographic data of NCM Form A.

As shown in Figure 22, intramolecular N-H···O H-bonds between the amine and hydroxyl groups lock the molecule into a nearly planar conformation. In contrast, intermolecular O-H···O H-bonds between the hydroxyl and carbonyl groups facilitate the formation of a layered structure. Additionally, there are stabilizing interactions between Cl···NO_2 groups (halogen bonds) (Figure 22). Figure 22 also illustrates the arrangement of NCM molecules within the crystal lattice, where the molecules form channels between the layers, stabilized by π–π interactions with distances of 3.39 Å and 3.34 Å [30].

According to a recent study, the poor aqueous solubility of anhydrous NCM is likely related not only to its parallel planar structure, which forms π-π interactions, but also to its antiparallel arrangement, which results in cation-π interactions (π ···NO_2). It has been hypothesized that NCM solubility could be enhanced by disrupting these cation-π interactions, thereby promoting the formation of parallel planar interactions [240].

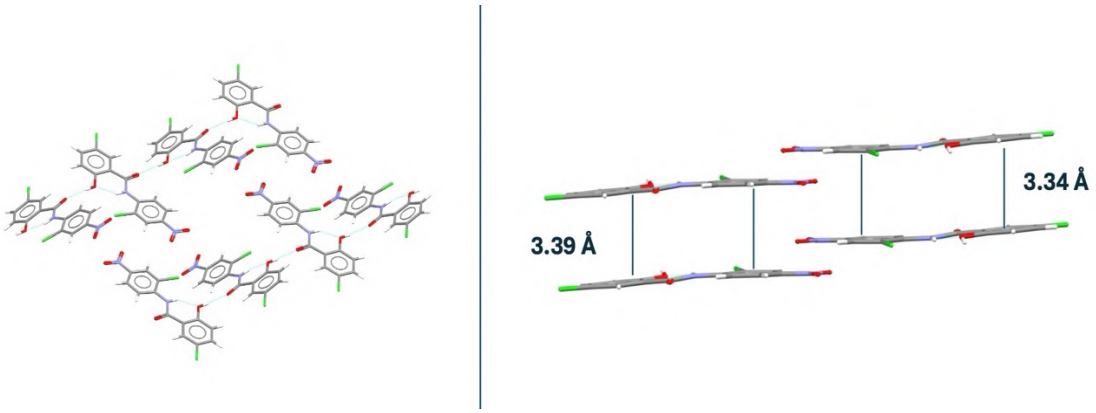

Figure 22. H-bonds between O-H···O form a layered structure (left), planar structure with π-π stacking interaction (right). Adapted from reference [30].

The SEM image provides a depiction of the crystalline habitus of anhydrous NCM: the drug exhibits peculiar rectangles with distinctive protrusions (Figure 23). The formation of this characteristic habitus is attributed to the hygroscopic properties of anhydrous NCM, resulting from moisture absorption [218].

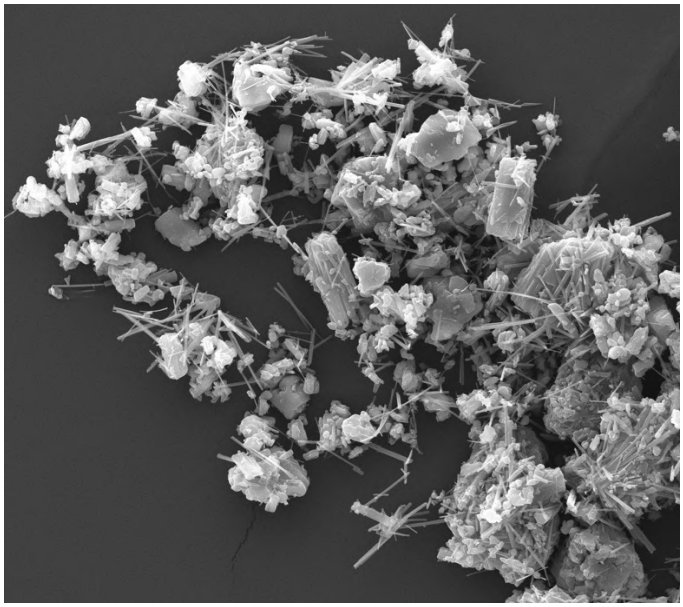

Figure 23. SEM image of NCM Form A at a magnification of 500x.

FT-IR characteristic bands and SSNMR spectrum with chemical assignments of anhydrous NCM are reported below (Figure 24).

NCM displays characteristic bands in the FT-IR spectrum that correspond to the various functional groups present in the molecule:

- In the range of 3300-3500 cm^{-1}, the two bands at 3242.7 cm^{-1} e 3199.5 cm^{-1} are attributed to the N-H stretching vibration of the secondary amide group, with their precise position influenced by H-bonding [241];
- The band at 897 cm^{-1} corresponds to the N-H bending of the amide group [241];
- In the range of 1650-1700 cm^{-1}, the two bands at 1681 cm^{-1} e a 1618 cm^{-1} are associated to the amide carbonyl group and the ester carbonyl C=O group, respectively [242];
- The C=O bending group absorbs at 1217 cm^{-1} [242];
- At 1192 cm^{-1}, it is visible the C-OH stretching band [242];
- In the range of 700-800 cm^{-1}, strong bands are due to the C-Cl stretching vibration in the aromatic ring where chlorine is substituted [242].

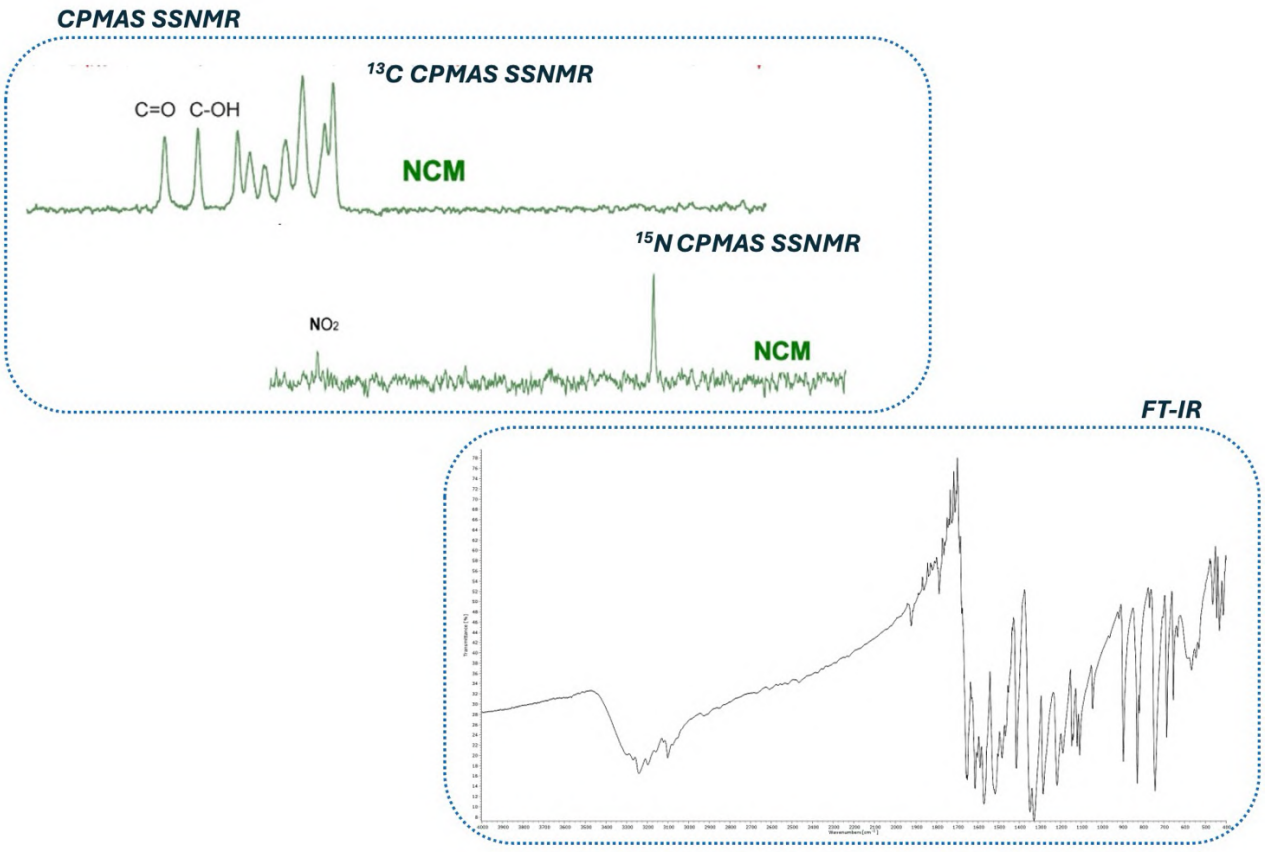

Figure 24. Chemical shifts assignments and ^{13}C and ^{15}N SSNMR spectrum and FTIR spectrum of NCM Form A.

The ^{13}C and ^{15}N CPMAS SSNMR spectra of NCM are shown in Figure 24. Detailed chemical shift assignments are provided in the work by Grifasi and colleagues [222].

The ^{13}C spectrum is characterized by well-defined signals corresponding to key functional groups in the NCM structure:

- A strong peak at 153.9 ppm is assigned to the C-OH carbon in the phenolic group.
- The signal at 139.9 ppm corresponds to the C-NH carbon, related to the amide group.
- The peak at 117.4 ppm is attributed to the C=O carbon of the ester functional group.

Additionally, the aromatic carbons are observed in the region of 110-140 ppm, where the overlapping signals indicate the multiple carbons of the benzene rings in the NCM structure. The ^{15}N spectrum clearly distinguishes the nitrogen environments of the two nitrogens within the molecule:

- The amide nitrogen (N-H) shows a chemical shift at 108.7 ppm**,** consistent with its position in the amide functional group.
- A prominent signal at 341.9 ppm is associated with the NO_2 (nitro) group, reflecting the highly deshielded nature of nitrogen in the nitro functionality [222].

1.2.2 NCM crystalline polymorphs

The other polymorphic form of NCM obtained so far is Form II (also referred to as Polymorph B of NCM), which has been deposited in the CSD under the refcode HEBFUR01 [221]. This new polymorph was produced through slow evaporation of Form A from an absolute EtOH solution.

The limited available information on Polymorph B primarily focuses on its crystallographic properties. It crystallizes in a monoclinic unit cell that contains four molecules in the ASU (Z' = 4) and belongs to the *P*2/*n* space group. Compared to Form A, Polymorph B exhibits pseudosymmetry, as seen in the formation of parallel layers along specific planes, which define its molecular rearrangement. Two out of the four molecules form a centered layer. Intermolecular H-bonds between O-H···O can be seen along the *b*-axis (Figure 25). This structural reorganization highlights the subtle differences between the two forms, with Polymorph B showing a distinct arrangement that can potentially influence its physical and chemical properties [221].

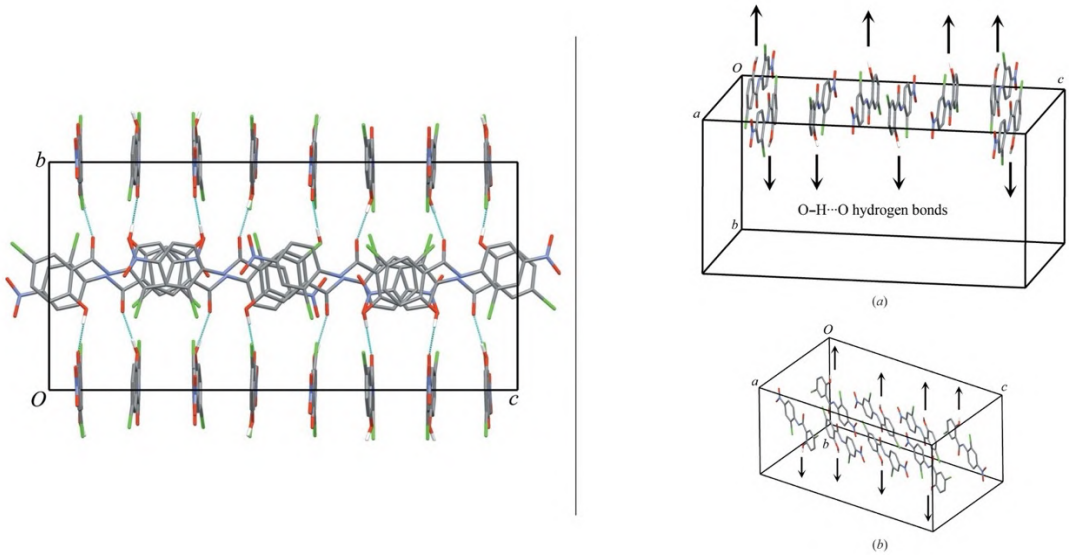

Figure 25. The typical layers of Form II connected throughout H-bonds (left); view of the (010) layers, indicating the direction of propagation of the O-H···O H-bonds with respect to the *b*-axis (right). Adapted from reference [221].

1.2.3 NCM amorphous forms

The available literature provides little information about the amorphous forms of NCM. The compound is primarily described as a poor glass former, exhibiting a strong tendency to recrystallize. This makes it almost impossible to obtain a stable amorphous solid from the pure substance by itself [243].

Most studies highlight the formation of ASDs of NCM in the presence of a secondary (or third) compound, such as polymers, to enhance amorphization and stability.

Jara et al. prepared, using the hot melt extrusion method, ASD in the presence of poly(1-vinyl pyrrolidone-co-vinyl acetate) (PVA-VA). These systems exhibited: a 60-fold enhancement in apparent solubility in FaSSIF at pH 6.5 and 37 °C and a remarkably ameliorated diffusion. These *in vitro* results were confirmed in animal studies, where the ASD showed a doubled oral bioavailability [243].

Bhanushali et al. developed a range of binary and ternary ASDs of NCM using various polymers and different polymer-to-NCM ratios [244]. Among these formulations, the most successful was the one that combined NCM with hydroxyethyl cellulose (HEC) at a ratio of 1:4. The PXRD results confirmed the amorphous transformation of NCM within this formulation, indicating a successful incorporation of the drug into an amorphous state. Notably, the water solubility of NCM increased dramatically, showing a 70-fold enhancement to 428.33 ± 14.14 μg/mL, compared to the solubility of the pure compound, which was only 6.14 ± 0.67 μg/mL. The study reported that Cmax, AUC_{0-t}, and AUC_{0-inf} increased four-fold compared to the pure drug after oral administration (25 mg/kg) in healthy female Wistar rats.

1.2.4 NCM multicomponent solid forms

NCM possesses several functional groups that enable it to form supramolecular interactions, thus forming cocrystals and solvates, like PZQ, but also salt species. Its chemical structure allows interactions that facilitate salt formation, expanding its potential for various solid-state modifications.

1.2.4.1 NCM Salts

According to IUPAC, a salt is a "*chemical compound consisting of an assembly of cations and anions*" [245]. In a pharmaceutical context, this refers to an ionizable API paired with a counterion, which can be either molecular (e.g., acetate, mesylate) or atomic (e.g., sodium, chloride). The

formation of a pharmaceutical salt is one of the most effective strategies for enhancing the solubility and bioavailability of a drug [246,247]. Over the past decades, this process has become increasingly prevalent in drug development, with more than half of the marketed drugs formulated as salts [14,246].

Unlike PZQ, NCM is well-known for its ability to form salts. However, the number of NCM salts reported in literature is relatively limited [224,233–235], despite its potential as a salt-forming agent.

Luedeker and collaborators report a salt of NCM with imidazole (NCM-IMI), the structure of which has been solved and deposited in the CSD under the reference code ELOQIH [224]. The crystal structure of NCM-IMI was solved in the monoclinic space group $P2_1/c$, with one molecule of NCM and one molecule of IMI in the ASU. The presence of an imidazolium ion is assumed, linking two molecules of NCM via a charge-assisted {N-H$^{+}\cdots^{-}$O} and a neutral {N-H$\cdots$O} synthon, leading to the formation of chains that constitute layers. The obtained unit cell is relatively flat and stabilized by π-π stacking (Figure 26).

This salt was obtained by NG the two components in a 1:1 molar ratio for 15 min. This new salt exhibited a single endotherm peak at 213.5 °C, ranging between those of the pristine drug [30] and imidazole coformer, thereby suggesting no decomposition before melting. The compound also demonstrated improved solubility characteristics (in absolute EtOH after 72h), with a NCM content in solution of 22 mg/L, compared to the anhydrous Form A (3.5 mg/L) [30].

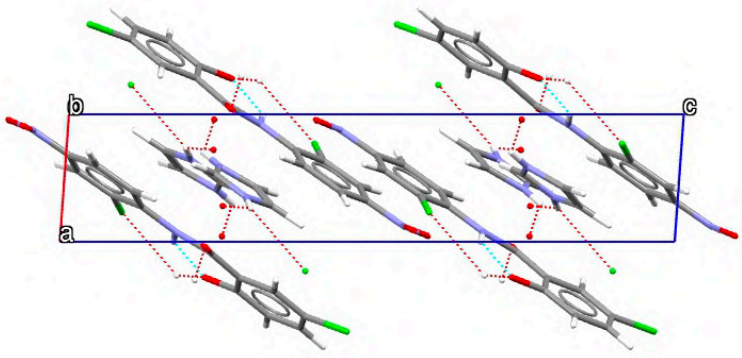

Figure 26. Unit cell formed by layers of NCM-IMI salt (ELOQIH) viewed along *b*-axis [248].

Two solvated sodium salts of NCM (i.e., NaNCM-DMSO-H_2O and NaNCM-DMSO-$2H_2O$) were synthetized by Grifasi and coauthors [222]. These two salts were obtained via salification of NCM with NaOH and subsequent kneading in DMSO. NaNCM-DMSO-$2H_2O$ generated single crystals suitable for SCXRD: it crystallizes in an orthorhombic unit cell with space group *Pnma* and its crystal structure is deposited in the CSD with refcode EKOHUJ. The packing is characterized by layers and each H_2O molecule bridges two sodium cations and donates two H-bonds to NCM and DMSO. The structure of the other salt, NaNCM-DMSO-H_2O, was instead deduced from SSNMR analysis. NaNCM-DMSO-H_2O salt formation is confirmed by the signal at 168.8 ppm which is typical of C-O- groups (δC−OH NCM = 153.9 ppm), while the CH_3 groups of DMSO fall at 41.0 and 40.3 ppm suggesting lower molecule symmetry than the dihydrated form. In the ^1H MAS spectrum, the peak at 15.0 ppm indicates a moderate intramolecular N-H···O- H-bond. The presence of one molecule of DMSO and one molecule of H_2O was confirmed by combining the integration of ^1H MAS peaks with TGA data.

Kapale et al. describe the synthesis of the NCM-ethanolamine (NCM-ETA) salt (also known as NES) and its corresponding patent, CN106496060A [235]. Initially, the primary objective of this salt form was to enhance the bioavailability of NCM as an anthelmintic agent by improving its solubility and absorption in the gastrointestinal tract. Ethanolamine was selected as the counterion to form the salt, resulting in a substantial increase in aqueous solubility compared to the original, poorly soluble form of NCM. Specifically, the solubility of NES increased to 180-280 mg/L at 20 °C (compared to 5-8 mg/L for NCM) and NES also demonstrated an excellent safety profile [234,235].
In recent years, the application of NCM-ETA has expanded far beyond its original use for treating parasitic infections. NCM itself has gained recognition for its potential in repurposing for various non-parasitic diseases, including cancer, metabolic disorders such as diabetes, and viral infections. NES has emerged as a preferred candidate due to its improved pharmacokinetic properties. In cancer therapy, preclinical studies have shown that the salt can induce apoptosis in cancer cells and suppress tumor growth in animal models [234]. Furthermore, NCM-ETA has been explored for its potential in managing metabolic disorders, particularly type 2 diabetes. Research suggests that NCM can enhance insulin sensitivity and reduce inflammation in diabetic models, highlighting its promise as a therapeutic option for metabolic diseases [233].

Kapale and colleagues also referenced the synthesis of a NCM-piperazine (NCM-PIP) salt, as detailed in patent CN102432493A. This patent describes a multi-step procedure where PIP and NCM are refluxed in a specific ratio for several hours, using solvents such as EtOH, MeOH, or MeOH/H_2O

solutions. After the reaction, the mixture is cooled, filtered, centrifuged, washed, and dried to produce a pale-yellow crystalline NCM-PIP salt. In 2012, Jingjing Guo and collaborators reported that NCM-PIP exhibited mitochondrial uncoupling activity comparable to NES and demonstrated potential in reducing obesity, hepatic steatosis, and high blood sugar in mouse models following oral administration [235].

1.2.4.2 NCM Salt Cocrystals

A salt cocrystal refers to a cocrystal composed of a salt (formed by an ion and its counterion) and a neutral molecule, held together by non-ionic interactions, typically H-bonds [249]. This distinguishes it from molecular cocrystals, which involve two or more neutral molecules, and from crystalline salts, which are solid-state adducts where proton transfer occurs from the acidic to the basic component, resulting exclusively in a cation and an anion.

Grifasi et al. successfully prepared four salt cocrystals of NCM (i.e., KNCM-NCM-H_2O, KNCM-NCM-$3H_2O$, NaNCM-NCM-$3H_2O$, and NaNCM-NCM-$2H_2O$) by grinding (through NG or LAG with little amount of solvent, such as pure EtOH or EtOH/H_2O mixtures in different ratios) NCM with carbonates and bicarbonates. These species were employed to supply the coformers (K^+ or Na^+ as counterions) and offer the added benefit of preventing NCM degradation during the process [222]. Only the crystal structure of KNCM-NCM-H_2O salt cocrystal was solved (CSD refcode EKOJAR): it crystallizes as triclinic *P*-1 and the ASU contains one NCM, its potassium salt (KNCM), and one H_2O molecule (Figure 27).

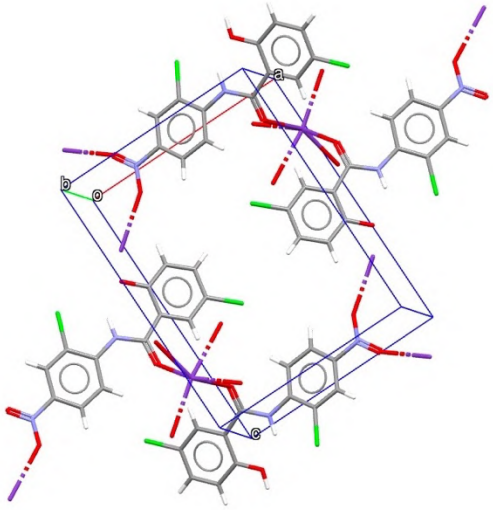

Figure 27. Unit cell of KNCM-NCM-H_2O salt cocrystal (EKOJAR) [248].

The other three salt cocrystals were fully characterized by means of SSNMR: the structures of all obtained samples are characterized by a strong (C-O···H···O-C) H-bond as confirmed by the large ^{1}H high frequency shift in OH signals (about 18 ppm).

All salt cocrystals showed an improvement in physical properties over pure NCM. In terms of increase in thermal stability, KNCM-NCM-H_2O has raised the melting point by up to 70 °C.

Also, solubility tests were conducted in absolute EtOH: the salt cocrystal NaNCM-NCM-$2H_2O$ exhibited a NCM concentration of 24 mg/L in solution after 72h, representing a significant improvement compared to the anhydrous Form A (3.5 mg/L). Additionally, IDR tests, performed in a 1:1 EtOH/H_2O solution, showed enhanced dissolution profiles for all four salt cocrystals obtained. Notably, NaNCM-NCM-$2H_2O$ improved the dissolution rate by five-fold compared to anhydrous NCM Form A.

1.2.4.3 NCM Cocrystals

Sanphui and colleagues were the first to report NCM cocrystals. In their study, they successfully synthesized six new anhydrous NCM cocrystals in a 1:1 molar ratio with caffeine (NCM-CAF), urea (NCM-URE), p-aminobenzoic acid (NCM-PABA), theophylline (NCM-THEO), nicotinamide (NCM-NCT), and isonicotinamide (NCM-INA), along with a 1:1:1 cocrystal solvate of NCM-THEO with acetonitrile (NCM-THEO ACN) [30].

The six anhydrous cocrystals were produced using NG, wet granulation, and slow evaporation methods, while the cocrystal solvate was prepared in mortar-pestle via 15-min LAG using NCM and THEO in a 1:1 molar ratio, with the addition of 5 drops of ACN. Crystallization was then performed in a 10 mL 1:1 mixture of EA and ACN.

Single crystals suitable for SCXRD were obtained for five out of the seven cocrystals (i.e., NCM-CAF, NCM-URE, NCM-PABA, NCM-THEO, and NCM-THEO ACN). For NCM-NCT and NCM-INA, due to the lack of suitable single crystals, characterization was carried out using ^{13}C SSNMR.

The crystal structures of NCM-CAF, NCM-URE, NCM-PABA, NCM-THEO, and NCM-THEO ACN have been deposited in the CSD with refcodes HEBDUP, HEBFOL, HEBFAX, HEBFEB, and HEBFIF, respectively. Structurally, in the cocrystal forms, the intermolecular O-H···O H-bond from the hydroxyl donor to the carbonyl acceptor in the NCM crystal structure was replaced by an acceptor atom from the coformer.

All six cocrystals showed improved dissolution rates (tested in 40% iPOH-H_2O) compared to the pure API. NCM-THEO ACN exhibited the highest solubility, with a six-fold increase, while NCM-THEO demonstrated similarly strong dissolution behavior with a five-fold increase over a 90-min period.

Equilibrium solubility experiments revealed that all cocrystals, as well as the pure API, transformed into NCM H_A within 24h in a 40% iPOH-H_2O slurry medium.
Stability tests under accelerated humidity conditions (75% RH, 40 °C) indicated that NCM-NCT and NCM-INA had superior stability compared to the other cocrystals.

Grifasi and coworkers, along with NCM salt cocrystals, also developed a classic cocrystal of NCM with imidazole (NCM-IMI). This cocrystal was obtained by grinding NCM and IMI in a 1:1 stoichiometric ratio at room temperature for 15 min. Due to the lack of single crystals, its structure and packing arrangement were deduced using ^{13}C, ^{15}N, and ^{1}H SSNMR.
The ^{13}C CPMAS spectrum of NCM-IMI indicated the formation of a cocrystal rather than a salt, although the classification remained somewhat ambiguous. The significant high-frequency shift of the NCM ^{13}C C-OH resonance from 153.9 to 161.6 ppm suggested the presence of a strong H-bond, likely formed with the tertiary nitrogen atom of IMI. Additionally, the ^{15}N chemical shift, showing a change of about 20 ppm (from 220.5 to 195.8 ppm), was consistent with the formation of a strong C-OH$\cdots N_{IMI}$ interaction.
The NCM-IMI cocrystal exhibited a significantly higher melting point (275.5 °C) compared to pure NCM (224 °C), along with an improved dissolution profile and much better solubility (22 mg/L) than pure NCM (reported in this article as 0.0035 mg/L) [222].

Luedeker and colleagues successfully obtained 1:1 NCM cocrystals with 2-aminothiazole (NCM-AT), benzamide (NCM-BA), isoniazid (NCM-ISO), and acetamide (two polymorphs, NCM-ACE I and NCM-ACE II) via LAG and/or slow SE [224].
No crystal structures were reported for NCM-BA and NCM-ISO, with their structural deductions made using SSNMR. For NCM-AT and the polymorphs NCM-ACE I and NCM-ACE II, structure solutions were derived from powder samples by combining PXRD and SSNMR data. These confirmed successful cocrystal formation, based on the presence of robust synthons such as {O-H$\cdots$O}, {N-H$\cdots$O}, and {O-H$\cdots$N}.
The crystal structure of NCM-AT (CSD refcode ELOPOM) was solved in the monoclinic space group $P2_1/c$, with one NCM and one AT molecule in the ASU, consistent with ^{1}H MAS NMR data (Figure 28a).
In the case of the NCM-ACE system, cocrystallization yielded polycrystalline mixtures of at least two polymorphs. LAG using EtOH predominantly produced NCM-ACE I, while ACN favored the formation of NCM-ACE II. NCM-ACE I (CSD refcode ELOPUS01) crystallizes in the triclinic space

group *P*-1 with one molecule of NCM and ACE in the ASU. In contrast, NCM-ACE II (CSD refcode ELOPUS) crystallizes in the orthorhombic space group $P2_12_12_1$ (Figure 28b).

A comparison of the cell parameters for NCM-ACE I and II revealed similarities with the hydrated forms NCM H_A and NCM H_B, respectively. However, upon transformation of NCM-ACE II to NCM-ACE I, the symmetry dropped from orthorhombic to triclinic.

Thermal stability was assessed via DSC analysis. NCM-AT, NCM-BA, and NCM-ISO each showed a single endothermic event at 187.5 °C, 156.1 °C, and 185.5 °C, respectively, within the range of the pure drug and coformers. Conversely, the DSC curve for NCM-ACE II revealed two endothermic peaks at 171.5 °C and 157.7 °C, likely due to residual NCM-ACE I, followed by ACE sublimation and NCM melting. NCM-ACE I, on the other hand, showed only one endothermic peak at 159.2 °C, alongside ACE sublimation and NCM melting.

Significant solubility improvement was observed for NCM-AT, whose equilibrium solubility was 2.8 times higher than that of pure NCM in 40% iPOH-H_2O medium.

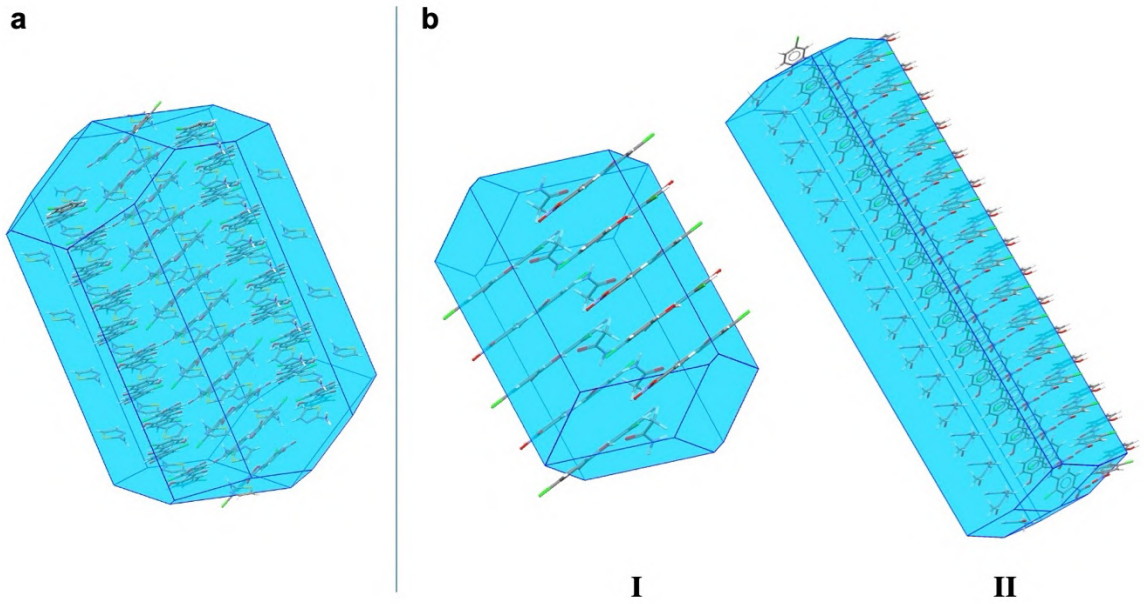

Figure 28. BFDH morphology of (a) NCM-AT cocrystal (ELOPOM) and (b) polymorphs NCM-ACE I (ELOPUS01) and NCM-ACE II (ELOPUS) [248].

1.2.4.4 NCM Hydrates

To date, two monohydrate forms of NCM have been identified: Form H_A and Form H_B. Studies examining the relationship between these two monohydrates have established that Form H_A is the kinetically favored form, which readily transforms into the thermodynamically more stable form H_B [218,228,250]. Dehydration of monohydrates is reported to give, in both cases, anhydrous Form A of NCM, even passing through different mechanistic pathways [223].

Jara et al. reported that the transition of NCM anhydrate to NCM H_A during storage can be visually confirmed, as the original yellowish-white powder of the anhydrate turns yellow in the H_A form [217].

The two monohydrate forms of NCM have been prepared using different methods starting from the anhydrous Form A. The formation of Form H_A was achieved through cooling crystallization of NCM suspensions in H_2O, followed by filtration to obtain the suspended material. In contrast, Form H_B was obtained from the suspension of both the anhydrous Form A and Form H_A in crystallization solvents [218].

Additionally, another study reported an alternative synthesis method for Form H_A through LAG. In this process, the monohydrate H_A was obtained using 160 µL of H_2O or a mixture of EA and H_2O or ACT and H_2O (with a molar fraction of H_2O of 0.67), achieving successful synthesis after just 30 min of milling [228].

Both monohydrate forms, H_A and H_B, exhibited a significant decrease in solubility compared to the anhydrous Form A, with solubility values of 0.90 µg/mL for H_A and 0.58 µg/mL for H_B, whereas the anhydrous form displayed a solubility of 13.32 µg/mL [218].

Single crystals of Form H_B were grown from wet ACT and its crystal structure was solved by Caira and coauthors and deposited in the CSD with refcode OBEQAN. Form H_B crystallizes in the monoclinic space group $P2_1/a$ with one molecule of NCM and one molecule of H_2O in the ASU ($Z' = 1$). The two H_2O molecules within the unit cell occupy a cavity bounded by the van der Waals envelopes of surrounding drug molecules. The cavity is separated from an identical cavity in the adjacent unit cell [229].

Form H_A was first deposited in the CSD under the refcode OBEQAN01 [221]. It crystallizes in the monoclinic space group $P2_1/a$ with one molecule of NCM and one molecule of H_2O in the ASU ($Z' = 1$). For comparative purposes, Luedeker et al. re-solved the structure again starting from a powder diffraction pattern. The monohydrate structure was independently refined in a monoclinic unit cell, like the previously reported crystal structure [221]. However, the positions of the cell axes a and c were exchanged to facilitate comparison with the pseudopolymorphic hydrate Form H_B. The

resulting structure of Form H_A crystallizes in the monoclinic space group $P2_1/c$, with $Z' = 1$ (CSD refcode OBEQAN02), matching the symmetry and arrangement of the original form, but offering improved comparability with Form H_B [229]. Figure 29 illustrates the two crystallographic unit cells of Form H_A, highlighting their structural features and symmetry.

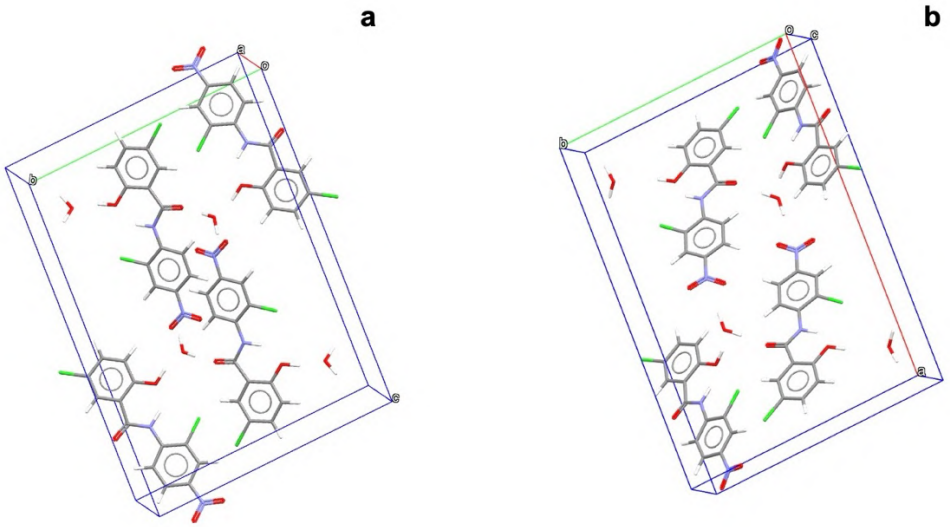

Figure 29. Crystal structures of (**a**) OBEQAN01 and (**b**) OBEQAN02 [248].

1.2.4.5 NCM Solvates

NCM pronounced tendency to form solvates/hydrates (rather than anhydrous forms) is well-documented in literature [218,221,229,231,240,251]. This tendency is largely attributed to planar molecular structure of NCM. This planarity allows its molecules to pack in a way that facilitates the creation of channel solvates, where solvent molecules are incorporated into the crystal lattice. To date, in addition to the above-mentioned two monohydrates (H_A and H_B [30,218,221–224,228]), twelve solvates of NCM with ten different solvents (i.e., ACT, ACN, MeOH, THF, TEG, DE, DMSO, DMF, DMA, DOX [221,229–232]) have been identified. These solvates are typically stabilized by π-π stacking interactions between the aromatic rings of the NCM molecules. The planar structure enables efficient stacking of these molecules, creating voids or channels in the crystal that can accommodate solvent molecules. The π-π stacking interactions, which occur between parallel aromatic rings, provide additional stability to the crystal structure by maximizing attractive forces between the π-electron clouds [230,240,251].

Moreover, recent studies by Kuri and others have highlighted that the strength of H-bonds between NCM and solvent molecules plays a crucial role in this behavior. They found that, while both

anhydrous and solvated forms are stabilized by H-bonds, those in solvated forms are significantly stronger, leading to a preference for solvate formation over anhydrous forms [232,236].

Based on the available information, the first study on NCM solvates was published in 1998 by Caira et al., in which single crystals of NCM H_B, along with two solvated NCM structures—one with tetrahydrofuran (1:1 NCM-THF) and one hemisolvate with tetraethylene glycol (1:0.5 NCM-TEG HEMI)—were obtained [229].

NCM-THF (CSD refcode OBEQER) crystallizes in the orthorhombic space group $Pn2_1a$, featuring one NCM molecule and one THF molecule in the ASU. In this structure, the THF molecules occupy void channels formed by the nearly planar conformation of the NCM molecules (intramolecular N-H···O H-bond) (Figure 30a).

A notable characteristic of this solvate is its rapid desolvation upon exposure to air. TGA showed an onset of mass loss at 30 °C, significantly lower—by 36 °C—than the boiling point of THF [252], indicating accelerated desolvation under ambient conditions.

NCM-TEG HEMI, deposited in the CSD under the refcode OBEQIV, crystallizes in the monoclinic space group $P2_1/c$. The ASU ($Z' = 1$) contains two NCM molecules and one TEG molecule. TEG adopts a folded conformation stabilized by intramolecular H-bonds and appears to be intercalated within the crystal structure. Perpendicular to the *b*-axis, the structure consists of alternating infinite layers of host NCM molecules and guest TEG molecules (Figure 30b).

TGA analysis revealed mass loss due to TEG release over a broad temperature range (65–230 °C). Desolvation of the crystals in ambient conditions at 20 °C occurs very slowly, consistent with the low volatility of TEG (328 °C [50]). This slow desolvation is also explained by the strong O-H···O H-bonds anchoring each TEG molecule to the surrounding host layers, between which it is intercalated.

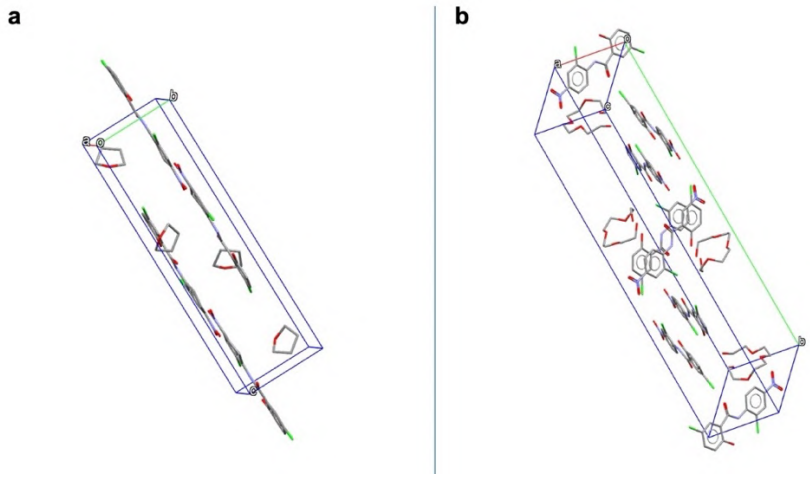

Figure 30. Crystal structures of (**a**) NCM-THF and (**b**) NCM-TEG HEMI [248].

In a subsequent study, Caira and coworkers focused on identifying the physicochemical, structural, and spectral properties of the previously mentioned NCM-THF and NCM-TEG HEMI solvates, along with four additional monosolvates (1:1 molar ratio) of NCM with methanol (NCM-MeOH), diethyl ether (NCM-DE), dimethyl sulfoxide (NCM-DMSO), and N,N-dimethylformamide (NCM-DMF) [231].

To obtain these solvates and the hemisolvate, saturated NCM solutions were prepared in the respective solvents at room temperature. These solutions were then gently heated (not exceeding 60 °C) under stirring until most of the anhydrous form dissolved. The solutions were filtered, covered, and left at room temperature to allow full crystallization. The resulting crystals were stored in their corresponding solutions to prevent desolvation.

SEM analysis revealed distinct morphologies for NCM solvates. NCM-MeOH formed needle-like crystals with sharp, uneven surfaces, while NCM-THF crystallized as long, flat yellow tabular crystals with a layered structure. Similarly, NCM-DMSO produced smooth, thin, plate-like needles, also showing a layered structure, though with uneven surfaces. NCM-DE solvate appeared as bent, tangled crystals with rough surfaces, and NCM-TEG HEMI crystallized into yellow prismatic forms. The DSC curves for all the solvates exhibited two endothermic peaks: one for desolvation and the other for melting. In the case of NCM-TEG HEMI, the endothermic peaks appeared at 103 °C and 205 °C, with the typical melting point of NCM at 229 °C shifted to 205 °C due to TEG acting as a solvent after its release from the crystals. This indicates that the crystals partially dissolved in TEG before melting between 195 °C and 205 °C. For NCM-MeOH and NCM-THF, the desolvation endotherms were observed at temperatures below 100 °C, while those for NCM-DMSO, NCM-DMF, and NCM-DE occurred between 140 °C and 170 °C. TGA analysis was conducted to assess solvent loss from the crystals and determine the stoichiometry of the solvates. Among the solvates, NCM-THF was the least stable; in contrast, NCM-TEG HEMI demonstrated the highest stability, desolvating gradually over a broad temperature range due to the mode of inclusion and the low volatility of TEG.

Solubility tests in H_2O (at 25 °C after 24h) showed that all these solvates are poorly soluble in H_2O (<1 mg/mL), being NCM-DE the most soluble solvate (±6.16 μg/mL).

The solubility of various crystal forms in H_2O at 25 °C after 24h follows this order: anhydrous NCM > NCM-DE > NCM-MeOH > NCM-TEG HEMI > NCM-DMSO > NCM-DMF. Among them, NCM-TEG HEMI exhibited the highest dissolution rate at 3.65 μg x cm^{-2} min^{-1}. In an alcoholic mixture, the dissolution rates of the other forms matched that of the monohydrate H_B, indicating that under the given dissolution conditions, all the solvated forms were converted to the monohydrate H_A [218,221].

However, no crystallographic data were reported in this work, and the structures of NCM-MeOH, NCM-DMSO, and NCM-DMF were later characterized by other research groups. To date, NCM-DE monosolvate remains the only crystal structure that has not yet been solved.

The crystal structure of NCM-MeOH was described by Harriss and colleagues [230]. Single crystals were grown by heating an equimolar mixture of NCM and nicotinic acid in MeOH. After separating the solution from the solid residue, it was refluxed for 10 min and then cooled to room temperature. Yellow needle-shaped crystals of NCM-MeOH began to form within a few hours. NCM-MeOH (CSD refcode GOJLIC) crystallizes in the orthorhombic space group $P2_12_12_1$, with one NCM and one MeOH molecule in the ASU. In this structure, NCM adopts a planar conformation within the crystal structure, creating channels where MeOH molecules are located. These molecules interact with NCM through intermolecular O-H···O H-bonds, between the hydrogen of the NCM hydroxyl group and the oxygen of the MeOH hydroxyl group. Notably, NCM-MeOH easily converts into NCM H_A when exposed to air. This phenomenon was explained by the authors as resulting from a structural correlation between NCM-MeOH and NCM H_A, which aligns with the low dehydration temperature of NCM H_A and the conversion of NCM-MeOH to the hydrate upon exposure to air.

In a 2015 study, two additional NCM monosolvates with acetone (NCM-ACT) and acetonitrile (NCM-ACN) were identified and deposited in the CSD under refcodes KUKRIT and KUKROZ, respectively [221]. They both crystallize in the triclinic *P*-1 space group.
NCM-ACT was obtained by dissolving anhydrous NCM in ACT under heat. Upon cooling, along with the rapid formation of a fibrous white material, a few crystals corresponding to NCM-ACT solvate were observed. In this structure, ACT molecules interact with NCM through intermolecular O-H···O H-bonds between the hydroxyl group of NCM and the carbonyl group of ACT. NCM molecules are stacked along the *a*-axis, and within these stacks, the NO_2 groups of neighboring NCM molecules form intermolecular interactions. The C=O groups of NCM face outward from the stacks, each participating in a C-H···O interaction with a NCM molecule from a neighboring stack.
NCM-ACN was, instead, obtained by dissolving anhydrous NCM in ACN with stirring at about 80 °C. The solution was then left at ambient conditions, leading to the formation of needle-like crystals within 24h. The crystals were removed from the mother liquor before complete SE, as prolonged exposure often resulted in the formation of NCM H_A.
In NCM-ACN, NCM molecules also stack, with intermolecular O-H···O H-bonds between the hydroxyl group of NCM and the cyano group of ACN molecules, which occupy channels between NCM stacks.

Kuri et al. successfully grew single crystals of NCM-DMSO and NCM-DMF solvates, previously reported by Van Tonder and colleagues. In addition, they identified four new solvate systems: two polymorphs with N,N-dimethylacetamide (1:1 NCM-DMA I and 2:2 NCM-DMA II) and two variable-stoichiometric solvates with 1,4-dioxane (1:0.5 NCM-DOX I and 2:1.5 NCM-DOX II) [232].

NCM-DMSO, NCM-DMF, and NCM-DOX I were crystallized via slow evaporation, while NCM-DOX II and NCM-DMA I were obtained using anti-solvent crystallization. NCM-DMA II, on the other hand, was grown using the vapor diffusion technique.

NCM-DMF crystallizes in the monoclinic space group $P2_1/n$ with one NCM and one DMF molecule in the ASU (CSD refcode WOXVEO). NCM-DMSO forms crystals in the monoclinic $P2_1/c$ space group, also with one NCM and one DMSO molecule in the ASU (CSD refcode WOXVIS). NCM-DMA I crystallizes in the monoclinic $P2_1/c$ space group with one NCM and one DMA molecule in the ASU (CSD refcode WOXVOY), while NCM-DMA II crystallizes in the triclinic P-1 space group with two NCM and two DMA molecules in the ASU (2:2) (CSD refcode WOXVOY01). Although the stoichiometry of NCM-DMA II matches that of NCM-DMA I, the multiple molecules in the ASU (high Z' or $Z' > 1$) indicate it is a polymorph of the low Z' form.

NCM-DOX I crystallizes in the triclinic P-1 space group with one NCM molecule and half a DOX molecule (positioned on an inversion center) in the ASU (CSD refcode WOXWAL). NCM-DOX II, also in the triclinic P-1 space group, has two NCM molecules, one full DOX molecule, and half a DOX molecule on an inversion center in the ASU (CSD refcode WOXWEP).

In all these crystal structures, the amide group of NCM forms an intramolecular N-H···O H-bond, stabilizing its planar conformation, while the hydroxyl group engages in intermolecular O-H···O H-bonding with solvent acceptors like carbonyl, sulfonyl, and ether oxygen atoms. A zigzag molecular arrangement is observed in NCM-DMF, whereas NCM-DMSO adopts a stacked layer structure with solvent molecules stabilizing adjacent layers. NCM-DMA is polymorphic, with NCM-DMA I featuring stacked 2D layers of NCM, while NCM-DMA II has corrugated 2D layers. The non-stoichiometric NCM-DOX solvates (1:0.5 and 2:1.5) also display layered structures, but with loose packing and open channels that accommodate solvent molecules (Figure 31).

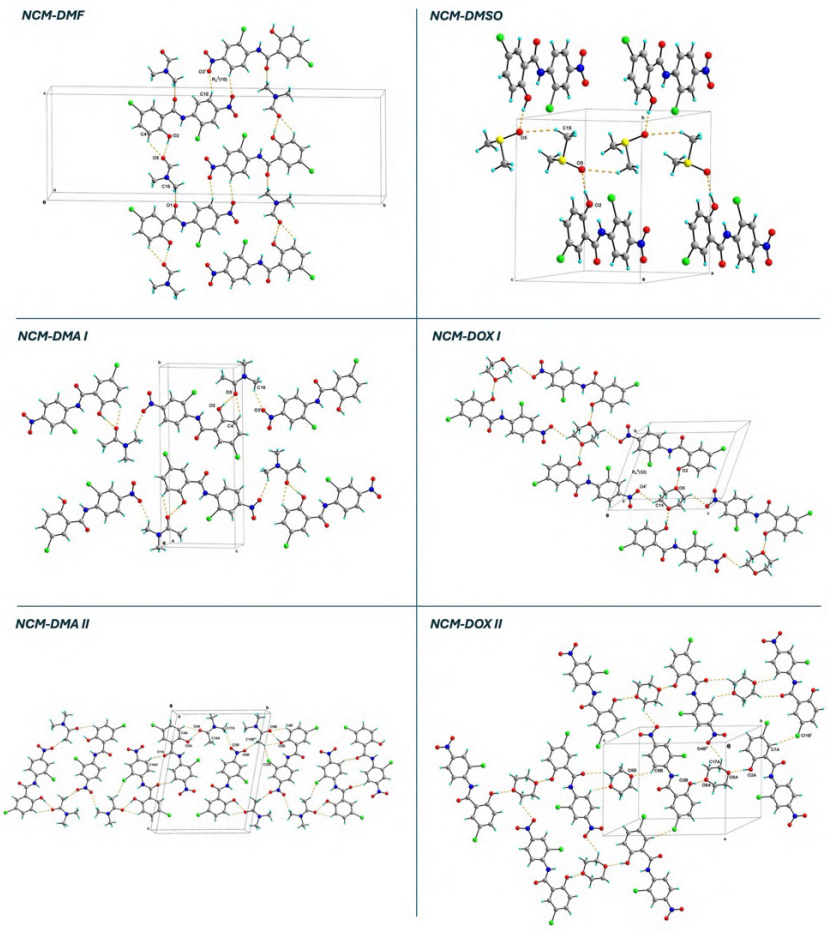

Figure 31. Crystal packing of NCM-DMF, NCM-DMSO, NCM-DMA I, NCM-DMA II, NCM-DOX I and NCM-DOX II. Adapted from reference [232].

In the DSC scans, all the NCM solvates exhibit two endothermic events: the first corresponding to desolvation and the second to melting. Once desolvated, they all melt at approximately the same temperature, around 229–230 °C, which aligns with the melting point of anhydrous polymorph I of NCM. The desolvation process occurs in a single step for most solvates, as indicated by a single desolvation endotherm: 129 °C for NCM-DMF, 168 °C for NCM-DMSO, 148 °C for NCM-DMA I, and 146 °C for NCM-DMA II. However, the NCM-DOX I solvate displays a two-step desolvation process, with peaks at onset temperatures of 83 °C and 127 °C.

All NCM solvates (discovered so far) were divided into two groups based on the interaction energy between the drug and solvent, as well as the solvent contribution to the crystal lattice. Solvents like THF, MeOH, DOX, and H_2O acted as moderate acceptors, while DMF, DMA, and DMSO were stronger acceptors, providing greater lattice stability and resulting in higher desolvation temperatures. Exceptions to this trend were NCM-DOX II and NCM-THF, which exhibited the lowest desolvation temperatures due to their loosely bound solvent molecules.

2. Aim of the research

Currently, PZQ and NCM are respectively considered the first- and second-choice drugs in the treatment of Schistosomiasis, and they are both listed in the WHO Model List of Essential Medicines for treating both adults and children.

Despite being available for over 50 years, PZQ has gained renewed interest only in the past decade, particularly due to its pronounced tendency to solid-state transformations—interacting with water, solvents, and various coformers. PZQ has shown compatibility with modern preparation techniques, such as mechanochemistry, and aligns well with advanced design strategies, including chemometric methods. To date, literature reports 7 anhydrous polymorphs of PZQ (including the commercially available Form A), 6 hydrates, 3 solvates, and 60 cocrystals, which include 2 cocrystal hydrates and 7 cocrystal solvates [43, 104, 110, 111, 124, 141-162].

NCM, originally developed for its antiparasitic properties, has recently emerged as a promising candidate for drug repurposing across a wide range of therapeutic areas. In addition to its antiparasitic use, NCM has attracted attention for its potential in antiviral (e.g., SARS-CoV-2), antibacterial, anticancer, and anti-inflammatory therapies. Given its broad therapeutic potential, the solid-state study of NCM is essential for optimizing its formulation across diverse applications. However, a significant challenge with NCM is its propensity to convert into a highly insoluble monohydrate form, which drastically reduces its solubility and bioavailability, limiting its therapeutic efficacy. To overcome these limitations, researchers have explored the intentional formation of multicomponent systems, such as salts, cocrystals, and solvates, primarily through mechanochemical methods. According to current literature, NCM is known to exist in 2 anhydrous polymorphs (including the commercially available Form A), 2 hydrates, 12 solvates, 4 salts, 4 salt cocrystals, and 12 cocrystals, as well as 1 cocrystal solvate [30, 218, 221, 222, 224, 228, 229-237].

The growing number of solid forms of PZQ and NCM discovered in recent years underscores their potential for innovative research and new pharmaceutical applications.

With this in mind, the main objective of this PhD thesis is to further explore the solid-state landscape of PZQ and NCM by developing novel drug-drug multicomponent systems using mechanochemistry. While some drug-drug multicomponent systems involving NCM have already been reported [30, 224], prior research on PZQ cocrystallization has mainly focused on using Generally Recognized as Safe (GRAS) coformers. No literature reports have yet explored drug-drug solid forms involving PZQ.

To fill this gap, this work begins with the mechanochemical cocrystallization of PZQ and NCM, both known for their strong tendency to undergo solid-state transformations, particularly through

mechanochemical activation. The rationale behind this novel drug-drug combination is twofold: to improve the physicochemical properties of both PZQ and NCM (especially preventing NCM conversion into the monohydrate), and to potentially create a synergistic pharmacological effect between the two drugs. Such a combination could lead to lower drug dosages, enhanced patient compliance, and reduced side effects, representing a significant advancement in anthelmintic therapy. Building on the promising results of a binary drug-drug system, the project expands to investigate ternary combinations involving PZQ, NCM, and other anthelmintics to develop systems with further enhanced therapeutic potential for antiparasitic applications.

The second section of the thesis introduces acetic acid (AA) into the cocrystallization of PZQ and NCM, leveraging recent findings that AA possesses antiparasitic activity, as shown against *Gyrodactylus kobayashii* trematodes [253]. The goal is to form a three-component cocrystal solvate that could take advantage of potential synergistic effects and contribute to a pharmaceutically viable ternary drug system.

In pursuit of ternary antiparasitic systems, the third part of this research focuses on combining PZQ and NCM with another anthelmintic drug, mebendazole (MBZ), aiming to produce homogeneous coamorphous systems rather than crystalline materials. This investigation explores how these amorphous combinations might further enhance therapeutic benefits and potentially unlock synergistic effects when the drugs interact in a non-crystalline state.

Finally, the project takes an in-depth look at the solid-state forms of NCM, by systematically screening new crystal forms via mechanochemical techniques with an emphasis on creating novel solvates. This phase aimes to mitigate tendency of NCM to convert into its highly insoluble monohydrate form, thus improving its solubility and stability for diverse pharmaceutical applications [191].

Altogether, these binary and ternary systems could hold the potential for significant advancements in anthelmintic properties and solid-state stability, paving the way for more robust, effective treatments for parasitic diseases.

3. Praziquantel meets Niclosamide: A dual-drug Antiparasitic Cocrystal

This section of results has already been published.

3.1 Abstract

In this first section, a successful example of combining drugs through cocrystallization is reported. Specifically, the novel solid is formed by two anthelminthic drugs, namely PZQ and NCM in a 1:3 molar ratio; the product can be obtained through a sustainable one-step mechanochemical process in the presence of micromolar amounts of methanol. A single crystal was obtained through solution crystallization of the mechanochemical product. The cocrystal structure was solved by Synchrotron XRD: the novel solid phase crystallizes in the monoclinic space group of $P2_1/c$, showing one PZQ and three NCM molecules linked through homo- and heteromolecular H-bonds in the ASU, as also attested by SSNMR and FT-IR results. A plate-like habitus is evident from SEM analysis with a melting point of 202.89 °C, which is intermediate to those of the parent compounds.

Physical and chemical stability under several conditions (i.e., drug recovery, physical stability as solid phase and in aqueous solution) were also investigated: the supramolecular interactions confer favorable properties to the cocrystal, preventing the NCM transformation into the insoluble monohydrate both in the solid-state and in aqueous solution.

Remarkably, the PZQ - NCM cocrystal exhibits higher anthelmintic activity against *in vitro* S. *mansoni* models than the corresponding PM of the APIs. Finally, due to *in vitro* promising results, *in vivo* preliminary tests on mice were also performed through the administration of minicapsules size M (Figure 32).

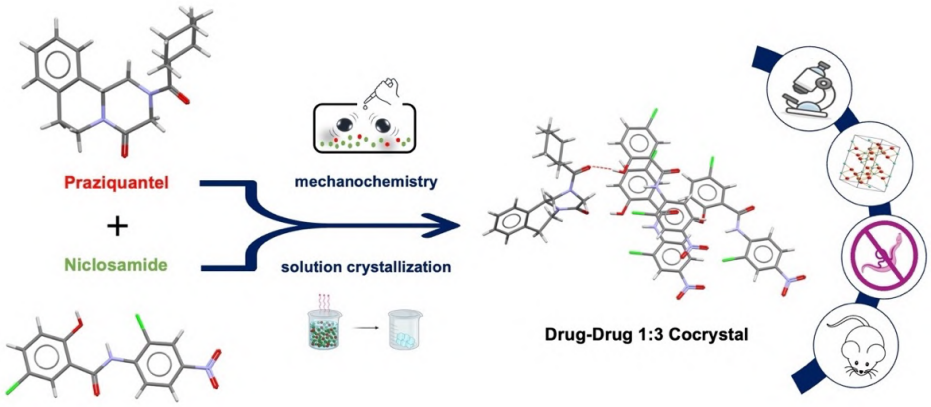

Figure 32. Graphical abstract of the experimental work applied on the new drug-drug cocrystal.

3.2 Materials and Methods

3.2.1 Materials

PZQ (11bRS)-2-(Cyclohexylcarbonyl)-1,2,3,6,7,11b-hexahydro-4-H-pyrazino[2,1-a] isoquinolin-4-one] of Ph. Eur. grade was kindly donated by Fatro S.p.a. (Bologna, Italy), while NCM (5-chloro-N-(2-chloro-4-nitrophenyl)-2-hydroxybenzamide) was purchased from Sigma-Aldrich (St. Louis, USA) with a declared purity of 98-101%. MeOH and EA were provided from Carlo Erba (Rodano-Milan, Italy) and Normapur (Fontenay sous Bois, France), respectively. HPLC-grade HXN, EtOH, AA, iPOH, triethylene glycol (TEG), AcT, ACN, 2-pyr, DMSO were purchased from Sigma-Aldrich (St. Louis, USA). All the actives and chemicals were used without further purification.

3.2.2 Methods

3.2.2.1 Preparation of the cocrystal

The mechanochemical synthesis of PZQ-NCM cocrystal was performed in Retsch MM400 vibrational mill (Retsch, Germany) equipped by two 25 mL stainless steel jars and one 10 mm Ø beads, respectively. After a set of preliminary trials where the drug-to-drug molar ratio, the amount and type of liquid and the milling time were varied, a phase pure cocrystal was obtained by milling 400 mg of PZQ-NCM mixture in a 1:3 molar ratio in the presence of 160 µL of MeOH for 120 min at 25 Hz. The same outcome can be obtained milling 200 mg of powder by using two 15 mL stainless steel jars with two 7 mm Ø grinding balls in the presence of 80 µL of MeOH for 120 min at 25 Hz. The new system was characterized by DSC, PXRD, SSNMR and FT-IR.

A single crystal of appropriate size for SXRD analysis was obtained by conventional solution crystallization, starting from preformed seeds of PZQ-NCM cocrystal.

Specifically, 20 mg of the powdered cocrystal obtained through mechanochemistry was transferred in a 20 mL lidded vial and dissolved in 16 mL of EA by stirring at room temperature. Subsequently, the lid was slightly pierced to let slow evaporation occur. Single crystals appeared after 15 days.

3.2.2.2 DSC analysis

For DSC analysis, each sample weighing 2-4 mg was introduced into an aluminum sealed and pierced 40 µL crucible and analyzed by a Mettler Toledo DSC 3 Star System (Milan, Italy) with a heating program of 30-240 °C (10 °C/min) under a nitrogen atmosphere (50 mL/min flow rate).

3.2.2.3 Laboratory PXRD analysis

Routine PXRD analysis was carried out by a Bruker D2 Phaser benchtop diffractometer (Bruker, Manheim, Germany) in the Bragg-Brentano geometry, using Cu-Kα radiation (λ = 1.5418 Å) with a 300W low-power X-ray generator (30 kV at 10 mA). All the measurements were conducted in a 2θ range of 3-60° with a step size of 0.02° and a scan speed of 0.6°/s.
Each sample was prepared by gently pressing approximately 200 mg of ground product into the cavity of a steel sample holder equipped with a cylindrical polyvinylidene fluoride (PVDF) reducer.

3.2.2.4 FT-IR analysis

Powdered samples were analyzed with a Shimadzu IRAffinity-1S FT-IR instrument (Kyoto, Japan) in a range of 400-4000 cm^{-1} with a resolution of 4 cm^{-1} and 20 scans.
Suitable discs for analysis were prepared by gently grinding in an agate mortar 200 mg of anhydrous KBr (99% infrared grade) with 1% w/w of analyte and then pressing the mixture with a hydraulic press (PerkinElmer, Norwalk, USA), applying a pressure of 10 Ton for 3 min.

3.2.2.5 SSNMR analysis

SSNMR spectra were acquired with a Bruker Avance II 400 Ultra Shield instrument, operating at 400.23, 100.63 and 40.56 MHz, respectively for ^{1}H, ^{13}C and ^{15}N nuclei.
The powdered sample was packed into cylindrical zirconia rotors with a 4 mm o.d. and a, 80 μL volume. A certain amount of sample was collected from the batch and used without further preparations to fill the rotor. ^{13}C CPMAS spectra were acquired at a spinning speed of 12 kHz, using a ramp cross-polarization pulse sequence with a 90° ^{1}H pulse of 3.60 μs, a contact time of 3 ms, an optimized recycle delays of 17.3 s and a scans number of 4744. ^{15}N CPMAS spectra were acquired at a spinning speed of 9 kHz using a ramp cross-polarization pulse sequence with a 90° ^{1}H pulse of 3.60 μs, a contact time of 4 ms, an optimized recycle delays of 17.3 s and a scans number of 8700. For every spectrum, a two-pulse phase modulation (TPPM) decoupling scheme was used, with a radiofrequence field of 69.4 kHz. The ^{13}C and ^{15}N chemical shift scales were calibrated through the signals of γ-glycine (^{13}C methylenic peak at 43.7 ppm and ^{15}N peak at 33.4 ppm with reference to NH_3).

3.2.2.6 Synchrotron X-ray Diffraction and solution of crystal structure

The data collection of the cocrystal obtained in powder form and single crystal were both performed the X-ray diffraction beamline (XRD2) of Elettra Synchrotron (Trieste, Italy) [253].

Both the samples' data were acquired using monochromatic wavelength of 0.620 Å on Pilatus ^M hybrid-pixel area detectors (DECTRIS Ltd., Baden-Daettwil, Switzerland). The powder sample was measured at 298 K in transmission mode filling a boron capillary of 0.5 mm of diameter. The single crystal was dipped in NHV oil (Jena Bioscience, Jena, Germany) and mounted on the goniometer head with kapton loops (MiTeGen, Ithaca, USA). Complete datasets were collected at 100 K and 298 K with a nitrogen stream supplied through an Oxford Cryostream 700, through the rotating crystal method. The diffraction data were indexed, integrated and scaled using XDS [254].The structures were solved by the dual space algorithm implemented in the SHELXT [255]. Fourier analysis and refinement were performed by the full-matrix least-squares methods based on F^2 implemented in SHELXL (Version 2018/3) [256]. The Coot program was used for modeling [257]. Geometry and thermal motion parameters restrain (SAME, DFIX, DANG and SIMU) have been used on disordered PZQ molecules. Hydrogen atoms were included at calculated positions with isotropic $U_{factors}= 1.2•U_{eq}$ or $U_{factors} = 1.5•U_{eq}$ for methyl and hydroxyl groups (U_{eq} being the equivalent isotropic thermal factor of the bonded non hydrogen atom). Pictures were prepared using Ortep-3 [258], CCDC Mercury [248] and Pymol software [259]. Table 4 reports crystal data collection and refinement results. Related files can be obtained free of charge from The Cambridge Crystallographic Data Centre via https://www.ccdc.cam.ac.uk/structures

Table 4. Crystallographic data and refinement details for PZQ-NCM cocrystal at 298 K and 100 K.

	1PZQ3NCM	**1PZQ3NCM**
CCDC Number	**2257493**	**2257492**
Chemical Formula	$C_{58}H_{48}Cl_6N_8O_{14}$	$C_{58}H_{48}Cl_6N_8O_{14}$
Formula weight	1293.74 g/mol	1293.74 g/mol
Temperature	298(2) K	100(2) K
Wavelength	0.620 Å	0.620 Å
Crystal system	Monoclinic	Monoclinic
Space Group	*P* $2_1/c$	*P* $2_1/c$
Unit cell dimensions	*a* = 13.465(3) Å	*a* = 13.391(3) Å
	b = 10.588(2) Å	*b* = 10.389(2) Å
	c = 40.090(8) Å	*c* = 39.841(8) Å
	α = 90°	*α* = 90°
	β = 97.62(3)°	*β* = 97.59(3)°
	γ = 90°	γ = 90°
Volume	5665(2) $Å^3$	5494.1(19) $Å^3$
Z	4	4
Density (calculated)	1.517 $g·cm^{-3}$	1.564 $g·cm^{-3}$
Absorption coefficient	0.259 mm^{-1}	0.259 mm^{-1}
F(000)	2664	2664
Theta range for data collection	1.3° to 31.1°	1.3° to 31.1°
Index ranges	$-22 \le h \le 22$,	$-22 \le h \le 22$,
	$-17 \le k \le 17$,	$-17 \le k \le 17$,
	$-61 \le l \le 61$	$-61 \le l \le 61$
Reflections collected	134317	129076
Independent reflections (data with I>2σ(I))	24562 (19327)	23754 (22858)

Resolution	0.60 Å	0.60 Å
Data multiplicity (max resltn)	4.82 (2.93)	4.77 (2.86)
I/σ(I) (max resltn)	31.42 (6.15)	50.40 (26.84)
R_{merge} (max resltn)	0.0234 (0.1569)	0.0207 (0.0374)
Data completeness (max resltn)	89.7% (73.2%)	89.5% (73.1%)
Refinement method	Full-matrix least-squares on F^2	Full-matrix least-squares on F^2
Data/restraints/parameters	24562 / 43 / 799	23754/ 43 / 799
Goodness-of-fit on F^2	1.033	1.020
Δ/σ_{max}	0.001	0.001
Final R indices [I>2σ(I)]	R_1 = 0.0499 wR_2 = 0.1457	R_1 = 0.0415 wR_2 = 0.1041
R indices (all data)	R_1 = 0.0605 wR_2 = 0.1542	R_1 = 0.0432 wR_2 = 0.1048
Largest diff. peak and hole	0.371 and -0.459 eÅ^{-3}	0.602 and -0.500 eÅ^{-3}
R.M.S. deviation from mean	0.048 eÅ^{-3}	0.070 eÅ^{-3}

3.2.2.7 SEM analysis

Images of PZQ-NCM cocrystal were collected through SEM. The powdered sample was placed on aluminum stubs covered with a carbon double-sided tape and sputter-coated with gold using a Sputter Coater K550X (Emitech, Quorum Technologies Ltd, UK), before being analyzed by a scanning electron microscope (Quanta 250 SEM, FEI, Oregon, USA) with the secondary electron detector. The working distance was set at 10 mm to obtain the appropriate magnifications, and the acceleration voltage was set at 30 kV.

3.2.2.8 Drug recovery

To check possible degradation of PZQ after milling, ^{1}H-NMR spectra were recorded on a Bruker Avance 600 spectrometer equipped with a 14 T superconducting magnet and two 5 mm probes. Analyzed samples (two different batches of the same cocrystal) were dissolved in deuterated DMSO-d_6 using tetramethyl silane (TMS) as reference. Measurements were performed at 300 K using a simple pulse-acquire sequence.

3.2.2.9 Cocrystal physical stability under several conditions

The solid-state stability of the PZQ-NCM was analyzed at room temperature (20 °C) by storing samples over a period of 12 months in a desiccator containing calcium chloride. At the end of such period, the stored samples were analyzed using PXRD, applying the operating conditions reported in section 3.2.2.3.

The stability of the cocrystal in aqueous solution was also investigated to determine if homo- and heteromolecular H-bonds are involved in improving the stability domain of PZQ-NCM cocrystal in comparison to the corresponding PM in solution. About 250 mg of compressed powder were

immersed together with a sample holder, previously used for IDR studies [43], in a vessel containing 900 mL of a solution of distilled H_2O with 0.5% p/v of sodium lauryl sulfate, kept at 37 °C and stirred at 100 rpm. After 60 min, as the tablet was still intact and did not disintegrate, sample surface areas exposed to the medium was retrieved and analyzed through PXRD to detect any solid-state conversion. For comparison purposes, the corresponding PM and pure APIs were subjected to the same procedure.

3.2.2.10 *In Vitro Activity*

In vitro and *in vivo* experiments were conducted in accordance with the local cantonal veterinary guidelines, license number 520. The *in vitro* anthelmintic activity of PZQ-NCM cocrystal was tested using NTS, which are immature Schistosoma, and adult S. *mansoni*.

NTS and adult S. *mansoni* were obtained by transforming cercariae from infected *B. glabrata* snails. Adult S. *mansoni* of both sexes were collected from the hepatic portal system and mesenteric veins of infected mice.

NTS (n=50) and S. *mansoni* (three pairs) were placed in the presence of culture media (M199 and RPMI culture medium supplemented with 1% penicillin (10,000 U/mL) and streptomycin (10 mg/mL solution) in 96 and 24 well plates, respectively and kept at 37 °C for 72h. Each plate contained concentrations of the samples, ranging from 0.1- 1 μM. An additional concentration of 0.01 μM was also carried out for adult S. *mansoni* model.

The results were determined as the effect in percentage of worm activity by microscopically observing the motility or damage to the tegument and changes to the morphology of NTS and adult S. *mansoni*. IC_{50} values were calculated using the CompuSyn software (ComboSyn Inc., Paramus, NJ., USA).

3.2.2.11 *In Vivo studies and ethics*

Animals were ordered from Charles-River (Sulzfeld, Germany). A total of 12 three-week-old NMRI mice were used for this study. Upon arrival, the animals were left for one week for acclimatization. The animals were housed at 25 °C in a controlled environment (temperature ~ 25 °C; humidity ~ 70%; 12-hour light and 12-hour dark cycle) with free access to water and rodent diet. The mice were infected subcutaneously with 100 S. *mansoni* cercaria in the neck area.

Seven weeks post-infection, mice (N=4/group) were treated with 600 mg/kg (corresponding to about 150 mg of PZQ/kg and 450 mg of NCM/kg) of the cocrystal or PM, as a powder.

For the oral administration, 6 hard gelatin capsules, size M (Torpac Europe BV, Heerlen, The Netherlands), were filled with the appropriate amount of powder and administered to each mouse. In

this context, capsules provide a suitable method for the oral dosage to laboratory mice weighing about 33 g by using a Torpac® dosing syringe. This procedure eliminates validation of suspension/solution homogeneity and vehicle excipients absorption effects. The procedure, which can be performed rapidly by trained personnel, is ideally suited for dispensing solid materials to fully conscious animals.

After treatment, the mice were monitored daily, for the next 21 days, before undergoing CO_2 euthanasia. The mice were then dissected, and their livers were excised. Adult worms were picked, sexed, and counted as described in section 3.2.2.10. The worm burden reduction (WBR) was calculated by comparing the average number of recovered worms from each treatment arm to the control arm. The detailed *in vivo* procedure is previously described by Lombardo and coauthors [260].

3.3 Results and Discussion

3.3.1 Preparation of the cocrystal

The mechanochemical preparation of PZQ-NCM cocrystal was performed varying the drug-to-drug molar ratio, the amount and type of liquid and the time of grinding, one at a time. On the contrary, frequency was always maintained at 25 Hz, and the filling volume of jars was fixed in a ratio of 400 mg of sample in 25 mL of jar capacity.

Starting from the drug-to-drug molar ratio, the cocrystal synthesis was first attempted by creating various PMs with different molar ratios of PZQ and NCM, whose DSC curves indicated best stoichiometries for generating the pure cocrystal (see Figure A1 in the Appendix A). Subsequently, mixtures of PZQ-NCM with 1:1, 1:2, 1:3 molar ratios were ground in LAG conditions and then analyzed by PXRD. PZQ-NCM 1:3 molar ratio provided the best outcome compared to the other molar ratios, since PXRD graphs confirmed the formation of a new solid phase without any unreacted residues of the two starting materials (see Figure A2 in the Appendix).

Given 120 min as the best grinding time, the type of liquid was also investigated.

The solvents were selected by considering liquids previously used for obtaining cocrystals of PZQ (e.g., EtOH, ACT, ACN, EA) [124,141,154,156,157] and NCM (e.g., iPOH, ACN) [30,222]. HXN, a commonly used liquid in LAG procedures [261] was also selected. All grinding liquids allowed for the cocrystallization of PZQ and NCM.

As a proof of concept, solvents able to form solvates with PZQ and NCM (e.g., AA, 2-pyr, MeOH, TEG, DMSO, DMF) [148,237,262], initially excluded to avoid the formation of solvated forms as byproducts, were then used as grinding liquids. Surprisingly, also this set of liquids favored the

formation of PZQ-NCM cocrystal with the exception for DMSO, 2-pyr and AA, which will be considered in the next sections. MeOH and HXN, having peculiarly different chemical properties, were the best catalytic liquids, as evident from PXRD results. MeOH resulted the preferred liquid for obtaining the new solid system with higher yield and crystallinity.

Table A1 lists all the liquid analyzed for the preparation of PZQ-NCM cocrystal, while Figure A3 in the Appendix reports the PXRD patterns of the ground solids.

The empirical parameter η (μL/mg) was maintained at LAG settings ($0 < \eta < 2$) to ensure catalytic conditions of the liquid [51]: precisely 160 μL of MeOH were added to 400 mg of sample and the grinding process was carried out for 120 min at 25 Hz.

To summarize, a PZQ-NCM cocrystal was discovered by mechanochemical activation, presenting a very peculiar 1:3 stoichiometry that is somewhat unusual in the variety of cocrystals reported in literature.

3.3.2 DSC analysis

The thermal behavior of PZQ-NCM cocrystal was investigated by DSC, and results are reported in Figure 33. Specifically, the thermogram of the cocrystal only showed an endothermic peak at 202.89 °C, with an enthalpy of 107.14 J/g, which was attributed to its melting point. The lack of additional endotherms testified the anhydrous nature of the solid and the absence of residual grinding liquid. This newly observed endothermic event clearly differs from the experimental melting points of raw PZQ and NCM, detected at 141.99 °C and 229.98 °C, respectively, both in agreement with literature data [30,43].

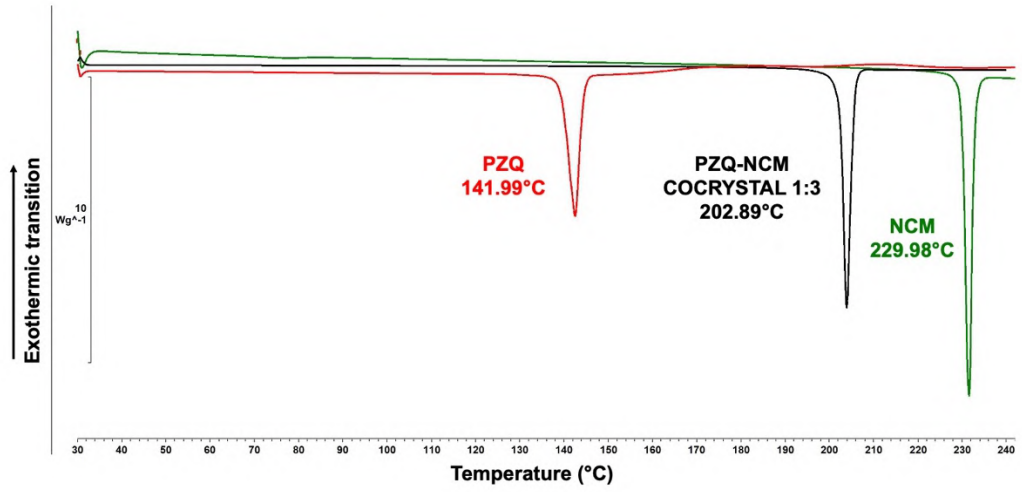

Figure 33. DSC experimental curves of mechanochemically prepared PZQ-NCM cocrystal (black), raw PZQ (red) and raw NCM (green).

3.3.3 PXRD analysis

The laboratory diffraction patterns of PZQ, NCM, PZQ-NCM cocrystal and the calculated pattern from PZQ-NCM single crystal are shown in Figure 34. The diffraction pattern of the mechanochemically prepared cocrystal shows reflections at 4.53, 7.54, 13.32, 14.62, 16.39, 18.26, 22.52, 24.61, 26.11, 26.63, clearly different from their corresponding starting materials, and the absence of signals attributable to original coformers confirms the purity of the new solid phase.

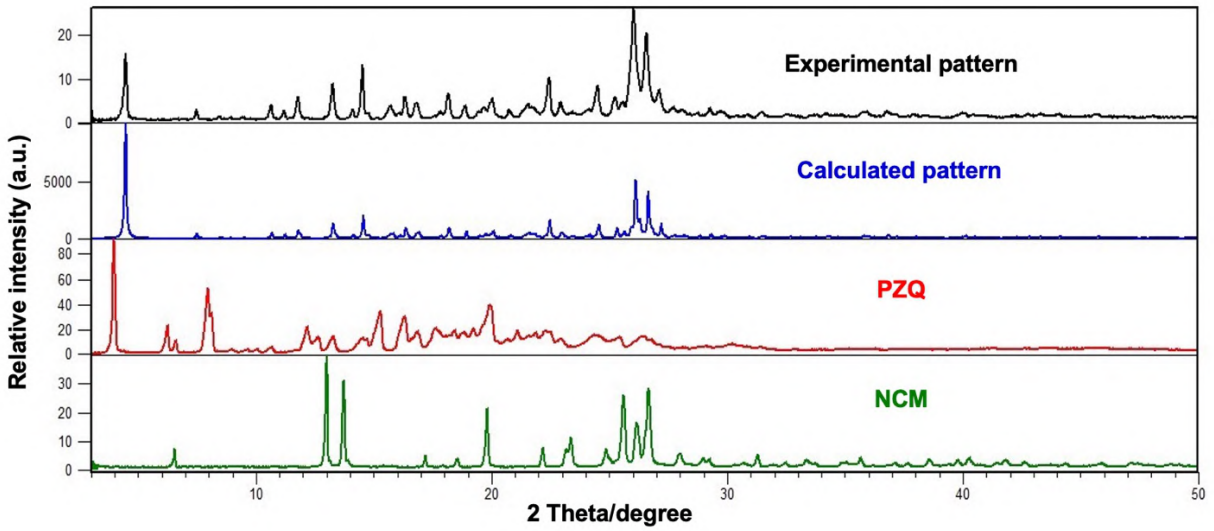

Figure 34. PXRD of PZQ (red), NCM (green), and PZQ-NCM cocrystal obtained mechanochemically (black) and the calculated pattern from the single crystal (blue).

3.3.4 FT-IR Spectroscopy

FT-IR measurements were carried out on PZQ, NCM, PZQ-NCM cocrystal and the corresponding PM. Figure 35 shows only fragments of particular interest of the four spectra (see Figure A4 in the Appendix for full spectra). PM is nothing but the sum of the signals of the pure APIs.

Differently from the PM, N-H stretching and bending peaks of NCM, originally at 3241-3101 cm^{-1} and 897 cm^{-1}, respectively, in agreement with Bushan et al. [241], are downward shifted, suggesting involvement of NCM N-H group in H-bonds with PZQ. Moving to the typical range of C=O stretching, signals of PZQ carbonyl groups are markedly shifted in the cocrystal, forming a doublet at 1694 and 1684 cm^{-1}, while in the PM the signal remains at 1650 cm^{-1} as in PZQ [43,45], confirming intermolecular interactions between the two APIs. Moreover, signals of C-OH stretching of NCM

can be seen at 1231 cm^{-1}, shifted at higher intensities in comparison to the raw NCM peak at 1219 cm^{-1} [242].

Therefore, it is worth to assume that the two C=O of PZQ and both N-H and C-OH signals of NCM are involved in molecular interactions between the two drugs in the cocrystal.

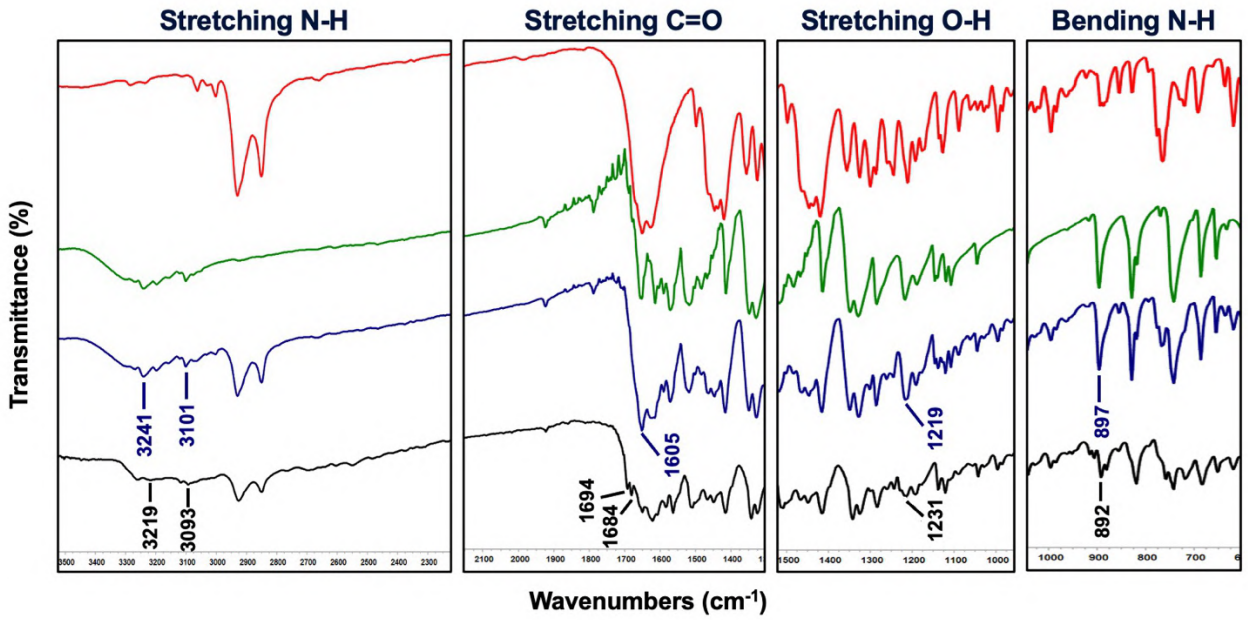

Figure 35. FT-IR spectra of PZQ (red), NCM (green), PZQ-NCM PM (blue) and PZQ-NCM cocrystal (black).

3.3.5 SSNMR analysis

The ^{13}C CPMAS spectrum recorded for the new system is shown in Figure 36a, where it is compared with those of pure PZQ and NCM. The ^{13}C SSNMR spectrum of PZQ-NCM cocrystal presented no traces of unreacted starting materials. Besides comparing the spectrum with the starting materials (PZQ and NCM), it was also investigated if there was a conversion of PZQ in the polymorphic form B during the synthesis since Form B is obtained by NG Form A for 4h. However, it is evident that the signals of the synthetized sample are not superimposable with those of the PZQ Form B (purple spectrum in Figure 36a) and the new signals are not due to a different polymorph of the starting material. So, the presence of new signals pattern leads to the conclusion that a new crystal form was obtained. The signals in the system exhibit an average full width half maximum value of ~160 Hz; this indicates a moderate degree of crystallinity. The aliphatic region of the sample shows significant changes in terms of both the shape of the signals and their chemical shifts, compared to the same region of the pure PZQ. The peaks between 25 and 35 ppm correspond to six CH_2 groups of PZQ. Moving to higher frequencies, the second group of signals (35-55 ppm) is attributable to C16, C10

and C4 carbons of PZQ. Finally, the signals at 57.6 ppm are related to C17 and it shows a shift of 1.3 ppm compared to the pure PZQ (56.3 ppm).

The aromatic region (120-140 ppm) is difficult to assign and shows overlapping signals from the aromatic carbons of PZQ and NCM. The splitted signal at about 153 ppm is attributable to NCM C13', while the signal at 175.6 is related to PZQ C1. These two signals, isolated in the spectrum, were used to evaluate the stoichiometric ratio of the cocrystal: the number of signals agrees with the presence of one molecule of PZQ and three molecules of NCM per ASU.

Figure 36b displays an analogous comparison between the ^{15}N CPMAS spectra of PZQ-NCM cocrystal and pure PZQ and NCM. The presence of a new signal pattern in the cocrystal ^{15}N spectrum confirms the formation of a new multicomponent system. The N amide and nitro group chemical shifts demonstrate the formation of supramolecular interactions between PZQ and NCM and a new crystalline packing. In addition, the split of the signals related to NCM confirms the stoichiometry PZQ-NCM 1:3.

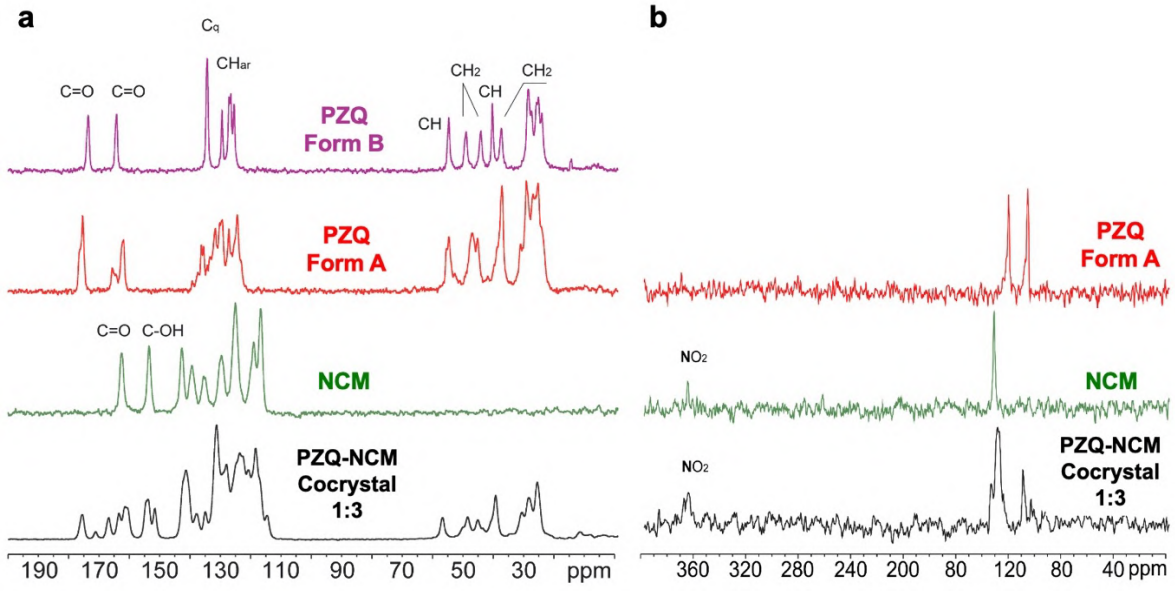

Figure 36. (a) ^{13}C (100 MHz) CPMAS spectra with relevant assignments of PZQ-NCM cocrystal (black), pure NCM (green), pure PZQ (red) and PZQ form B (purple) acquired at a spinning speed of 12 kHz at room temperature. (b) ^{15}N (40.6 MHz) CPMAS spectra with relevant assignments of PZQ-NCM cocrystal (black), pure NCM (green) and pure PZQ (red), acquired at a spinning speed of 9 kHz at room temperature.

3.3.6 Cocrystal Structure Solution

Figure 37 shows PZQ-NCM single cocrystal obtained through crystallization by slow evaporation used for the crystal structure solution.

The PXRD pattern simulated from the single crystal used for the solution of the cocrystal structure was in good agreement with the experimentally acquired PXRD pattern of the cocrystal (see Figure 34).

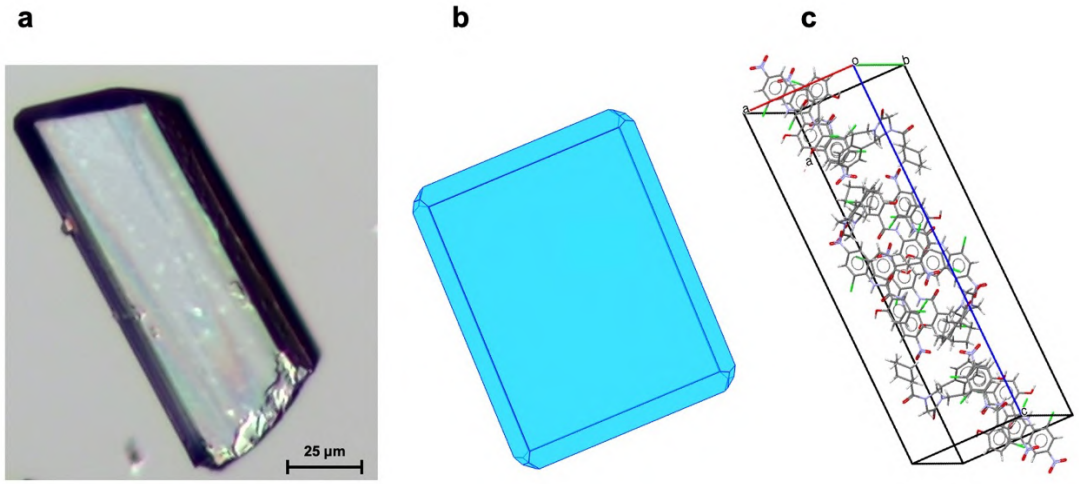

Figure 37. (a) Optical image of PZQ-NCM single crystal obtained through solution crystallization at a magnification of 10x, (b) BFDH morphology, (c) orientation of PZQ and NCM molecules into the unit cell.

The single crystal shows one PZQ and three NCM crystallographic independent molecules in the ASU at 298 K. Data collected at 100 K confirm the same crystal form found at room temperature, with small cell volume contractions (~3%). No solvent has been found inside the crystal packing, confirming the DSC results. All NCM molecules adopt a rigid, extended and planar conformation, defined by central amidic bond planarity constrain and homomolecular H-bonds (with average δNH···O = 2.65(1) Å and δNH···Cl = 2.92(2) Å). NCM moieties bear extensive electronic delocalization and are prone to stack through π•••π interactions (average δπ···π = 3.70(1) Å with 1.5 Å slippage between ring centroids). NCM molecules are coordinated to PZQ through H-bonds (Table 5): the two PZQ carbonyl groups act as acceptors bound to NCM donor hydroxyl groups. The additional NCM present in the cocrystal ASU is linked to the carbonyl of one NCM bound to PZQ, confirming FT-IR results. The relative orientation of PZQ respect to NCM molecules is almost perpendicular in the cocrystal structure (Figure 38). Interestingly, both PZQ carbonyl groups are oriented in a *syn*-conformation, as in PZQ Form A [43]. This is an unusual feature, as all the PZQ

cocrystals, reported in great number in literature, except for a few, exhibit an *anti*-conformation [141,153,154,156,157,210].

The crystal structure results in a monoclinic unit cell with a space group of $P2_1/c$.

Centrosymmetric crystal packing is consistent with the usage of racemic PZQ which is also partially disordered in the ASUs, suggesting that the inversion of PZQ chirality does not alter its steric hindrance and conserve carbonyl acceptors positions (i.e., without altering the H-bond network that keeps molecules tightly bound).

Table 5. Geometrical parameters of H-bonds found in PZQ-NCM cocrystal at 298 K and 100 K.

1PZQ3NCM at 298K				
D-H···A	d(D-H) (Å)	d(H···A) (Å)	d(D···A) (Å)	<(DHA) (°)
O4_2-H4_2×××O1_1	0.82	1.82	2.642(2)	177.0
O4_3-H4_3×××O2_1	0.82	1.80	2.617(2)	175.0
O4_4-H4_4×××O3_3	0.82	1.92	2.721(2)	164.8
N2_2-H2_2×××Cl1_2	0.86	2.44	2.923(1)	116.3
N2_3-H2_3×××Cl1_3	0.86	2.40	2.891(1)	116.4
N2_4-H2_4×××Cl1_4	0.86	2.46	2.941(1)	115.7
N2_2-H2_2×××O4_2	0.86	1.93	2.653(2)	141.0
N2_3-H2_3×××O4_3	0.86	1.92	2.636(2)	140.2
N2_4-H2_4×××O4_4	0.86	1.93	2.653(2)	141.4
1PZQ3NCM at 100K				
D-H···A	d(D-H) (Å)	d(H···A) (Å)	d(D···A) (Å)	<(DHA) (°)
O4_2-H4_2×××O1_1	0.84	1.80	2.635(1)	177.9
O4_3-H4_3×××O2_1	0.84	1.77	2.607(1)	174.3
O4_4-H4_4×××O3_3	0.84	1.88	2.695(1)	164.2
N2_2-H2_2×××Cl1_2	0.88	2.43	2.927(1)	115.8
N2_3-H2_3×××Cl1_3	0.88	2.39	2.887(1)	116.4
N2_4-H2_4×××Cl1_4	0.88	2.45	2.940(1)	115.3
N2_3-H2_3×××O4_3	0.88	1.90	2.637(1)	140.2
N2_2-H2_2×××O4_2	0.88	1.91	2.653(1)	140.9
N2_4-H2_4×××O4_4	0.88	1.91	2.651(2)	141.3

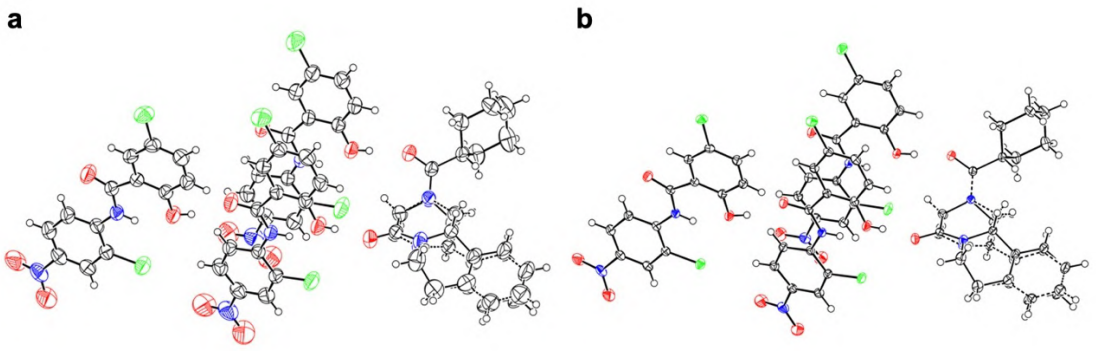

Figure 38. Ellipsoids representation of ASU contents (50% probability) for PZQ-NCM cocrystal at 298K (a) and 100K (b).

3.3.7 SEM analysis

Figure 39 shows SEM images of PZQ, NCM and PZQ-NCM powdered cocrystal. The newly cocrystal form consisted of agglomerates of small plates (more evident at higher magnifications), showing a habitus clearly different from the reported needle-shaped particles of PZQ [45] and the peculiar rectangles with protrusions of NCM [218]. The particle size of the plates varies in the range 150-1500 nm, as roughly determined by Fiji/Imagej software [263].

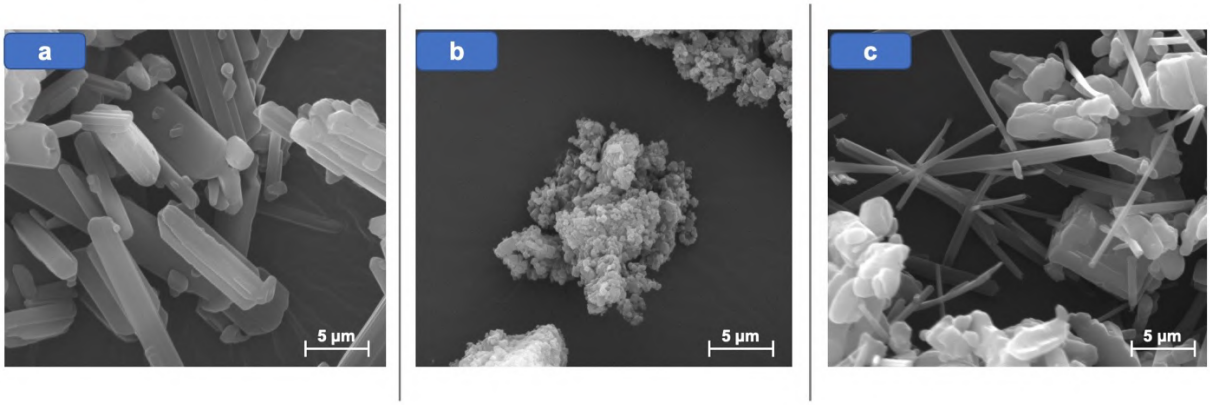

Figure 39. SEM images of (a) PZQ, (b) PZQ-NCM cocrystal and (c) NCM at a magnification of 5000x.

3.3.8 Drug recovery

From literature is well-known the degradation tendency of PZQ under milling conditions [42,45,264]. While PZQ did not degrade upon milling when the drug was milled alone [43,142], in binary ground mixes a diminished drug recovery was noticed with the insurgence of peculiar degradation products as a function of the excipient used [42,45,264]. Therefore, spectrometric evaluations have been carried out to understand whether PZQ undergoes chemical degradation when ground in the presence of NCM upon LAG conditions.

Recorded ^{1}H-NMR spectra in DMSO-d_6 showed only the presence of the starting materials PZQ and/or NCM, attesting the lack of chemical changes both in PZQ and NCM after mechanochemical treatment under all experimental conditions. The absence of any new signal in the two different batches analyzed indicates that there are no new structures present in the samples. Based on all obtained information and comparison of the crucial parts of the ^{1}H-NMR spectra of PZQ (a), NCM (b), cocrystal batch n°1 (c) and cocrystal batch n°2 (d) (see Figure A5 in the Appendix), a high chemical stability of PZQ and NCM under the applied grinding conditions is confirmed.

3.3.9 Physical stability under several conditions

PZQ-NCM cocrystal was periodically analyzed by PXRD for 12 months to check for possible modifications. Indeed, there are examples in literature where the presence of defects on the surface of crystalline solids [265] or different humidity conditions [266] are reported as possible precursors/factors for cocrystal dissociation. Further, since anhydrous NCM is known to transform to greenish monohydrate H_A within one month of storage at ambient conditions [30,218,221–224], the aim of checking PZQ-NCM cocrystal stability was also to recognize the insurgence of the hydrate. The hydrate formation is highly undesired as it exhibits a solubility even lower than anhydrous NCM. The physical stability results, reported in Figure A6 in the Appendix, attested that the new multicomponent system remained unchanged over a period of 12 months, with no signs of cocrystal dissociation of hydrate formation.

Further, in the context of PZQ-NCM cocrystal physical stability in aqueous solution, a flat tablet of PZQ-NCM cocrystal was immersed in an aqueous solution for 60 min. After that time, the solid sample was retrieved and analyzed through PXRD and DSC to visualize any solid-state conversion. The same procedure was adopted for corresponding PZQ-NCM PM, pure PZQ and NCM.

PXRD and DSC results are displayed in Figure 40. No phase conversion was visualized for raw PZQ after 60 min of exposure to medium. Conversely, pure NCM and PZQ-NCM PM showed a rapid transformation into the well-known monohydrate H_A [30,218,221–224]. Instead, PZQ-NCM

cocrystal maintained its crystalline integrity in aqueous solution, preventing thus the formation of poorly soluble NCM monohydrate H_A. In accordance with previous studies [30,267], this cocrystal is an example of a solid with a very stable profile and distinctive properties in aqueous solutions, ameliorated with respect to pure coformers and their free combination.

This means that PZQ-NCM cocrystal structure provides several peculiar features versus the simple PZQ-NCM PM and the coformers alone in relation to its physical stability in aqueous solution. The differential behavior of the cocrystal over the PM is attributable to the PZQ-NCM supramolecular interactions imparting strength to the cocrystal lattice (NCM molecules are linked together and with PZQ molecules through H-bonds in the 3D supramolecular network, as previously mentioned). In literature one can find other examples of cocrystal with similar aqueous stability [30,267]. In relation to the individual components, and in particular to NCM, thanks to the supramolecular interactions, the cocrystal structure confers a resistance to the otherwise predominant transition into the undesired monohydrate NCM H_A having even lower solubility than NCM (0.45–0.55 mg/L) and characterized by a "*cement-like*" behavior in aqueous suspension [30].

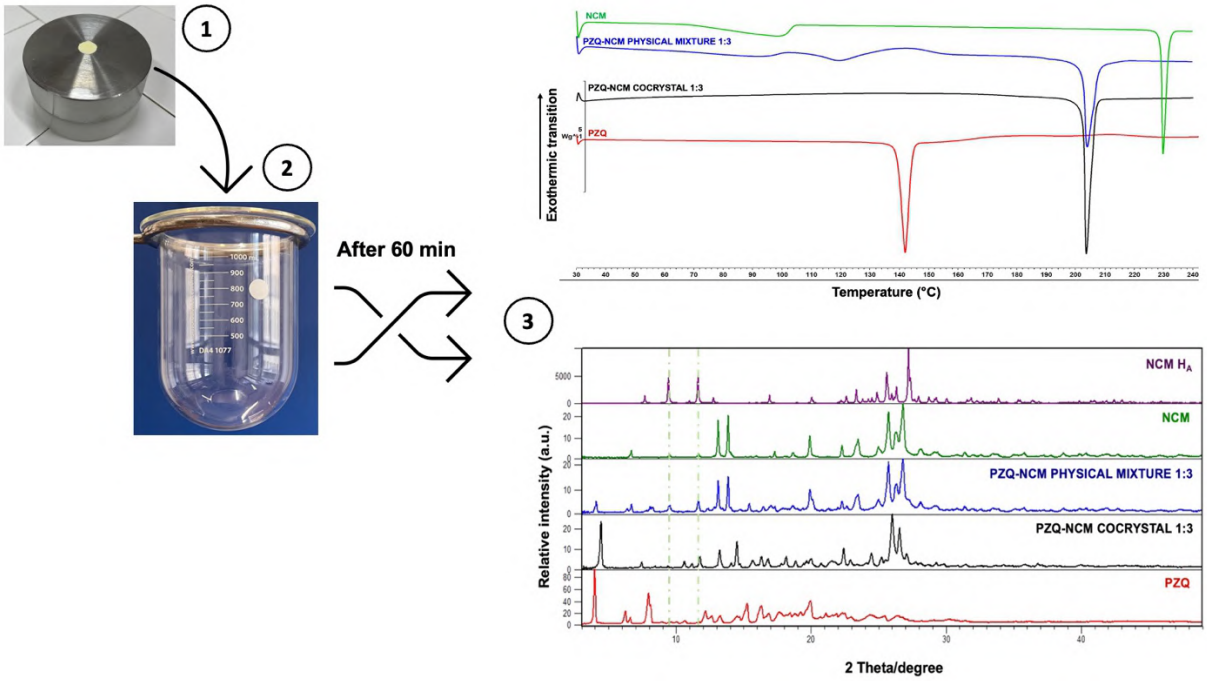

Figure 40. Schematic representation of the investigation of cocrystal physical stability in aqueous solution: (1) compressed powder in the IDR sample holder, (2) vessel containing the aqueous solution, (3) DSC and PXRD results of solid samples retrieved after 60 min of exposure to the medium.

3.3.10 *In Vitro* Activity

In vitro NTS and S. *mansoni* models were placed in well plates with variable concentrations of two cocrystal batches and the corresponding PZQ-NCM PM. Effects were rated microscopically by observing the motility or damage to the tegument and changes to the morphology of NTS and S. *mansoni* adults.

Results in Table 6 attests that, in the case of S. *mansoni* adults, the new 1:3 cocrystal exhibits higher efficacy than that observed for PZQ-NCM PM at 0.1 μM. As for the NTS, results show that mechanochemical treatment and cocrystallization have no negative effects on *in vitro* activity. In fact, PZQ-NCM cocrystal has no significative difference in response compared to the PM of the two APIs.

Table 6. *In vitro* anthelmintic activity after 72h on NTS and S. *mansoni* adults *in vitro* models of cocrystals and corresponding PM having the same composition.

Samples	NTS	NTS	NTS	S. *mansoni* adult	S. *mansoni* adult	S. *mansoni* adult	S. *mansoni* adult
	Effect in % (dead, 72h) +SD Testconc. 1μM	**Effect in % (dead, 72h) +SD Testconc. 0.1μM**	**IC50 (μM) (72h) Dm**	**Effect in % (dead, 72h) +SD Testconc. 1μM one round**	**Effect in % (dead, 72h) +SD Testconc. 0.1μM one round**	**Effect in % (dead, 72h) +SD Testconc. 0.01μM one round**	**IC50 (μM) (72h) Dm**
PM 1:3	100 (0)	28.85 (1.9)	0.12282	100 (0)	53.9 (2)		0.0961
PZQ-NCM Cocrystal 1:3	92.31 (3.8)	25 (1.9)	0.20256	100 (0)	71.95 (4)	39.55 (6.3)	0.02123

3.3.11 *In vivo* preliminary tests

In vivo pilot tests were performed on PZQ-NCM cocrystal and compared to pure PZQ and the corresponding PM (Table 7). Interestingly, to mimic the administration praxis of the two APIs (marketed as solid oral tablets), the samples were administered as a powder in minicapsules size M (specific for mice), instead of the conventional aqueous suspensions, commonly used during *in vivo* administration in animal subjects [183].

When compared to methods used in previous studies, such procedure prevents regurgitation and revulsion of the animal to the bitter taste of the drug and allows the administration of the correct dose.

Additionally, this procedure avoids the use of excipients or solvents that may interfere with the API absorption or with animal physiology, allowing a proper comparison of different solid forms.
Even though these are preliminary results on a limited number of subjects coming from the difficulties of administering 6 capsules to each mouse, and though the high variability of the results, it can be attested that there was no significant difference between the number of worms recovered from infected mice treated with cocrystal or PM.
Considering the treatment with pure PZQ capsules, a comparison with the cocrystal is ineffective due to un underdosage compared to PZQ monotherapy. Despite this limitation, it is worth mentioning that the administration of capsules filled with the pure component is somewhat a positive control group, since it confirms that the treatment with minicapsules worked. Therefore, higher doses of cocrystal administered in minicapsules result promising for future *in vivo* studies.

Table 7. Effect of cocrystal, PM and raw PZQ (administered as oral minicapsule size M) on the WBR in mice harboring a chronic S. *mansoni* infection.

Application date: 09. November 2022 / Dissection date 30.11-01.12.2022		
Sample	**Average of WBR %**	**Number of mice**
PZQ around 300mg/kg with capsules	91.11	4
PZQ-NCM PM 1:3 around 600mg/kg with capsules	15.56	2*
PZQ-NCM Cocrystal 1:3 around 600mg/kg with capsules	4.44	4

*Treated 4 mice, but 2 died during treatment

3.4 Conclusions

A novel drug-drug antiparasitic cocrystal consisting of PZQ and NCM in a 1:3 molar ratio was synthetized for the first time. The novel PZQ-NCM cocrystal, showing this very peculiar stoichiometry, relatively uncommon in cocrystallization field, can be obtained through a sustainable one-step mechanochemical process in the presence of micromolar amounts of common solvents in 120 min. Even though the mechanochemical cocrystallization was found not to be particularly influenced by the type of solvent for LAG experiments, MeOH was finally preferred as adjuvant liquid for its higher efficiency. The phase was obtained as pure solid, without traces of unreacted starting coformers and absence of residual solvent. The same 1:3 cocrystal can be obtained in 2 weeks by conventional solution crystallization, starting from preformed seeds of PZQ-NCM cocrystal.

The novel solid phase crystallized in the monoclinic space group of $P2_1/c$, showing one PZQ and three NCM molecules linked through homo- and heteromolecular H-bonds in the ASU, confirming SSNMR and FT-IR results.

The new 1:3 cocrystal exhibited a plate-like habitus, as evident from SEM analysis, and a melting point of 202.89 °C, which was intermediate to those of PZQ and NCM.

No typical PZQ tendency of decay was seen in the experimental grinding conditions and the cocrystal showed a very stable profile under several conditions. In the context of physical stability in aqueous solution, the new multicomponent system provided a higher efficiency in avoiding solid-state transformation into NCM monohydrate, in comparison to PZQ-NCM PM. Cocrystal solid-state remained unchanged over a period of 12 months at ambient temperature, with no signs of dissociation in the parent compounds or transition in NCM monohydrate, typically appearing within one month of storage at ambient conditions.

More importantly, *in vitro* anthelmintic activity was carried out: PZQ-NCM cocrystal exhibited higher anthelmintic activity (%-effect of activity reduction) against *in vitro* S. *mansoni* models than that observed for PZQ-NCM 1:3 PM and, in the case of NTS, the new system showed no significative difference in response compared to APIs PM.

Finally, considering *in vitro* promising results, *in vivo* preliminary tests were also performed on the cocrystal, pure PZQ and corresponding PM: despite the limited number of mice treated, there was no significant difference between the number of worms recovered from infected mice treated with cocrystal or PM. In the case of treatment with pure PZQ, a comparison with the cocrystal was ineffective due to un underdosage compared to PZQ monotherapy. Nevertheless, the administration of pure PZQ to mice resulted a positive control group, since it confirmed that the treatment with minicapsules worked, showing that higher doses of cocrystal are encouraging for future *in vivo* studies.

4. Assembling three anthelmintic molecules in a single solid: a Praziquantel/Niclosamide/Acetic Acid Cocrystal Solvate

4.1 Abstract

A pharmaceutically acceptable cocrystal solvate composed of three anthelmintic molecules—PZQ, NCM, and AA—is here introduced. This cocrystal was successfully synthesized using mechanochemical methods. The study demonstrates an innovative approach for creating ternary cocrystals, which involves not only the use of individual coformers but also the application of preformed synthons to guide the assembly of the cocrystal structure. By combining different building blocks (e.g., from individual coformers; from preformed PZQ-NCM 1:3 anhydrous cocrystal, raw PZQ and AA; from preformed PZQ-AA monosolvate, raw NCM and AA; from preformed PZQ-NCM 1:1 coamorphous and AA; from individual coformers in the presence of preformed seeds of the cocrystal solvate), it was possible to obtain the same cocrystal solvate, though with varying yields, either as a pure phase or with residual other phases.

The cocrystal solvate can be achieved as a pure phase by grinding preformed PZQ-AA monosolvate with NCM in an equimolar ratio and with an excess of AA beyond the equimolar ratio (AA acts both as a solvent for the solvate and as a grinding liquid). For comparative purposes, slurry experiments were also conducted, which did not result in the formation of the cocrystal solvate at any point. The cocrystal structure was solved from the Synchrotron PXRD pattern and optimized by DFT calculations. The novel solid phase crystallizes in the triclinic space group of *P*-1, showing one PZQ, one NCM and one AA molecule linked through H-bonds in the ASU, as also attested by ^{1}H-NMR and FT-IR results. The solid phase shows agglomerates of small plates through SEM analysis and exhibits at the DSC a desolvation event at roughly 111 °C (corresponding to 10.91±0.57% weight loss in TGA). Moreover, the new system exhibits higher anthelmintic activity against *in vitro* S. *mansoni* adults and NTS, in comparison to pure PZQ and NCM. Due to *in vitro* promising results, *in vivo* preliminary tests on mice were also performed through the administration of an oily suspension of the novel phase. Finally, the new crystal was stable over a period of 24 months at room temperature in the solid-state (Figure 41).

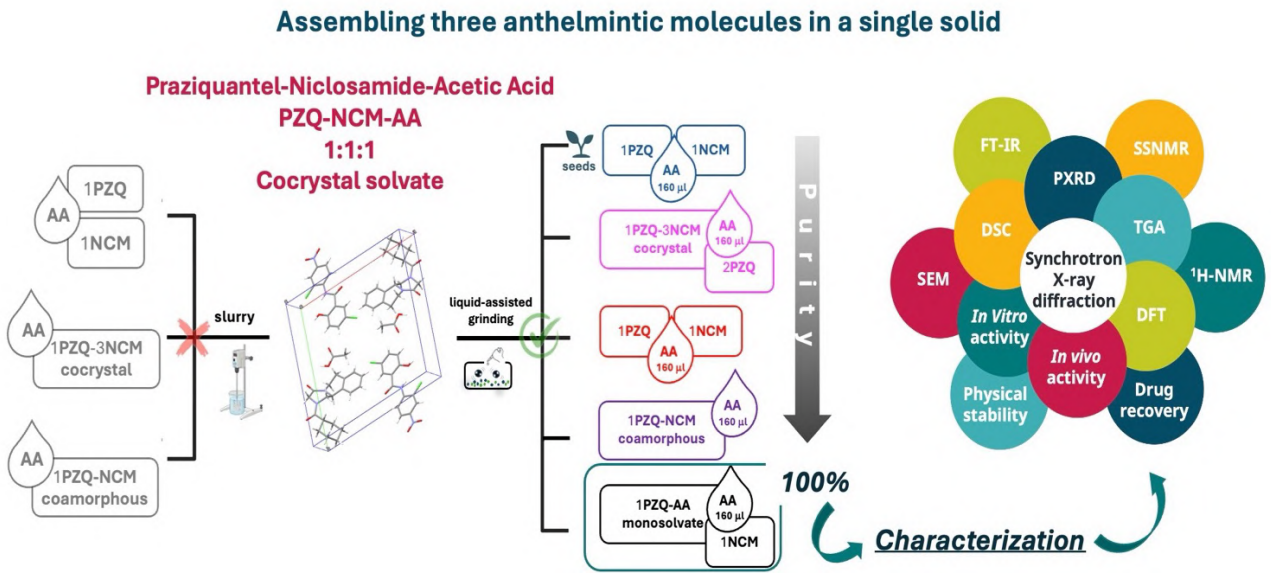

Figure 41. Graphical representation of the experimental work of this section.

4.2 Materials and Methods

4.2.1 Materials

PZQ, (RS)-2-(Cyclohexylcarbonyl)-1,2,3,6,7,11b-hexahydro-4-H-pyrazino[2,1-a]-isoquinolin-4-one], of Ph. Eur. grade was kindly donated by Fatro S.p.a. (Bologna, Italy), while NCM (5-chloro-N-(2-chloro-4-nitrophenyl)-2-hydroxybenzamide) was purchased from Sigma-Aldrich (St. Louis, USA) with a declared purity of 98-100%. AA was provided from Carlo Erba (Rodano-Milan, Italy). All the actives and chemicals were used without further purification.

4.2.2 Methods

4.2.2.1 Synthetic strategies for preparing PZQ-NCM-AA cocrystal solvate

4.2.2.1.1 Mechanochemical routes

The mechanochemical synthesis of the ternary cocrystal solvate was performed in Retsch MM400 vibrational mill (Retsch, Germany) equipped by two 25 mL stainless steel jars and one 10 mm Ø bead, respectively. Both screw cap and plug-in jars were used, with no significant differences observed in the yield of the experiments.

Five different synthetic strategies were explored to obtain the cocrystal solvate. The milling frequency for each pathway was maintained at 25 Hz, and the void volume in the jar was also kept constant (i.e., a total of 400 mg of powder per 25 mL jar).
Each synthetic strategy was tested with three different milling times: 30, 60 and 120 min.
After a set of preliminary trials, the volume of AA added to each experiment was 160 μL (η [51] = 0.4).

4.2.2.1.1.1 From individual coformers

An equimolar ratio of commercial PZQ Form A and NCM Form A (i.e., 0.625 mmol which equals to 195.4 mg and 204.6 mg, respectively) was ground with 160 μL of AA.

4.2.2.1.1.2 From preformed PZQ-NCM 1:3 anhydrous cocrystal, raw PZQ and AA

Preformed PZQ-NCM 1:3 anhydrous cocrystal (indexed as RIPFOP01 in the CSD) in the amount of 269.74 mg, obtained according to the procedure reported in our previous work [206], was ground in the presence of 130.26 mg of raw PZQ Form A (to get PZQ-NCM equimolar ratio) and 160 μL of AA.

4.2.2.1.1.3 From preformed PZQ-AA monosolvate, raw NCM and AA

Preformed PZQ-AA monosolvate (reported as DAJCEA in the CSD) (i.e., 212.97 mg), mechanochemically obtained according to Zanolla and coauthors' procedure [148], was ground with an equimolar ratio of solid NCM (i.e., 187.03 mg) in the presence of AA.

4.2.2.1.1.4 From preformed PZQ-NCM 1:1 coamorphous and AA

400 mg of PZQ-NCM 1:1 coamorphous, mechanochemically obtained through 4h of NG, was ground in the presence of 160 μL of the liquid at 25 Hz.

4.2.2.1.1.5 From individual coformers in the presence of preformed seeds of cocrystal solvate

An equimolar ratio of commercial PZQ Form A and NCM Form A (i.e., 175.86 mg and 184.14, respectively) was ground with 160 μL of AA in the presence of preformed seeds of the cocrystal solvate (i.e. 40 mg, corresponding to 10% wt ratio).

4.2.2.1.2 Slurry bridging routes

For comparative purposes, slurry experiments were conducted adopting the procedure reported in a previous experimental study [268]. Specifically, 300 mg of solid and 5 mL of AA were placed into 10 mL glass vials equipped with a screw cap and sealed with parafilm. The suspensions (prepared in duplicate) were continuously stirred at room temperature (20 °C) for 7 days. Subsequently, the excess solid phases were recovered, filtered under vacuum pump through paper filters and characterized.
For obvious reasons, not all the above-mentioned mechanochemical routes are viable via slurry approach; three (out of the five) starting points were hence tested for comparison:

1. An equimolar ratio of commercial PZQ Form A and NCM Form A (i.e., 146.55 mg and 153.45 mg, respectively) in 5 mL of AA;
2. Preformed PZQ-NCM 1:1 coamorphous (300 mg) in 5 mL of AA;
3. Preformed PZQ-NCM 1:3 anhydrous cocrystal (300 mg) in 5 mL of AA.

4.2.2.2 Laboratory PXRD analysis

Laboratory PXRD analysis was carried out by a Bruker D2 Phaser benchtop diffractometer (Bruker, Manheim, Germany) using the Bragg-Brentano geometry, using Cu-Kα radiation (λ = 1.5418 Å) with a 300 W low-power X-ray generator (30 kV at 10 mA). All the measurements were conducted in a 2θ range of 3-40° with a step size of 0.02° and a scan speed of 0.6°/s.
Each sample was prepared by gently pressing approximately 200 mg of ground product into the cavity of a steel sample holder equipped with a cylindrical PVDF reducer.

4.2.2.3 Synchrotron X-ray Diffraction and solution of the crystal structure

The data collection of the cocrystal obtained in powder form was performed at the XRD2 of Elettra Synchrotron (Trieste, Italy) [253]. The powder sample was measured at 298 K in transmission mode filling a boron capillary of 0.5 mm of diameter. The powder data was acquired using monochromatic wavelength of 1.00 Å on Pilatus 6M hybrid-pixel area detectors (DECTRIS Ltd., Baden-Daettwil, Switzerland). The two-dimensional powder pattern has been integrated using Fit2D program [269,270], after preliminary calibration of hardware setup, using a capillary filled with LaB_6 standard reference powder (NIST 660a).
The structure of the cocrystal form was solved through a simulated annealing (SA) protocol using EXPO2014 [271]. The starting structural model containing one PZQ molecule (TELCAQ model) [272], one molecule of NCM and one of AA were built with Material studio software v 7.0. (MS)

[273] and then geometrically optimized by the Dmol3 code implemented in MS. During the SA the cyclohexyl group of the PZQ molecule and methyl group of AA were allowed to freely rotate.

CCDC number 2391439 contains the supplementary crystallographic data for the cocrystal solvate. These data can be obtained free of charge from The Cambridge Crystallographic Data Centre via https://www.ccdc.cam.ac.uk/structures.

4.2.2.4 DSC analysis

For DSC analysis, each sample weighing 2-4 mg was introduced into an aluminum sealed and pierced 40 μL crucible and analyzed by a Mettler Toledo DSC 3 Star System (Milan, Italy) with a heating program of 30-250 °C (10 °C/min) under a nitrogen atmosphere (50 mL/min flow rate).

4.2.2.5 TGA analysis

TGA analysis was performed using a Mettler Toledo TGA TDA851 (Milan, Italy). Briefly, 3-6 mg of the powdered sample were inserted into aluminum 40 μL crucibles and analyzed with a heating program of 30-250 °C (10 °C/min) under a nitrogen atmosphere (50 mL/min flow rate).

4.2.2.6 FT-IR analysis

Powdered samples were analyzed with a Shimadzu IRAffinity-1S FT-IR instrument (Kyoto, Japan) in a range of 400-4000 cm^{-1} with a resolution of 4 cm^{-1} and 20 scans.
Suitable discs for analysis were prepared by gently grinding in an agate mortar 200 mg of anhydrous KBr (99% infrared grade) with 1% w/w of analyte and then pressing the mixture with a hydraulic press (PerkinElmer, Norwalk, USA), applying a pressure of 10 Ton for 3 min.

4.2.2.7 SSNMR analysis

The PZQ-NCM-AA cocrystal solvate and PZQ-AA monosolvate ^{13}C CPMAS spectra were acquired with a Jeol ECZR 600 instrument, operating at 600.17 and 150.91 MHz, respectively for ^{1}H and ^{13}C nuclei. The powder samples were packed into cylindrical zirconia rotors with a 3.2 mm o.d. and a 60 μL volume. A certain amount of sample was used without further preparation to fill the rotor. The ^{13}C CPMAS spectra were collected at room temperature at a spinning speed of 20 kHz, using a ramp cross-polarization pulse sequence with a 90° ^{1}H pulse of 2.2 μs, a contact time of 3.5 ms, an acquisition time of 29.5 ms, an optimized recycle delay of 4.2 s for PZQ-NCM-AA and 63.5 s for

PZQ-AA and a number of scans between 938 and 1579. A TPPM decoupling scheme was used, with a radiofrequency field of 108.5 kHz. The ^{13}C chemical shift scale was calibrated through the methylenic signal of external standard adamantane (at 38.48 ppm with respect to TMS).

The PZQ, NCM, PZQ-NCM 1:3 anhydrous cocrystal and PZQ-NCM 1:1 coamorphous ^{13}C CPMAS spectra were acquired with a Bruker Avance II 400 Ultra Shield instrument, operating at 400.23 and 100.63, respectively for ^{1}H and ^{13}C nuclei. Powder sample was packed into cylindrical zirconia rotors with a 4 mm o.d. and a 80 μL volume. A certain amount of sample was collected from the batch and used without further preparations to fill the rotor. ^{13}C CPMAS spectra were acquired at a spinning speed of 12 kHz, using a ramp cross-polarization pulse sequence with a 90° ^{1}H pulse of 3.60 μs, a contact time of 3 ms, optimized recycle delays between 4.4 and 40.0 s and scans numbers between 95 and 4744. For every spectrum, a twoTPPM decoupling scheme was used, with a radiofrequence field of 69.4 kHz. The ^{13}C chemical shift scale was calibrated through the methylenic signal of external standard glycine (at 43.7 ppm).

4.2.2.8 ^{1}H-NMR analysis

^{1}H-NMR (with $CDCl_3$) spectra were acquired on a Jeol ECZR 600 instrument operating at 600.2 MHz. In the ^{1}H spectrum, to obtain quantitative information, it was necessary to employ a relaxation delay of 60 s. The number of scans acquired was 8.

4.2.2.9 DFT calculations

Solid-state DFT calculations were performed with Quantum Espresso (QE, v. 6.4.1) [274], adopting the following methodology: we used the projector augmented wave (PAW) with the non-local vdW-DF2 approach [275] and the B86r functional [276]], employing the SSSP set of pseudopotentials [277,278]. An energy cut-off of 60 Ry was used for geometry optimizations. NMR calculations were performed using the Gauge Including Projected Augmented Wave (GIPAW) [279] and the PBE pseudopotentials from PS Library 1.0.0 [280] with an energy cut-off of 80 Ry, following the methodology previously described [281–283]. The theoretical absolute isotropic magnetic shielding (σ_{iso}) values were converted into isotropic chemical shifts (δ_{iso}) relative to the absolute magnetic shielding of the reference substance DABCO computed at the same level, applying the following equation 2:

$$\delta_{iso}(calc) = \sigma_{iso}(ref) - \sigma_{iso}(calc) + \delta_{iso}(ref) \quad \textbf{(2)}$$

δ_{iso} (ref) ^{13}C value for DABCO has been experimentally evaluated as 47.74 ppm, while the absolute isotropic constant shielding σ_{iso} (ref) is 120.59 ppm, calculated from the reported neutron diffraction crystal structure [284].

4.2.2.10 SEM analysis

Images of the cocrystal solvate were collected through SEM. The powdered sample was placed on an aluminum stub covered with a carbon double-sided tape and sputter-coated with gold using a Sputter Coater K550X (Emitech, Quorum Technologies Ltd, UK), before being analyzed by a scanning electron microscope (Quanta 250 SEM, FEI, Oregon, USA) with the secondary electron detector. The working distance was set at 10 mm to obtain the appropriate magnifications, and the acceleration voltage was set at 5 kV.

4.2.2.11 Drug recovery

To check possible degradation of PZQ-NCM-AA cocrystal solvate after preparation, ^{1}H-NMR spectra were recorded on a Bruker Avance 600 spectrometer equipped with a 14 T superconducting magnet and two 5 mm probes. Analyzed samples were dissolved in $CDCl_3$ using TMS as reference. Measurements were performed at 300 K using a simple pulse-acquire sequence.

4.2.2.12 Cocrystal physical stability under several conditions

The solid-state stability of the cocrystal solvate was analyzed at room temperature (20 °C) by storing the sample for 24 months in a desiccator containing calcium chloride. Periodically (every 3 months) and at the end of this period, the stored sample was analyzed by means of PXRD, applying the operating conditions reported in section 4.2.2.2.

Solid-state changes possibly caused by mechanical stresses were tested by compressing PZQ-NCM-AA at 10 Ton for 3 min, and by grinding the sample for 200 min at 25 Hz.

Further, the stability of the new system was also evaluated under high RH conditions. Specifically, the sample was stored for 6 months in a sealed enclosure containing a saturated aqueous NaCl solution, known to maintain a RH of 75% at room temperature [285].

4.2.2.13 In Vitro and In Vivo Activity

In vitro experiments were conducted in accordance with the local Swiss cantonal veterinary guidelines, license number 520. The *in vitro* anthelmintic activity of the cocrystal solvate was tested using NTS and adult S. *mansoni*.

NTS and adult *S. mansoni* were obtained by transforming cercariae from infected *B. glabrata* snails. Adult S. *mansoni* of both sexes were collected from the hepatic portal system and mesenteric veins of infected mice.

Around 50 NTS were placed in each well of a 96-well plate with culture medium and the test compound for a final well volume of 200-250 µL. Culture medium was composed of M199 medium (Gibco, Waltham MA, USA) supplemented with 5% fetal calf serum (iFCS, 100 U/mL), 1% penicillin/streptomycin mixture (Invitrogen, 100 U/mL) and 1% Mäser Mix. Each compound was tested in triplicate and repeated. NTS incubated with no more than 1% DMSO served as control. NTS were kept in the incubator at 37 °C and 5% CO_2 for up to 72h.

3 pairs of adult worms were placed in each well of a 24-well plate with 2-2.5 mL culture medium and the test compound. Culture medium was composed of RPMI 1640 (Invitrogen, Carlsbad, CA) supplemented with 5% horse serum (Gibco, Waltham MA, USA) and 1% penicillin/streptomycin mixture (Invitrogen, 100 U/mL). Each compound was initially tested in duplicate and repeated. Schistosomes incubation with no more than 1% DMSO served as control. Worms were kept in an incubator at 37 °C and 5% CO_2 for up to 72h.

Worms and NTS are scored as 0= dead; 0.25-1= reduced motility and significant tegument damage; 1.25-2= reduced motility or marked tegument damages 2.25-3= viable, nice tegument, good motility. IC_{50} values were calculated using the CalcuSyn software (ComboSyn Inc., Paramus, NJ., USA).

For the *in vivo* studies groups of 4 infected NMRI mice characterized by a patent S. *mansoni* infection (23 days postinfection) were treated orally with the test drugs via single oral doses (400 mg/kg) as oily suspensions. Untreated mice (n = 4) served as controls.

Three weeks post-treatment, animals were sacrificed by the CO_2 method and dissected. Worms were sexed and counted [286].

Worm burdens of treated mice were compared to those of control animals, and WBR % were calculated.

4.3 Results and Discussion

4.3.1 Synthetic routes for preparing PZQ-NCM-AA cocrystal solvate

In the study presented in chapter 3 [206], we noticed traces of a new solid phase when combining PZQ and NCM by LAG with AA (as visible in Figure B1 in the Appendix B). Due to the inherent interest of AA as anthelmintic molecule recently recognized (antiparasitic activity against *Gyrodactylus Kobayashii* trematode [287]), this new multicomponent solid composed of PZQ, NCM and AA warranted further investigation. Via preliminary mechanochemical experiments and characterization analyses, it was determined that the correct molar ratio for the new system was PZQ-NCM-AA 1:1:1 (see Figure B2 in the Appendix as example of characterization analyses performed). AA is an excipient classified as a GRAS substance by the FDA [288] and used in the food industry as an antimicrobial agent, flavor enhancer, flavoring agent, adjuvant and pH control agent [289].
According to the ICH Q3C guidelines, which regulate the amount of residual solvents in pharmaceutical products, AA is grouped into Class 3, and can be used for up to 50 mg/day with minimal risk to human health [290]. Considering the stoichiometric content of AA in the cocrystal solvate and the high dosage of PZQ for Schistosoma worm infection [91,96], the solvate under examination can be defined as a pharmaceutically acceptable solid.
Interestingly, during the mechanochemical screening, we observed that milling PZQ, NCM and AA in equimolar ratio did not lead to the formation of a pure PZQ-NCM-AA 1:1:1 phase, and residues of the previously reported binary solid phase PZQ-NCM 1:3 anhydrous cocrystal (hereinafter referred to as its CSD refcode RIPFOP01 [206]) were consistently observed (see Figure B3 for the results of these analyses). We concluded that the appropriate volume of AA for obtaining the cocrystal solvate was 160 μL (corresponding to 4.5 mmol), which largely exceeds the equimolar ratio among the components. The need of such a large amount of AA cannot be explained only to the evaporation of the volatile solvent. A more plausible explanation would be that AA acts both as a reactant for the inclusion into the multicomponent solid and as a liquid that facilitates the mechanochemical reaction. The importance of the grinding liquid volume has been established for the formation of anhydrous solid phases [52,53,76] and we have demonstrated here that it is equally critical for the crystallization of solvate phases.
Given our knowledge of the solid-state landscape of PZQ, NCM and AA, having already synthetized some binary combinations of these coformers [148,206], and considering the high versatility of mechanochemistry [17,58,291], which allows the combination of multiple techniques within the same

process, it was decided to explore various mechanochemical synthetic routes to assemble the same cocrystal solvate. The results are reported in the summary diagram depicted in Figure 42.

The first approach consisted of starting from the 3 individual coformers using the classic LAG method for 120 min (with the previously mentioned excess volume of 160 μL of AA).

The second synthetic route encompassed the use of preformed PZQ-NCM 1:3 anhydrous cocrystal, pure PZQ Form A (to reach the PZQ-NCM equimolar ratio) and 160 μL of AA. In such conditions, the best results (e.g., highest cocrystal solvate content) were obtained with 120 min of milling.

A third approach consisted of the use of preformed PZQ-AA monosolvate [148] plus an equimolar ratio of solid NCM and 160 μL of AA. In such conditions, the best result was achieved within 60 min of milling.

In the fourth strategy, a PZQ-NCM 1:1 coamorphous was used as starting material for the synthesis of the cocrystal solvate. This intrinsically reactive solid system [292] was chosen as starting point of the solvation reaction, adopting the same rationale as in Zanolla's work [146], where, to hydrate PZQ Form A, a two-step grinding mixed process has been carried out, under neat conditions, followed by LAG conditions. A homogenous amorphous PZQ-NCM 1:1 binary system was obtained by NG for 4h. The typical halo diffusion characteristic of amorphous materials was documented using laboratory PXRD and confirmed with Synchrotron PXRD. SSNMR confirmed the formation of a new solid, as it showed no signals attributable to the starting materials and exhibited the typical broadening of signals seen in amorphous solids (LWHM ~280 Hz). SEM image showed the absence of a crystalline habitus. Most importantly, the DSC curve exhibited a unique T_g (59.09 °C), confirming the formation of a homogeneous binary system (see Figure B4 in the Appendix for the results of these analyses). This new solid was then added of 160 μL of AA to perform the cocrystal synthesis. The best result was obtained after 30 min of grinding.

A fifth synthetic route involved PZQ and NCM individual coformers in equimolar ratio (with the previously mentioned excess volume of AA of 160 μL) in the presence of seeds of preformed cocrystal solvate (10% wt). In this pathway, the most crystalline cocrystal solvate with minor traces of RIPFOP01was obtained with 120 min of milling

All five explored strategies successfully resulted in the formation of the cocrystal solvate with very high yield, except for minor traces of RIPFOP01, in some synthetic routes.

Thus, with this work, it was demonstrated a strategy for synthesizing ternary cocrystals by using not only individual coformers but also starting from preformed synthons. This approach allows for a more versatile and efficient pathway to achieve the desired cocrystal solvate. Specifically, different building blocks were assembled, including the three pure coformers as well as various preformed combinations. Through these five different combinations, the same cocrystal solvate with very high

yield was consistently obtained and it was identified the best synthetic strategy to achieve the new system in an almost pure phase (i.e., from preformed PZQ-AA monosolvate plus an equimolar ratio of solid NCM and 160 μL of AA). These results highlight the flexibility and robustness of the "puzzle" approach, enabling the optimization of the synthesis process and the selection of the most efficient combination of starting materials.

For comparative purposes, slurry experiments were also performed using three strategic routes out of the five explored via mechanochemistry. However, the suspension-phase synthetic routes, which were fewer in number and involved significantly longer times (7 days), did not yield the cocrystal solvate in any case. Instead, the synthesis outcome was consistently RIPFOP01. This emphasizes the significant potential and versatility of mechanochemistry in efficiently achieving the desired product. Figure 42 shows a cartoon which reports all the synthetic pathways explored through mechanochemistry and slurry to get the new cocrystal solvate.

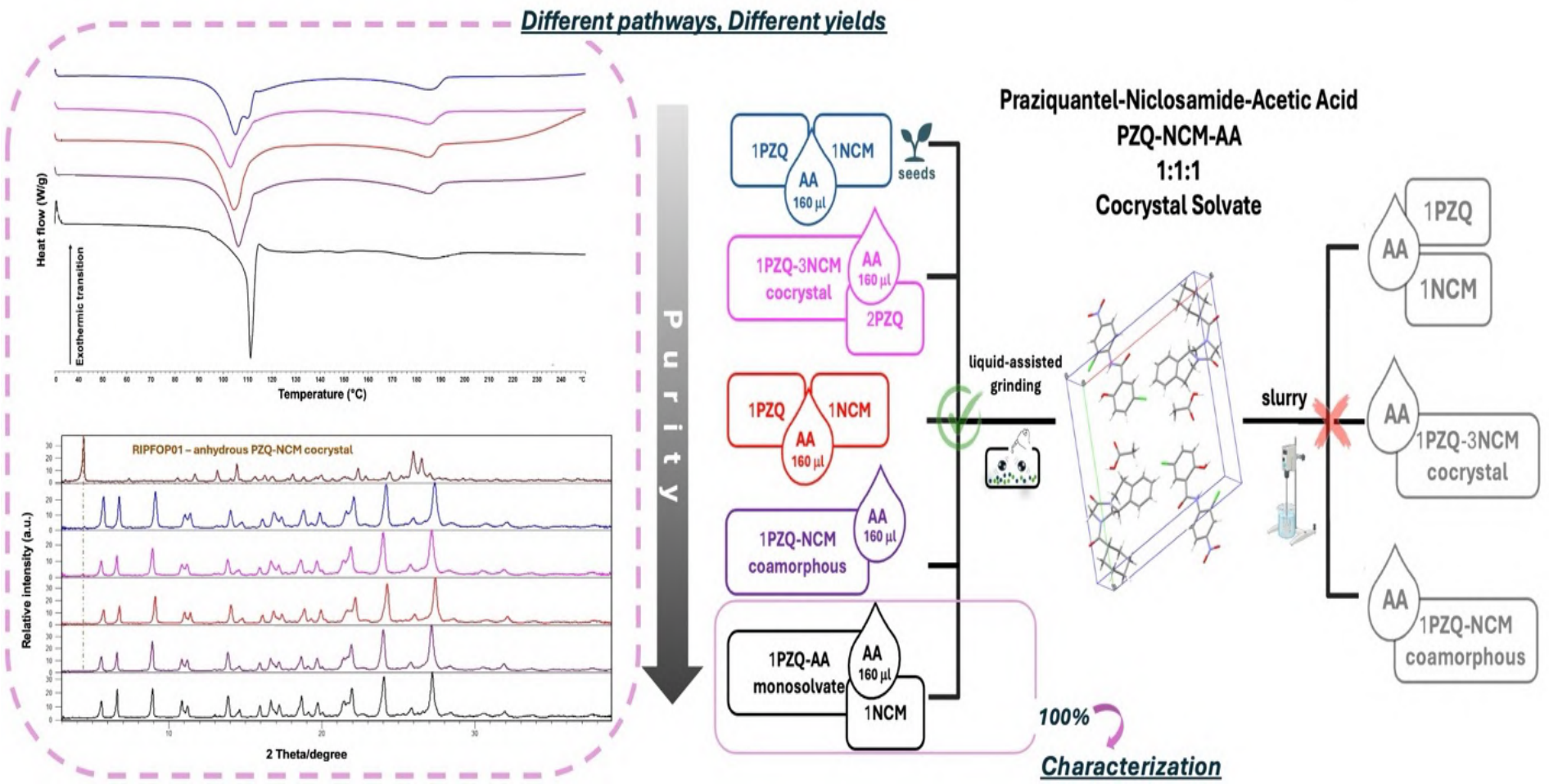

Figure 42. Cartoon illustrating the synthetic strategies for the cocrystal solvate (right) and characterization analyses by DSC (top left) and PXRD (bottom left).

As visible from Figure 42, although all mechanochemical methods allow for the formation of PZQ-NCM-AA cocrystal solvate, only the combination of PZQ-AA monosolvate and raw NCM in an equimolar ratio with the addition of 160 μL of AA achieved a 100% pure phase. The time needed for completing the solid-state reaction was only 60 min. All other combinations resulted in PZQ-NCM-AA cocrystal solvate with very minor residues of RIPFOP01.

The comprehensive characterization, presented below, was exclusively performed on the pure cocrystal solvate obtained from the best synthetic route. The new crystalline phase at the end of the mechanochemical process appeared as a white powder.

4.3.2 Laboratory PXRD analysis

The laboratory diffraction patterns of PZQ, NCM, PZQ-NCM-AA cocrystal solvate are shown in Figure 43. The diffraction pattern of pure PZQ-NCM-AA shows reflections at 3.68, 4.33, 5.92, 7.10, 7.40, 14.20, 15.60, 17.70° 2θ, which are distinctly different from those of the starting materials. The absence of signals corresponding to PZQ-NCM 1:3 anhydrous cocrystal further confirms the purity of the new solid phase.

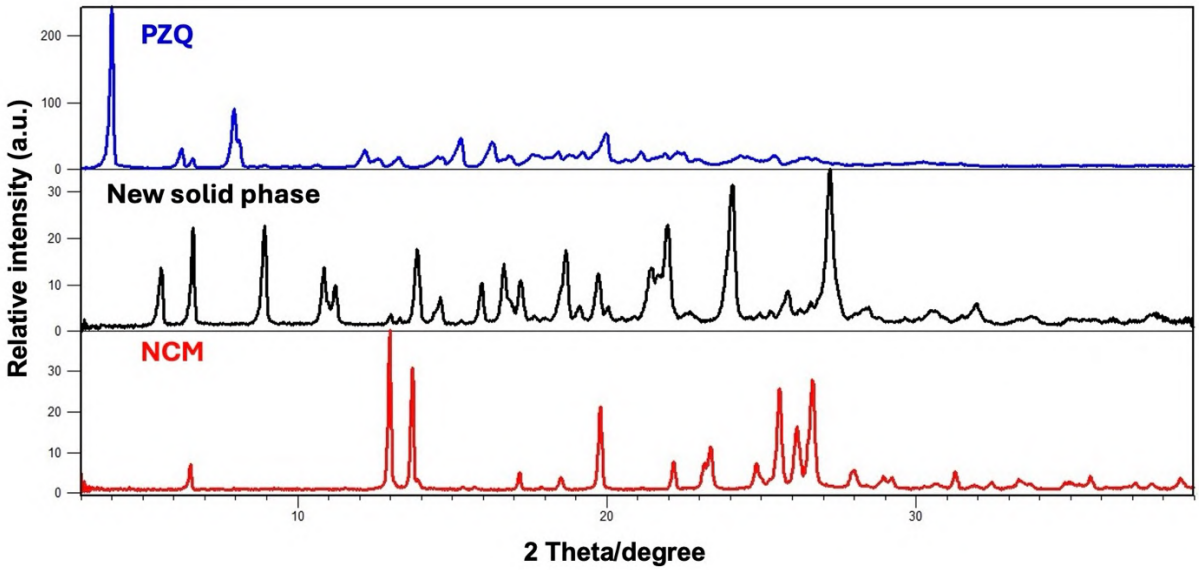

Figure 43. PXRD of PZQ (blue), NCM (red), and the new phase obtained mechanochemically (black).

4.3.3 Synchrotron X-ray Diffraction and solution of the crystal structure

The crystal structure of the cocrystal was solved from the Synchrotron PXRD, presented in Figure 44. The sample showed high crystallinity, and the indexing has been done using the program EXPO2014 [271]. The samples resulted in a *P*-1 triclinic unit cell with the following parameters: a= 6.780(1) Å, b= 16.308(5) Å, c= 16.508(5) Å, α= 107.3089(8) °, β= 92.409(1)°, γ= 91.873(1), density =1.339 g/cm^3 and volume 1739.37(3) Å^3, The number of formula units (1PZQ:1NCM:1AA) per unit cell is two (Z=2), containing one independent molecule of PZQ, one independent molecule of NCM and one independent molecule of solvent AA in agreement with SSNMR results (see section 4.3.6). A first whole powder pattern fitting (Pawley method) on the experimental powder pattern resulted in a good Rwp of 1.36%. The final Rietveld refinement, where soft restrains on the atom distances (±0.03Å) and angles (±0.1°) were applied, was performed in TOPAS V5 resulted in an R-Bragg factor of 3.32%.

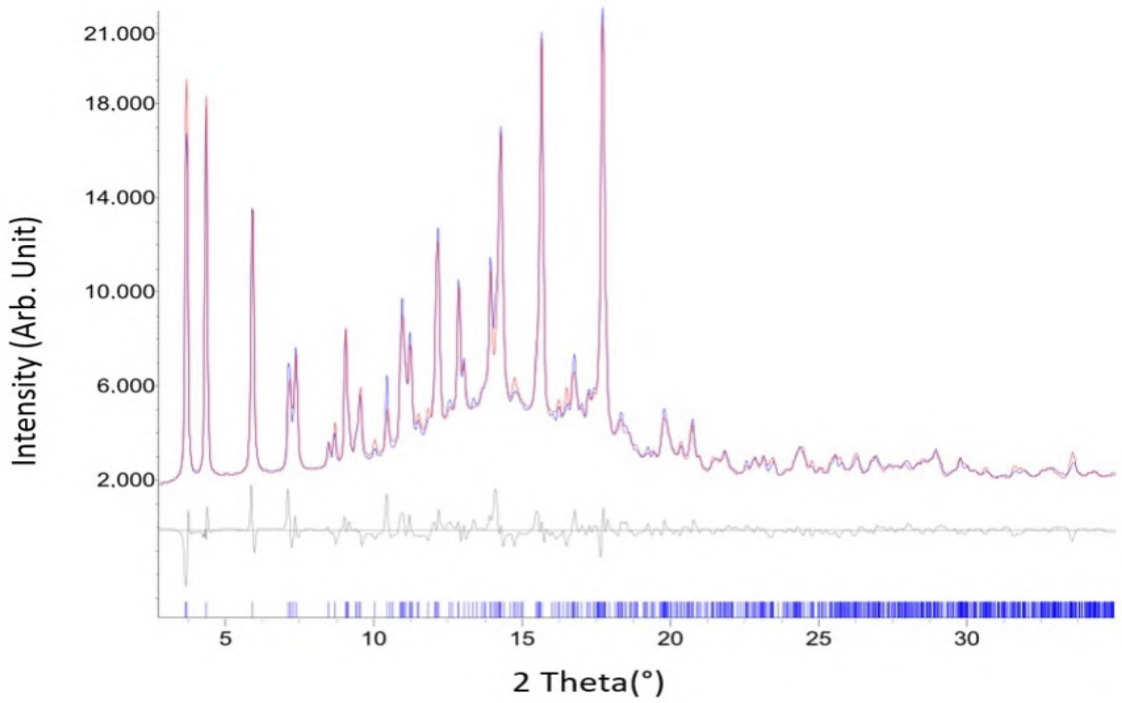

Figure 44. Rietveld refinement profile fit (obtained after the simulated annealing with EXPO14) of the cocrystal: in blue the experimental pattern (recorded using Synchrotron radiation, wavelength: 1.00 Å), in red the calculated one. The residuals are displayed on the bottom in gray and the reflection ticks in blue.

The cocrystal packing is showed in Figure 45. In this structure the cocrystal partners are tightly bounded through H-bond and molecules are coplanar. Particularly, PZQ carbonyl groups adopt the less preferred *syn* conformation in the cocrystal solvate. Similar H-bonds take place between PZQ and NCM as has been founded in the anhydrous 1:3 PZQ-NCM cocrystal [206].

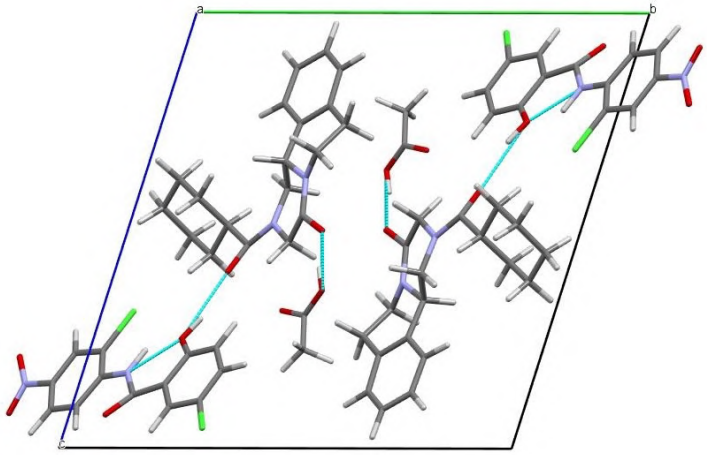

Figure 45. Capped-stick representation of the proposed structure of PZQ-NCM-AA viewed along *a*-axis. H-bonds showed with dashed blue lines.

The powder structure solved by the Synchrotron data has been confirmed by the DFT simulation (see below the paragraph on DFT calculations).

4.3.4 Thermal analyses

Figure 46 shows the DSC curve of the new system, compared to pure PZQ and NCM. Specifically, the cocrystal solvate is characterized by a broad endothermic event at 111.27 °C (enthalpy of 70.30 J/g), which was attributed to the desolvation process. Subsequently, the solid collapses, showing no melting events for either PZQ or NCM, whose melting points are usually detected at 141 and 230 °C, respectively [30,43].

The TGA analysis revealed one distinct event corresponding to a weight loss of 9.77 ± 0.18% (Figure B5 in the Appendix). The first derivative of the TGA curve showed a sharp peak at 107.23 ± 2.00 °C, confirming that the weight loss corresponded to the desolvation event already observed as an endothermic peak in the DSC curve.

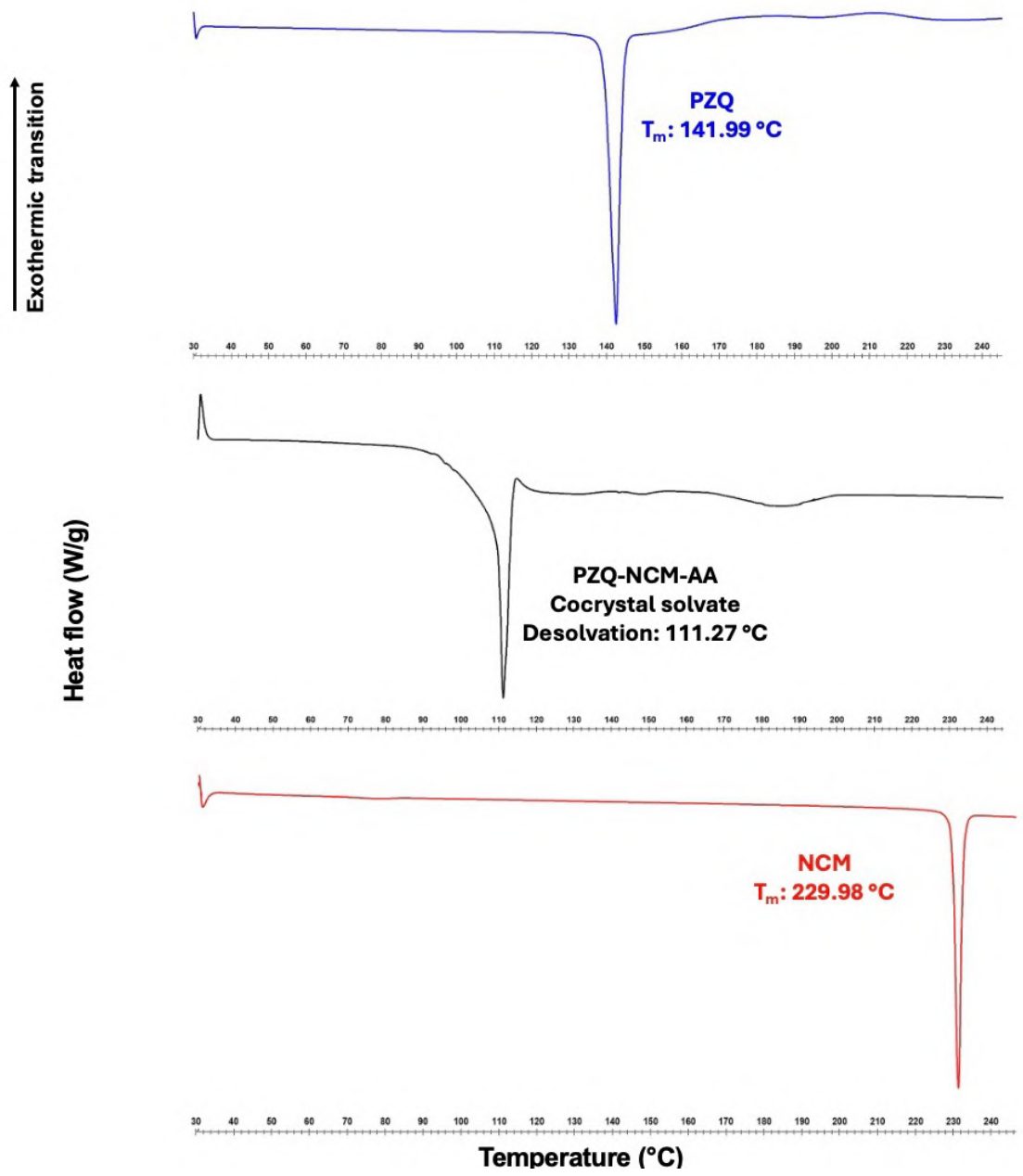

Figure 46. DSC curves of mechanochemically prepared PZQ-NCM-AA cocrystal solvate (black), raw PZQ (blue) and raw NCM (red).

4.3.5 FT-IR analysis

A detailed comparison between the spectrum of the PZQ-NCM-AA 1:1:1 cocrystal solvate shown in Figure 47 compared to the spectra of the starting materials brings to the following observations:

- In the region from 3300 to 3000 cm^{-1}, the two bands at 3242.7 cm^{-1} and 3199.5 cm^{-1}, corresponding to the -NH stretching of NCM [241], are absent in the cocrystal solvate spectrum, suggesting the involvement of the -NH amine group of NCM in H-bonding.

- The band at 897 cm^{-1}, corresponding to the -NH bending of NCM [241], converts into a doublet at 893 and 886 cm^{-1} in the cocrystal solvate spectrum, further supporting the observed changes in -NH stretching.
- The complex bands at 2800-2400 cm^{-1} range, typically related to the O-H stretching vibrations in AA [293], are absent in the cocrystal solvate spectrum, indicating the involvement of hydroxyl groups in interactions.
- In the cocrystal solvate, two bands are observed at 1681 cm^{-1} and 1618 cm^{-1}, which are attributed to the two C=O stretching of PZQ initially at 1647 and 1624 cm^{-1} [294]. This can be explained by the involvement of both C=O groups in H-bonding, as observed in the crystal lattice.
- The C-OH stretching of NCM, initially at 1192 cm^{-1} [242], shows a small shift.

The FT-IR spectrum of the cocrystal solvate aligns perfectly with the interactions observed in the crystal lattice: the bands corresponding to the two C=O groups of PZQ, both N-H and C-OH signals of NCM and -OH of AA are involved in molecular interactions within the crystal structure.

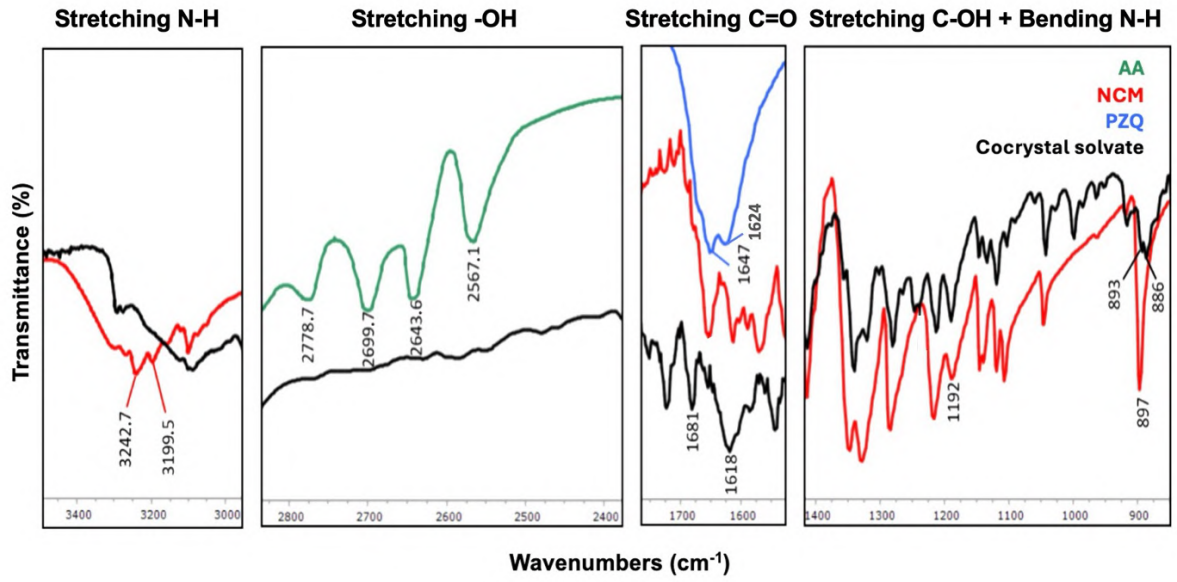

Figure 47. FT-IR spectra of PZQ (blue), NCM (red), AA (green) and PZQ-NCM-AA cocrystal solvate (black).

4.3.6 SSNMR analysis

The ^{13}C CPMAS spectra of PZQ, NCM, PZQ-NCM-AA cocrystal solvate, PZQ-NCM 1:3 anhydrous cocrystal and PZQ-AA monosolvate are shown in Figure 48. Details about ^{13}C chemical shifts (ppm) for PZQ, NCM and PZQ-NCM-AA are reported in Table 8.

Table 8. Experimental (exp) ^{13}C chemical shifts (ppm) for PZQ [43], NCM [222] and PZQ-NCM-AA and computed (calc) ^{13}C chemical shifts (ppm) for PZQ-NCM-AA, with assignments.

Group	Atom	PZQ exp	NCM exp	PZQ-NCM-AA exp	PZQ-NCM-AA calc
C = O	1	175.4, 176.2 sh		175.2	176.02
C = O	14	165.8, 164.6, 162.1		167.4	166.56
C_q	12	137.7, 136.5		133.1	134.52
C_q	11	135.8, 134.6		129.0	129.27
CH	8	129.7, 127.5, 124.8		130.1	131.02
CH	18	133.7		122.0	126.72
CH	19	132.0		129.0	129.23
CH	7	130.5		127.4	129.2
CH	17	56.3, 55.5		57.3	56.92
CH_2	15	46.1		46.2	43.34
CH_2	16	47.9		50.0	48.03
CH	4	39.7		42.1	40.57
CH_2	10	38.1		39.1	36.34
CH_2	3	32, 30.1, 27.9, 26.3, 25.3		31.3	29.51
CH_2	5			28.1	26.94
CH_2	9			28.1	25.15
CH_2	13			26.4	23.68
CH_2	6			26.4	24.36
CH_2	2			26.4	24.29
C = O	7'		162.9	163.0	163.24
C - OH	13'		153.9	156.1	159.04
C - NO_2	4'		143.3	142.3	143.44
C - NH	1'		139.9	142.3	142.49
CH_{Ar}	12'		136.1, 130.3, 125.7, 119.7	119.2	119
	11'			136.1	137.63
	9'			133.1	133.18
	3'			122.0	123
	5'			125.5	128.68
	6'			122.0	121.63
C - Cl	10'		129.8 sh	129.0	131.33
	2'			125.5	127.68
C - CO	8'		117.4	119.2	118.31
COOH	1"			173.7	177.8
CH_3	2"			20.2	15.66

PZQ-NCM-AA cocrystal solvate spectrum appears different from the spectra of pure PZQ and NCM (see also Figure B6 in Appendix), confirming the formation of a new system; the absence of residual signals of PZQ – in particular those at 165.8, 55.5, 47.9 and 38.1 ppm – and of NCM – in particular those at 153.9, 139.9 and 117.4 ppm – highlight that there is no presence of pristine PZQ and NCM. The purity of this new solid phase is further confirmed by the absence of signals corresponding to PZQ-NCM 1:3 anhydrous cocrystal – especially that at 161.5, 154.1, 151.8, 138.2, 115.0 ppm – and to PZQ-AA solvate – particularly that at 172.2, 134.8, 53.7 and 37.2 ppm (see also Figure B7 in the Appendix).

The presence of AA can be observed from the peak at 20.2 ppm corresponding to the CH_3 group, highlighted in Figure 48 with a green arrow. The AA carbonyl group is visible as shoulder around 173.7 ppm, see green arrow in Figure 48.

The number of signals in the NCM, PZQ-NCM-AA cocrystal solvate spectrum suggests the presence of one independent molecule of PZQ, one of NCM and one of AA, confirmed also from ^{1}H-NMR analysis (see below).

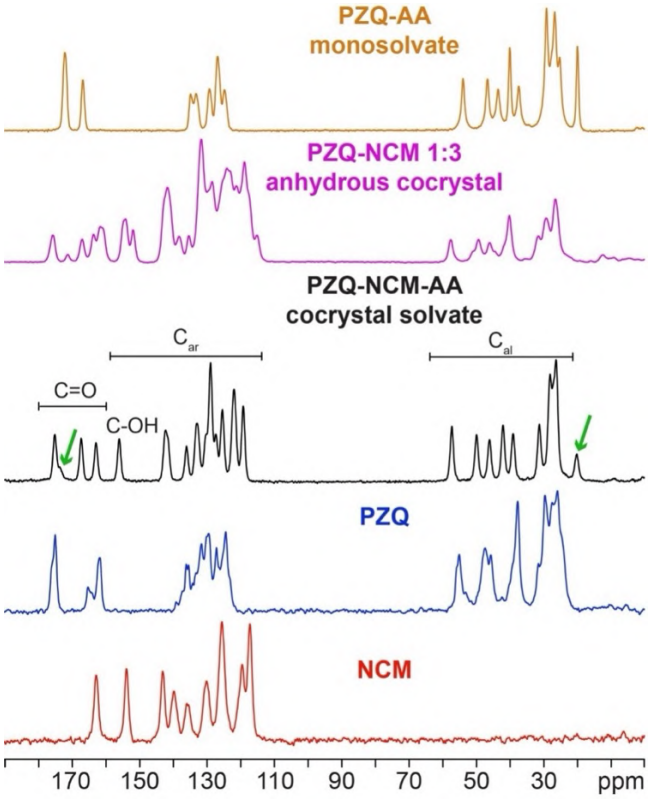

Figure 48. ^{13}C (150.91 MHz) CPMAS spectrum of PZQ-NCM-AA cocrystal solvate (black), acquired at a spinning speed of 20 kHz at room temperature, compared to ^{13}C (100.63 MHz) CPMAS spectra of pure NCM (red), pure PZQ (blue), PZQ-NCM 1:3 anhydrous cocrystal (pink), acquired at a spinning speed of 12 kHz at room temperature, and ^{13}C (150.91 MHz) CPMAS spectrum of PZQ-AA monosolvate (orange), acquired at a spinning speed of 20 kHz at room temperature. The two green arrows highlight the signals attributed to AA.

4.3.7 ^{1}H-NMR analysis

The ^{1}H-NMR spectrum of PZQ-NCM-AA cocrystal solvate is reported in Figure B8 in the Appendix. The integrations of the signals at 2.6 and 2.5 ppm, corresponding to PZQ H4 (it is splitted due to the presence of two coformers of PZQ [295]), at 8.7 ppm, related to an aromatic CH of NCM, and at 2.1 ppm, corresponding to the three protons of the CH_3 of AA, confirm the stoichiometric ratio of 1PZQ:1NCM:1AA, in agreement with Synchrotron PXRD results.

4.3.8 DFT calculations

The initially Rietveld refined structure was re-optimized at DFT level with Quantum Espresso and submitted for a second refining. This "quasi self-consistent" process, which combines experimental and theoretical data, has proven to be very useful in helping to refine the resolution of particularly difficult structures [296,297]. The final structure has been optimized with a fixed cell scheme, in which only atoms were allowed to move, while the cell shape and volume were kept constant. The comparison between the experimental data and the simulated one (fixed cell) is shown in Figure 49. The root-mean-square error (RMSE) relative to the overlap between the two structures was calculated by the crystal packing similarity tool implemented in Mercury and it is 0.245, typical of reliable structures [298]. It should be mentioned, however, that full free cell optimization resulted in a structure very similar to the experimental one (RMSE = 0.245), which indicates a very good agreement with the theoretical structure computed at 0 K. To further validate the structure from powder data the experimental and computed chemical shifts (see Table 8) were compared and a low ^{13}C RMSE (2.13) was obtained. Figure B9 in the Appendix displays the good correlation between the experimental and computed chemical shifts.

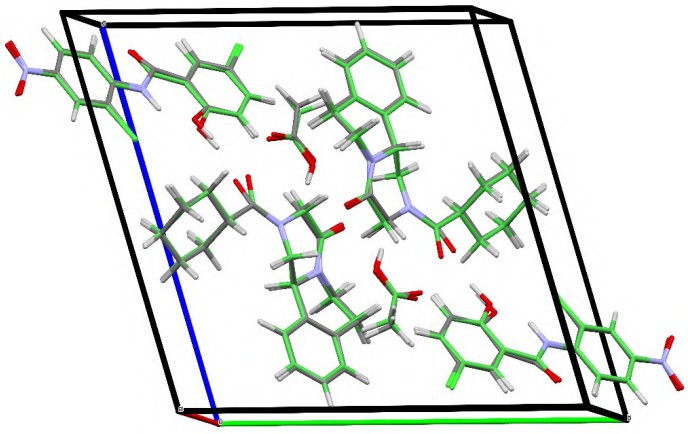

Figure 49. Overlap conformations between the experimental refined crystal structures and the computed one (fixed cell) by DFT (cyano).

4.3.9 SEM analysis

SEM images of powders of PZQ, NCM and PZQ-NCM-AA cocrystal solvate are reported in Figure 50. The new system is composed of agglomerates of small thin plates (with an approximate diameter less than 1 μm), exhibiting a habitus distinctly different from the needle-shaped particles typically observed in PZQ [45] and the rectangles with protrusions characteristic of NCM [218].

Figure 50. SEM images of (a) PZQ (5000x), (b) PZQ-NCM-AA cocrystal solvate (20000x) and (c) NCM (5000x).

4.3.10 Drug recovery

^{1}H-NMR spectroscopy was also used to determine whether component degradation occurs after different synthesis procedures. The spectra of pure PZQ, NCM, with two samples of PZQ-NCM-AA cocrystal solvates, which only differ from the process used for obtaining the solid product, were compared (Figure B10 in the Appendix). One sample was obtained through the synthesis reported in section 2.1.1.1 and the other one following the procedure of section 2.1.1.4. Spectroscopic evaluations have shown no evidence of PZQ degradation upon grinding in the presence of NCM and AA, even though is well-known from literature the PZQ propensity to degradation when ground in the presence of other substances, with the insurgence of peculiar degradation products as a function of the excipient used [42,45,264].

4.3.11 Cocrystal physical stability under several conditions

The stability of solvates is a critical aspect of pharmaceutical science, since these materials are inherently prone to desolvation, a process where the solvent molecules are expelled from the crystal

lattice, often leading to significant structural and thermodynamic changes which result in potential loss of desired properties [299,300].

In the present case, the physical stability of the cocrystal solvate was assessed under various conditions. The main objectives were to determine if there were signs of (spontaneous or induced) desolvation leading to cocrystal dissociation or conversion into the corresponding PZQ-NCM anhydrous cocrystal, and to evaluate if the new system could prevent the formation of the insoluble NCM monohydrate, which typically occurs within a month of exposure to ambient humidity [30].

Under static conditions (i.e., 20 °C, 0% RH), the new multicomponent crystal remained stable for 24 months with no signs of cocrystal dissociation or conversion into the anhydrous cocrystal (see Figure B11 in the Appendix). During this period, the sample retained its white crystalline powder appearance, unlike the samples containing trace amounts of RIPFOP01 (obtained by the other synthetic routes), which exhibited a pinkish hue during storage under similar conditions (Figure B12 in the Appendix). Interestingly, this pink coloration could not be attributed to RIPFOP01 itself (reported to be a white powder [206]), nor to impurity B of PZQ (as demonstrated by ^{1}H-NMR analysis), which is indeed reported as a pink solid [301]. A plausible explanation of the appearance of such coloration, therefore, remains uncertain.

Additionally, the physical stability of PZQ-NCM-AA upon mechanical stress was also evaluated since it is well known that solvates tend to desolvate and undergo structural relaxation when subjected to compression, which can significantly impact their physical stability and performance [302–304]. We therefore aimed to evaluate the physical stability of the cocrystal solvate under compression to better understand its behavior under potential practical pharmaceutical manufacturing conditions.

Specifically, 200 mg of solid was subjected to compression under the same operating conditions used for creating KBr discs for FT-IR analysis (see section 4.2.2.6). In this case, mechanical compression did not cause any dissociation or the formation of other phases, as evidenced by PXRD, however, DSC analysis indicated a reduction in the overall crystallinity of the sample (see Figure B13 in the Appendix).

The mechanical resistance was also tested through milling the cocrystal solvate for 200 min at 25 Hz, following the procedure adopted by Zanolla and coauthors [148]. The PXRD and DSC results demonstrated that, despite the cocrystal solvate being subjected to intense and impactful mechanical stress, the new phase remained almost intact. Only partial desolvation with conversion into the corresponding PZQ-NCM 1:3 anhydrous cocrystal was observed, as could be expected (Figure B14 in the Appendix).

PZQ-NCM-AA cocrystal solvate was also placed for 6 months in a sealed enclosure with a saturated aqueous NaCl solution (75% RH) and periodically analyzed by means of PXRD. These analyses were

carried out as the phenomenon of cocrystal dissociation at high humidity is well known [265]. Further, the possibility of the formation of NCM monohydrate is a constant risk when handling this drug [30,218]. The new ternary cocrystal remained stable throughout the entire six-month period under such conditions (Figure B15 in the Appendix). Importantly, the maintenance of the powdered material at high humidity conditions did not bring in the typical greenish color of NCM monohydrate. This is, therefore, one of those cases where cocrystallization enhances the physical stability of moisture-sensitive drugs [305].

4.3.12 *In Vitro and in Vivo Activity*

Table 9. *In vitro* activity of the cocrystal solvate against NTS and S. *mansoni* adult, compared to pure PZQ, NCM and PZQ-AA monosolvate.

S. *mansoni* adult					
Testconc.	**Effect in % (72h) +SD**				**IC_{50} (µM) (72h) Dm**
	10µM	**1µM**	**0.1µM**	**0.01µM**	
New cocrystal solvate	**100 (0)**	**100 (0)**	**90.75 (1.9)**	**53.7 (5.6)**	**0.01**
PZQ	92.1 (1.6)	92.1 (1.6)	51.05 (4.7)		0.44
NCM	100 (0)	62.1 (1.6)	77.75 (3.2)	49.5 (0)	0.09
PZQ monosolvate*	100 (0)	87.50 (0)	41.65 (8.3)		0.18
PZQ-NCM cocrystal **		100 (0)	71.95 (4)	39.55 (6.3)	0.02
NTS					
Testconc.	**Effect in % (72h) +SD**				**IC_{50} (µM) (72h) Dm**
	10µM	**1µM**	**0.1µM**	**0.01µM**	
New cocrystal solvate	**100 (0)**	**100 (0)**	**100 (0)**	**41.67 (1.67)**	**0.01**
PZQ	82.35 (2)	70.83 (4.2)	31.25 (2.1)		0.34
NCM	100 (0)	83.33 (0)	31.25 (2.1)		0.21
PZQ-AA monosolvate*	87.50 (0)	62.50 (0)	31.25 (2.1)		0.39
PZQ-NCM cocrystal**		92.31 (3.8)	25 (1.9)		0.20

*obtained as previously reported [148]; **taken from reference [206].

The new cocrystal solvate revealed the highest activity against both NTS and adult *S. mansoni* (Table 9). Concentrations of 0.1-10 µM resulted in death of all worms. A concentration of 0.01 µM revealed an activity of 41.7% (NTS) and 53.7% (adult worms). This translates to IC_{50} values of 0.01 µM against adult worms and NTS, respectively. For comparison, against NTS, pure PZQ and NCM, binary PZQ-NCM cocrystal and PZQ-AA monosolvate showed a 10-fold lower activity, i.e., were only active at 1 and 10 µM – Against adult worms only NCM and the PZQ-NCM cocrystal showed a similar good performance as the new cocrystal solvate with moderate activity still observed at 0.01 µM.

In a pilot study, the cocrystal solvate was orally administered as an oily suspension to a group of four mice infected with a patented S. *mansoni* infection, at a single dose of 400 mg/kg. Twenty-three days post-infection, the mice treated with the cocrystal solvate showed a 74.3% WBR, compared to approximately 87% in mice treated with the original PZQ [183] (Table 10). These results suggest that the cocrystal solvate retains its antischistosomal activity relative to the raw PZQ.

However, the *in vitro* activity tests were more promising, as the three APIs in the new multicomponent system appeared to exert a synergistic effect. The discrepancy between the *in vitro* and *in vivo* results could potentially be attributed to the vehicle used for administration: the cocrystal solvate was difficult to dissolve in corn oil, resulting in a cloudy suspension rather than a clear suspension.

Moreover, the use of an oil-based vehicle suspension, although better than the aqueous-based one, may not be ideal for showcasing the full potential of the cocrystal, which would likely benefit from being administered in a solid form, such as in minicapsules of size M. However, the minicapules are very difficult to administer to mice, as observed in the previous study, where many animals died during administration [206]. Future *in vivo* studies should be conducted using minicapsules size M, following thorough training and refinement of the administration technique for these pharmaceutical forms.

Table 10. Effect of the cocrystal solvate (administered as oily suspension) on the WBR in mice harboring a chronic S. *mansoni* infection.

Sample	Average of WBR %	Number of mice
Control	-	4
PZQ-NCM-AA cocrystal solvate	74.3	4

4.4 Conclusions

In this section, a cocrystal solvate composed of three compounds namely PZQ, NCM and AA, all having documented anthelmintic properties, is presented.

Mechanochemical methods demonstrated a great potential by successfully producing the new system across five investigated routes, and a pure phase could be obtained by milling for 60 min preformed PZQ-AA monosolvate and raw NCM in an equimolar ratio in the presence of 160 μL of AA. In contrast, slurry experiments did not result in the formation of the cocrystal solvate at any stage.

The structure of the cocrystal solvate was successfully solved and refined from the Synchrotron PXRD data, with support of theoretical periodic calculations and an integrated SSNMR approach. The new system crystallizes in the triclinic space group of *P*-1, showing one PZQ, one NCM and one AA molecules linked through homo- and heteromolecular H-bonds in the ASU.

The new phase was also thoroughly characterized by means of SSNMR, liquid ^{1}H-NMR, FT-IR and thermal analyses. The cocrystal solvate shows agglomerates of small plates through SEM analysis and exhibits at the DSC analysis a desolvation event at roughly 111 °C (corresponding to 10.91 ± 0.57% weight loss in TGA).

Spectrometric evaluations have shown no evidence of degradation of PZQ upon grinding. Such observation is important considering the tendency of this molecule to degrade under mechanochemical processing in the presence of excipients with the insurgence of peculiar degradation products as a function of the excipient used.

Importantly, the new cocrystal solvate demonstrated higher anthelmintic activity (%-effect of activity reduction) against *in vitro* S. *mansoni* adults and NTS, compared to that of pure PZQ and NCM. The anthelmintic potential of the ternary cocrystal is notably superior compared to the significantly lower efficacy observed in both the binary PZQ-NCM cocrystal and the PZQ-AA monosolvate. Due to *in vitro* promising results, *in vivo* preliminary tests on mice were also performed through the administration of an oily suspension of the novel phase. Future *in vivo* studies should be conducted using minicapsules size M.

Finally, the new multicomponent crystal remained stable for 24 months at ambient temperature and demonstrates physical stability under high RH conditions (75% RH), effectively preventing the formation of the well-known NCM monohydrate, which typically forms within just one month of air exposure at room temperature. Analysis of solid-state transformations after mechanical treatments revealed that extended grinding (200 min) just led to a decrease of crystallinity degree, whereas compression (10 Ton for 3 min) just promotes a partial conversion into the PZQ-NCM 1:3 anhydrous cocrystal.

5. Ternary Drug-Drug-Drug coamorphous systems obtained through mechanochemistry and physical stability analyses

5.1 Abstract

The objective of this PhD thesis section was to investigate the feasibility of developing drug-drug coamorphous systems—both two- and three-component—by combining three anthelmintic drugs: PZQ and NCM, plus mebendazole (MBZ).

The choice of these APIs, all with anthelmintic activity – which also justifies their use in combination therapies (e.g., PZQ and MBZ [306]) –is due to their poor aqueous solubility and low bioavailability [97]. These three APIs are known to exist into multiple crystalline solid forms indexed in the CSD [168], confirming their ability to interact in the solid-state with various coformers. Furthermore, they all have demonstrated the ability to form coamorphous systems [307] or ASDs [45,308]. Additionally, literature reports several examples of the use of these three drugs in mechanochemical experiments [206,309].

Using a mixture design approach, ten different (binary and ternary) mixtures were formulated and prepared by NG in a lab-scale vibrational mill. The solvent-free one-step process was reproducible, requiring only 4h to generate coamorphous systems in the whole experimental domain. Structural analyses by PXRD and FT-IR confirmed the absence of crystalline domains and presence of molecular interactions. The T_g temperature was calculated theoretically according to Gordon-Taylor (G-T) equation for a three-component system and then determined by DSC. In most cases a single T_g was seen, indicating the formation of homogeneous multicomponent systems. Stability studies on seven systems, stored for six months under different temperature conditions (-30 °C, 5 °C, 25 °C, and 40 °C), demonstrated that all systems were physically stable according to the " T_g – 50°C" stability rule, with only two exceptions out of seven. Humidity effects were minimal, as shown by dynamic vapor sorption (DVS) data, which revealed only superficial water sorption and no recrystallization. Additionally, the investigation of recrystallization pathways revealed that, depending on the interactions of the system, some coamorphous systems separated into their original crystalline phases and others formed new entities such cocrystals.

A graphical abstract of this experimental work is presented in the Figure 51 below.

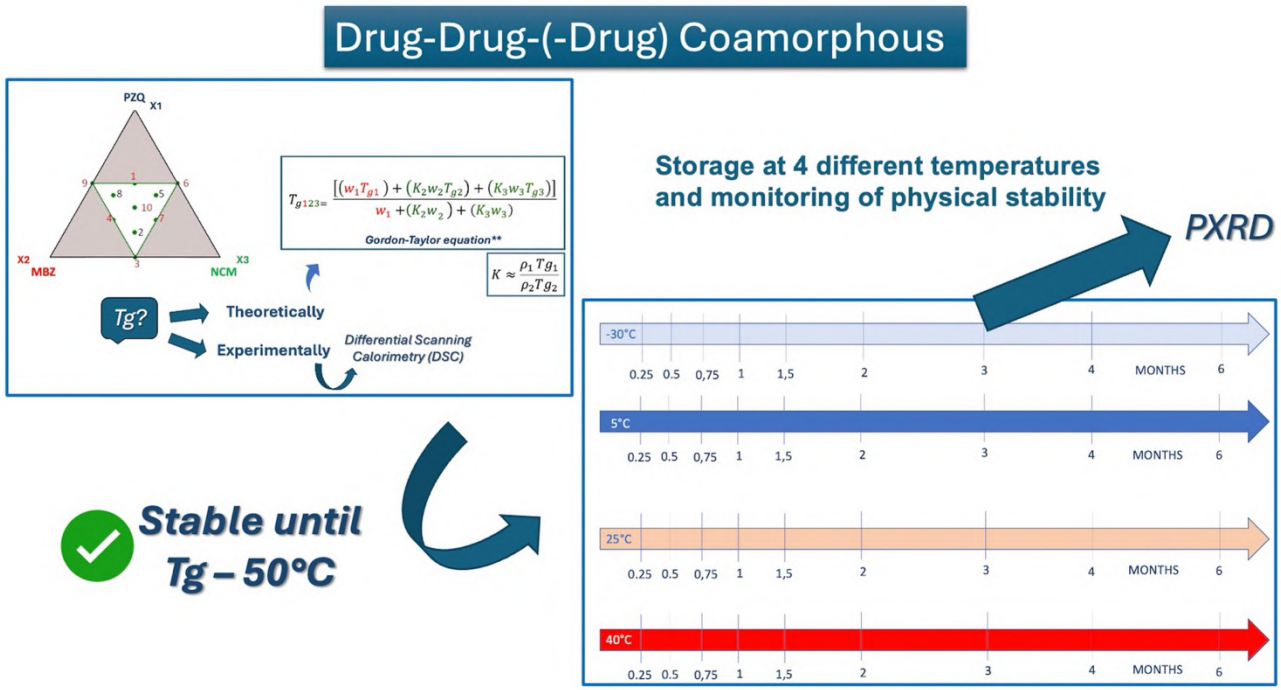

Figure 51. Graphical abstract of the experimental work applied on the coamorphous experimental work.

5.2 Materials and Methods

5.2.1 Materials

PZQ, (RS)-2-(Cyclohexylcarbonyl)-1,2,3,6,7,11b-hexahydro-4-H-pyrazino[2,1-a]-isoquinolin-4-one], of Ph. Eur. grade was kindly donated by Fatro S.p.a. (Bologna, Italy), while NCM (5-chloro-N-(2-chloro-4-nitrophenyl)-2-hydroxybenzamide)(purity of 98-101%) and MBZ (methyl N-(6-benzoyl-1H-benzimidazol-2-yl)carbamate)(purity ≥ 98%) were purchased from Sigma-Aldrich (St. Louis, USA). All the actives were used without further purification before grinding.

5.2.2 Methods

5.2.2.1 Samples preparation

5.2.2.1.1 Mixture composition and Experimental design

The composition of the mixtures was formulated using a mixture design approach [310], implemented via NEMRODW software [311]. The mixtures subjected to grinding consisted of three powdered components: PZQ (X1), MBZ (X2), and NCM (X3). The limits of each component in the mixtures

were defined during the preliminary trials obtaining the following values: $0 \leq X \leq 0.5$ (expressed as molar ratio in the mixture). The experimental matrix is detailed in Table 11, and the ternary diagram representing the experimental design space is shown in Figure 52.

Table 11. Experimental matrix.

Exp. N°	Molar ratio		
	PZQ X1	**MBZ X2**	**NCM X3**
1	0.500	0.250	0.250
2	0.167	0.417	0.417
3	0	0.500	0.500
4	0.250	0.500	0.250
5	0.417	0.167	0.417
6	0.500	0	0.500
7	0.250	0.250	0.500
8	0.417	0.417	0.167
9	0.500	0.500	0
10	0.333	0.333	0.333

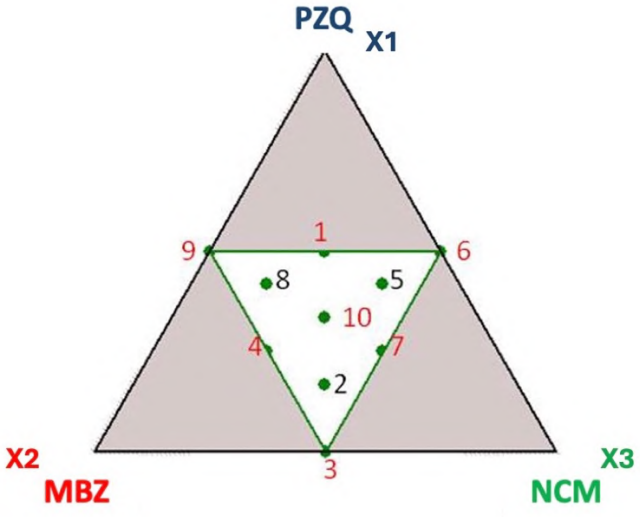

Figure 52. Ternary diagram representing the experimental design space.

5.2.2.1.2 NG experiments

Milling was carried out using a Retsch MM400 vibrational mill (Retsch, Germany) equipped with two 25 mL stainless steel jars, each containing a 10 mm Ø stainless steel bead. The milling frequency was consistently set at 25 Hz for all experiments, with the void volume in the jars kept constant by maintaining a total powder mass of 400 mg per 25 mL jar. The milling duration was 4h.
To ensure reproducibility, each mixture was milled in at least four replicates. Pure crystalline drugs (MBZ and NCM) (400 mg per drug) were also milled individually under the same conditions. PZQ was not milled alone, as its behavior under these conditions had already been well-documented in previous studies [43,142].

5.2.2.1.3 Physical mixtures preparation

Physical mixtures (PMs) were prepared by manually mixing the APIs in an agate mortar for a standardized time of 3 min. Both binary and ternary mixtures were prepared, with a total mass of 400 mg for each batch. The molar ratios of the APIs were varied according to the experimental mixture design (Table 10).

5.2.2.2 Samples characterization

5.2.2.2.1 PXRD analysis

PXRD analysis was carried out by a Bruker D2 Phaser benchtop diffractometer (Bruker, Manheim, Germany) using the Bragg-Brentano geometry, using Cu-Kα radiation (λ = 1.5418 Å) with a 300W low-power X-ray generator (30 kV at 10 mA). All the measurements were conducted in a 2θ range of 3-40° with a step size of 0.02° and a scan speed of 0.6°/s. Each sample was prepared by gently pressing approximately 200 mg of ground product into the cavity of a steel sample holder equipped with a cylindrical PVDF reducer.
PXRD patterns were recorded for the starting materials, PMs, all milled samples, and a selection of aged coamorphous samples.

5.2.2.2.2 DSC analysis

Selected samples, weighing 2-4 mg, were introduced into an aluminum sealed and pierced 40 µL crucible and analyzed by a Mettler Toledo DSC 3 Star System (Milan, Italy) using STARe software version 16.40 for data analysis. The heating program employed a temperature ramp of 10 °C per minute, from 30 °C to 350 °C, under a nitrogen flow rate of 50 mL/min.

The following samples were analyzed: pure APIs, PMs, coamorphous samples produced via NG, and a selection of aged coamorphous samples.

DSC was mainly applied to experimentally evaluate T_{g}s of the ten coamorphous and the T_g temperature was expressed as inflection point in the thermal curve.

To obtain MBZ T_g, DSC heating/cooling/heating cycles were applied. These cycles were performed under a nitrogen flow of 50 mL/min, following this protocol: 1. Heating from 30 °C to 335 °C at a rate of 10 °C/min; 2. Isotherm at 335 °C for 5 min; 3. Cooling from 335 °C to -30 °C at a rate of 50 °C/min; 4. Isotherm at -30 °C for 5 min; 5. Reheating from -30 °C to 330 °C at a rate of 40 °C/min.

In certain cases, such as with NCM, where the T_g could not be detected using conventional DSC analysis, MTDSC was performed by using a DSC1 Stare System (Mettler Toledo, CH) equipped with a refrigerated cooling system (RCS). Samples of about 10 mg were quantitatively transferred to pin-holed aluminum pans, sealed, weighed and subjected to heating cycles from 10 to 350 °C (1 K/min), for a period of 90 s and an amplitude 0.5 °C. The DSC cell and RCS were purged with dry nitrogen at 80 and 120 mL/min, respectively. The system was calibrated using an indium standard. All data were treated with Stare System software (Mettler Toledo, CH).

5.2.2.2.3 True density determinations

The true density of the three pure powdered APIs was measured using a helium pycnometer (Ultrapyc 5000, Anton Paar GmbH, Graz, Austria). The device is based on gas pressure determinations, in connected, sealed chambers of specified volume. At first, a chamber is filled with powders and gas; the latter is later allowed to flow in a second chamber, free of powders. The difference in helium pressure in the two chambers is used to calculate the volume occupied by the powders, using Boyle's law [312]. The density is finally determined by the ratio between mass of powders and calculated volume. The accuracy of the measurement relies on the penetration of inert gas in any void between particles. The density values of crystalline materials were used as crude density values for the amorphous components and serve to calculate the constant, K (equation 3):

$$K = \frac{Tg_1 * \rho_1}{Tg_2 * \rho_2} \quad (3)$$

K is a fundamental constant of Gordon-Taylor (G-T) equation (equation 4), which considers the weight fractions and T_g values of the individual components, as well as the true density values of their powders, to calculate a theoretical T_g for a coamorphous system [313,314]:

$$\mathrm{Tg}_{mix} = \frac{[(w_1\mathrm{Tg}_1) + (K_2 w_2 \mathrm{Tg}_2) + (K_3 w_3 \mathrm{Tg}_3)]}{[(w_1 + (K_2 w_2) + (K_3 w_3)]} \quad \textbf{(4)}$$

where:

-pedix 1 refers to PZQ;

-pedix 2 refers to NCM;

-pedix 3 refers to MBZ.

The T_g values included in the equation for the individual components are the experimentally determined values, as measured and described in section 5.2.2.2.2.

5.2.2.2.4 FT-IR spectroscopy

Powdered samples were analyzed with a Shimadzu IRAffinity-1S FT-IR instrument (Kyoto, Japan) in a range of 400-4000 cm^{-1} with a resolution of 4 cm^{-1} and 20 scans.

Suitable discs for analysis were prepared by gently grinding in an agate mortar 200 mg of anhydrous KBr (99% infrared grade) with 1% w/w of analyte and then pressing the mixture with a hydraulic press (PerkinElmer, Norwalk, USA), applying a pressure of 10 Ton for 3 min.

Data interpretation and comparisons were performed using SpectraGryph 1.2 software.

5.2.2.2.5 SEM analysis

Images of some coamorphous were collected through SEM. The powdered sample was placed on an aluminum stub covered with a carbon double-sided tape and sputter-coated with gold using a Sputter Coater K550X (Emitech, Quorum Technologies Ltd, UK), before being analyzed by a scanning electron microscope (Quanta 250 SEM, FEI, Oregon, USA) with the secondary electron detector. The working distance was set at 10 mm to obtain the appropriate magnifications, and the acceleration voltage was set at 5 kV.

5.2.2.2.6 Stability studies

Selected samples (exp. N° 1, 3, 4, 6, 7, 9, 10) were stored at four different temperatures (-30 °C, 5 °C, 25 °C, and 40 °C) for 6 months to assess their physical stability under various temperature conditions. To protect the samples from atmospheric humidity, they were stored in sealed vials placed inside sealed plastic bags during the aging process. Samples were withdrawn during the first month

on a weekly basis and then on a biweekly basis and tested to investigate the possible recrystallization using PXRD (as described in section 5.2.2.2.1). Samples stored for 6 months under the most severe conditions (i.e., -30 °C and 40 °C) were also evaluated for drug recovery (see section 5.2.2.2.7).
Additionally, it is well-established in literature that amorphous systems are prone to hygroscopicity [315,316]. Therefore, to gather preliminary data on the effects of RH on these coamorphous systems, selected samples were further analyzed using the DVS technique. Specifically, samples from exp. N° 3, 6, 9, and 10 were placed in crucibles and subjected to a gradual RH increase from 0% to 90% at a constant temperature of 25 °C. This allowed for the evaluation of mass changes, providing insights into surface moisture absorption and, consequently, powder hygroscopicity.

5.2.2.2.7 Drug recovery

To check possible degradation of coground samples after preparation, ^{1}H-NMR spectra were recorded on a Bruker Avance 600 spectrometer equipped with a 14 T superconducting magnet and two 5 mm probes. Analyzed samples were dissolved in $CDCl_3$ using TMS as reference. Measurements were conducted at 300 K using a simple pulse-acquire sequence.
Drug recovery analyses were performed on the same seven samples (i.e., exp. N° 1, 3, 4, 6, 7, 9, 10) used for the physical stability study, specifically those stored in the freezer and those subjected to stressed conditions at 40 °C.

5.3 Results and Discussion

In the above section, five different synthetic strategies for preparing PZQ-NCM-AA cocrystal solvate are presented. In one of them, an intrinsically reactive solid system [292] such as a PZQ-NCM 1:1 coamorphous (obtained through 4h of NG) was used as starting material for the synthesis of the cocrystal solvate. PZQ-NCM coamorphous also served as the starting point for another experimental project presented in this part.

Coamorphous systems are well-known for overcoming the solubility challenges that typically affect crystalline drugs, leading to faster dissolution rates that are crucial for ensuring consistent and rapid drug absorption *in vivo* [317,318]. Additionally, when properly formulated, they exhibit superior physical stability compared to individual amorphous forms, which are often unstable and prone to recrystallization when subjected to storage or environmental stresses. The intimate molecular-level mixing of drugs with coformers in coamorphous systems reduces molecular mobility and significantly lowers the risk of phase separation or crystallization [46,319–323].

Traditionally, coamorphous systems consist of two low-molecular-weight coformers (e.g., drugs, amino acids, dicarboxylic acids, flavonoids, sugars, etc. [46,307,324]) and exhibit a single T_g. Recent advancements are increasingly focusing on the design of three-component coamorphous systems, which, despite being more complex and challenging to formulate due to the need for optimized molecular compatibility, offer even greater physical stability. The inclusion of a third component could promote stronger molecular interactions, such as H-bonds and van der Waals forces, which further disrupt potential recrystallization pathways, resulting in superior stabilization of the amorphous state compared to two-component systems [322,325,326].

Specifically, based on the recent development of dual-drug coamorphous through mechanochemistry [324,327], this study aimed to determine whether PZQ – NCM – MBZ mixtures could give origin to homogenous coamorphous systems, and whether these systems could be produced through neat NG, without the need for solvents [17,46,47]. The research focused on assessing whether such systems could stabilize each drug in its amorphous state, enhancing their stability during storage. By creating coamorphous mixtures, it is assumed that the combination of these drugs will promote molecular-level interactions, such as H-bonding, which could prevent recrystallization and enhance individual amorphous stability. The study compared two-component systems, where one drug acts as a coformer for the other, to three-component systems, where the third drug – if properly selected – is expected to further improve stability through added intermolecular complexity.

The first step of this experimental work involved the planning of an experimental matrix using the NEMROWD software to design binary and ternary mixtures of the three APIs (PZQ, NCM and

MBZ). The goal was to explore a sufficient compositional space of the three-component system; for this reason, ten points in the ternary phase diagram were selected corresponding to ten different mixtures of the three APIs (refer to Table 10 for N° of experiment and compositions). These ten mixtures were then subjected to NG for 4h at a frequency of 25 Hz (in batches, each weighing 400 mg).
As a control, PMs with the same compositions as those in the experimental matrix were also prepared. This allowed for a detailed comparison between the coground samples and their unprocessed counterparts, providing valuable insights into the structural differences between the two.

The solid-state nature of the coground samples and PMs was then assessed through PXRD analysis. Diffractograms of all ten milled mixtures revealed a typical halo pattern characteristic of amorphous compounds (see Figures C1-C10 in the Appendix C) [328], in contrast to the PMs, where the PXRD patterns simply reflected the combined crystalline patterns of the two or three (depending on the mixture composition) starting materials (Figure C11 in the Appendix). This comparison clearly indicated that manual physical mixing was insufficient to amorphize the three APIs, whereas NG was essential to achieve complete amorphization in all ten systems.

At this stage, some coground samples (all three binary plus one ternary system, i.e., exp. N° 3, 6, 9 and 10) were analyzed using FT-IR spectroscopy to investigate the presence of possible interactions between the components, which would indicate the formation of coamorphous systems rather than mere physical blends of the three amorphous components.
Figure 53 shows FT-IR spectrum of exp. N° 3 (i.e., binary NCM-MBZ 1:1) compared to the corresponding PM and pure components. Starting with MBZ, the N-H amide stretching band at 3404 cm^{-1} [329] is still present in the PM, whereas it disappears in the coamorphous spectrum, indicating its involvement in H-bonding. Similarly, the amide C=O stretching band at 1717 cm^{-1} [329] is no longer detectable in the coamorphous system, suggesting that the carbonyl amide group could also be involved. At 1648 cm^{-1} [329], the benzoyl C=O stretching of MBZ exhibits broadening in the coamorphous spectrum, though the extent of its involvement remains uncertain.
Turning to NCM, the functional group clearly involved in interactions is the N-H, as its stretching bands at 3241 and 3110 cm^{-1} [241], still visible in the PM, completely disappear in the coamorphous spectrum. At 1651 cm^{-1} [242], the C=O stretching band shows broadening in the coamorphous spectrum, though its involvement in H-bonding is less clear. Additionally, the C-OH stretching band at 1192 cm^{-1} [242] appears in both spectra, suggesting no interaction with this group. In conclusion,

the N-H amide groups from both components and the MBZ amidic carbonyl appear to be involved in H-bonding.

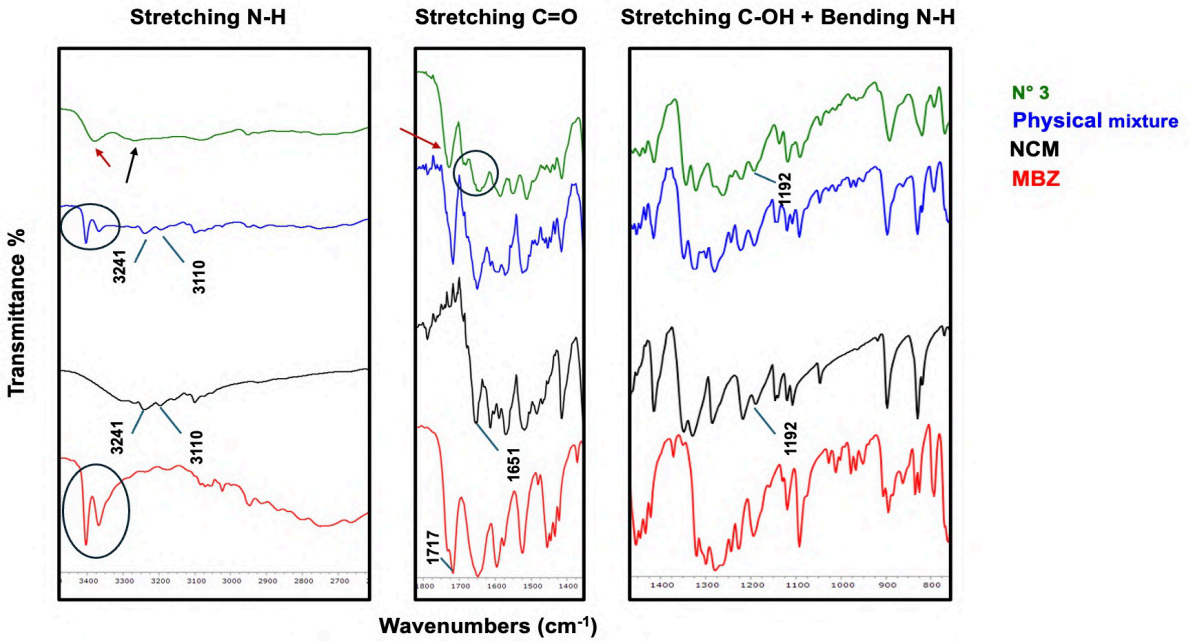

Figure 53. FT-IR spectra of NCM-MBZ 1:1 coamorphous (green) compared with its PM (blue) and pure components (black line represents NCM and red line MBZ).

Also, FT-IR of exp. N° 6 (i.e., binary PZQ-NCM 1:1) was useful to elucidate some possible interactions between the two components. The FTIR spectrum of the new coamorphous system exhibits the typical band broadening characteristic of amorphous materials, differently from the pure crystalline components and the PM. This broadening is particularly evident in the wavenumber region between 3241 and 3110 cm^{-1}, where the N-H stretching bands of NCM are located [241], making it difficult to clearly determine whether the donor group is involved in H-bonding. Additionally, the band at 1624 cm^{-1}, corresponding to the C=O stretching of PZQ [43,45,141,169], disappears in the coamorphous spectrum, confirming the involvement of the carbonyl group as a H-bond acceptor. Conversely, the C-OH stretching band of NCM at 1192 cm^{-1} [242] is still present in both the PM and the coamorphous spectra, suggesting that this group is not acting as a H-bond donor. The broadening observed in the coamorphous spectrum makes it difficult to definitively identify all the groups involved in H-bonding. However, a PZQ carbonyl group seems to be implicated as a H-bond acceptor. Figure 54 shows the FT-IR spectra described above.

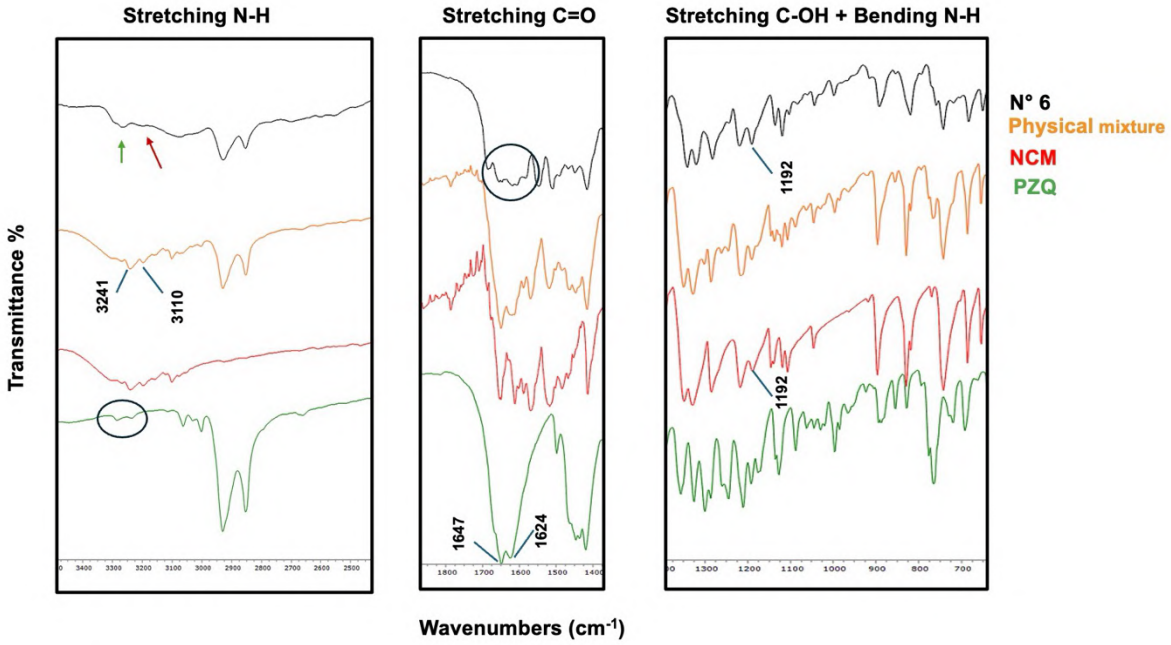

Figure 54. FT-IR spectra of PZQ-NCM 1:1 coamorphous (black) compared with its PM (orange) and pure components (green line represents PZQ and red line NCM).

FT-IR of exp. N° 9 (binary PZQ-MBZ 1:1) are reported in Figure 55. By comparing the FT-IR spectra of the new coamorphous system, its PM, and the individual components, it can be hypothesized the presence of solid-state interactions. In the region related to PZQ carbonyl stretching vibrations, the coamorphous merges into a single broad and shifted carbonyl band at 1641 cm^{-1}, compared to the double peak at 1647 and 1624 cm^{-1} observed for anhydrous PZQ [43,45,141,169]. PZQ bands are still visible in the PM, confirming that no interactions involving these functional groups occur in the simple mixture. Regarding MBZ, the sharp N-H amide stretching band at 3404 cm^{-1} [329], which is still prominent in the PM, is absent in the coamorphous system. This could indicate that the N-H amide group participates in H-bonding. Additionally, the band at 1278 cm^{-1}, associated with the C-N stretch of the imidazole [329], shows significant broadening in the coamorphous spectrum, suggesting its involvement in interactions. In contrast, no such broadening is observed in the simple PM.

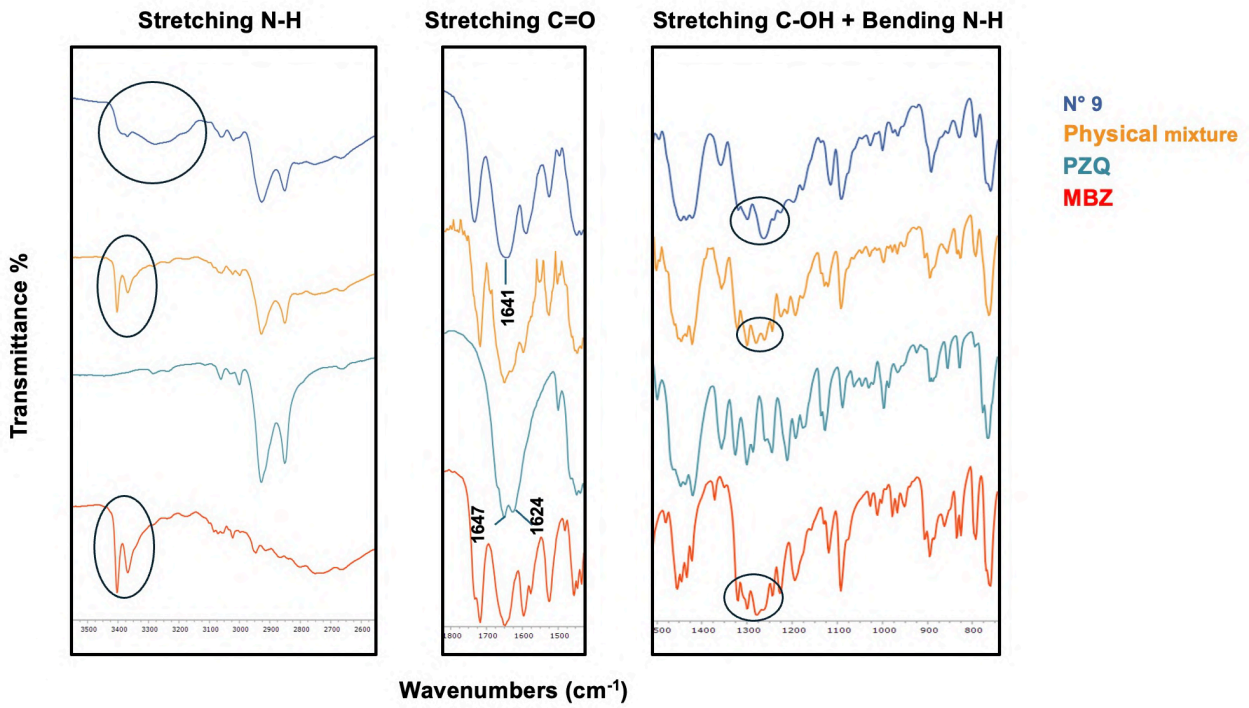

Figure 55. FT-IR spectra of PZQ-MBZ 1:1 coamorphous (blue) compared with its PM (orange) and pure components (light blue line represents PZQ and red line MBZ).

Figure 56 reports FT-IR spectra for ternary PZQ-NCM-MBZ 1:1:1 coamorphous, the corresponding PM and the three APIs. The FT-IR spectra reveal several informative bands. Considering MBZ, the sharp N-H stretching band at 3404 cm^{-1} [329] completely disappears in the coamorphous spectrum, indicating the involvement of a H-bond. The C-N stretching band at 1278 cm^{-1} [329] shows significant broadening in the ternary system, reflecting its amorphous nature, while the C=O stretching band, originally at 1717 cm^{-1} [329], is absent, confirming the involvement in the interactions. On the contrary, the C=O stretching band at 1647 cm^{-1} [329] remains visible, suggesting that this group is not involved in the interactions. Regarding NCM, the N-H stretching and bending at 3241 and 3195 cm^{-1} and 897 cm^{-1} [241], respectively, disappear in the ternary system spectrum, indicating their involvement in H-bonding. The C=O stretching band at 1651 cm^{-1} is significantly broadened but still present, while the C-OH stretching band at 1192 cm^{-1} is broadened and shifted, a behavior also observed in the PM spectrum, making it unclear whether this group participates in H-bonding. As for the C=O groups in PZQ, the carbonyl stretching band at 1624 cm^{-1} disappears in the coamorphous spectrum, indicating its definite involvement in H-bonding. In conclusion, the groups most certainly involved in H-bonding are the amide N-H and carbonyl groups of MBZ, the amide N-H of NCM, and the carbonyl group of PZQ.

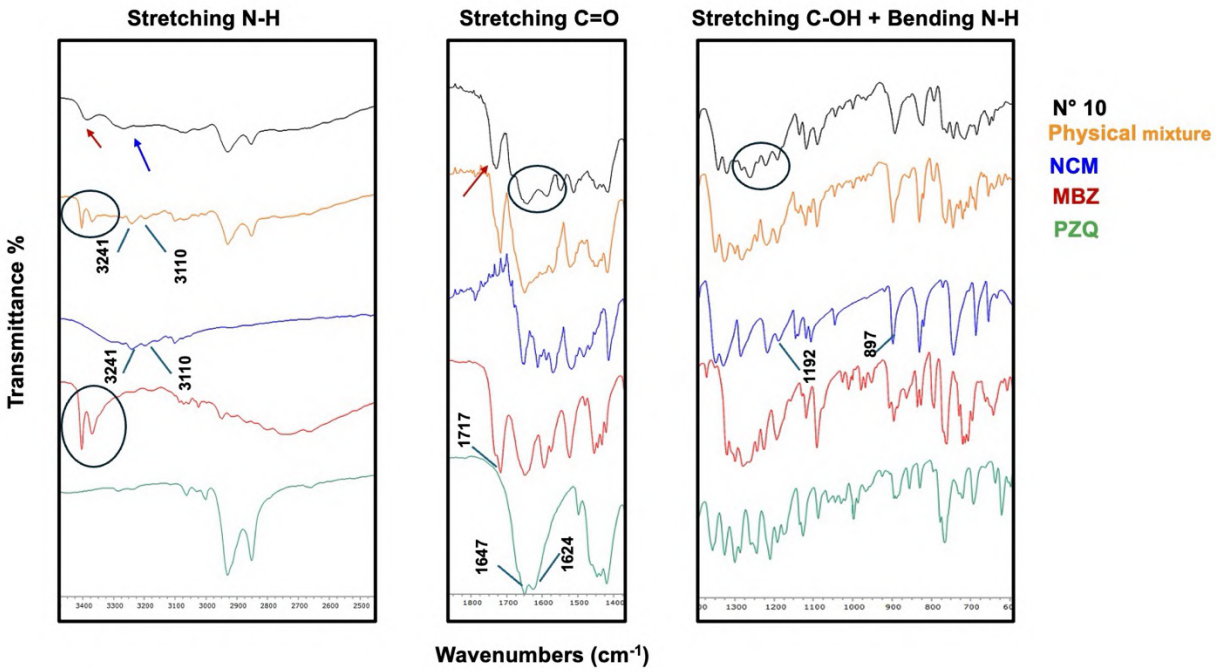

Figure 56. FT-IR spectra of PZQ-NCM-MBZ 1:1:1 coamorphous (black) compared with its PM (orange) and pure components (green line represents PZQ, blue line NCM and red line MBZ).

Given the complexity of FT-IR results of coamorphous systems—particularly the ternary ones—and the fact that the starting commercial form of MBZ is itself a mixture of two polymorphs [330] (as also confirmed by experimental DSC and PXRD analyses), the confirmation of the existence of homogeneous coamorphous systems was obtained through the evaluation of the T_g of the system, as it is one of the key features that distinguishes amorphous and coamorphous systems from crystalline materials. Particularly to coamorphous systems, which are homogeneous multicomponent systems, one would expect to observe a single T_g value. Therefore, experimentally determining the T_g and confirming a unique value for each of the ten mixtures could provide further evidence that homogeneous coamorphous systems were successfully obtained.

The experimental T_g values were primarily determined using conventional DSC analysis. However, in some cases where it was not possible to detect T_g through traditional DSC, MTDSC was employed. To provide a comparison of the experimental results, theoretical T_g values of the (binary or ternary) drug mixtures were also calculated using the Gordon-Taylor (G-T) equation reported in section 5.2.2.2.3 [313,314].

As for the individual APIs, T_g was determined experimentally by DSC (or MTDSC, in NCM case) and compared to theoretical T_g values. The experimental values, not in good agreement with the conventional Rule of 2/3 [333], were in satisfactory accordance with the predicted model proposed by Alzghoul and coauthors [188], unless for MBZ. The experimental T_g values of PZQ and MBZ were found to be consistent with those previously reported in literature [42,331], while T_g of NCM

was experimentally determined for the first time. Table 12 summarizes experimental and calculated T_g values for the ten mixtures and the three pure APIs.

Table 12. Experimental T_g values compared to theoretical ones according to G-T equation.

Sample / Exp. N°	Molar ratio			Experimental T_g (°C) ± S.D.	Theoretical T_g according to G-T equation (°C)
	PZQ	NCM	MBZ		
PZQ	1	0	0	40.94* ± 0.90	28.56§
NCM	0	1	0	82.90* ± 0.64	85.47§
MBZ	0	0	1	111.98 ± 0.73	142.95§
1	0.500	0.250	0.250	/	63.54
2	0.167	0.417	0.417	/	84.17
3	0	0.500	0.500	98.33 ± 0.34	96.95
4	0.250	0.500	0.250	79.54 ± 0.59	75.40
5	0.417	0.167	0.417	74.02 ± 0.59	71.02
6	0.500	0	0.500	69.31 ± 0.87	68.67
7	0.250	0.250	0.500	83.31 ± 0.76	81.58
8	0.417	0.417	0.167	60.40 ± 0.13	65.40
9	0.500	0.500	0	59.15 ± 0.95	57.87
10	0.333	0.333	0.333	76.77 ± 0.09	73.15

*MTDSC; §Single compound, not applicable to calculate a theoretical T_g according to G-T equation; T_g was predicted through the model proposed by Alzghoul et al. [188].

As highlighted in this table, the experimental T_g values of the mixtures obtained via DSC were generally in good agreement with the theoretical values calculated using the G-T equation. The similarity between the experimental T_g and the theoretical T_g values indicated that there might be not strong molecular interactions between the drugs [307]. In these mixtures, slight positive deviations were observed, generally indicating a slightly higher rigidity of the vitreous state, as also confirmed by FT-IR analyses, which remain to be verified by stability studies [332–334].

However, experimental analyses (i.e. DSC and MTDSC) were unable to clearly determine the T_g in two out of the thirteen systems investigated. This issue could be attributed to several reasons: the known difficulty in detecting T_g in some amorphous formulations prepared by grinding, as these systems occasionally fail to produce a distinct T_g signal, possibly due to incomplete amorphization or other physical disruptions introduced during the grinding process [318,335], or simply to the fact that these two systems are not coamorphous systems.

In the remaining eight cases, a single T_g value was observed, demonstrating that these were homogeneous multicomponent systems. The presence of a unique T_g is a key indicator that the components are well-integrated at the molecular level, supporting the conclusion that true coamorphous systems were formed rather than simple PMs of individual amorphous substances.

The experimental and computed T_g values provided useful insights into the expected stability of the coamorphous systems. Stability is a critical factor for the practical application of coamorphous materials, particularly because of their inherent tendency to revert to a crystalline state over time or under certain environmental conditions [46,316,318]. It is widely reported in literature that amorphous and coamorphous systems are generally stable up to a temperature approximately 50 °C below their T_g, a principle often referred to as the " T_g – 50 °C" rule. According to this rule, molecular mobility within an amorphous solid becomes negligible 50 °C below its T_g, whereas temperatures exceeding this threshold can lead to significantly increased molecular mobility, which is sufficient to induce physical changes such as recrystallization or phase separation.

This "T_g – 50 °C" guideline serves as a practical tool for predicting the long-term stability of coamorphous systems, helping to ensure that their amorphous nature is maintained during storage and use [336–338]. As a result, coamorphous systems with a T_g above 75 °C are generally expected to remain stable under ambient conditions (or even at 40 if the T_g exceeds 90 °C). In contrast, systems with lower T_g values are more prone to recrystallization at room temperature and therefore require to be stored in a refrigerator or in a freezer to maintain their physical integrity.

To assess the physical stability of the coamorphous systems under different temperature conditions, selected samples (exp. N° 1, 3, 4, 6, 7, 9, 10) were stored at four distinct temperatures: -30 °C, 5 °C, 25 °C, and 40 °C, over a period of six months. The solid-state nature of these samples was closely monitored over time using PXRD, with analyses conducted on a weekly basis during the first month and then on a biweekly basis.

Figure 57 presents a summary of the results from this 6-month stability study. The findings largely aligned with the expectations regarding the physical stability of the coamorphous systems, as predicted by the "T_g – 50 °C" rule; only two out of seven systems partially deviated from these expectations. All systems remained stable in the freezer throughout the entire six-month period. Furthermore, one of the samples, specifically exp. N° 1, which corresponds to a ternary coamorphous formulation, for which the T_g could not be measured experimentally, considering the T_g – 50 °C rule and the calculated T_g (through G-T equation), demonstrated stability greater than expected. This led to conclude with good approximation that this was also a coamorphous system.

Exp N°	Experimental Tg (°C)	Expected temperature threeshold for stability (Tg-50°C)	Storage temperatures				Expectations about the physical stability
			-30°C	5°C	25°C	40°C	
1	63.54*	13.54	✓	✓	✓	✗	Fully Confirmed
3	98.33	48.33	✓	✓	⊗	⊗	Partially Confirmed
4	79.54	29.54	✓	✓	✓	✗	Fully Confirmed
6	69.31	19.31	✓	⊗	✗	✗	Partially Confirmed
7	83.31	33.31	✓	✓	✓	✗	Fully Confirmed
9	59.15	9.15	✓	✓	✗	✗	Fully Confirmed
10	76.77	26.77	✓	✓	✓	✗	Fully Confirmed

Figure 57. Physical stability of seven coamorphous systems after six months of storage at different temperatures. Full sticks indicate that sample meets expectations according to "T_g – 50 °C" rule. Full green ticks stand for "stable as expected according to "T_g – 50 °C" rule"; full red crosses stand for "unstable, as expected according to "T_g – 50 °C" rule"; empty green ticks stand for "stability superior to expectations"; empty red crosses stand for "stability inferior to expectations". * T_g value calculated from G-T equation.

Remaining in the context of physical stability, one of the most critical challenges associated with amorphous and coamorphous materials is their inherent hygroscopicity. These materials have a high tendency to absorb moisture from the environment due to their disordered molecular structure, which creates an increased surface area and more accessible sites for water interaction. The absorption of moisture can generate several negative consequences. Water molecules, once absorbed, can act as plasticizers, lowering the T_g and increasing molecular mobility within the material. This can lead to a destabilization of the amorphous or coamorphous matrix, weakening or completely disrupting the intricate molecular interactions that maintain the material in its high-energy state. Such destabilization brings to unwanted phenomena, like phase separation, loss of cohesion in the coamorphous system, or most detrimentally, recrystallization or hydrates formation. These latter phenomena not only compromise the solubility and dissolution rate advantages of amorphous forms but also risk reducing bioavailability [315,316]. Therefore, understanding and meticulously controlling hygroscopicity is crucial to preserving the physical stability of amorphous and coamorphous powders over time. To assess the effects of RH on the obtained coamorphous systems, selected samples (i.e., N° 3, 6, 9, and 10) were subjected to a gradual RH increase from 0% to 90% at a constant temperature of 25 °C. Figure 58 provides a summary of the sorption-desorption curves for all four coground systems investigated.

In each case a limited mass uptake can be noticed, not exceeding the 3% of the starting mass. It can be concluded hence that this maximum observed value neither is imputable to a recrystallization event, since after the cycle of desorption the mass corresponds to the starting one, nor to a bulk transformation such as a hydrate formation. In fact, considering the molecular weight of the three APIs and water, a hydrate formation would correspond to a mass gain percentage of about 15% for the binary and 9.6% for the ternary systems. Conversely, a mass uptake ranging about 3% is related to a superficial water adsorption, since amorphous phases demonstrates hygroscopic properties and they sorbs relatively more water as compared with crystalline solid phases [339].

The mass uptake of the four samples is between 1.8 and 2.8%, attesting an analogous behavior not depending on the composition. Moreover, measurable hysteresis (i.e., difference in water vapor uptake between sorption and desorption isotherms), are visible on the graph but they are not attributable to any recrystallization phenomena since, as explained above, the final mass after the cycle of desorption corresponds to the initial one.

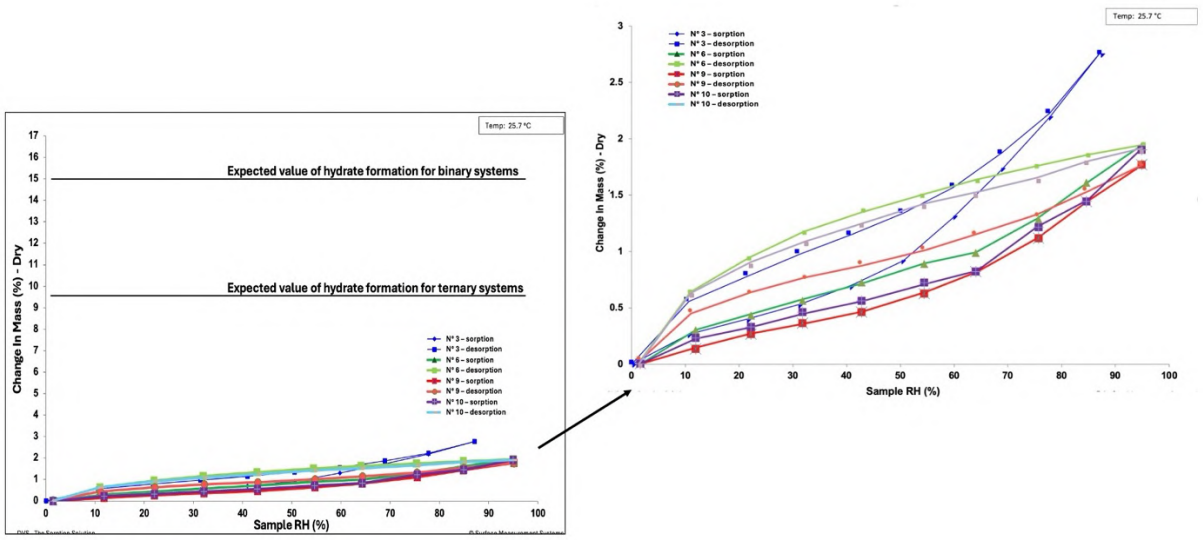

Figure 58. Sorption-desorption curves for exp. N° 3 (dark blue-light blue), 6 (dark green-light green), 9 (red-orange), and 10 (purple-grey).

Subsequently, drug recovery analyses were carried out on the same seven samples (i.e., exp. N° 1, 3, 4, 6, 7, 9, and 10) used in the physical stability study, focusing on those stored in the freezer at -30 °C and those exposed to stressed conditions at 40 °C (a total of fourteen samples).

The degradation tendency of PZQ under milling conditions is well-documented in literature [42,45,264]. While PZQ does not degrade when milled alone [43,142], binary ground mixtures have shown reduced PZQ recovery, along with the insurgence of specific degradation products depending on the excipient used [42,45,264]. To determine whether PZQ undergoes chemical degradation when co-ground with NCM and/or MBZ under NG conditions, spectrometric evaluations were conducted.

The recorded ^{1}H-NMR spectra revealed signs of PZQ degradation in only one out of fourteen samples (exp. N° 6), likely due to the fact that this sample was stored under stressed conditions at 40 °C. Encouragingly, all other thirteen samples, including those stored at 40 °C, showed only the presence of the starting materials—PZQ, NCM, and/or MBZ—indicating the absence of chemical changes after mechanochemical treatment under all experimental conditions. Figures C12-C25 in the Appendix report all the recorded ^{1}H-NMR spectra.

The final phase of this experimental work involved clarifying the recrystallization phenomena observed in the newly developed systems.

Recrystallization of coamorphous systems can lead to different outcomes, depending on the nature of the components and their interactions. In some cases, recrystallization may result in the separation of the initial phases, where each component reverts to its crystalline form independently. Alternatively, recrystallization can lead to the formation of a new entity that corresponds to the coamorphous system but in a crystalline form, known as cocrystal. This transformation into a cocrystal indicates that the components have not only maintained their interactions but have rearranged into a well-defined crystalline lattice, preserving the combined properties of the coamorphous phase while gaining the stability of a crystalline structure [340–342].

Here, we present two examples of recrystallization pathways, noticed during stability studies: one illustrating the recrystallization of a coamorphous system into its individual components, and the other showcasing its transformation into a new cocrystal. In some cases, to gain a deeper understanding of the solid forms obtained after recrystallization, SEM images of both the fresh and recrystallized products were acquired and combined with PXRD analyses (see Figure C26 in the Appendix as an example).

The first example of recrystallization is that observed in exp. N° 6, which corresponds to the binary PZQ-MBZ 1:1 coamorphous system. As shown in Figure 59, which presents the PXRD data of the fresh and recrystallized products, the recrystallization process leads to the phase separation of the original components, PZQ and MBZ. In fact, the PXRD patterns clearly show distinct peaks corresponding to the separate crystalline forms of PZQ and MBZ (as a mixture of Polymorphs A and C).

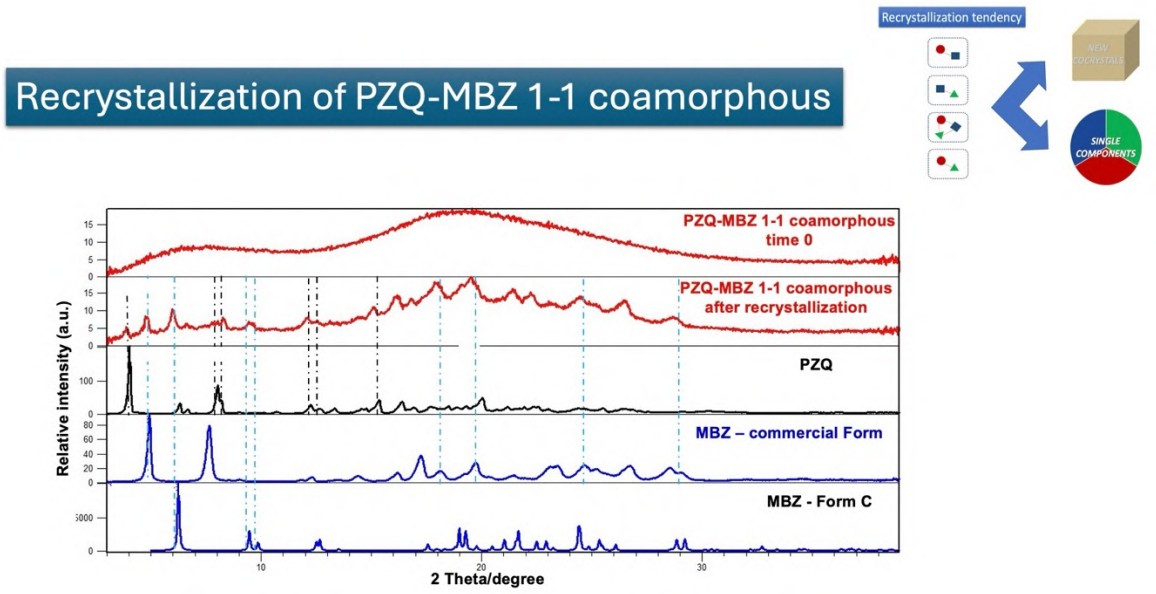

Figure 59. Cartoon depicting the recrystallization of binary PZQ-MBZ 1:1 coamorphous into individual components through PXRD analyses. Black dotted lines represent PZQ peaks, while light blue dotted lines MBZ reflections.

The second example is exp. N° 9, which involves the binary PZQ-NCM 1:1 coamorphous system. In this instance, recrystallization did not result in the formation of individual crystalline materials. Instead, it led to the creation of a "new" entity that, through detailed analysis, was identified as the previously reported PZQ-NCM 1:3 anhydrous cocrystal (described in the first section of the thesis) [206].

What is particularly intriguing about this coamorphous system is its unique behavior during recrystallization. Specifically, the PZQ-NCM 1:1 coamorphous system transforms into a combination of the well-known polymorph C of PZQ and PZQ-NCM 1:3 anhydrous cocrystal (Figure 60). This indicates a significant change in the stoichiometry between the two components, suggesting that the coamorphous state can influence the pathways of crystallization in unexpected ways.

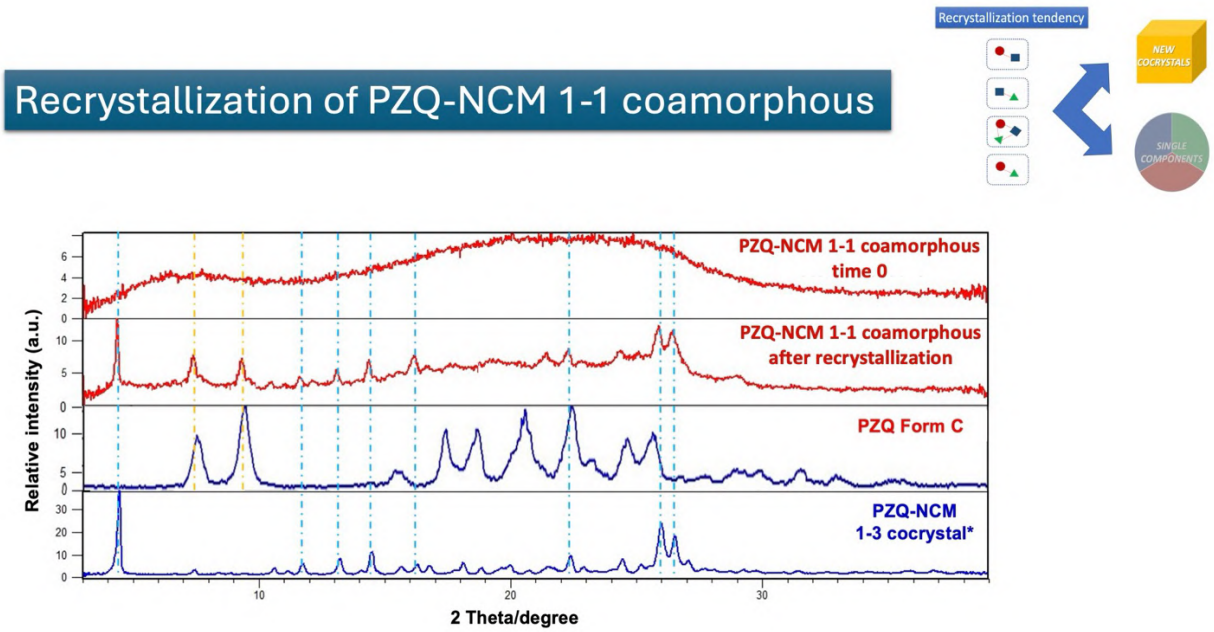

Figure 60. Cartoon depicting the recrystallization of binary PZQ-NCM 1:1 coamorphous into polymorph C of PZQ and the PZQ-NCM 1:3 anhydrous cocrystal. Yellow dotted lines represent PZQ polymorph C reflections, while light blue dotted lines PZQ-NCM 1:3 anhydrous cocrystal reflections.

However, recrystallization phenomena are inherently slow processes, and understanding them, particularly in ternary coground systems, can often be challenging and not immediately straightforward. Due to the complexity of these systems and the gradual nature of recrystallization, this aspect of the research is still in progress and continues to expand.

5.4 Conclusions

In this section, the possibility of preparing coamorphous systems composed exclusively of APIs, specifically PZQ, NCM, and MBZ, is presented.

The coamorphous systems were prepared via a one-step, solvent-free process—NG—using a lab-scale vibrational mill. The process proved to be reproducible, requiring only 4h of grinding to achieve the coamorphous state. All systems were characterized by PXRD and, in some cases, FTIR analysis, and compared against the starting components and their corresponding PMs to confirm the absence of crystalline domains in the samples. T_g temperatures of the coamorphous systems were experimentally determined using DSC and compared to theoretical T_g values calculated via the Gordon-Taylor equation. Despite the complex DSC curves, particularly for ternary coamorphous, the presence of a single T_g in each case confirmed the formation of a homogeneous multicomponent system.

Stability studies were conducted on seven systems (three binary and four ternary coground samples) for six months under four different temperature conditions (-30 °C, 5 °C, 25 °C, and 40 °C), based on the "T_g – 50 °C" stability rule. The results largely aligned with expectations for physical stability, with only two deviations out of the seven systems. All systems remained stable when stored in the freezer for the entire six-month period, and one ternary coamorphous formulation exhibited a higher stability temperature than anticipated.

Regarding the influence of RH, DVS results indicated that water had minimal impact on the new solid phases. Only superficial sorption was observed, with no signs of recrystallization triggered by humidity.

Recrystallization pathways were also investigated to better understand the potential outcomes of this process. Depending on the molecular interactions within the system, recrystallization led either to the separation of the initial components into their crystalline forms or to the formation of a new entity, such as a cocrystal previously described in the thesis.

Future directions of this work will focus on a deeper examination of the recrystallization phenomena, which are slow processes, particularly in ternary systems. Additionally, the biopharmaceutical properties of these promising drug-drug coamorphous systems—such as solubility, dissolution, permeability, and their anthelmintic activity—will be investigated to further evaluate their therapeutic potential.

6. Five new Niclosamide Solvates to Prevent the Formation of Insoluble Niclosamide Monohydrate

6.1 Abstract

NCM is a well-established anthelmintic drug that has recently gained attention for its therapeutic potential in a range of applications, leading to its repositioning in pharmaceutical research. Given its pronounced tendency to form solvates, this study investigates the solid-state behavior of anhydrous NCM Form A through a comprehensive crystal form screening using LAG and slurry-bridging experiments with 12 commonly used solvents, including acetic acid (AA), acetone (ACT), benzyl alcohol (BENZOH), methanol (MeOH), dimethyl sulfoxide (DMSO), 2-pyrrolidone (2-pyr), acetonitrile (ACN), ethanol (EtOH), ethyl acetate (EA), isopropanol (iPOH), 4-methyl tetrahydropyran (4-MTHP), and hexane (HXN). The experiments were conducted at different solid-to-solvent molar ratios (1:1, 1:2).

A comprehensive solid-state characterization analysis (PXRD, DSC, TGA, HSM, FT-IR, SSNMR AND ^{1}H-NMR analyses) of the NCM solvates was performed. No solvates were formed in the presence of ACN, EtOH, EA, iPOH, MeOH, 4-MTHP, or HXN. However, five new crystalline solvates were identified with the other solvents (DMSO, 2-pyr, AA, ACT, and BENZOH). These solvates were classified into two distinct subgroups based on their structural characteristics: stoichiometric solvates (NCM-DMSO, NCM-2-pyr) and non-stoichiometric/channel solvates (NCM-AA, NCM-ACT, NCM-BENZOH).

Importantly, all five solvates demonstrated excellent mechanical stability under compression (10 Tons for 3 min). A key finding was the remarkable stability of the newly discovered solvates, which resisted conversion to the undesirable NCM monohydrate form, even after 144h of humidity exposure. This is in stark contrast to anhydrous NCM Form A, which undergoes rapid transformation to the monohydrate within just a few hours under similar conditions.

A graphical abstract summarizing the experimental work of this PhD thesis section is reported in Figure 61.

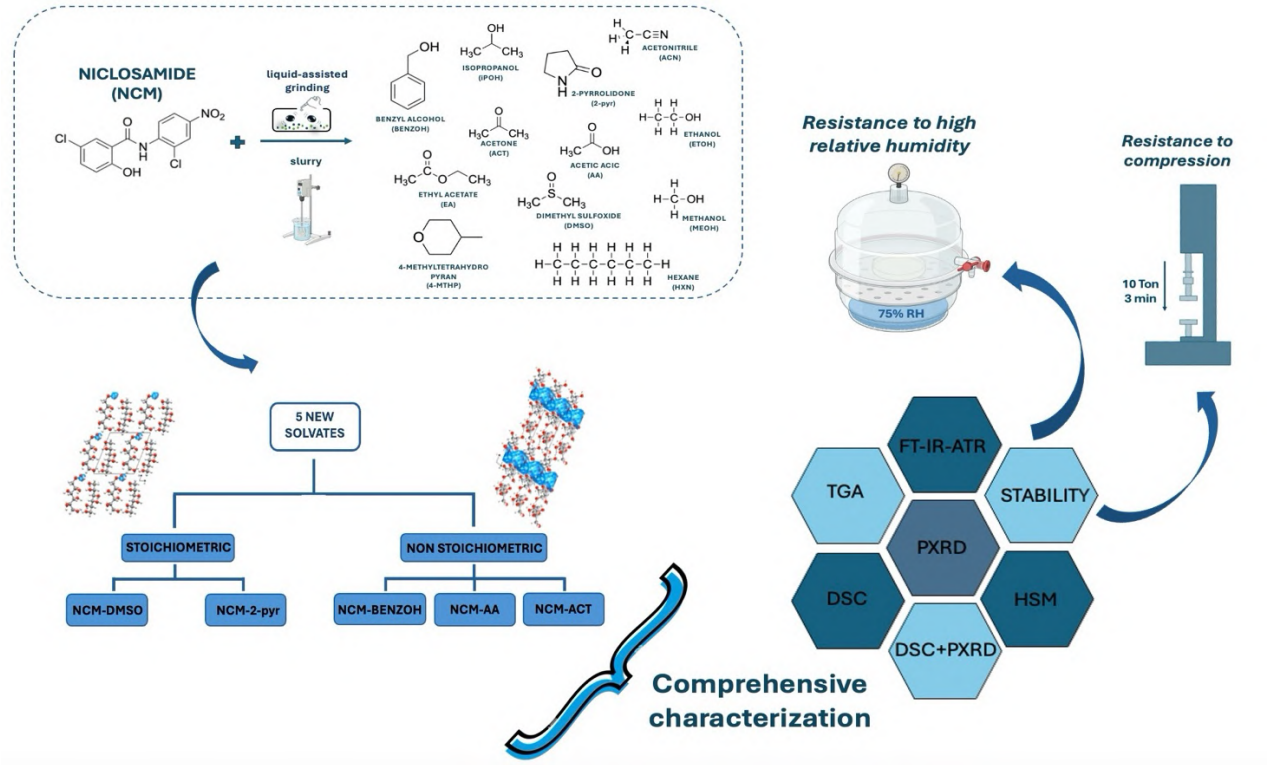

Figure 61. Graphical abstract depicting the new solid forms of NCM reported in this section.

6.2 Materials and Methods

6.2.1 Materials

NCM (5-chloro-N-(2-chloro-4-nitrophenyl)-2-hydroxybenzamide) was purchased from Sigma-Aldrich (St. Louis, USA) with a declared purity of 98-101%. AA and 4-MTHP were provided from Carlo Erba (Rodano-Milan, Italy), while HXN, MeOH, 2-pyr, DMSO and iPOH were purchased from Sigma-Aldrich (St. Louis, USA). EtOH was provided from Honeywell Riedel-de Haën (St. Louis, USA), ACN from Merck KGaA, (Darmstadt, Germania), EA from Normapur (Fontenay sous Bois, Francia), ACT from Galeno (Comeana, Prato, Italy) and BENZOH from A.C.E.F. s.p.a. (Fiorenzuola D'Arda, Italy). All the actives and chemicals were used without further purification.

6.2.2 Methods

6.2.2.1 Sample preparation

6.2.2.1.1 Mechanochemical synthesis

The mechanochemical synthesis of NCM solvates was performed in Retsch MM400 vibrational mill (Retsch, Germany) equipped by two 25 mL stainless steel jars and one 10 mm Ø bead, respectively. The milling frequency for each pathway was maintained at 25 Hz, the void volume in the jar was also kept constant (i.e., a total of 400 mg of powder per 25 mL jar) and the milling time was kept fixed (i.e., 60 min).
NCM was ground with 12 different solvents using two different NCM-solvent molar ratios, i.e., 1:1 and 1:2. Based on the results obtained with the above-mentioned stoichiometries, additional molar ratios (i.e., 1:0.5, 1:1.5, 1:3) were used in case of DMSO, 2-pyr, and BENZOH.

6.2.2.1.2 Slurry bridging experiments

For comparison, slurry experiments were conducted using the method outlined in a previous study [268]. Specifically, 300 mg of solid material (NCM) and 5 mL of each of the 12 selected solvents were added to 10 mL glass vials, which were then sealed with screw caps and parafilm. The suspensions were prepared in duplicate and continuously stirred at room temperature (20 °C) for 7 days. After this period, the excess solid phases were separated by vacuum filtration using paper filters and then analyzed by PXRD.

6.2.2.2 Characterization analyses

6.2.2.2.1 PXRD analysis

PXRD analysis was performed using a Bruker D2 Phaser benchtop diffractometer (Bruker, Manheim, Germany) operating in Bragg-Brentano geometry with Cu-Kα radiation (λ = 1.5418 Å) from a 300W low-power X-ray source (30 kV, 10 mA). Data were collected over a 2θ range of 3-40°, with a step size of 0.02° and a scan speed of 0.6°/s. Each sample was prepared by carefully pressing around 200 mg of the ground product into a steel sample holder fitted with a cylindrical PVDF reducer.

6.2.2.2.2 DSC analysis

For DSC analysis, samples weighing 2-4 mg were placed in 40 µL aluminum crucibles that were sealed and pierced. The analyses were performed using a Mettler Toledo DSC 3 Star System (Milan, Italy) with a heating rate of 10 °C/min from 30 to 250 °C, under a nitrogen atmosphere with a flow rate of 50 mL/min.

6.2.2.2.3 TGA analysis

TGA was carried out using a Mettler Toledo TGA TDA851 instrument (Milan, Italy). Approximately 5-12 mg of the powdered sample were placed in 100 µL platinum crucibles and subjected to a heating program from 30 to 250 °C at a rate of 10 °C/min, under a nitrogen atmosphere with a flow rate of 50 mL/min.

6.2.2.2.4 HSM analysis

A Reichert Biovar optical microscope with 10x magnification was used alongside a Mettler FP5 hot-stage microscope to visually monitor the sample during heating. Images were captured through the microscope integrated camera and viewed using Webcam Companion software. The heating conditions for the samples were the same used in DSC and TGA analyses.

6.2.2.2.5 (FT-IR)-ATR analysis

Infrared spectra using attenuated total reflectance ((FT-IR)-ATR) were acquired with a Shimadzu IRAffinity-1S FT-IR spectrometer (Kyoto, Japan). Measurements were conducted over a range of 400-4000 cm^{-1} with a resolution of 4 cm^{-1} and involved 20 scans.

6.2.2.2.6 SSNMR analysis

The ^{13}C CPMAS spectrum of NCM was acquired with a Bruker Avance II 400 Ultra Shield instrument, operating at 400.23 and 100.63 MHz, respectively for ^{1}H and ^{13}C nuclei. The powder samples were packed into cylindrical zirconia rotors with a 4 mm o.d. and a 80 µL volume. A certain amount of sample was collected from each batch and used without further preparations to fill the rotor. The ^{13}C CPMAS spectrum was collected at room temperature at a spinning speed of 12 kHz, using a ramp cross-polarization pulse sequence with a 90° ^{1}H pulse of 3.60 µs, a contact time of 3 ms, an acquisition time of 34.9 ms, an optimized recycle delay of 40 s and a number of scans of 95. A two-pulse phase modulation (TPPM) decoupling scheme was used, with a radiofrequency field of

69.4 kHz. The ^{13}C chemical shift scale was calibrated through the signal of γ-glycine (^{13}C methylenic peak at 43.7 ppm) as a secondary external standard.

The ^{13}C CPMAS spectrum of NCM-AA was acquired with a Jeol ECZR 600 instrument, operating at 600.17 and 150.91 MHz, respectively for ^{1}H and ^{13}C nuclei. The powder samples were packed into cylindrical zirconia rotors with a 3.2 mm o.d. and a 60 μL volume. A certain amount of sample was collected from each batch and used without further preparations to fill the rotor. The ^{13}C CPMAS spectrum was collected at room temperature at a spinning speed of 20 kHz, using a ramp cross-polarization pulse sequence with a 90° 1H pulse of 2 μs, a contact time of 3.5 ms, an acquisition time of 29.5 ms, optimized recycle delays of 79.2 s and a number of scans of 250. A two-pulse phase modulation (TPPM) decoupling scheme was used, with a radiofrequency field of 108.5 kHz. The ^{13}C chemical shift scale was calibrated through the methylenic signal of external standard adamantane (at 38.48 ppm with respect to tetramethylsilane, TMS).

6.2.2.2.7 ^{1}H-NMR analysis

^{1}H-NMR solution (acetone-d6) spectrum was acquired on a Jeol ECZR 600 instrument operating at 600.2 MHz. In the ^{1}H spectrum, to obtain quantitative information, it was necessary to employ a relaxation delay of 60 s. The number of scans acquired is 64.

6.2.2.2.8 Physical stability tests under several conditions

The solid-state stability of NCM solvates was assessed at room temperature (20 °C) by storing the sample in a desiccator with calcium chloride for 6 months. Periodic analyses and a final evaluation of the stored samples were conducted using PXRD, under the conditions specified in section 6.2.2.2.1. To test the impact of mechanical stress, NCM solvates were compressed at 10 Ton for 3 min. This test was important as solvates, especially non-stoichiometric ones, often exhibit low compression resistance [303], and NCM is predominantly available as oral tablets [30].

6.2.2.2.9 Resistance to conversion into NCM H_A under high RH %

To determine if NCM solvates could prevent the formation of insoluble NCM monohydrate, which typically forms within a month of exposure to ambient humidity [30,218,221–224], the stability of these multicomponent systems was evaluated under high RH conditions. Specifically, samples were stored in a sealed chamber containing a saturated aqueous NaCl solution, which maintains an RH of

75% at room temperature [285]. PXRD analysis was performed after 24, 48 and 144h of exposure to monitor any changes.

6.3 Results and Discussion

6.3.1 Screening of NCM solvates - Introduction

A crystal form screening of NCM was conducted by LAG and slurry-bridging experiments of pure anhydrous NCM Form A in the presence of 12 commonly used solvents in different solid-to-solvent molar ratios (1:1, 1:2). The screened solvents and the LAG and slurry outcomes (as evident from PXRD analyses) are reported in Table 13. Specifically, LAG with EtOH and EA, as well as slurry experiments with 4-MTHP, HXN and iPOH, led to the formation of anhydrous NCM Form A (CSD refcode HEBFUR). In contrast, slurry with EtOH and EA yielded polymorph B of NCM (CSD refcode HEBFUR01), while slurry with ACN and LAG with 4-MTHP, HXN and iPOH resulted in the formation of NCM monohydrate (NCM H_A, CSD refcode OBEQAN02) [30,218,221–224]. LAG and slurry with MeOH gave a mixture of the known NCM-MeOH 1-1 solvate previously reported in literature (CSD refcode GOJLIC) and NCM H_A. Notably, no solvated forms of NCM were observed with ACN, EtOH, EA, 4-MTHP, HXN, iPOH and MeOH. As a result, the PXRD patterns for these experiments have been included in the supplementary materials (Figures D1-D7 in Appendix D).
Conversely, 5 crystalline solvates were obtained from DMSO, 2-pyr, AA, ACT, and BENZOH, which were labeled as NCM-DMSO, NCM-2-pyr, NCM-AA, NCM-ACT and NCM-BENZOH, respectively. Their PXRD patterns are depicted in Figures 62, 67 and 71.
PXRD suggested that the formation of the new phases was complete, since no evidence of the starting materials was found.
The five new crystalline forms were subsequently divided into two subgroups based on the results of various characterization analyses:

- The first subgroup is composed of NCM-DMSO and NCM-2-pyr, which have been shown to be two stoichiometric solvates.
- The second subgroup includes non-stoichiometric (channel) solvates: NCM-AA, NCM-BENZOH, and NCM-ACT.

Table 13. 12 screened solvent and observed NCM solid forms via LAG and slurry in the presence of each liquid additive (bold characters indicate unreported solvates)

Solvent	Outcomes	
	LAG	**Slurry-bridging**
ACN	NCM-ACN monosolvate (CSD refcode KUKROZ [221])*	NCM H_A
EtOH	NCM Form A	NCM Form B
EA	NCM Form A	NCM Form B
4-MTHP	NCM H_A	NCM Form A
HXN	NCM H_A	NCM Form A
iPOH	NCM H_A	NCM Form A
MeOH	NCM-MeOH monosolvate (CSD refcode GOJLIC [230]) + NCM H_A	NCM-MeOH monosolvate (CSD refcode GOJLIC [230]) + NCM H_A
DMSO	NCM-DMSO monosolvate (CSD refcode WOXVIS [232])	NCM-DMSO monosolvate
2-pyr	**NCM-2-pyr**	**NCM-2-pyr**
AA	**NCM-AA**	NCM Form A
ACT	**NCM-ACT**	NCM Form A
BENZOH	**NCM-BENZOH**	**NCM-BENZOH**

*Not further investigated because mixture of phases (i.e., KUKROZ + isostructural solvate)(Figure D1 in the Appendix)

6.3.1.1 NCM-DMSO and NCM-2-pyr solvates

The use of DMSO and 2-pyr as solvents upon grinding led to the formation of two stoichiometric solvates. Slurry experiments of NCM Form A suspended in DMSO and 2-pyr gave origin to the same solvates. The formation process of both solvates was reproducible, both through mechanochemistry and slurry methods. The NCM-DMSO solvate corresponded to that recently reported by Kuri and colleagues [232], whose structure was deposited with refcode WOXVIS in the CSD. As for the NCM-2-pyr solvate, it was entirely new in the scientific literature and its structure has not yet been solved.

Figure 62 presents the patterns of the NCM-DMSO and NCM-2-pyr solvates in comparison to commercial NCM Form A, polymorph B, and NCM H_A. The distinct differences between these two new patterns and the reference compounds confirm the formation of novel solid forms of NCM.

The NCM-DMSO pattern is characterized by four intense peaks at approximately 9.3°, 15.3°, 25.2°, and 27.5° 2θ (the same recently observed by Kuri et al. [232]), while the NCM-2-pyr pattern exhibits a prominent peak around 25.9° 2θ. Both patterns suggest a high yield of the synthesis process, since no evidence of the starting materials was found.

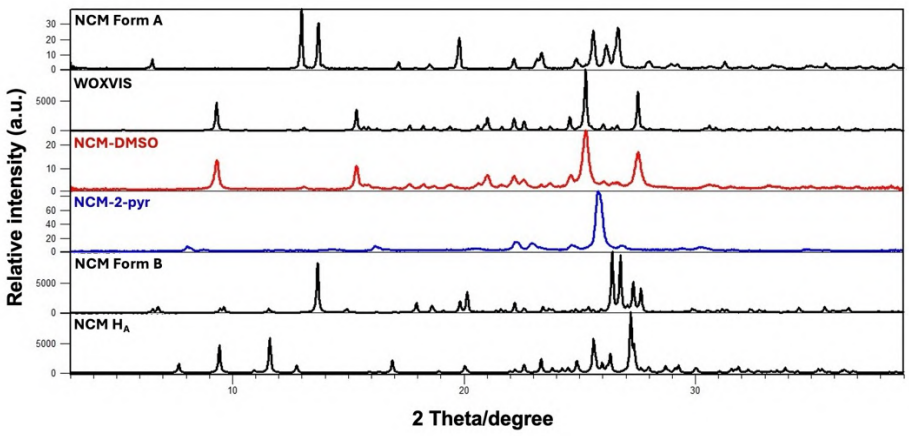

Figure 62. PXRD of NCM Form A, NCM Form B and NCM H_A (black) and WOXVIS [232] (black) and the new phases NCM-DMSO (red), NCM-2-pyr (blue).

Figures 63 and 64 show the DSC and TGA curves of NCM-DMSO (red) and NCM-2-pyr (blue), respectively.

The thermogram of NCM-DMSO displays two bands: the first is a high-temperature endothermic desolvation band, peaking at 171.62 °C with an enthalpy of 87.04 J/g; the second is an endothermic band with a peak at 229.73 °C and enthalpy of 108.21 J/g, corresponding to the melting of anhydrous NCM. The narrow and elongated shape of the desolvation endotherm is typical of stoichiometric solvates with isolated sites [226]. The same DSC result was also reported by Kuri and coauthors

[232]. PXRD analysis of the material retrieved after heating up to crystal desolvation (185 °C) revealed the presence of Form A, with a small amount of NCM-DMSO solvate, as indicated by a minor signal at around 9.3° 2θ (brown pattern in Figure D8 in the Appendix). In agreement with that, HSM analysis showed at approximately 190 °C the crystal desolvation, which was followed by the melting of anhydrous NCM form A around 230 °C. TGA curve (Figure 64a) shows a single event between 125 °C and 175 °C (consistent with the DSC observations), corresponding to a weight loss of 18.75% of the initial mass. This percentage aligns with the NCM-DMSO monosolvate.

As for NCM-2-pyr, the DSC curve shows a broad and shallow endothermic event ending around 175 °C (not integrated in the graph) and an additional endothermic band with a peak at 200.97 °C and an enthalpy of 113.57 J/g. This band, as confirmed by subsequent analyses, corresponds to both the desolvation process and the concurrent collapse of the solid structure. At the HSM, NCM-2-pyr desolvation occurred at the same temperature as the endothermic peak observed in the DSC curve, after which the solid structure collapsed, forming a fully liquid phase without then recrystallizing. TGA curve, depicted in Figure 64b, reveals two distinct events: the first between 105 °C and 145 °C, corresponding to a weight loss of 15.66% of the initial mass, which is consistent with a stoichiometric ratio of NCM-2-pyr of 1:0.7; the second between 170 °C and 210 °C, showing a weight loss of 17.25%, compatible with a stoichiometric ratio of 1:1. Thus, the stoichiometry of NCM-2-pyr appears to be higher than that of NCM-DMSO, likely in the range of 1:1.7 or 1:2. This finding is not surprising, considering that 2-pyr is known to form solvates with stoichiometries exceeding the equimolar ratio; for instance, it is reported to form a sesquisolvate with theophylline, with a drug-solvent stoichiometric ratio of about 1:1.6 [18]. Indeed, the DSC curve of theophylline sesquisolvate shows similarities to that of NCM-2-pyr, particularly in the shape of the broad desolvation endotherm anticipating the crystal lattice collapse. PXRD analyses of the solid remaining after desolvation was in complete agreement with DSC results (Figure D9 in the Appendix). Two different heating processes were conducted (up to 185 °C and 225 °C), as TGA revealed two distinct weight loss steps. In both cases, the NCM-2-pyr solvate persisted, with an increase in the amorphous content with respect to the freshly prepared solvate, as expected. These analyses confirmed that, differently from previous NCM-DMSO solvates, NCM-2-pyr does not recrystallize upon heating in NCM form A.

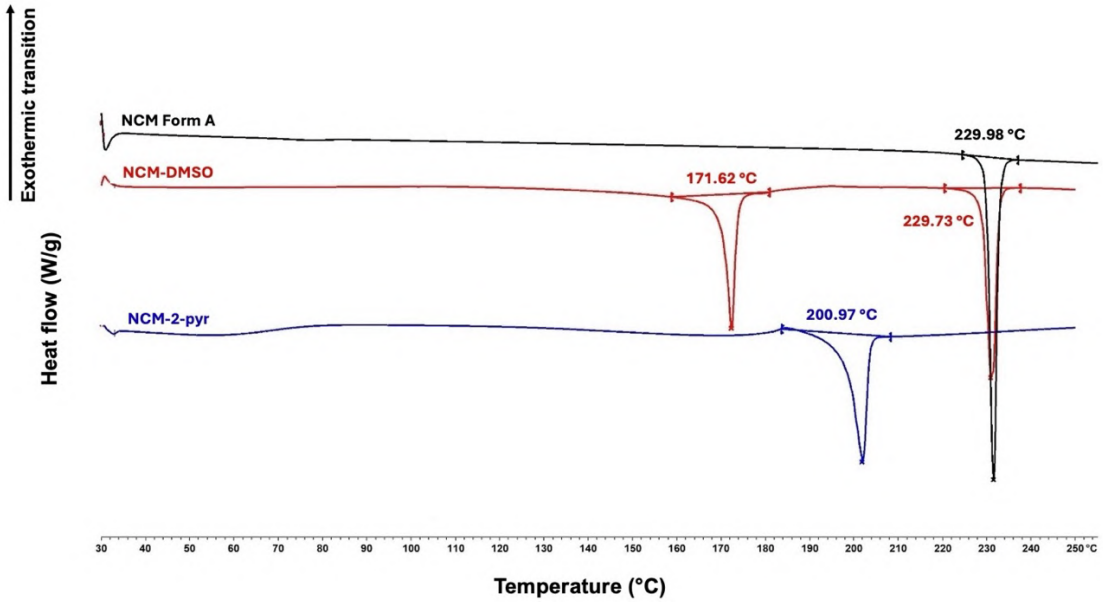

Figure 63. DSC curves of NCM Form A (black) and the new phases NCM-DMSO (red), NCM-2-pyr (blue)

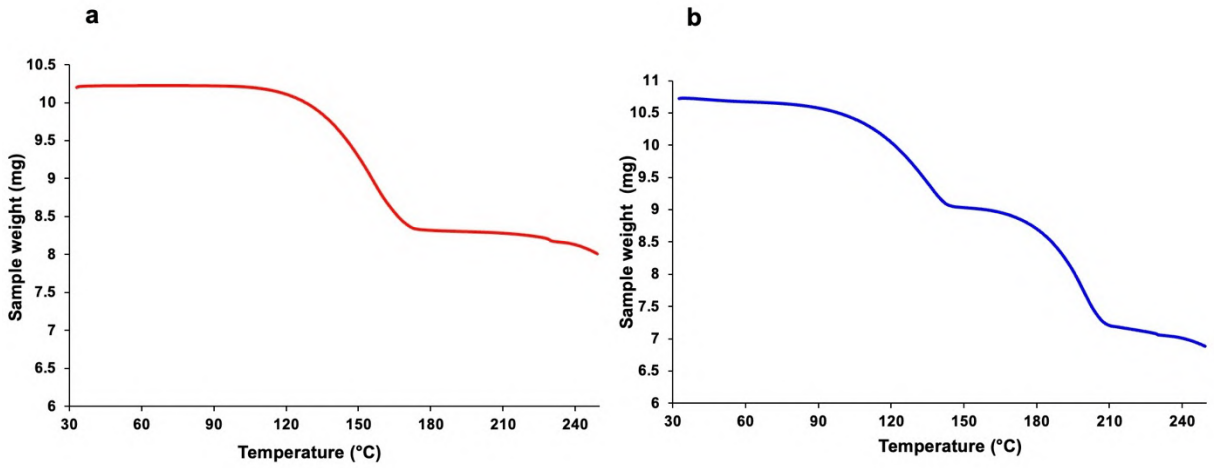

Figure 64. TGA curves of NCM-DMSO solvate (a) and NCM-2-pyr solvate (b).

The (FT-IR)-ATR spectra of the NCM-DMSO and NCM-2-pyr solvates, shown in Figures 65 and 66, are entirely different from that of anhydrous NCM Form A, confirming the formation of two new solid forms of NCM.

A detailed comparison between the spectrum of the NCM-DMSO solvate and that of anhydrous NCM Form A (Figure 65) revealed several key differences that indicate the involvement of the NCM molecule in interactions with DMSO:

- The absence of the doublet at 3576 cm^{-1} and 3491 cm^{-1}, which corresponds to -OH stretching in the spectrum of anhydrous NCM [343], along with a slight shift of the C-OH stretching band from 1192 cm^{-1} [242] to 1188 cm^{-1}, confirmed that the -OH group of NCM was involved in the interaction with DMSO.

- The amine -NH group of NCM appeared involved in the interaction, as both the stretching (3237.8 cm^{-1} and 3194.4 cm^{-1} [241]) and bending (897 cm^{-1} [241]) vibration bands result slightly shifted to higher wavenumbers.
- The C=O stretching band of NCM at 1651 cm^{-1} [242] was missing in the NCM-DMSO spectrum, while the C=O bending band showed a slight shift from 1217 cm^{-1} [242] to 1225 cm^{-1}, suggesting that the C=O group of NCM might also be involved in some interactions.
- The characteristic DMSO peaks in the 1100-900 cm^{-1} range [344] were shifted to lower wavenumbers (1000-900 cm^{-1}) in the solvate, indicating that DMSO was likely participating in the interactions.
- The fingerprint region of the NCM-DMSO solvate, below 1500 cm^{-1}, differed significantly from that of anhydrous NCM, further confirming the formation of a new solid phase.

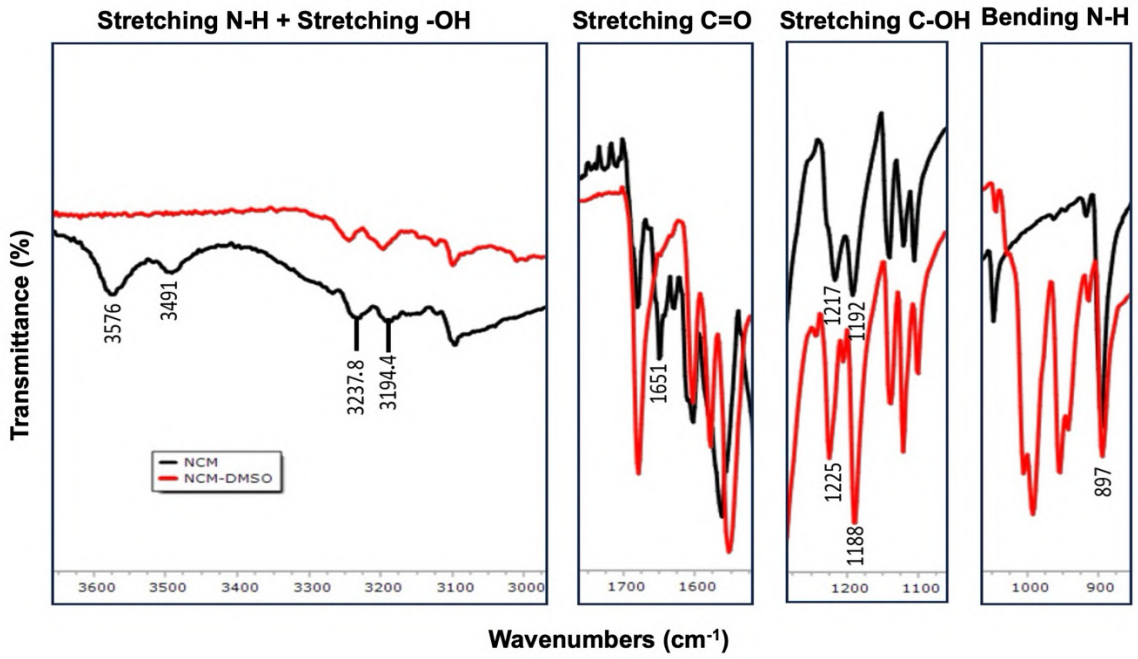

Figure 65. FT-IR spectra of NCM Form A (black) and the new phase NCM-DMSO (red).

Figure 66 compares the spectrum of the NCM-2-pyr solvate with that of anhydrous NCM Form A, helping to identify the functional groups of the NCM molecule involved in interactions with 2-pyr. The analysis revealed the following:

- The absence of the doublet at 3576 cm^{-1} and 3491 cm^{-1}, associated with -OH stretching [343] in the (FT-IR)-ATR spectrum of NCM, suggested that the -OH hydroxyl group of NCM is involved in the interaction with 2-pyr.
- The amine -NH group of NCM also seemed to participate in the interaction, as the bands corresponding to both stretching (3237.8 cm^{-1} and 3194.4 cm^{-1} [60]) and bending (897 cm^{-1}

[60]) bands were shifted in the NCM-2-pyr spectrum to 3257 cm^{-1}, 3214 cm^{-1}, and 890 cm^{-1}, respectively.

- Significant differences in the 1700-1200 cm^{-1} region, which corresponds to C=O stretching and bending in NCM [62], further suggested that these functional groups were also involved in the interactions within the NCM-2-pyr solvate.
- Additionally, the fingerprint region of the NCM-2-pyr solvate, below 1500 cm^{-1}, showed a distinct pattern compared to anhydrous NCM, confirming the formation of a new species.

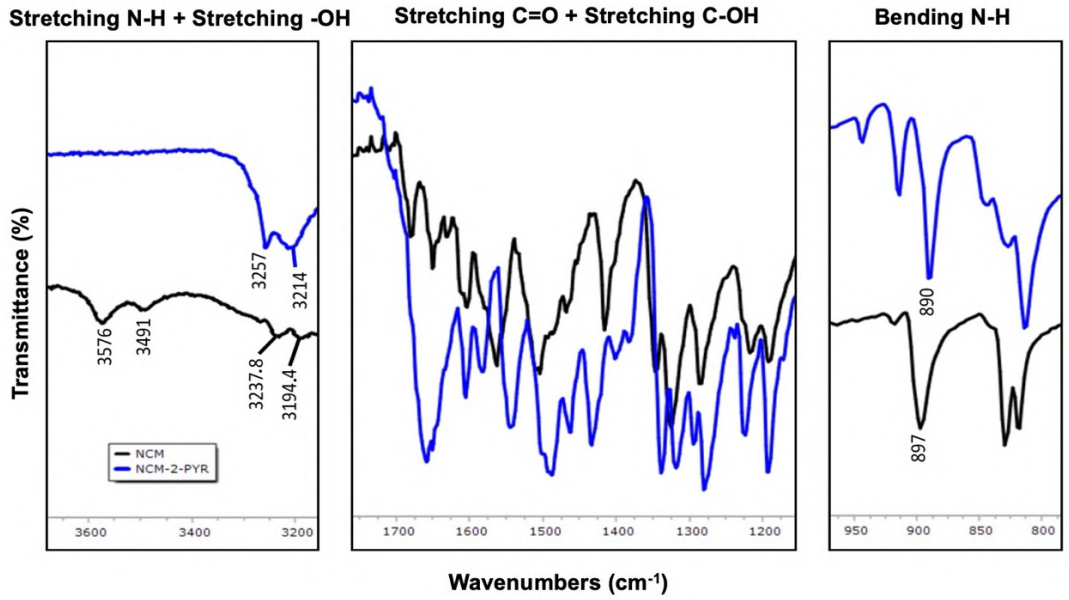

Figure 66. FT-IR spectra of NCM Form A (black) and the new phase NCM-2-pyr (blue).

6.3.1.2 NCM-AA, NCM-BENZOH and NCM-ACT solvates

Using AA, BENZOH, and ACT as solvents gave rise to the formation of non-stoichiometric solvates, presumably isostructural with each other. These solvates were obtained via mechanochemistry, or by slurry only in the case of BENZOH. In non-stoichiometric solvates, solvent molecules occupy channels or void spaces within the crystal, unlike the isolated site positioning observed in stoichiometric solvates. The formation of this type of solvates is supported by the tendency of NCM molecules to adopt a planar arrangement within the crystals, creating voids between the planes [30]. Thus, it is unsurprising that NCM tends to form such non-stoichiometric solvates, as recently noted by Mann and colleagues [251].

The variation in solvent content in these non-stoichiometric solvates is attributable to the solid capability to absorb or release solvent molecules based on the temperature and pressure conditions during synthesis and storage. Typically, if a solid can form channel solvates with one solvent, it is

also capable of forming such solvates with water or other solvents [191]. This is evident in the solvates formed by NCM with AA, BENZOH, and ACT, which show low reproducibility (described as "seasonal") and can be obtained by grinding with all three solvents, or by slurry only with BENZOH. In addition, a preliminary SSNMR analysis performed on the NCM-AA solvate further confirmed the low stability of this class of solvates. Specifically, a comparison between the CPMAS spectra of pure NCM and NCM-AA (shown in black and green in Figure 67, respectively) reveals that the spectrum of NCM-AA lacks any signal corresponding to AA (whose CH_3-related signal would be expected around 20 ppm). Moreover, Figure 67 highlights the presence of a significant amount of unreacted pure NCM (clearly visible in the peaks marked with black arrows) and the presence of an additional phase (indicated by red arrows).

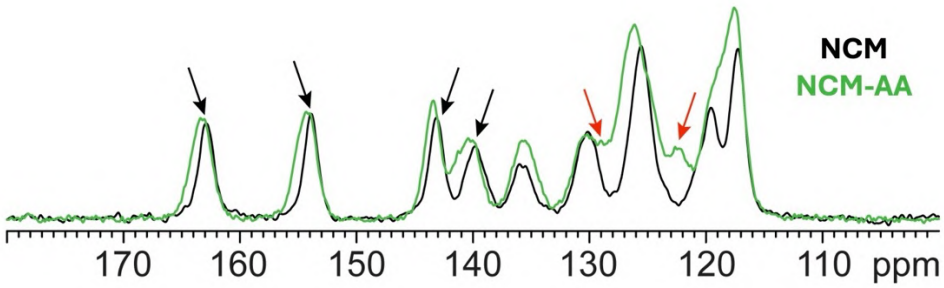

Figure 67. Comparison between the ^{13}C (100.63 MHz) CPMAS spectrum of NCM (black), acquired at a spinning speed of 12 kHz, and the ^{13}C (150.91 MHz) CPMAS spectrum of NCM-AA (green), acquired at room temperature at a spinning speed of 20 kHz.

As a validation step, the ^{1}H spectrum of NCM-AA was recorded as well (Figure 68). A signal attributed to AA was observed at 2.0 ppm. This signal (marked in blue in Figure 68) was integrated and compared to the signal at 8.42 ppm, corresponding to an aromatic CH group of NCM (marked in orange). This analysis yielded an NCM-AA ratio of 1:0.08, whereas TGA results (reported below in Section x) indicate a stoichiometric ratio of 1:0.25. To further evaluate stability of this solid form, the ^{1}H spectrum of NCM-AA was recorded again after approximately one week. Integration of the same signals revealed an NCM-AA ratio of 1:0.06, indicating that NCM-AA solvate is unstable and that AA content is non-stoichiometric.

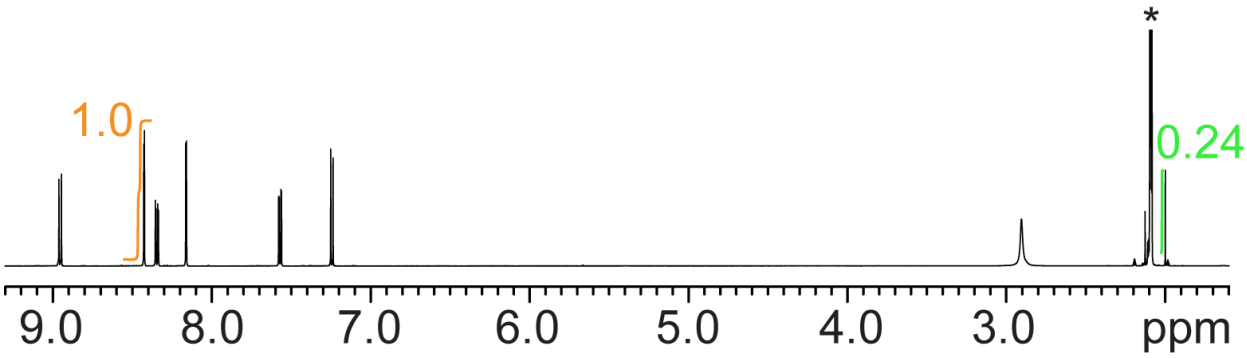

Figure 68. ^{1}H NMR spectrum of NCM-AA. The integrals of a NCM signal (in orange) and an AA signal (in green) are highlighted. The asterisk indicates the signal corresponding to the solvent used for the analysis (acetone-d6).

In summary, these solvates not only exhibit low reproducibility in their formation—some were obtained only once, while others were initially formed using two techniques but later only reproducible through one, etc.— but also demonstrate temporal instability, reflected in fluctuations of solvent content within the structure. This instability has been corroborated by DSC and TGA analyses for NCM-BENZOH, NMR for NCM-AA, and further supported by evidence of isostructurality identified through PXRD and FT-IR analyses.

The PXRD analysis confirmed the formation of three new solid forms of NCM, with remarkably similar diffraction patterns (AA, BENZOH, or ACT).

Figure 69 compares the patterns of the new NCM solvates formed with AA, BENZOH, and ACT to those of commercial NCM Form A, polymorph B, NCM H_A, and the previously reported NCM-ACT monosolvate (CSD refcode KUKRIT) [218,221]. Three distinct new patterns are clearly visible. They are nearly to each other (despite being derived from three different solvents) but distinct from the reference compounds, which confirms the formation of three new solid forms of NCM.

The pattern of these three compounds also differs from those of NCM-DMSO and NCM-2-pyr, and is characterized by signals at 10.3°, 13°, 17.5°, 20.9°, 22.3°, and 27.3° 2θ. The samples obtained with the three different solvents show only slight shifts in signal positions, but the overall pattern, including peak positions and relative intensities, corresponds to the same solid phase. This suggests that the three solvates are likely isostructural.

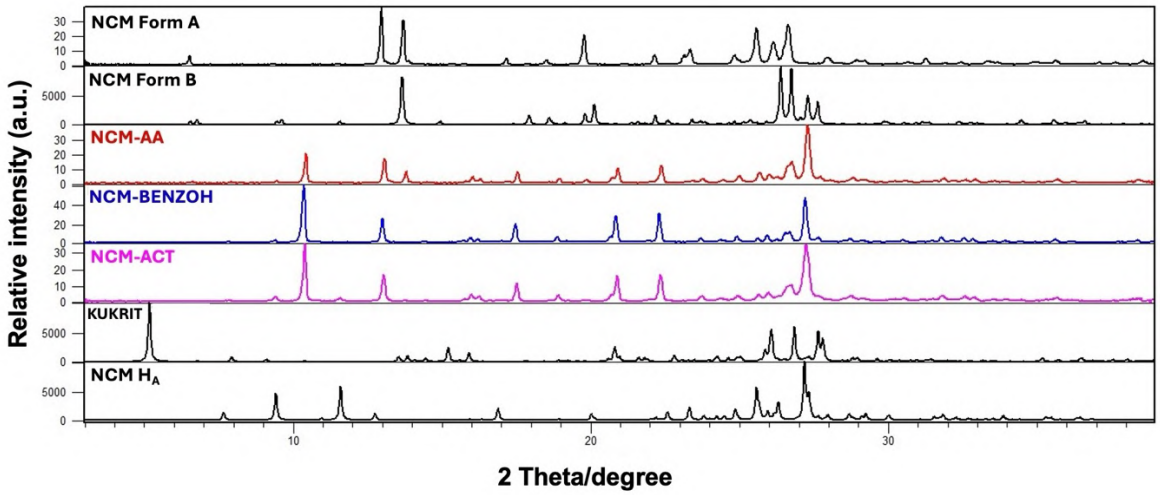

Figure 69. PXRD of NCM Form A, NCM Form B, NCM H_A and KUKRIT (black) and the new phases NCM-AA (red), NCM-BENZOH (blue) and NCM-ACT (pink).

Figure 70 presents a comparison of the thermograms for anhydrous NCM Form A, NCM-AA, NCM-BENZOH, and NCM-ACT.

Unlike the overlapping PXRD patterns, the thermograms of NCM-AA, NCM-BENZOH, and NCM-ACT are not completely superimposable, reflecting differences in solvent content and the nature of the solvent itself. However, all three curves display broad desolvation bands at low temperatures, which is a characteristic feature of non-stoichiometric solvates [191], where solvent molecules are not strongly bound to the solid and primarily interact with one another.

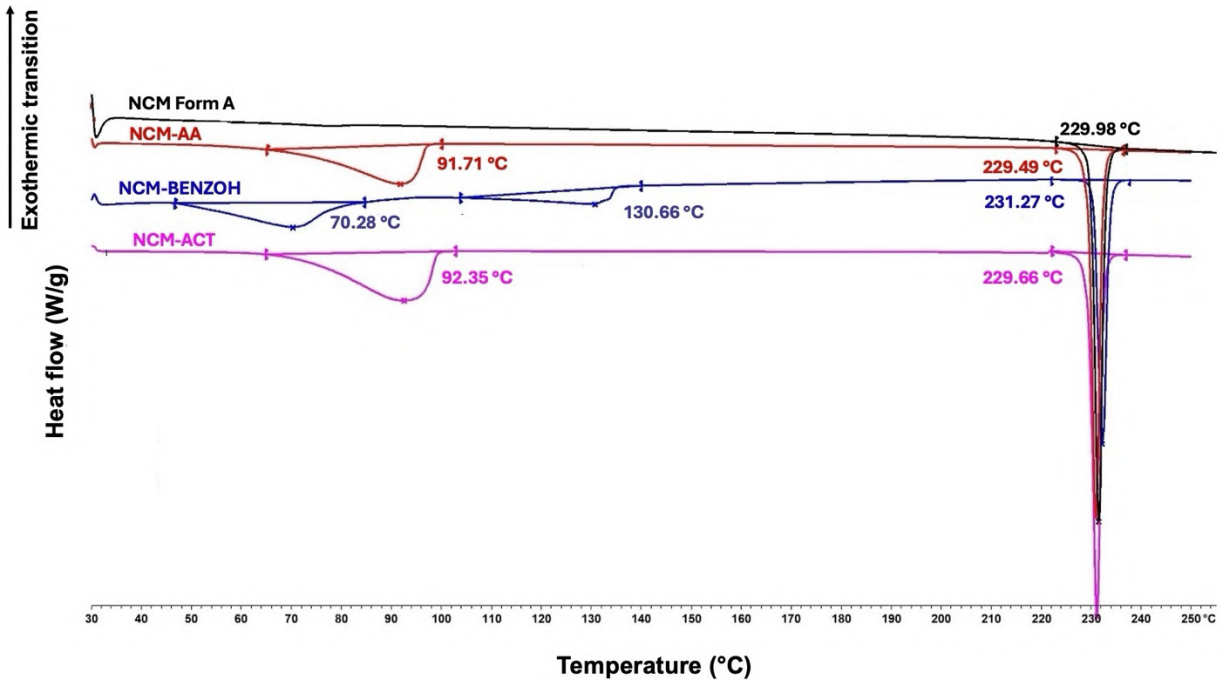

Figure 70. DSC curves of NCM Form A (black) and the new phases NCM-AA (red), NCM-BENZOH (blue) and NCM-ACT (pink).

Specifically, the thermograms of NCM-AA and NCM-ACT are almost identical, both displaying an initial endothermic desolvation band followed by an endothermic melting band, occurring within the same temperature range.

For NCM-AA, the desolvation band peaks at 91.71 °C with an enthalpy of 108.87 J/g, while the melting band peaks at 229.49 °C with an enthalpy of 135.29 J/g, similarly to NCM Form A. TGA analysis (Figure 71a) evidenced a single event between 70 °C and 95 °C, consistent with the desolvation endotherm observed in DSC. This event corresponds to a weight loss of 4.18% of the initial weight, which aligns with a stoichiometric ratio of 1-0.25 for NCM-AA, thereby confirming the formation of a non-stoichiometric solvate [191].

In the case of NCM-ACT, the desolvation peak appears at 92.35 °C, with a higher enthalpy of 151.54 J/g compared to NCM-AA. The melting peak is at 229.66 °C with an enthalpy of 134.88 J/g, again in correspondence of NCM-AA. TGA (Figure 71b) was consistent with the DSC findings, showing a single event between 70 °C and 100 °C. This corresponds to a weight loss of 4.55% of the initial weight, aligning with a stoichiometric ratio of 1-0.25 for NCM-ACT, like non-stoichiometric NCM-AA solvate.

The thermogram of NCM-BENZOH, however, differs by showing two distinct endothermic desolvation bands: the first at 70.28 °C with an enthalpy of 79.72 J/g, and the second at 130.66 °C with an enthalpy of 43.60 J/g. The typical endothermic melting event at 231.27 °C with an enthalpy of 101.35 J/g, corresponding to NCM Form A, is also visible. This melting occurs at slightly higher temperatures than in the other cases and with a lower enthalpy. A potential explanation for this phenomenon could be that part of the solvent, rather than being incorporated into the crystal lattice, may be adsorbed only on the crystal surface. TGA for the NCM-BENZOH solvate (Figure 71c) reveals a single event between 50 °C and 120 °C, corresponding to a weight loss of 15.59% of the initial weight. This percentage matches a stoichiometric ratio of 1-0.6 for NCM-BENZOH, confirming again the formation of a non-stoichiometric solvate. This fraction of surface-bound solvent was detectable only by DSC, while TGA, intentionally conducted a few days after preparation, showed a single inflection point. The BENZOH molecules may have undergone a different reorganization or attained a different equilibrium in the solid due to the mobility of solvent molecules in channel solvates. In all three cases, the solids retrieved after heating and subsequent desolvation of AA, ACT and BENZOH appeared to be anhydrous NCM Form A at the PXRD analysis (Figure D10 in the Appendix).

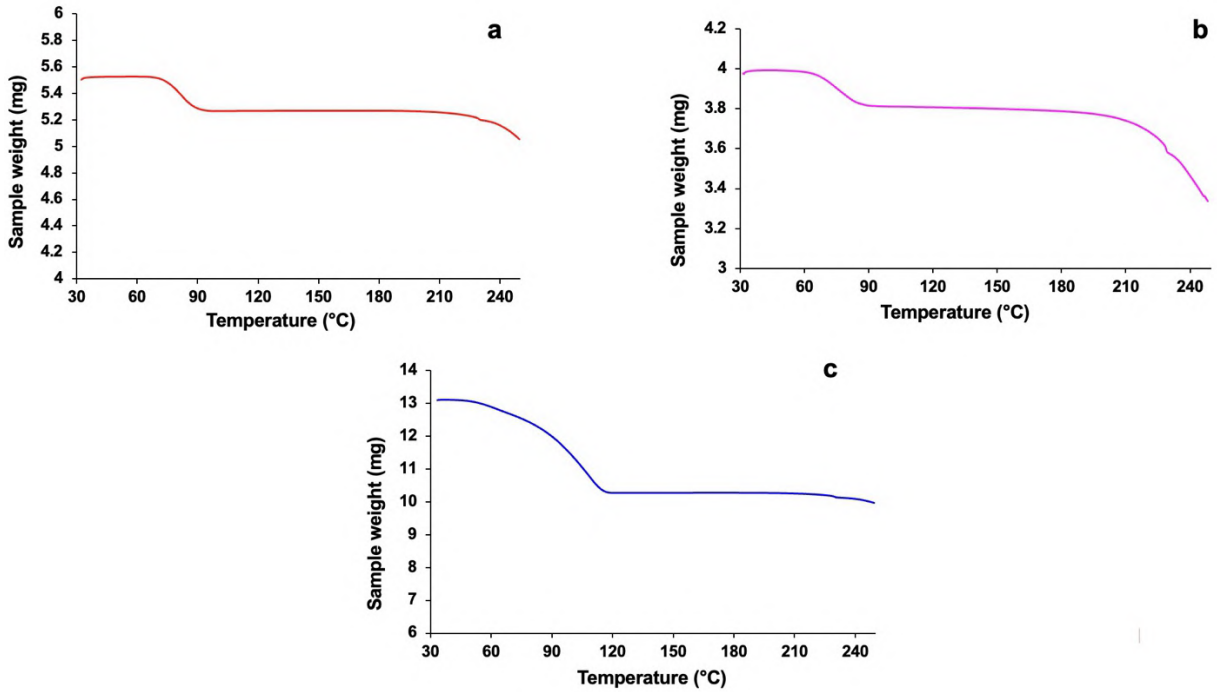

Figure 71. TGA curves of (**a**) NCM-AA solvate (red), (**b**) NCM- ACT solvate (pink) and (**c**) NCM-BENZOH (blue).

According to literature, isostructural solvates tend to convert into an isomorphic desolvate upon desolvation. This form represents an intermediate state between the solvated structure and the most stable anhydrous form, and usually exhibits a PXRD pattern that is very similar to the original channel solvate, with only minor shifts in the signals [191,345]. Given the isostructurality of the three non-stoichiometric solvates observed in PXRD, one would expect that DSC coupled with PXRD analyses would produce patterns like the initial ones, indicating the formation of isomorphic desolvates. However, this was not observed in our case, presumably due to the low stability of these solids. This issue may be directly related to the limitations of the current technique, which could potentially be solved with more advanced equipment, such as variable-temperature diffractometers.

The (FT-IR)-ATR spectra of the NCM-AA, NCM-BENZOH, and NCM-ACT solvates were found to differ from those of the previously analyzed solvates, but were identical to each other, confirming the formation of an isostructural solvate. In this case, (FT-IR)-ATR analysis proved to be particularly useful for demonstrating the isostructurality of the three phases. A comparison of the spectra for AA, BENZOH, and ACT is shown in Figure D11 in the Appendix. For simplicity, Figure 72 compares the spectrum of NCM-AA (which overlaps with the spectra of BENZOH and ACT) and that of anhydrous NCM Form A. Clear differences between these spectra further confirmed the presence of interactions between NCM and the three solvents in the isostructural solvates:

- Specifically, the bands at 3576 cm^{-1} and 3491 cm^{-1}, corresponding to the -OH stretching of NCM [343], were shifted to lower wavenumbers in the NCM-AA spectrum, appearing at 3541 cm^{-1} and 3441 cm^{-1}, respectively. This suggested possible involvement of the -OH hydroxyl group of NCM in these interactions. A slight shift was also observed in the C-OH stretching band of NCM, from 1192 cm^{-1} [242] to 1197 cm^{-1}.
- The -NH amine group of NCM did not seem to participate in these interactions, as both the stretching bands (3237.8 cm^{-1} and 3194.4 cm^{-1} [241]) and the bending band (897 cm^{-1} [241]) remained at the same wavenumbers as in the NCM spectrum.
- The C=O stretching (1651 cm^{-1} [242]) and C=O bending (1217 cm^{-1} [242]) bands of NCM were slightly shifted to higher wavenumbers in the NCM-AA spectrum, at 1660 cm^{-1} and 1224 cm^{-1}, respectively.
- The region between 1500 and 400 cm^{-1} in the spectrum of the examined solvate was very similar across all three channel solvates and when compared to the spectrum of anhydrous NCM Form A, providing further evidence that the three systems are isostructural.

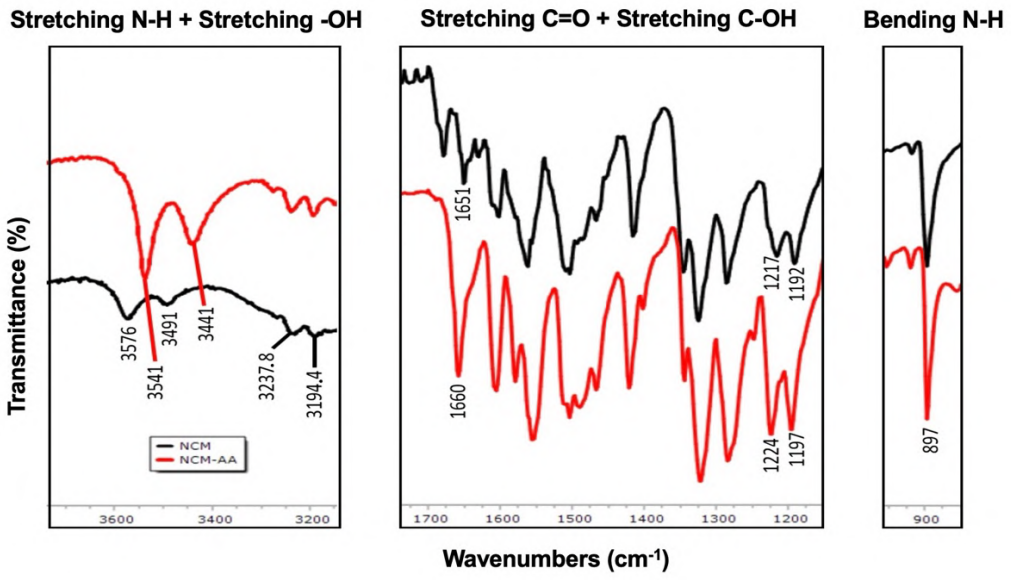

Figure 72. FT-IR spectra of NCM Form A (black) and the new phase NCM-AA (red).

6.3.2 Physical stability tests of NCM solvates under several conditions

6.3.2.1 Physical stability in the solid-state over time

The solid-state stability of NCM solvates was assessed at room temperature (20 °C) by storing the samples in a desiccator with calcium chloride for 6 months. Periodic analyses and a final evaluation of the stored samples were conducted using PXRD.

The solvates were all found to be stable at room temperature: no changes were observed between the fresh products and the samples after 6 months (Figure D12-D16 in the Appendix). This is particularly noteworthy considering that some of these solvates are non-stoichiometric, which are typically characterized by low stability [191].

6.3.2.2 Resistance to compression

To test the impact of mechanical stress, NCM solvates were compressed at 10 Ton for 3 min. This test was important as solvates, especially non-stoichiometric ones, often exhibit low compression resistance [303], and NCM is predominantly available as oral tablets [30].

All five solvates proved to be resistant to compression, as no changes were observed in the initial PXRD patterns (Figures D17-D21 in the Appendix).

6.3.3 Resistance to conversion into NCM H_A under high RH %

Since these five new NCM solvates demonstrate satisfactory stability under various stress conditions, the next step was to evaluate their ability to prevent the formation of insoluble NCM H_A. NCM monohydrate, which typically forms within a month of exposure to ambient humidity, poses significant challenges, primarily due to its extremely low solubility, often described as "*cement-like*" behavior. This characteristic, together with other physicochemical properties, negatively impacts the dissolution rate and bioavailability of NCM, ultimately compromising its therapeutic efficacy [30,218,221–225]. Therefore, the purpose of these experiments was to assess whether these five new NCM solvates could inhibit NCM H_A formation, thereby mitigating its undesirable physicochemical properties.

Specifically, samples were stored in a sealed chamber containing a saturated aqueous NaCl solution, which maintains an RH of 75% at room temperature [285]. PXRD analysis was performed after 24, 48 and 144h of exposure to monitor any changes.

Comparing the diffractograms obtained before and during exposure to humidity, no formation of NCM H_A was observed. Specifically, all five NCM solvates remained stable, preventing conversion into the monohydrate form even after 144h of exposure to humidity. This contrasts with anhydrous NCM Form A, which converts to the monohydrate after just a few hours under the same conditions. Comparisons of the individual NCM solvates as fresh products and after 144h of high RH exposure are included in the Appendix (Figures D22-D26).

6.4 Conclusions

Through the experimental work presented in this thesis section, the previously reported tendency of NCM to form solvates/hydrates, both stoichiometric and non-stoichiometric (channel), has been confirmed. This is evident from the discovery of five new solvates with solvents used in the pharmaceutical field. Based on the extensive characterization of these compounds, the new systems were classified into two subgroups:

- The first subgroup includes stoichiometric solvates, such as NCM-DMSO with a confirmed 1:1 stoichiometry, as reported by Kuri et al. [232], and NCM-2-pyr, which likely has a 1:1.7 or 1:2 stoichiometry.
- The second subgroup consists of non-stoichiometric solvates, presumably isostructural channel solvates, given the similarity in PXRD and FTIR analyses. These include NCM-AA, NCM-ACT, and NCM-BENZOH. These solvates both demonstrate low reproducibility in their formation and temporal instability (in terms of solvent content within the structure). reflected in fluctuations of solvent content within the structure. This instability was confirmed by DSC, TGA and NMR analyses, along with isostructurality evidenced through PXRD and FT-IR.

Importantly, all five niclosamide solvates were found to be stable under several stressed conditions. Furthermore, these solvates prevented the conversion into the undesirable monohydrate NCM H_A, offering several advantages for industrial applications in formulation development.

7. General considerations

Improving the physical properties of drugs is a key objective in pharmaceutical science, as most active pharmaceutical ingredients are delivered in solid forms. The physical properties of these solids play a crucial role in various stages of drug development and administration, directly impacting processing, bioavailability, and therapeutic efficacy. For instance, it is estimated that up to 40% of current pharmaceuticals and as much as 90% of new chemical entities suffer from limited aqueous solubility, a property that is intrinsically linked to the crystal structure of the compound [346]. This relationship between crystal structure and solubility highlights how the solid-state characteristics of a drug can impact its overall performance.

Two primary strategies have emerged to modify the physical properties of molecular solids. The first, more traditional approach involves altering the chemical structure of the molecule via covalent synthesis. However, in recent years, a second strategy—rooted in the principles of supramolecular chemistry—has gained increasing prominence. This approach focuses on modifying the intermolecular interactions, such as hydrogen bonds, van der Waals forces, and π-π stacking, to alter the three-dimensional arrangement of molecules within a crystal lattice or amorphous form.

Supramolecular chemistry, often described as "chemistry beyond the molecule", emphasizes that the macroscopic properties of molecular solids are shaped not only by the intrinsic structure of individual molecules but also by how these molecules organize within a given space. By controlling the complex network of non-covalent forces, supramolecular chemistry enables the design of organized, stable molecular assemblies with enhanced properties, such as improved solubility, stability, and bioavailability [347].

In this thesis, the principles of supramolecular chemistry have been applied to develop innovative multicomponent systems—particularly binary and ternary drug-drug combinations of antiparasitic agents—using mechanochemical techniques. This approach offers novel solutions to persistent challenges in pharmaceutical development, particularly in addressing the solubility and stability issues of many drugs. The resulting systems hold great promise for more effective therapies, especially in the treatment of parasitic diseases.

The first part of this thesis focuses on the cocrystallization of two anthelmintic drugs - praziquantel and niclosamide - via mechanochemical methods. Both drugs are known for their strong tendency to undergo solid-state transformations, making them ideal candidates for cocrystallization. The motivation for investigating this novel drug-drug combination stems from the fact that, while several drug-drug multicomponent systems involving niclosamide have been previously reported, none have

been explored for praziquantel. This is surprising given praziquantel long-standing therapeutic use and the extensive number of cocrystals discovered for the drug.

The mechanochemical cocrystallization process was successful, leading to the formation of a novel drug-drug cocrystal of praziquantel for the first time. This was achieved using a sustainable, one-step mechanochemical process that required only micromolar amounts of common solvents and was completed in just 120 minutes.

The novel anhydrous cocrystal was fully characterized through extensive collaboration with a network of scientists across various disciplines, whose combined expertise greatly contributed to the comprehensive analysis of its physical and structural properties. The crystal structure was successfully solved and deposited in the Cambridge Structural Database, providing a valuable resource for further study.

One of the most remarkable features of this new solid form was its unique stoichiometry, which revealed a 1:3 praziquantel-niclosamide ratio. This is particularly notable because such asymmetric stoichiometries are relatively uncommon in the field of cocrystallization, where 1:1 and 2:1 drug-to-coformer ratios are more frequently observed [348].

Crucially, the cocrystal exhibited promising *in vitro* anthelmintic activity. The anhydrous cocrystal demonstrated a higher reduction in parasite activity compared to the physical mixture of the two drugs, particularly in Schistosoma *mansoni* models. This suggests that the synergistic effect between praziquantel and niclosamide, facilitated by their supramolecular arrangement, could provide more effective treatment options for parasitic diseases.

The promising results from this binary drug-drug system have paved the way for broadening the scope of the project. This has led to the exploration of additional combinations of praziquantel and niclosamide with other anthelmintic compounds, with the aim of developing ternary drug-drug systems that could further enhance therapeutic efficacy and address unmet needs in antiparasitic treatments.

In the second section of the PhD thesis, the cocrystallization of praziquantel and niclosamide in the presence of acetic acid was further investigated using mechanochemical methods. This exploration was driven by the recent identification of acetic acid as an anthelmintic agent, as evidenced by its antiparasitic activity against *Gyrodactylus kobayashii* trematodes [287]. The objective was to develop a three-component drug system that could leverage synergistic effects and potentially result in a pharmaceutically acceptable cocrystal solvate.

A 1:1:1 cocrystal solvate was successfully synthesized through a one-hour liquid-assisted grinding process. Notably, acetic acid was used in substantial excess compared to the equimolar ratios of the components. This requirement for a larger volume of acetic acid could be attributed to the fact that

acetic acid acts both as a reactant incorporated into the multicomponent solid and as a liquid medium that facilitates the mechanochemical reaction.

Moreover, the new cocrystal solvate exhibited enhanced anthelmintic activity against both in vitro Schistosoma *mansoni* adults and Newly Transformed Schistosomula, outperforming pure praziquantel and niclosamide. This observation underscores the potential for synergistic effects in combination therapies.

A particularly innovative aspect of this synthesis is that mechanochemical methods reveal great potential for creating ternary cocrystals by not only using individual coformers but also by applying preformed synthons to guide the assembly of the cocrystal structure. This strategy provides a more versatile and efficient pathway to achieving the desired cocrystal solvate. Various building blocks, including three pure coformers and several preformed combinations, were employed in the synthesis. Remarkably, through five different combinations, the same cocrystal solvate was consistently obtained with high yield, identifying the optimal synthetic strategy to achieve the new system in an almost pure phase. These results highlight the flexibility and robustness of the "puzzle" approach, enabling the optimization of the synthesis process and the selection of the most effective combination of starting materials.

One of the synthetic strategies employed to obtain the cocrystal solvate involved using an intrinsically reactive solid system, specifically a 1:1 coamorphous system of praziquantel and niclosamide, which was obtained through four hours of neat grinding. This coamorphous system served as the starting point for the experimental project detailed in the third part of the thesis. Neat grinding is well-documented in the literature as an effective method for producing amorphous materials, as it provides conditions that more readily disrupt the crystalline structure [46–48].

In line with the goal of developing ternary drug-drug antiparasitic systems, this section aimed to combine praziquantel and niclosamide with another anthelmintic drug, mebendazole, to create coamorphous homogeneous systems. By exploring these combinations, the research seeks to enhance the therapeutic potential of these drugs and investigate the synergistic effects that can arise from their interaction in an amorphous state.

A combinatorial approach using a mixture design strategy, combined with experimental lab-scale milling, enabled the creation of ten distinct mixtures (both binary and ternary) composed exclusively of active ingredients.

Comprehensive characterization of these new solids demonstrated that they were all homogeneous multicomponent systems rather than mere physical mixtures of amorphous materials. Notably, the ternary compounds exhibited greater stability than theoretically anticipated, illustrating -once again-

how controlling the complex network of non-covalent forces in supramolecular chemistry can enable the design of more organized and stable molecular assemblies with enhanced properties.

The development of all these novel solid forms highlights the promise of supramolecular chemistry and mechanochemistry in enhancing both the physical properties of drugs and their biological efficacy through synergistic interactions.

The final section of this PhD project delved deeper into the anthelmintic drug niclosamide, which has recently emerged as a promising candidate for drug repurposing across a range of therapeutic areas. Initially employed for its antiparasitic properties, niclosamide has gained renewed attention for its potential applications in antiviral (e.g., SARS-CoV-2), antibacterial, anticancer, and anti-inflammatory treatments. This wide-ranging pharmacological profile highlights the ability of niclosamide to meet various unmet medical needs beyond its original use in parasitology [214,216,217]. However, one significant challenge associated with niclosamide is its propensity to convert into a highly insoluble monohydrate form [218,221]. This conversion severely restricts its bioavailability, creating a substantial barrier to its therapeutic application [30,218,221–225]. To tackle these solubility issues, this research undertook a comprehensive screening of crystal forms using mechanochemical methods, with a focus on the deliberate formation of new solvates. These new solid forms can help prevent or slow the transition to the monohydrate, thereby improving the solubility and stability of niclosamide in different formulations [191].

Five new crystalline solvates were successfully synthesized and, after thorough characterization, classified into two distinct subgroups based on their structural properties: stoichiometric solvates and non-stoichiometric/channel solvates. Notably, all five solvates exhibited excellent mechanical stability, with a key observation being their remarkable resistance to conversion into the undesirable NCM monohydrate form. Even after 144h of exposure to humidity, these solvates maintained their integrity, in contrast to anhydrous niclosamide, which rapidly transforms into the monohydrate within just a few hours under similar conditions.

The successful creation of all these novel solid forms highlights the significant potential of supramolecular chemistry and mechanochemistry in pharmaceutical development. By using the principles of supramolecular chemistry, researchers can engineer complex molecular architectures that leverage non-covalent interactions - such as hydrogen bonding, π-π stacking, and van der Waals forces - to create more organized and stable drug systems. These interactions not only enhance the physical properties of the drugs, such as the stability, but they also open avenues for improving pharmacological efficacy. Moreover, mechanochemistry facilitates the transformation of solid-state materials through physical processes, allowing for more efficient synthesis routes that are often more sustainable compared to traditional solvent-based methods. The integration of these two fields enables

the design of drug formulations that can exhibit synergistic interactions, where the combined effect of multiple active ingredients exceeds the sum of their individual effects. This is particularly valuable in developing combination therapies for complex diseases, such as parasitic infections, where enhancing the therapeutic action of existing drugs can lead to improved treatment outcomes.

However, as we look to the near future, it becomes clear that several important aspects not fully explored in this thesis warrant further investigation. First, one of the fundamental parameters for the future optimization of these promising new systems is the evaluation of solubility. Preliminary tests, not included in this thesis, have demonstrated analytical challenges in quantifying the active ingredients, due to the persistence of an inseparable complex in solution (as seen in the cases of the anhydrous cocrystal of praziquantel and niclosamide and the cocrystal solvate with acetic acid). Future developments will certainly need to establish a quantification method that can account for complexation in solution.

Additionally, the results of *in vitro* tests of the cocrystal solvate were promising, as the active ingredients in the new multicomponent systems appeared to exert a synergistic effect. However, this synergy was not observed in the *in vivo* pilot tests. The discrepancy between the *in vitro* and *in vivo* results could potentially be attributed to the vehicle used for administration; the minicapsules used for the anhydrous cocrystals were challenging to administer, and the cocrystal solvate proved difficult to dissolve in corn oil, resulting in a cloudy rather than clear suspension. Furthermore, while the use of an oil-based vehicle suspension was an improvement over an aqueous-based one, it may not be ideal for showcasing the full potential of the cocrystal. A solid form, such as size M minicapsules, would likely yield better results. However, administering these minicapsules to mice has proven to be difficult, as evidenced in the study of the anhydrous cocrystal where several animals died during administration. Future *in vivo* studies should therefore employ size M minicapsules, accompanied by thorough training and refinement of the administration technique for these pharmaceutical forms.

Expanding our understanding of these principles, along with addressing other limitations not yet highlighted, could pave the way for more effective and innovative preformulation studies and therapeutic strategies. By delving deeper into the complexities of solubility, stability, and bioavailability, researchers can unlock new opportunities for improving drug formulation and efficacy. Moreover, a comprehensive examination of the interactions within multicomponent systems could reveal valuable insights that inform the design of next-generation therapies. This holistic approach will not only enhance our knowledge of existing compounds but also guide the discovery and development of novel formulations that are better suited to meet the diverse needs of patients. In doing so, we can significantly advance the field of pharmaceutical sciences and ultimately improve therapeutic outcomes for a wide range of diseases.

Appendix A

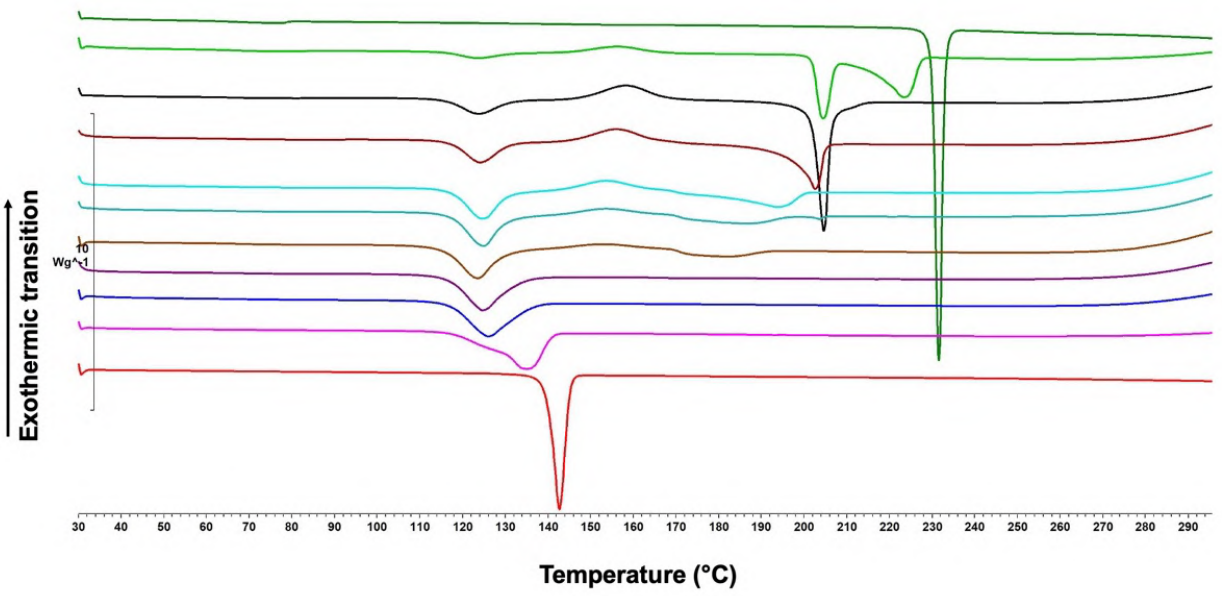

Figure A1. DSC curves of pure PZQ (red), pure NCM (dark green) and various PMs with different molar ratios of PZQ and NCM: PZQ-NCM 0.10-0.90 (light green), PZQ-NCM 0.25-75 (black), PZQ-NCM 0.33-0.67 (dark red), PZQ-NCM 0.44-0.56 (light blue), PZQ-NCM 0.50-0.50 (aquamarine), PZQ-NCM 0.56-0.44 (brown), PZQ-NCM 0.67-0.33 (violet), PZQ-NCM 0.75-0.25 (blue), PZQ-NCM 0.90-0.10 (pink).

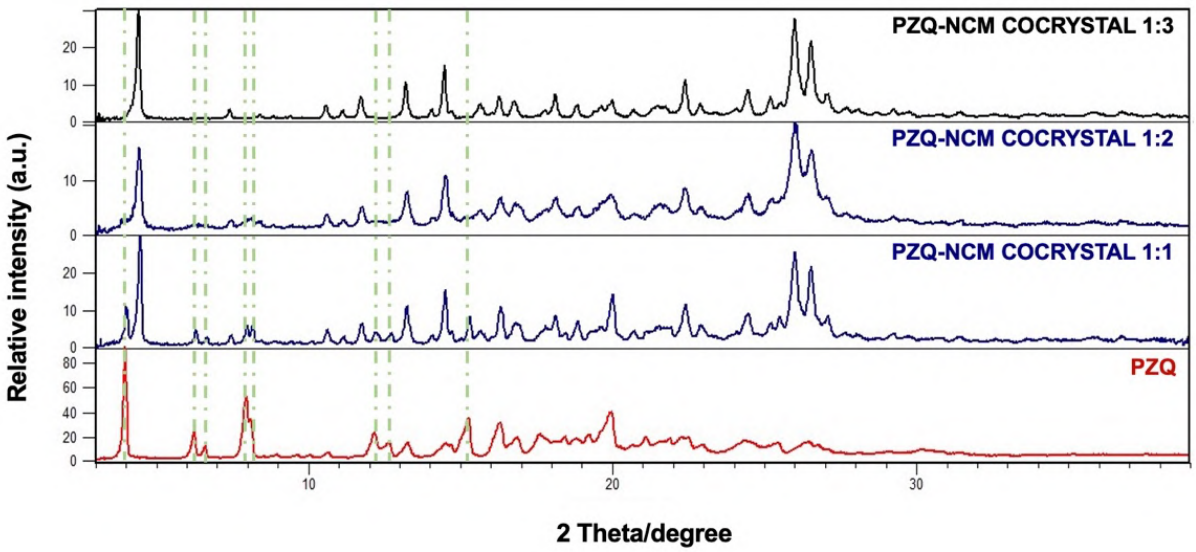

Figure A2. PXRD comparison of PZQ-NCM coground in different molar ratios.

Table A1. Different liquids investigated for LAG according to their polarity, protic properties and previously reported for PZQ and NCM cocrystals and solvates formation.

	Not previously used for cocrystals or solvates	Previously used for PZQ cocrystals or solvates	Previously used for NCM cocrystals or solvates
Non-polar	HXN		
Polar and protic		• EtOH • AA	• iPOH • MeOH • TEG
Polar and aprotic		• EA • AcT:ACN 1:1 • 2-pyr	• DMSO • DMF*

*Not used for toxicity reasons.

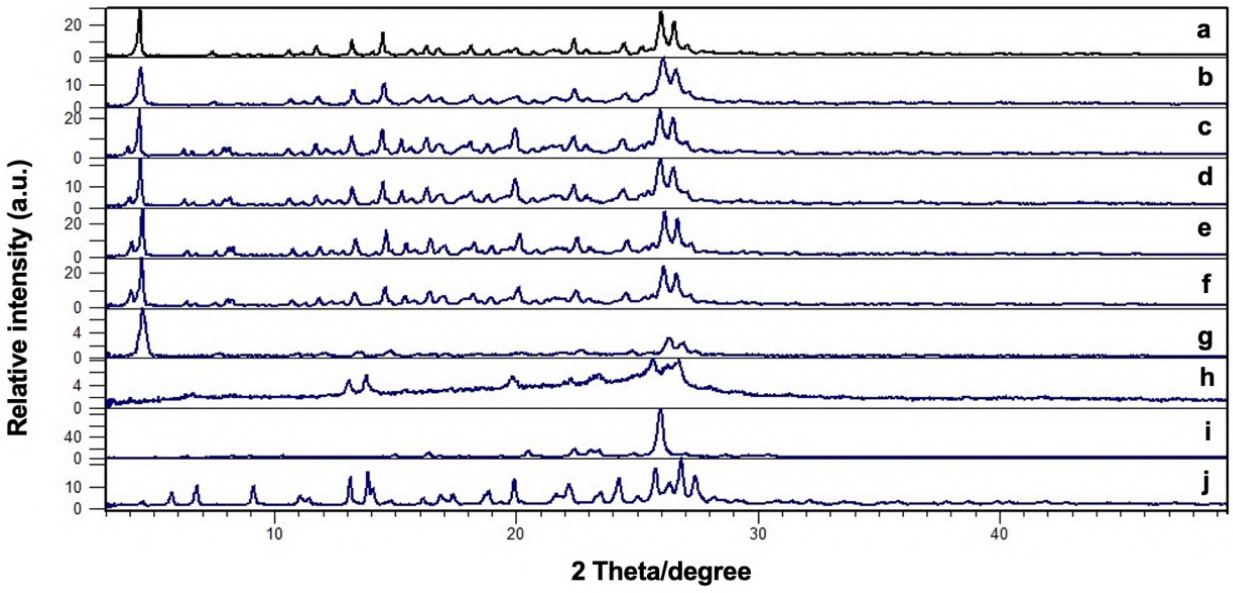

Figure A3. PXRD comparison of PZQ-NCM coground in 1:3 molar ratio in the presence of MeOH (a), HXN (b), TEG (c), EA (d), ACT-ACN (e), EtOH (f), iPOH (g), DMSO (h), 2-pyr (i), AA (j).

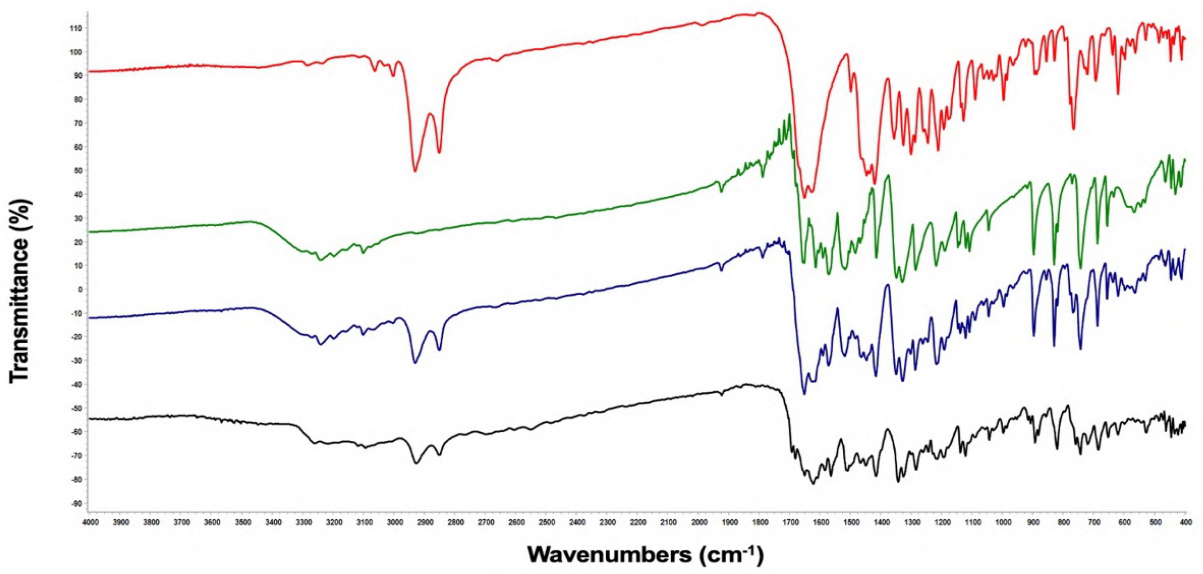

Figure A4. FT-IR full spectra of PZQ (red), NCM (green), PZQ-NCM PM (blue) and PZQ-NCM cocrystal (black).

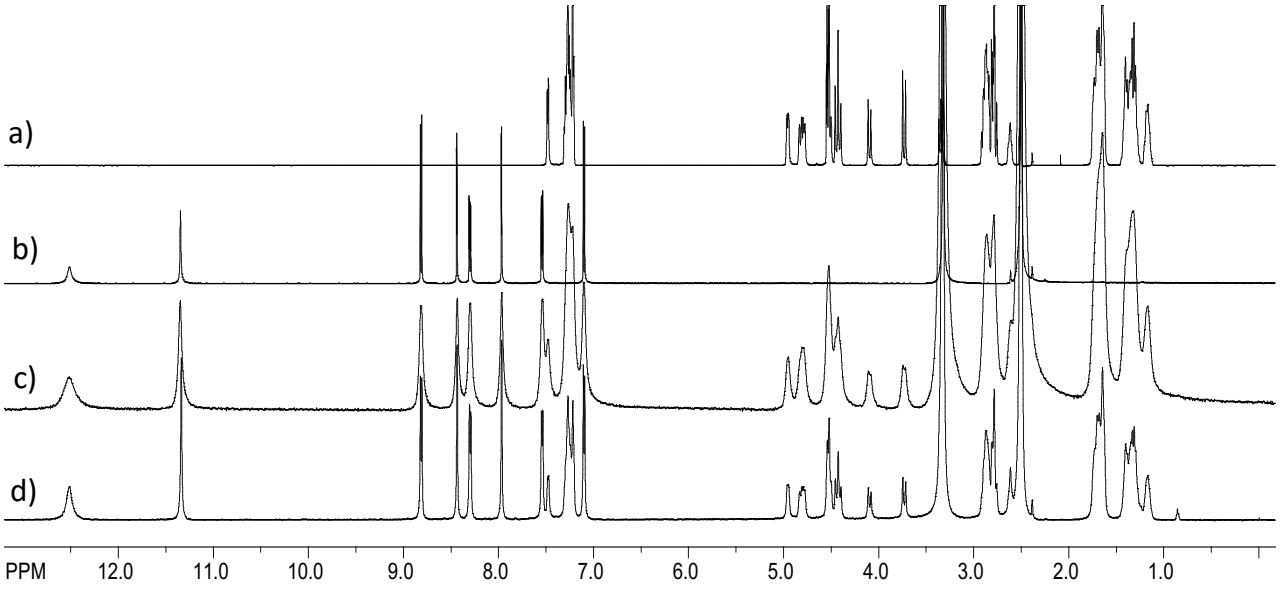

Figure A5. Comparison of the ^{1}H-NMR spectra (DMSO-d_6) of PZQ (a), NCM (b), cocrystal batch n°1 (c) and batch n°2 (d).

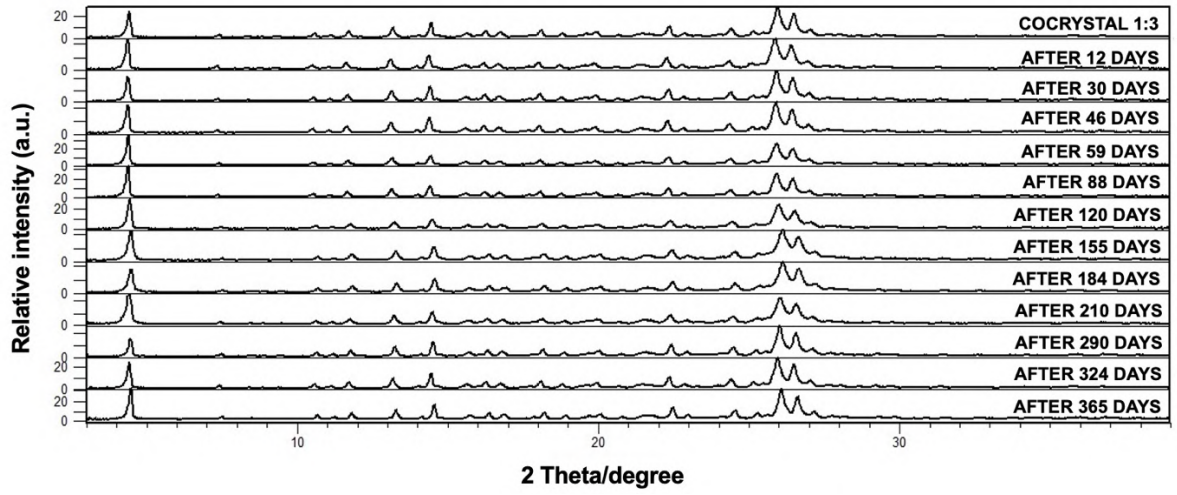

Figure A6. PXRD comparison of PZQ-NCM cocrystal over time.

Appendix B

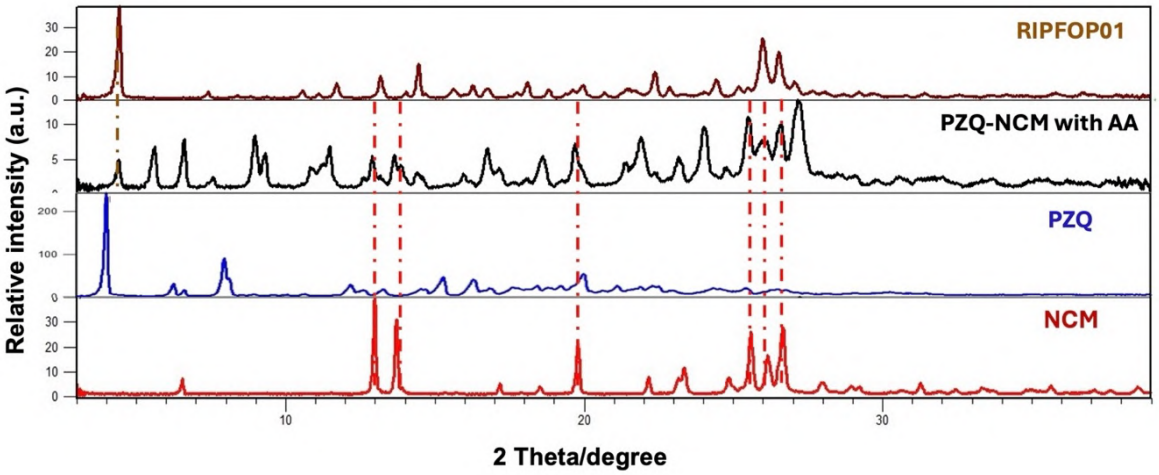

Figure B1. PXRD comparison of PZQ-NCM 1:3 anhydrous cocrystal, new phase obtained by grinding PZQ and NCM with AA and raw PZQ and NCM.

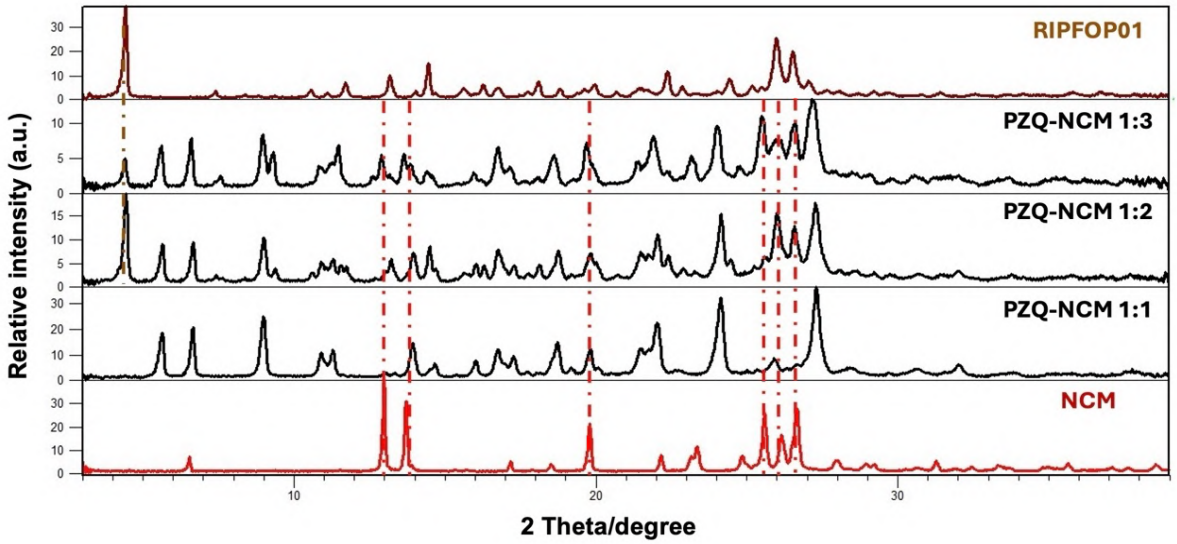

Figure B2. PXRD comparison of PZQ-NCM coground in different molar ratios in the presence of 160 μL of AA.

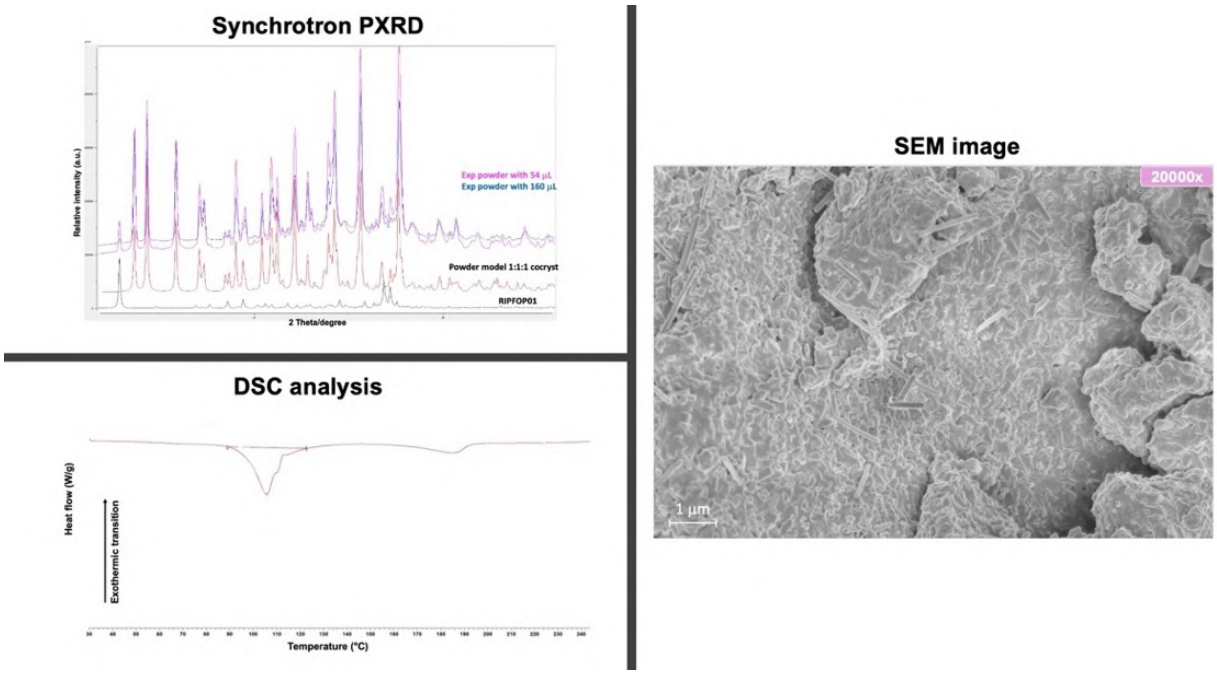

Figure B3. Characterization analyses of PZQ-NCM 1:1 molar ratio ground with equimolar ratio of AA.

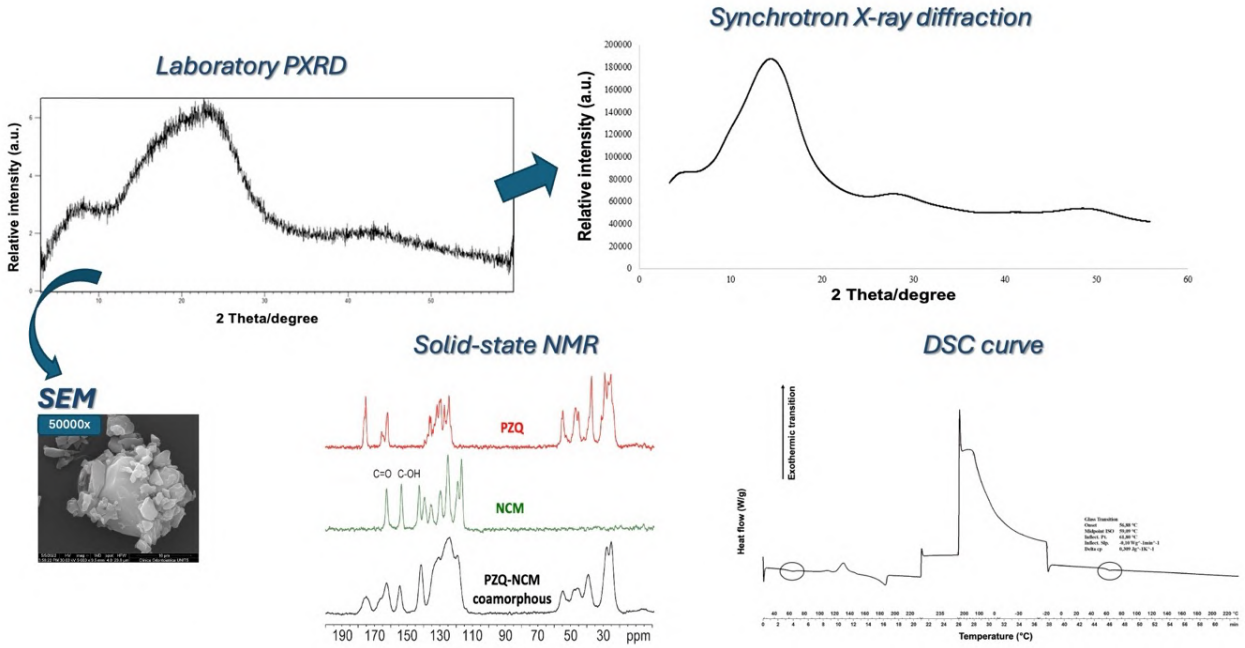

Figure B4. Characterization analyses of PZQ-NCM 1:1 coamorphous.

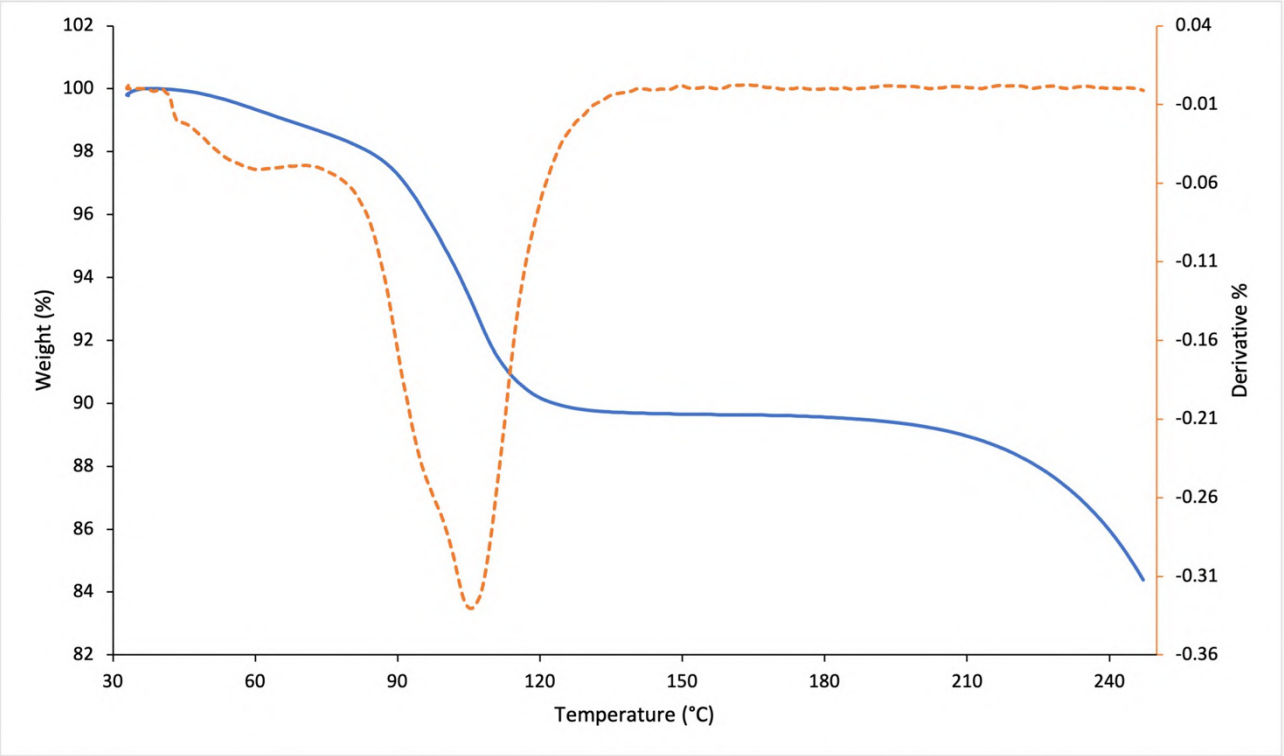

Figure B5. TGA curve of mechanochemically prepared PZQ-NCM-AA cocrystal solvate.

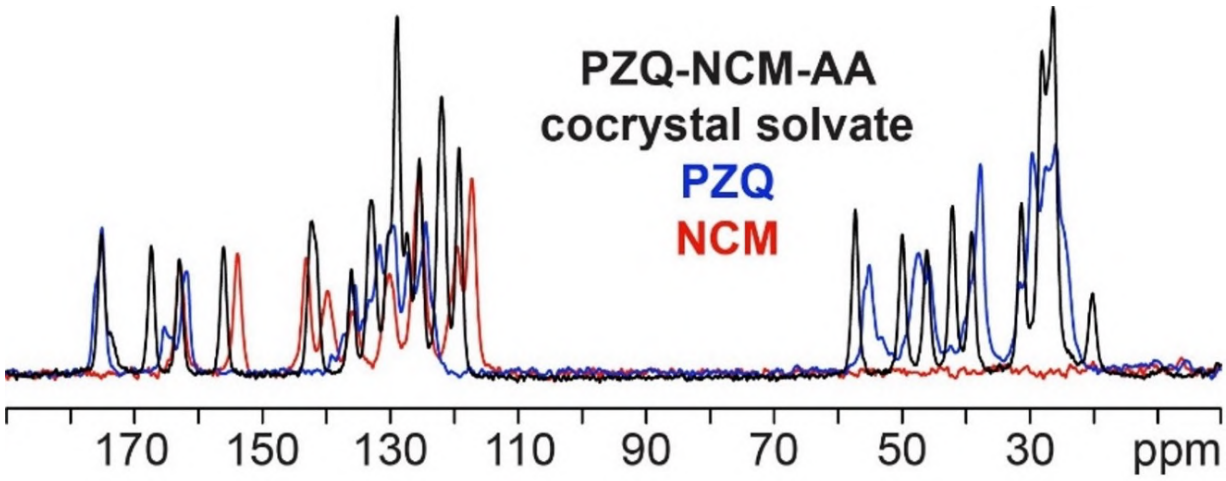

Figure B6. Overlay of the ^{13}C (150.91 MHz) CPMAS spectrum of PZQ-NCM-AA cocrystal solvate (black), acquired at a spinning speed of 20 kHz at room temperature, with the ^{13}C (100.63 MHz) CPMAS spectra of pure NCM (red), pure PZQ (blue), acquired at a spinning speed of 12 kHz at room temperature.

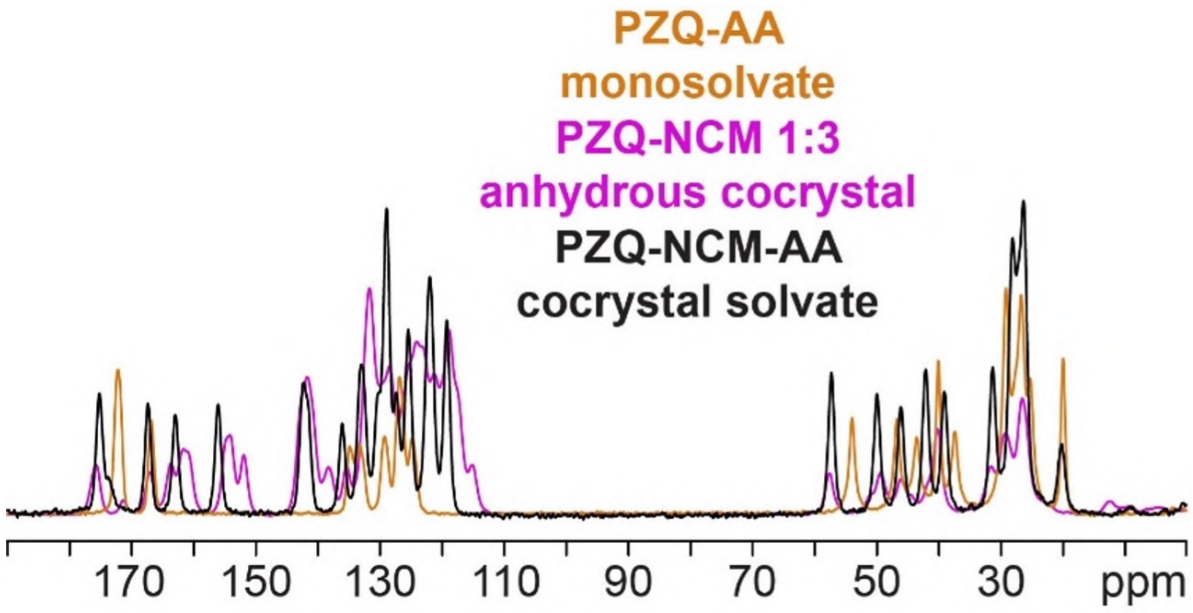

Figure B7. Overlay of the^{13}C (150.91 MHz) CPMAS spectrum of PZQ-NCM-AA cocrystal solvate (black), acquired at a spinning speed of 20 kHz at room temperature, with the ^{13}C (100.63 MHz) CPMAS spectra of PZQ-NCM 1:3 anhydrous cocrystal (pink), acquired at a spinning speed of 12 kHz at room temperature, and ^{13}C (150.91 MHz) CPMAS spectrum of PZQ-AA monosolvate (orange), acquired at a spinning speed of 20 kHz at room temperature.

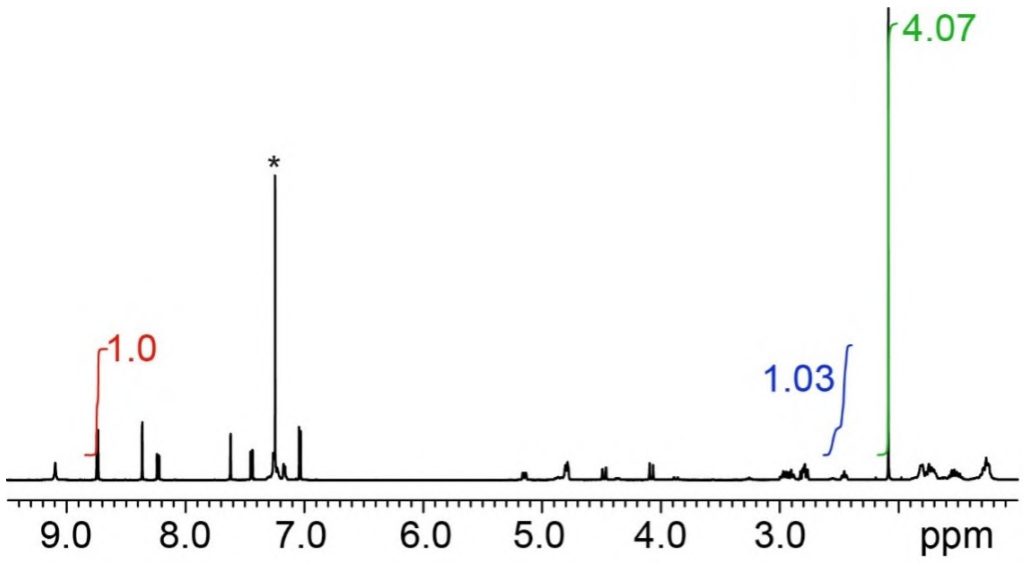

Figure B8. ^{1}H-NMR spectra of PZQ-NCM-AA cocrystal solvate. The integrals of the signals are highlighted in red for NCM, in blue for PZQ and in green for AA. The * symbol indicates the signal corresponding to the solvent used for the analysis, deuterated chloroform $CDCl_3$.

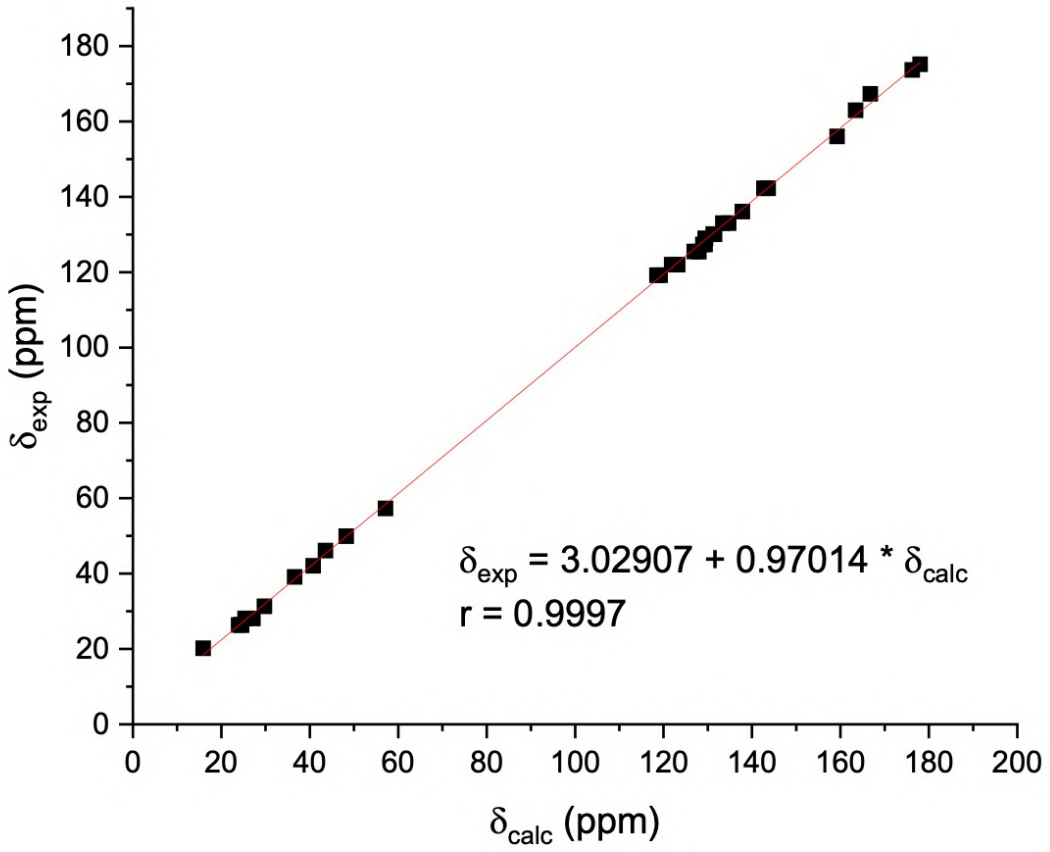

Figure B9. Plot of experimental vs. calculated ^{13}C ppm.

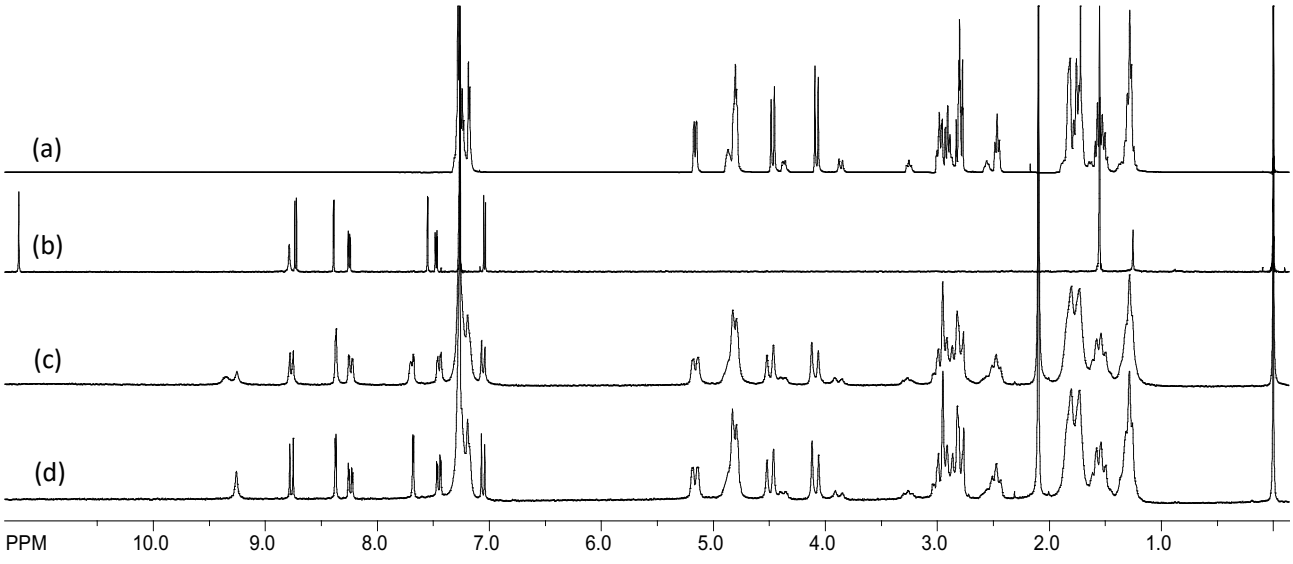

Figure B10. [1]H-NMR spectra of PZQ (a); NCM (b); PZQ-NCM-AA cocrystal solvate obtained by grinding raw PZQ and NCM in the presence of AA for 2h (c) and PZQ-NCM-AA cocrystal solvate achieved through NG for 4h (to obtain PZQ-NCM 1:1 coamorphous) plus LAG for 2h (d).

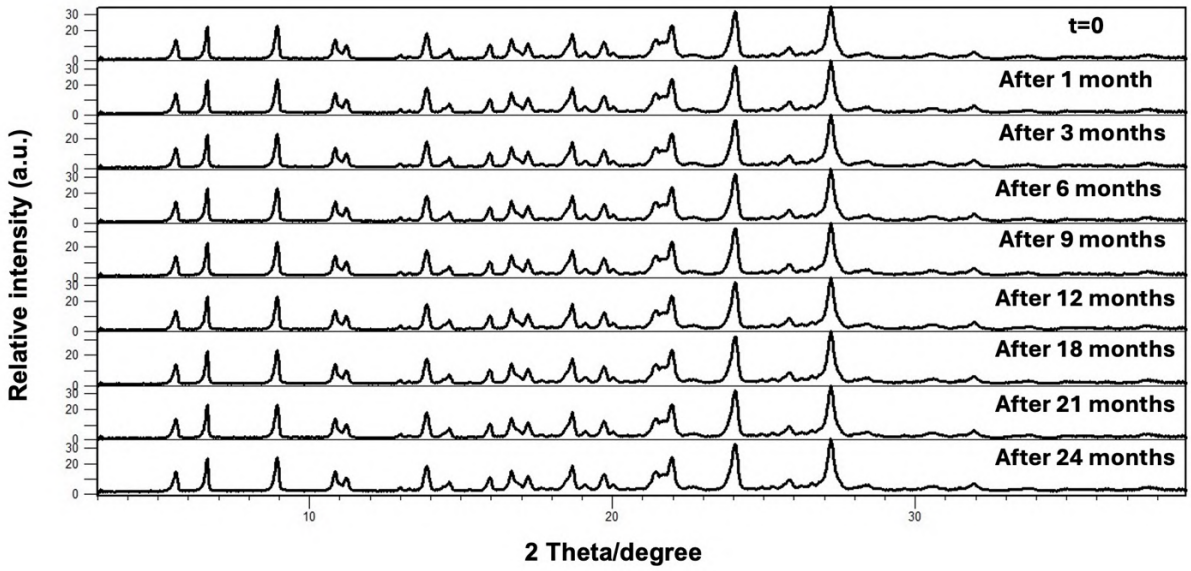

Figure B11. PXRD comparison of PZQ-NCM-AA cocrystal solvate over time.

Figure B12. Samples of pure cocrystal solvate (white) and cocrystal solvate with traces of RIPFOP01 (pink).

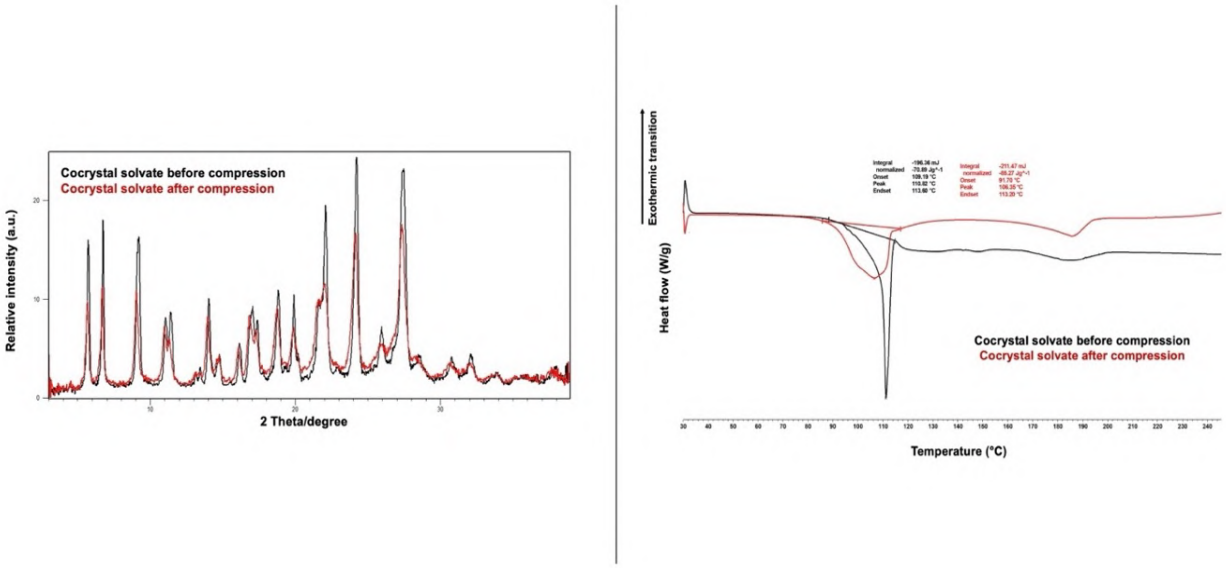

Figure B13. PXRD (left) and DSC (right) results of cocrystal solvate physical stability before and after compression.

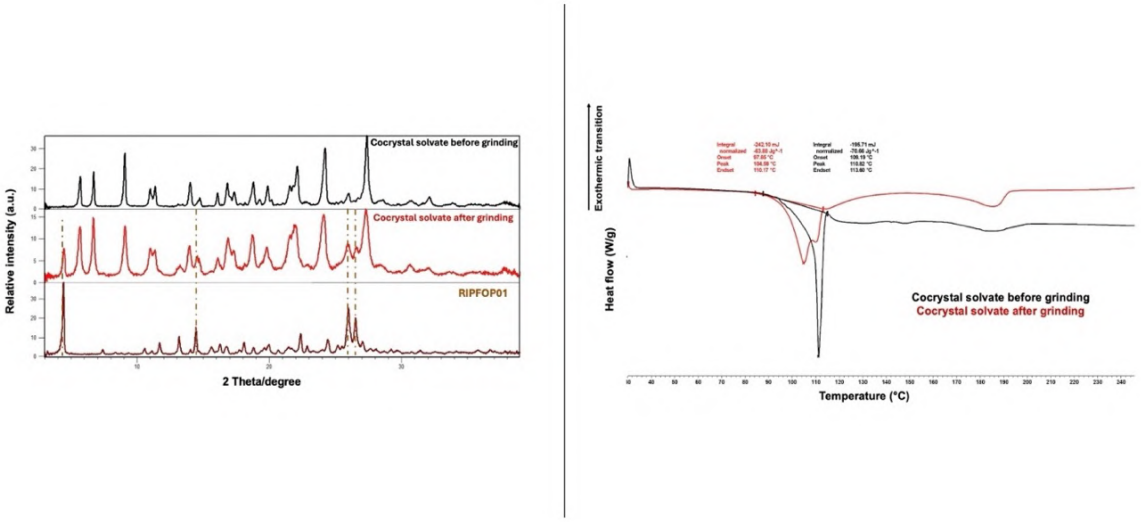

Figure B14. PXRD (left) and DSC (right) results of cocrystal solvate physical stability before and after grinding.

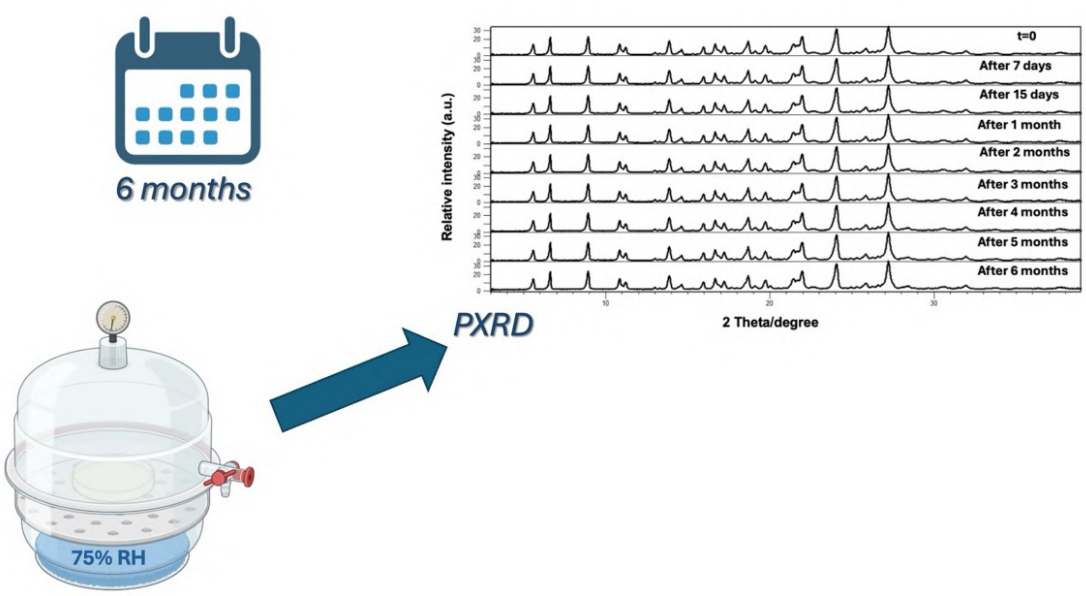

Figure B15. Schematic representation of physical stability tests for evaluating resistance of the cocrystal solvate to high RH.

Appendix C

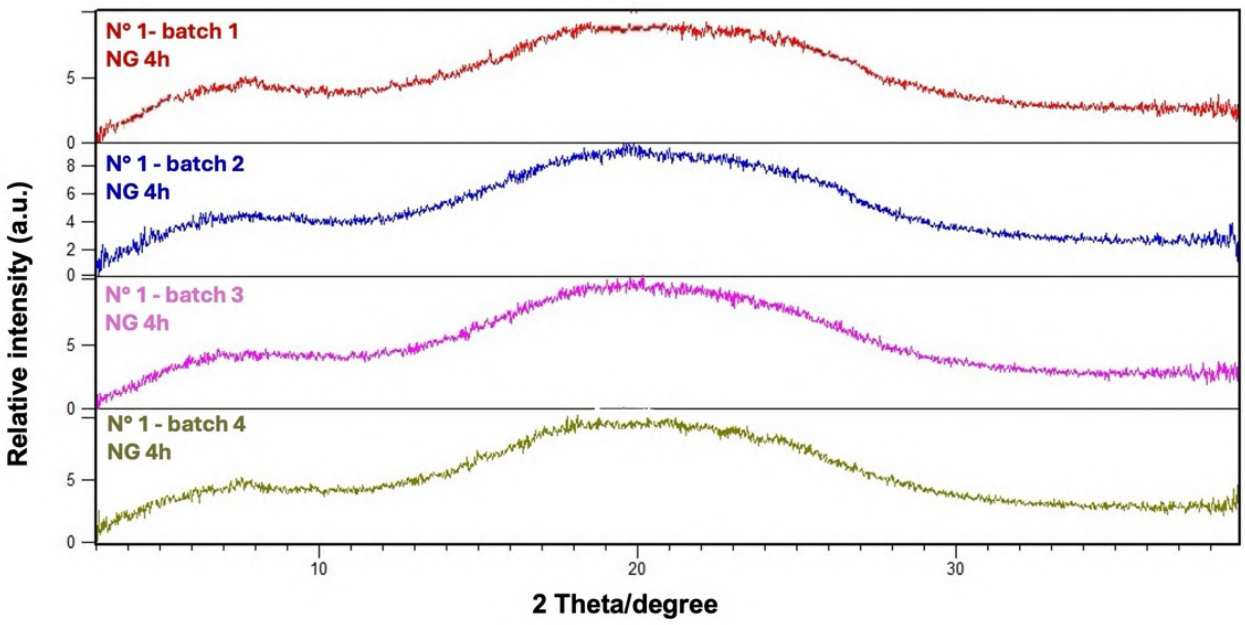

Figure C1. PXRD analysis of 4 repetitions of NG of exp. N° 1 (ternary PZQ-NCM-MBZ 1:0.5:0.5 system).

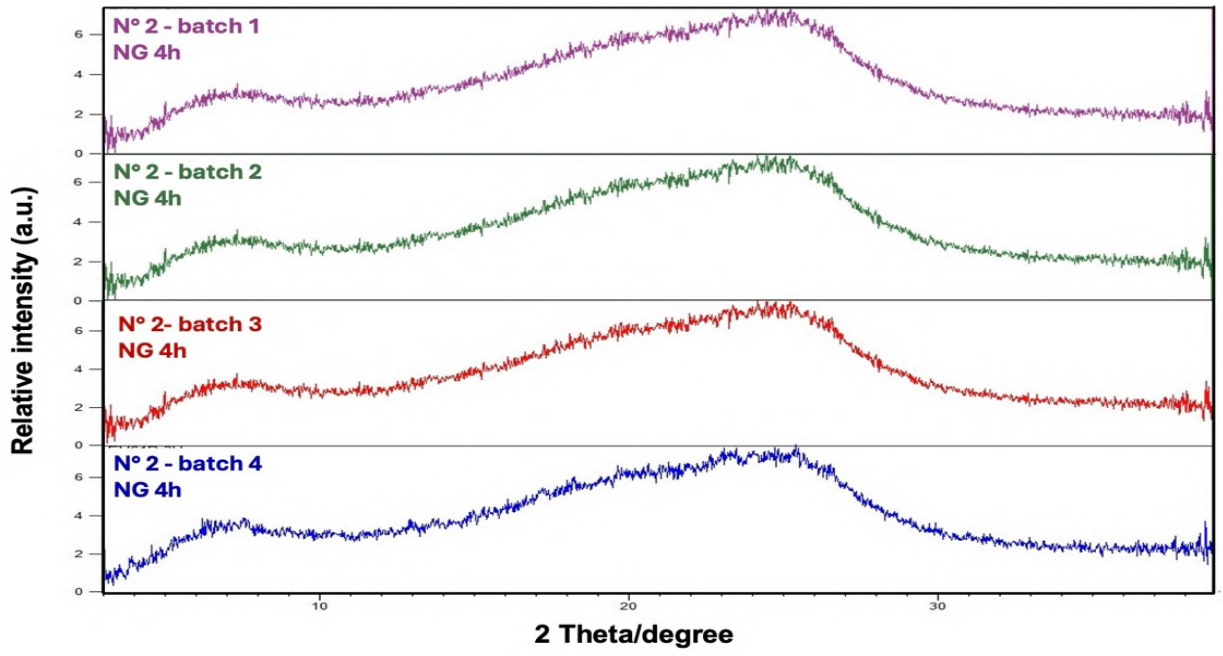

Figure C2. PXRD analysis of 4 repetitions of NG of exp. N° 2 (ternary PZQ-NCM-MBZ 1:2.5:2.5 system).

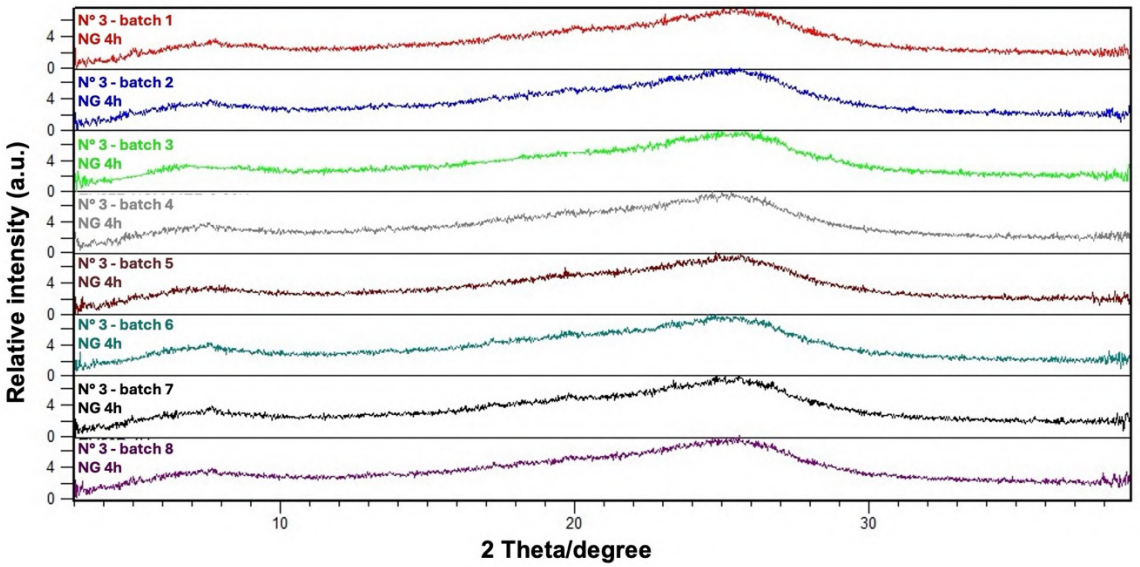

Figure C3. PXRD analysis of 8 repetitions of NG of exp. N° 3 (binary NCM-MBZ 1:1 system).

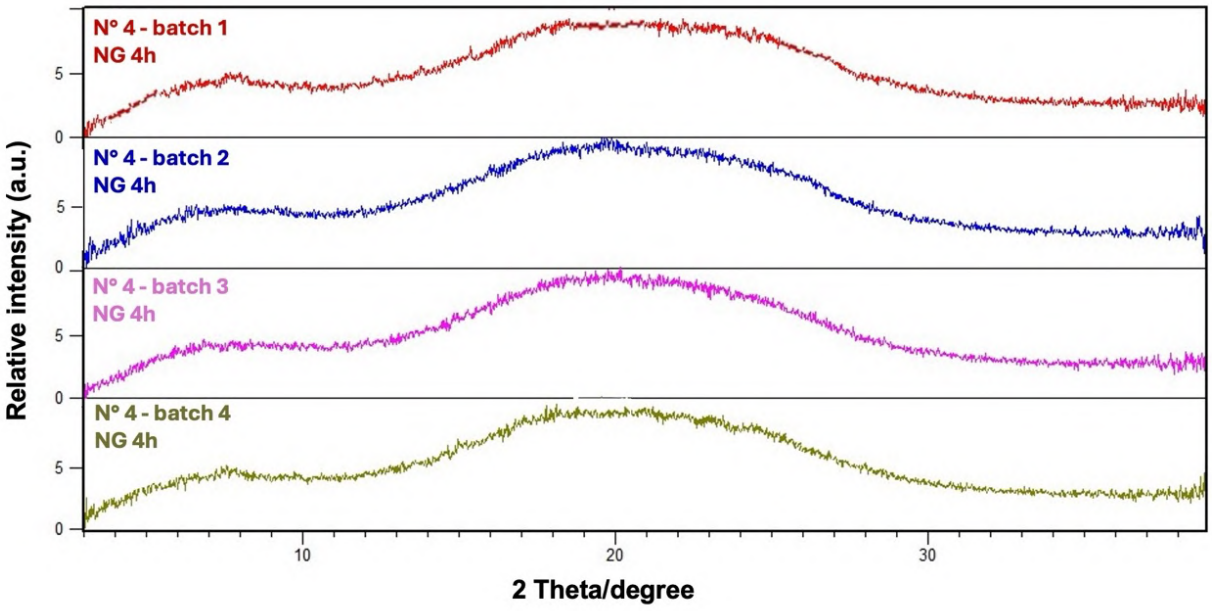

Figure C4. PXRD analysis of 8 repetitions of NG of exp. N° 4 (ternary PZQ-NCM-MBZ 0.5:0.5:1 system).

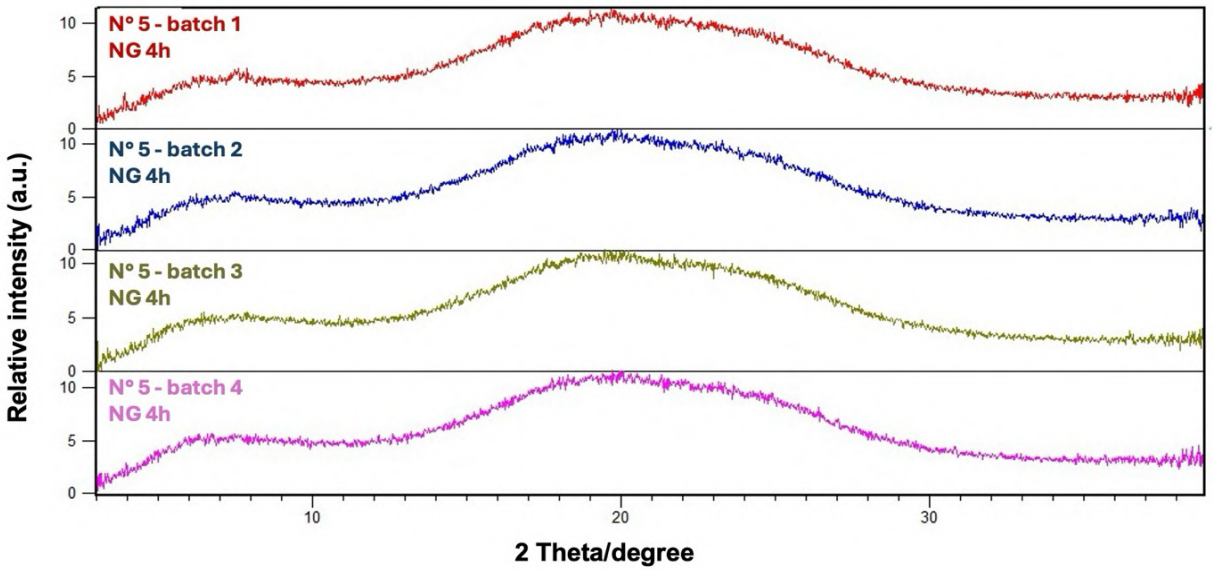

Figure C5. PXRD analysis of 4 repetitions of NG of exp. N° 5 (ternary PZQ-NCM-MBZ 2.5:2.5:1 system).

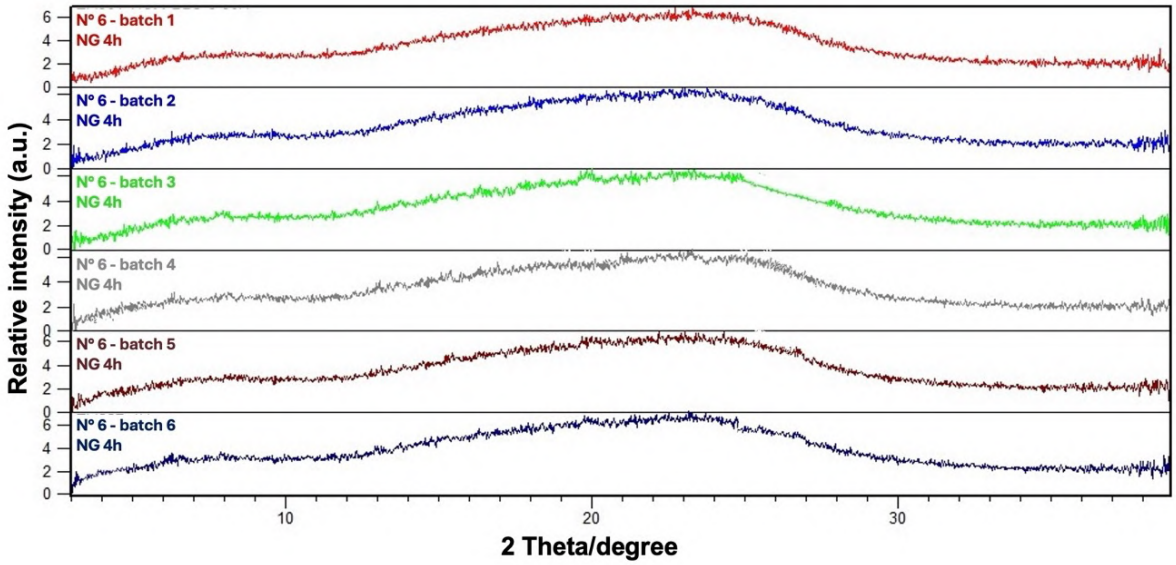

Figure C6. PXRD analysis of 6 repetitions of NG of exp. N° 6 (binary PZQ-NCM 1:1 system).

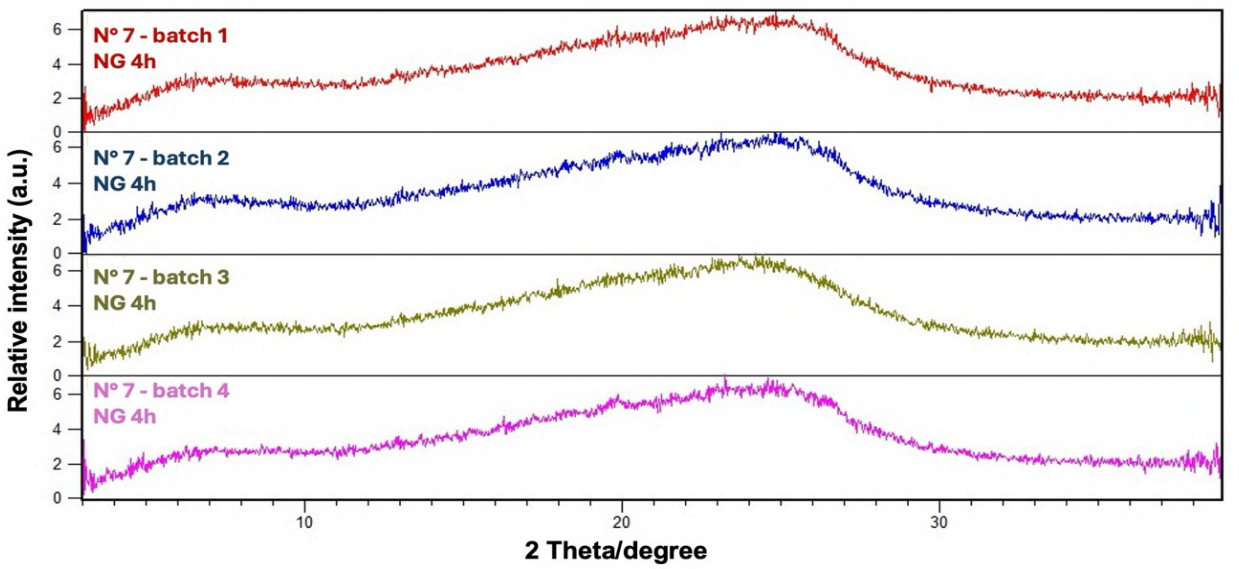

Figure C7. PXRD analysis of 4 repetitions of NG of exp. N° 7 (ternary PZQ-NCM-MBZ 0.5:1:0.5 system).

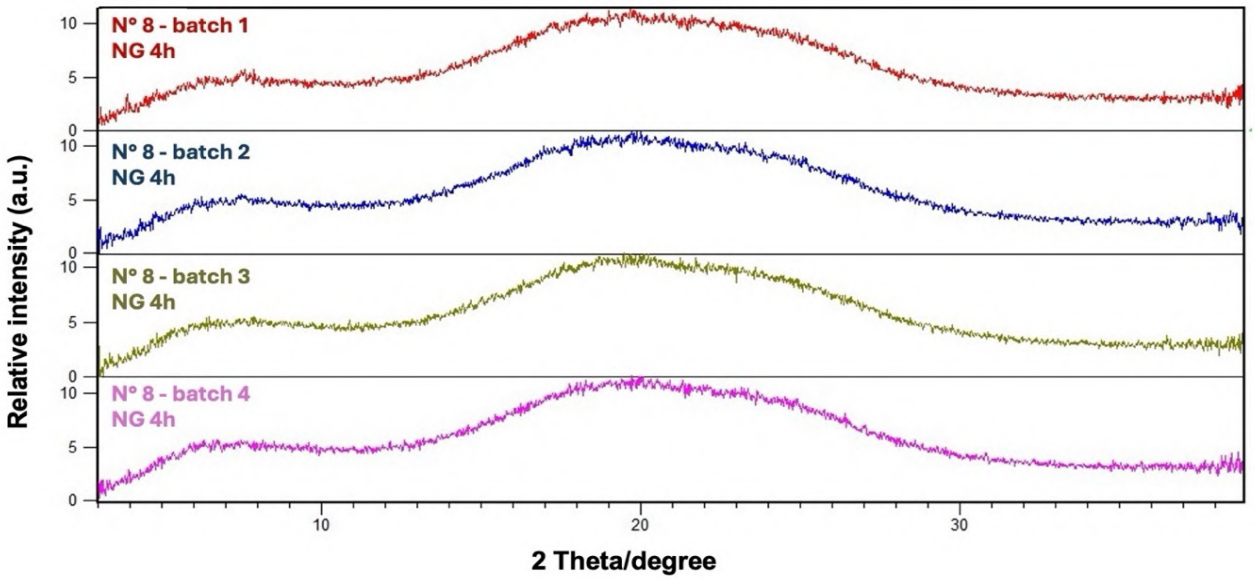

Figure C8. PXRD analysis of 4 repetitions of NG of exp. N° 8 (ternary PZQ-NCM-MBZ 2.5:1:2.5 system).

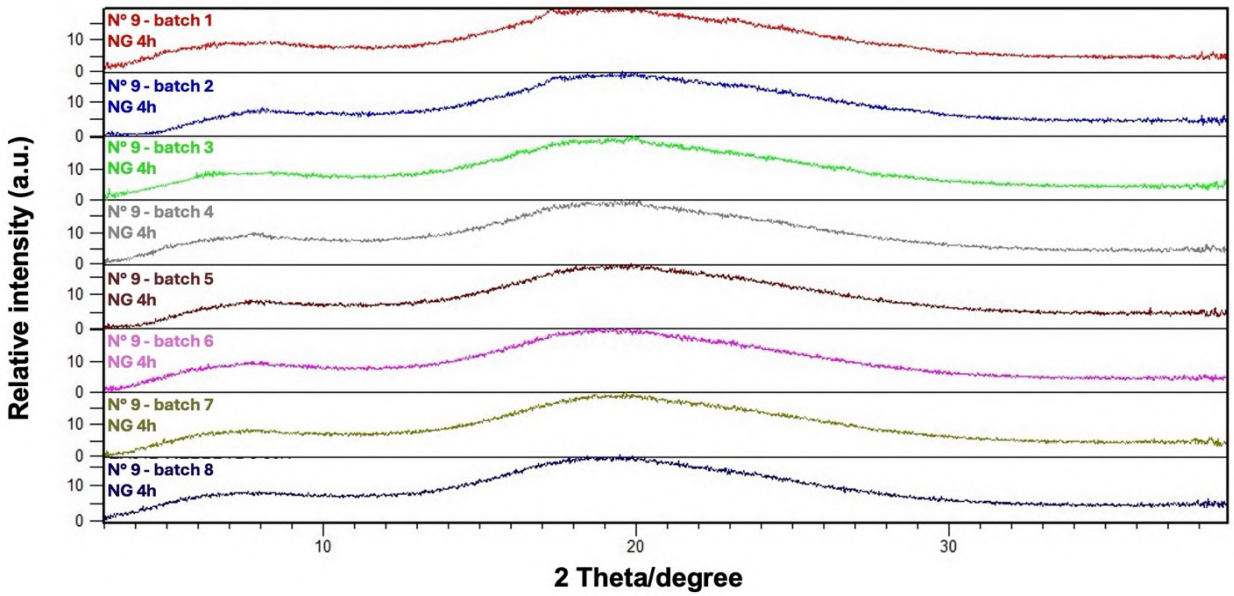

Figure C9. PXRD analysis of 8 repetitions of NG of exp. N° 9 (binary PZQ-MBZ 1:1 system).

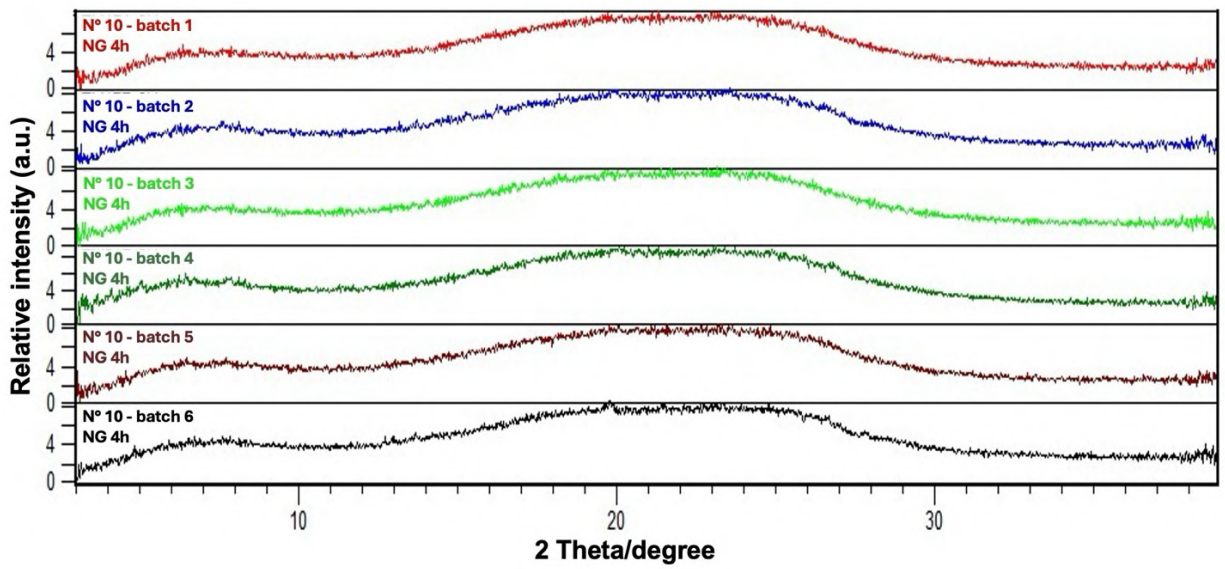

Figure C10. PXRD analysis of 6 repetitions of NG of exp. N° 10 (ternary PZQ-NCM-MBZ 1:1:1 system).

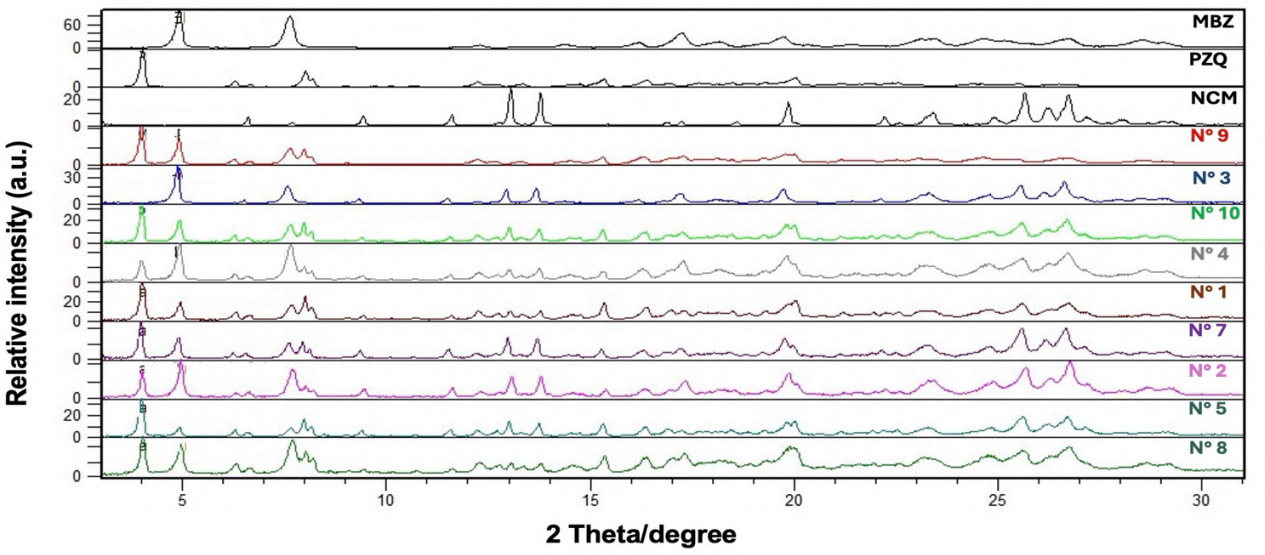

Figure C11. PXRD analysis of pure MBZ, PZQ and NCM compared to the PMs of the matrix systems.

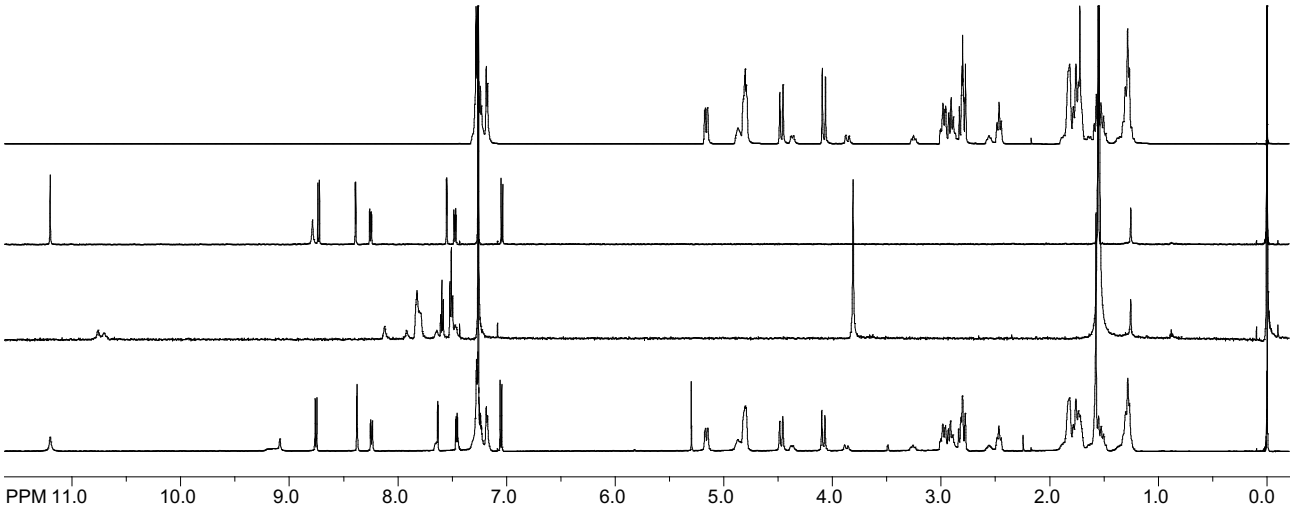

Figure C12. ^{1}H-NMR analysis (from top to bottom) of pure PZQ, NCM and MBZ compared to the sample of exp. N° 1.

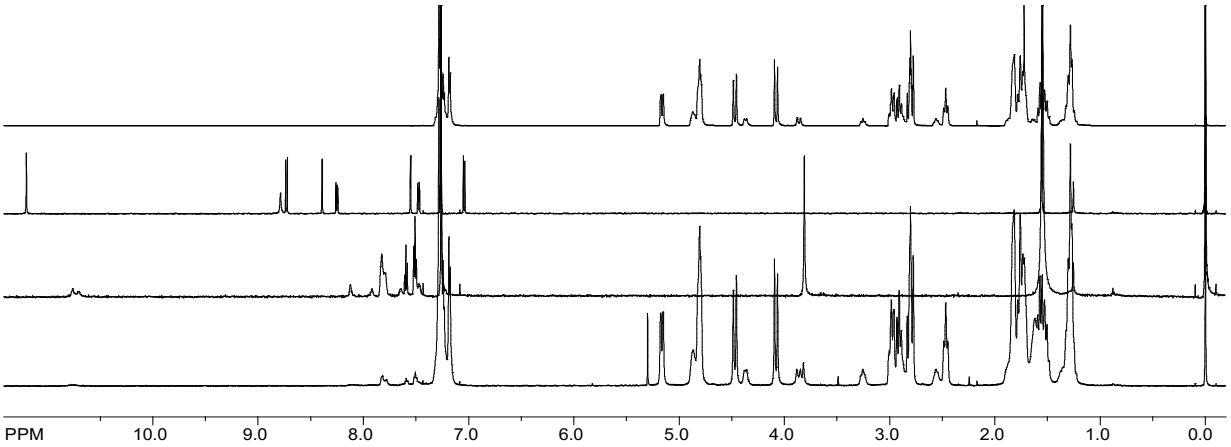

Figure C13. [1]H-NMR analysis (from top to bottom) of pure PZQ, NCM and MBZ compared to the sample of exp. N° 2.

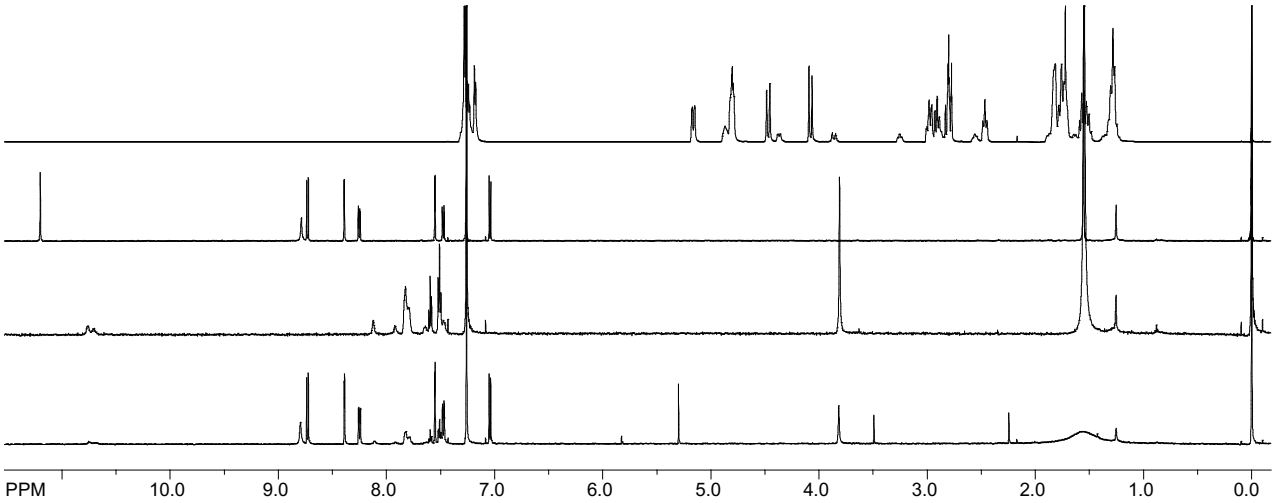

Figure C14. [1]H-NMR analysis (from top to bottom) of pure PZQ, NCM and MBZ compared to the sample of exp. N° 3.

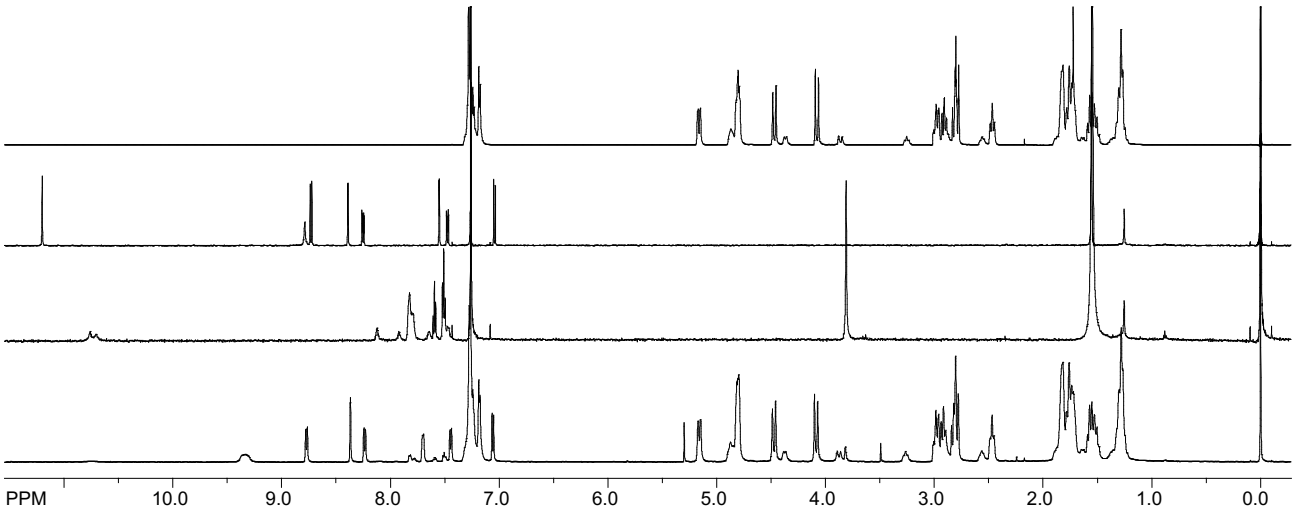

Figure C15. [1]H-NMR analysis (from top to bottom) of pure PZQ, NCM and MBZ compared to the sample of exp. N° 4.

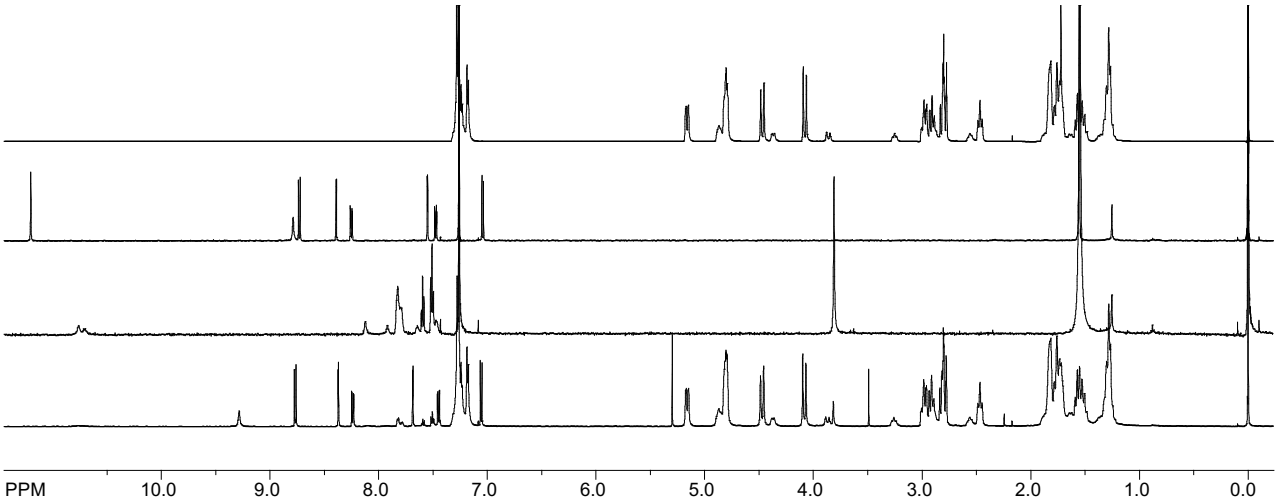

Figure C16. [1]H-NMR analysis (from top to bottom) of pure PZQ, NCM and MBZ compared to the sample of exp. N° 5.

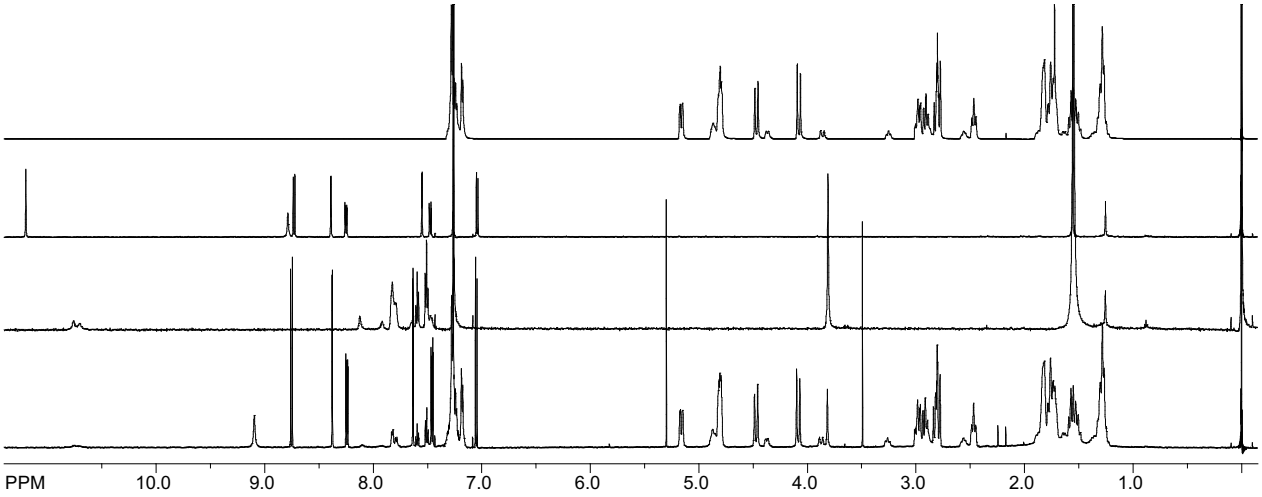

Figure C17. [1]H-NMR analysis (from top to bottom) of pure PZQ, NCM and MBZ compared to the sample of exp. N° 6.

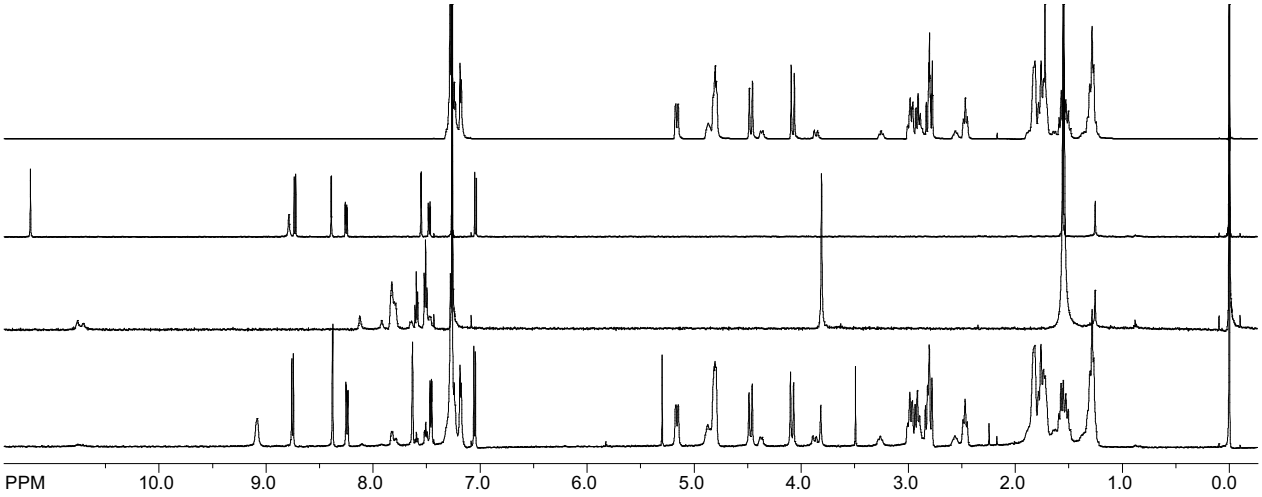

Figure C18. [1]H-NMR analysis (from top to bottom) of pure PZQ, NCM and MBZ compared to the sample of exp. N° 7.

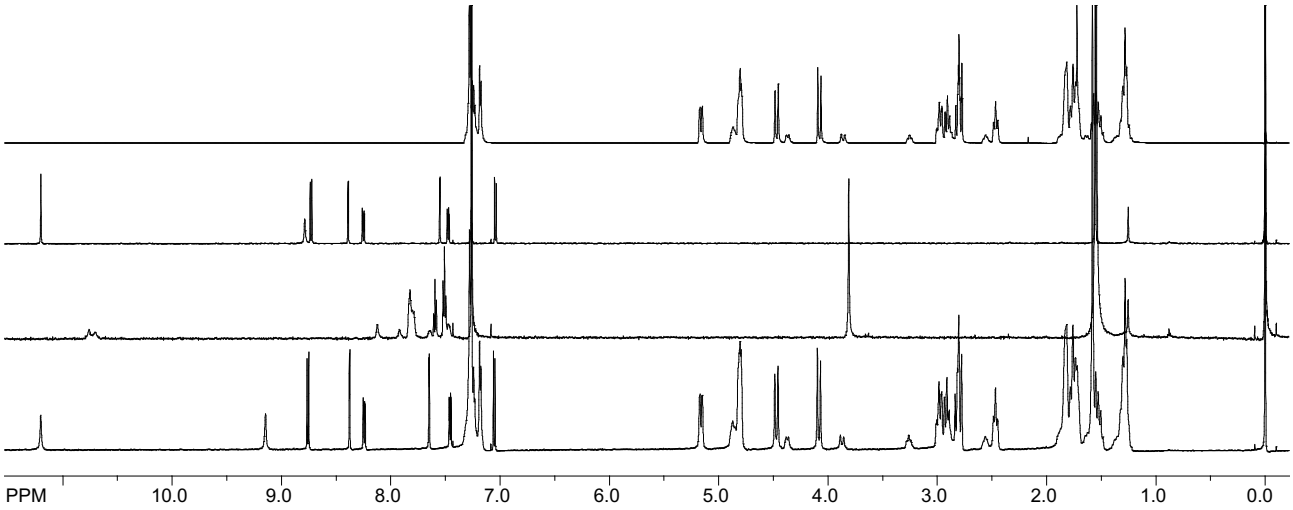

Figure C19. [1]H-NMR analysis (from top to bottom) of pure PZQ, NCM and MBZ compared to the sample of exp. N° 8.

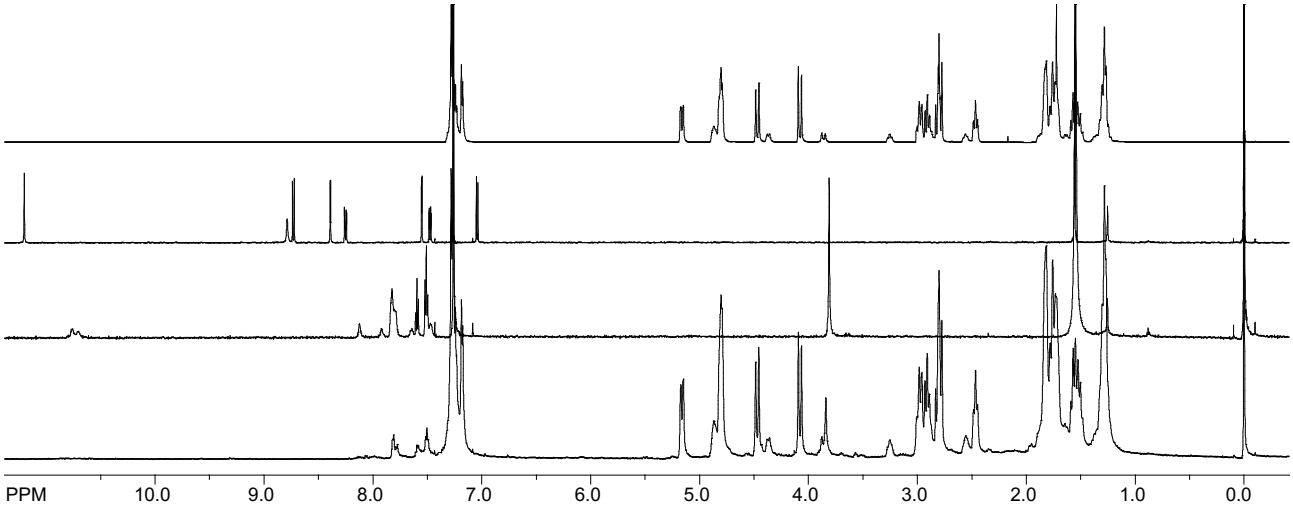

Figure C20. [1]H-NMR analysis (from top to bottom) of pure PZQ, NCM and MBZ compared to the sample of exp. N° 9.

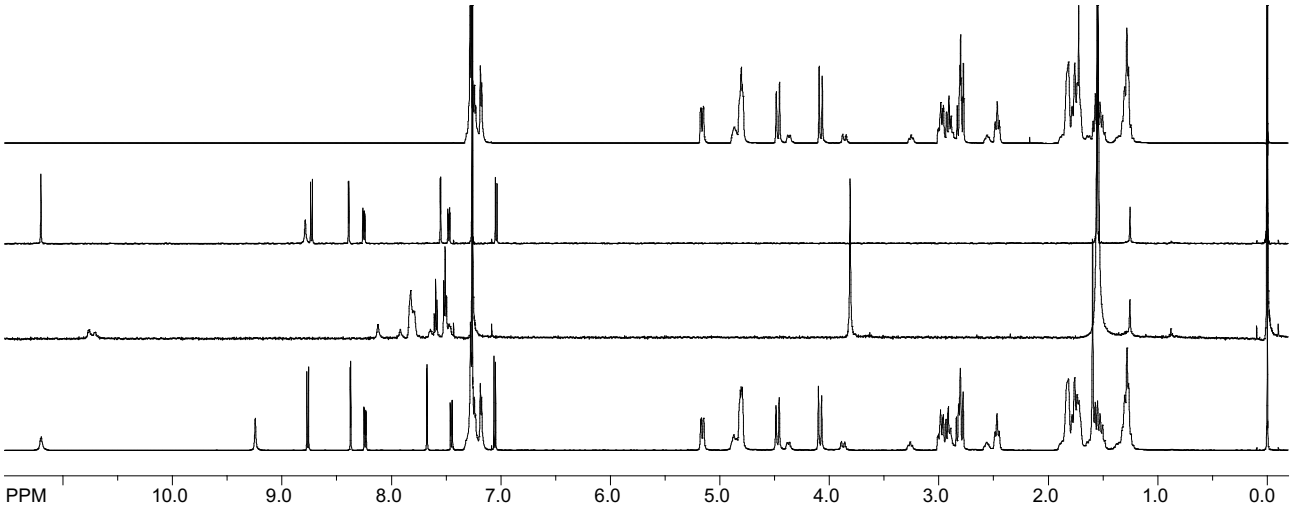

Figure C21. [1]H-NMR analysis (from top to bottom) of pure PZQ, NCM and MBZ compared to the sample of exp. N° 10.

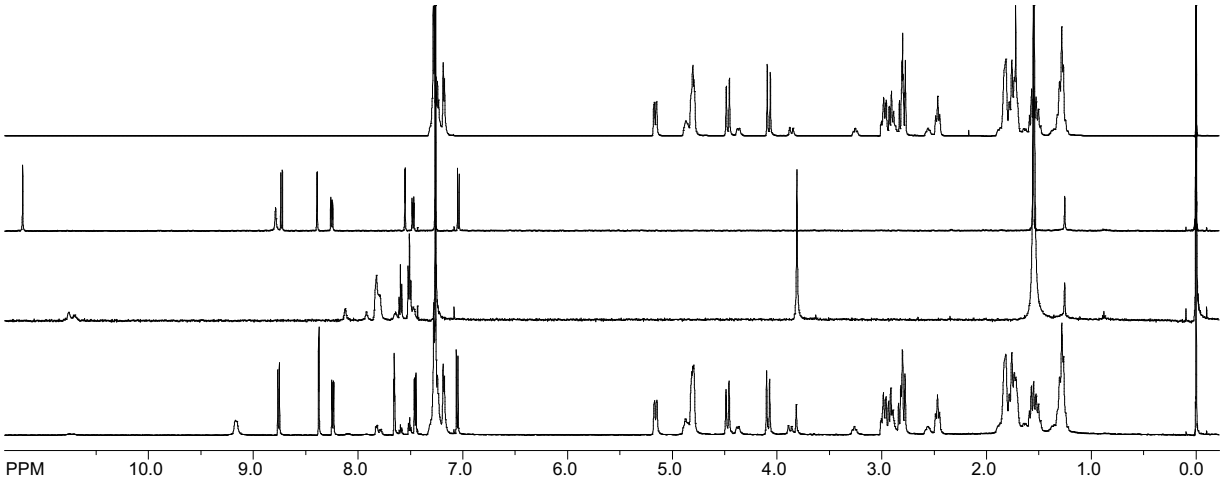

Figure C22. [1]H-NMR analysis (from top to bottom) of pure PZQ, NCM and MBZ compared to the sample of exp. N° 11.

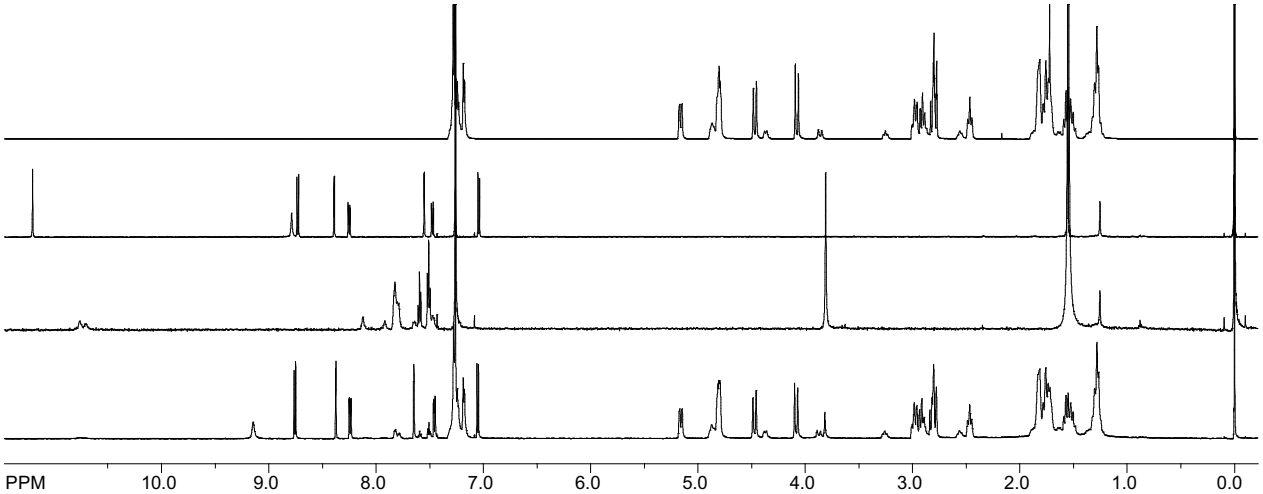

Figure C23. [1]H-NMR analysis (from top to bottom) of pure PZQ, NCM and MBZ compared to the sample of exp. N° 12.

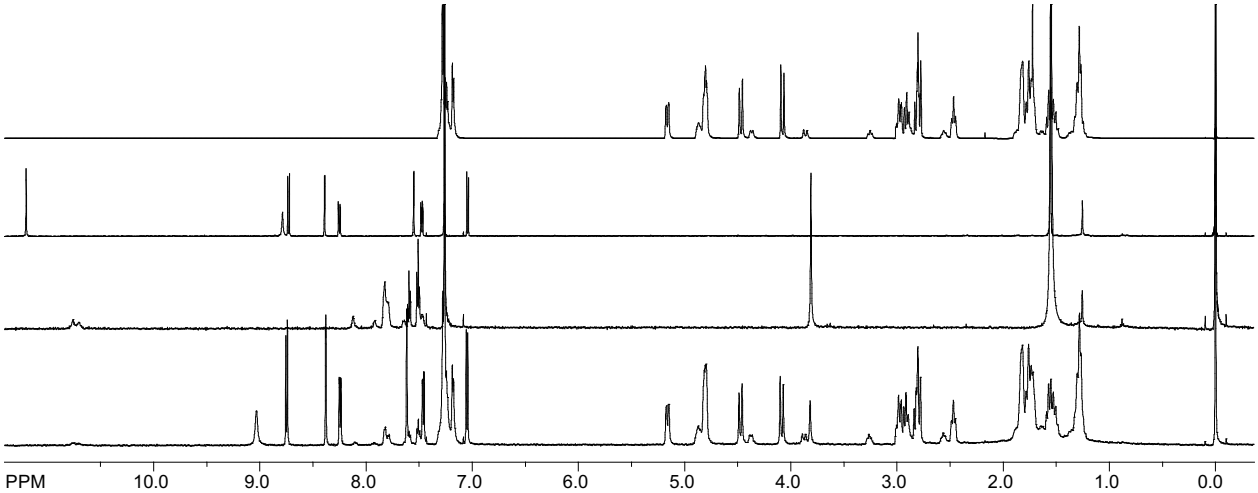

Figure C24. [1]H-NMR analysis (from top to bottom) of pure PZQ, NCM and MBZ compared to the sample of exp. N° 13.

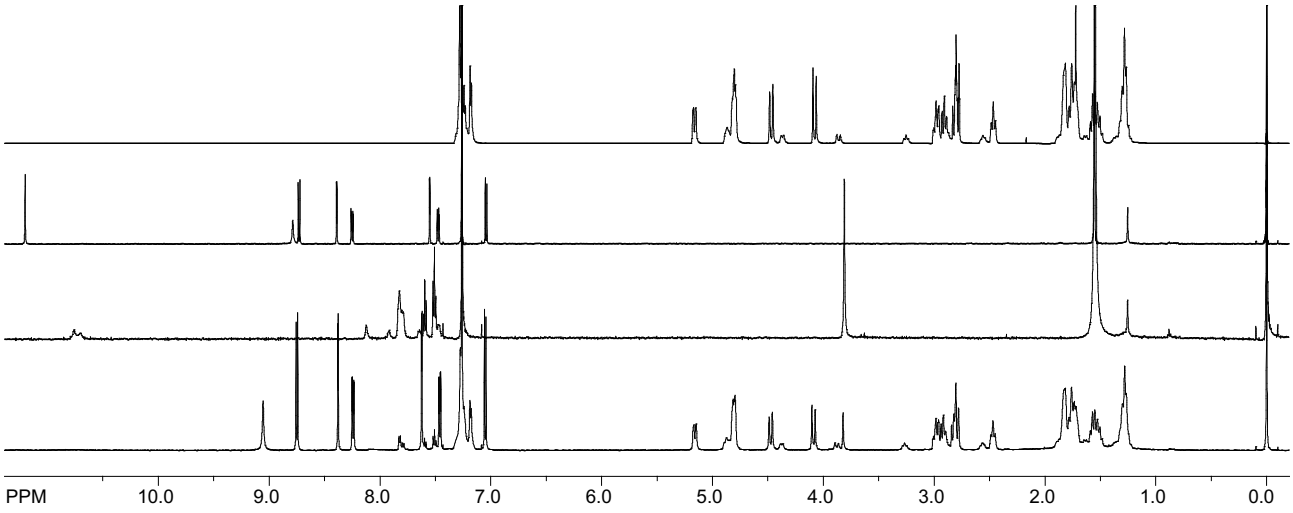

Figure C25. [1]H-NMR analysis (from top to bottom) of pure PZQ, NCM and MBZ compared to the sample of exp. N° 14.

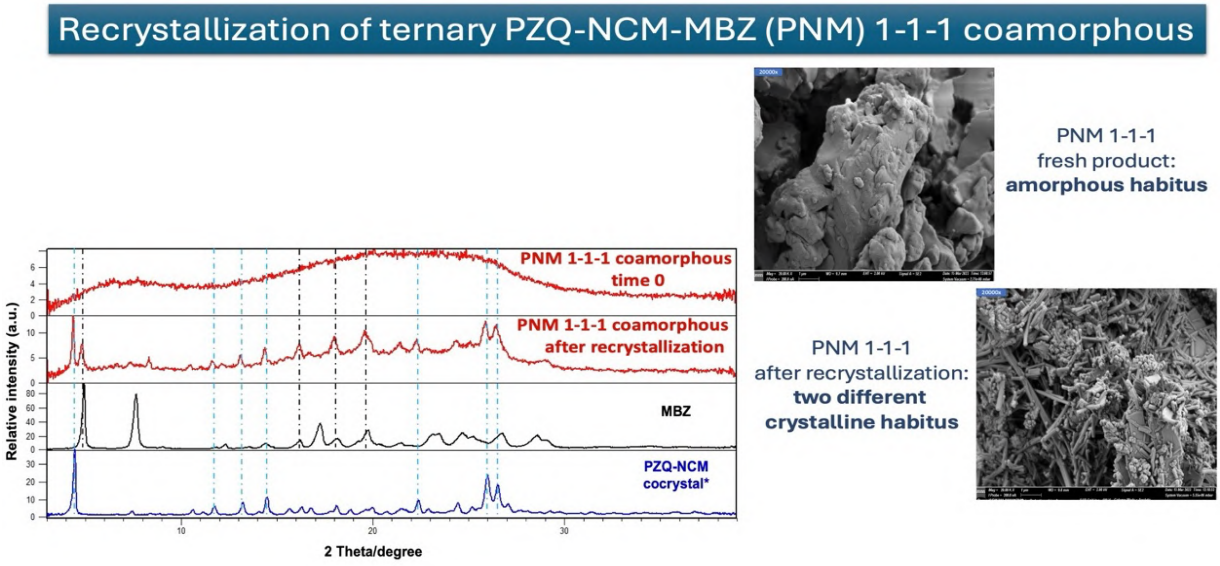

Figure C26. Cartoon depicting the recrystallization of ternary PZQ-MBZ-NCM 1:1:1 coamorphous into a mixture of MBZ and PZQ-NCM 1:3 anhydrous cocrystal through SEM and PXRD. Black dotted lines represent MBZ reflections, while light blue dotted lines PZQ-NCM 1:3 anhydrous cocrystal reflections.

Appendix D

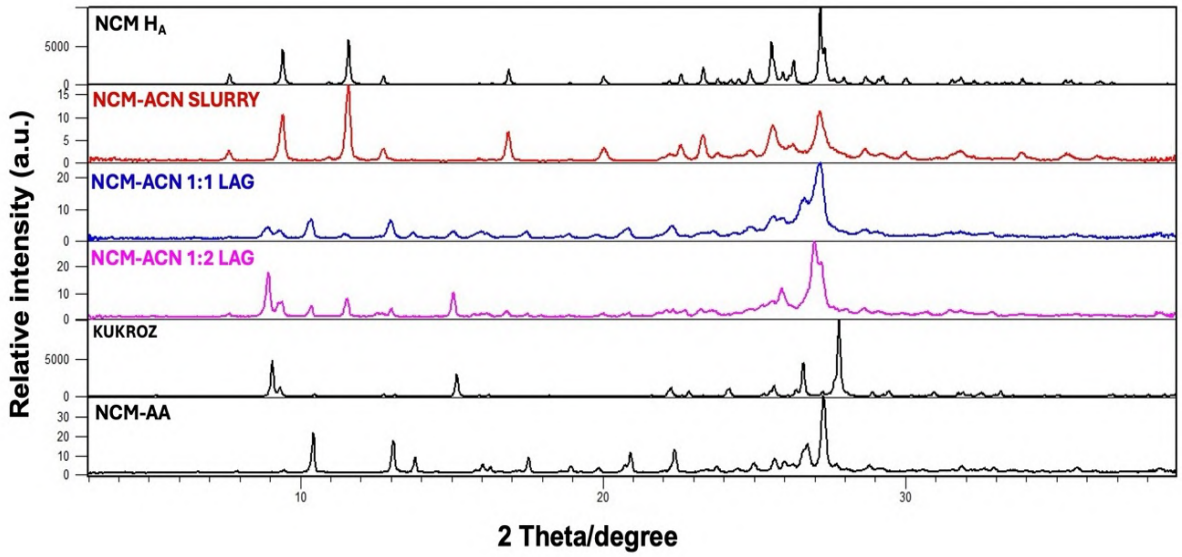

Figure D1. PXRD of NCM H_A, previously reported NCM-ACN monosolvate (CSD refcode KUKROZ [221]) and NCM-AA solvate (black), slurry of NCM-ACN (red), LAG of NCM-ACN 1:1 (blue) and LAG of NCM-ACN 1:2 (pink).

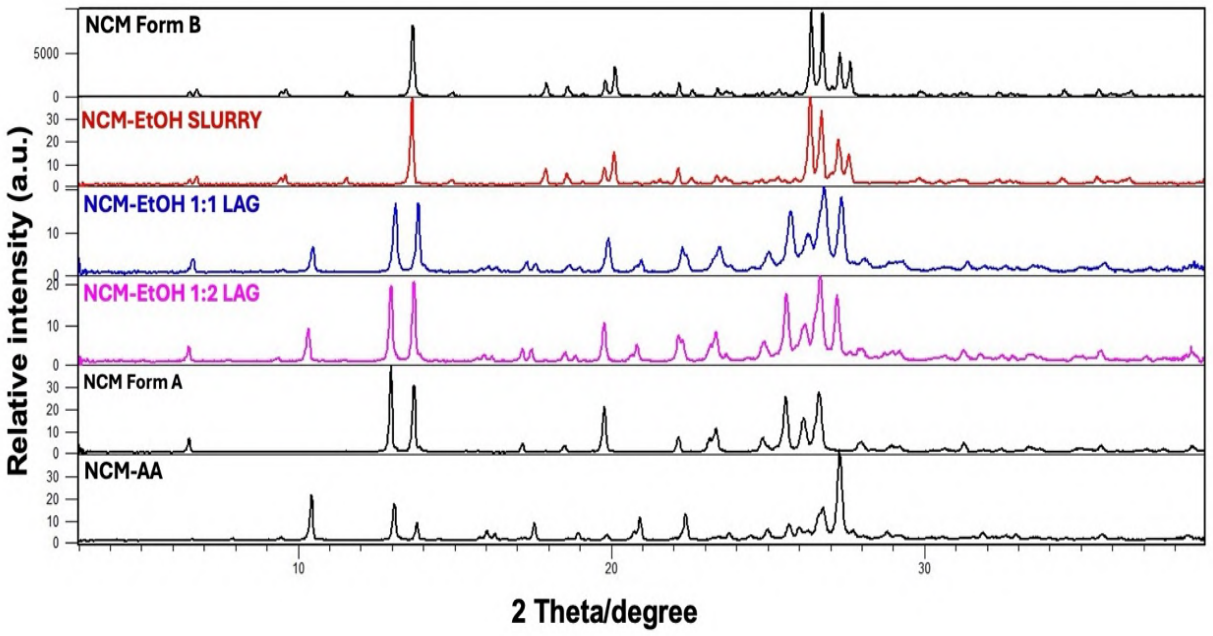

Figure D2. PXRD of NCM Form A, NCM Form B and NCM-AA solvate (black), slurry of NCM-EtOH (red), LAG of NCM-EtOH 1:1 (blue) and LAG of NCM-EtOH 1:2 (pink).

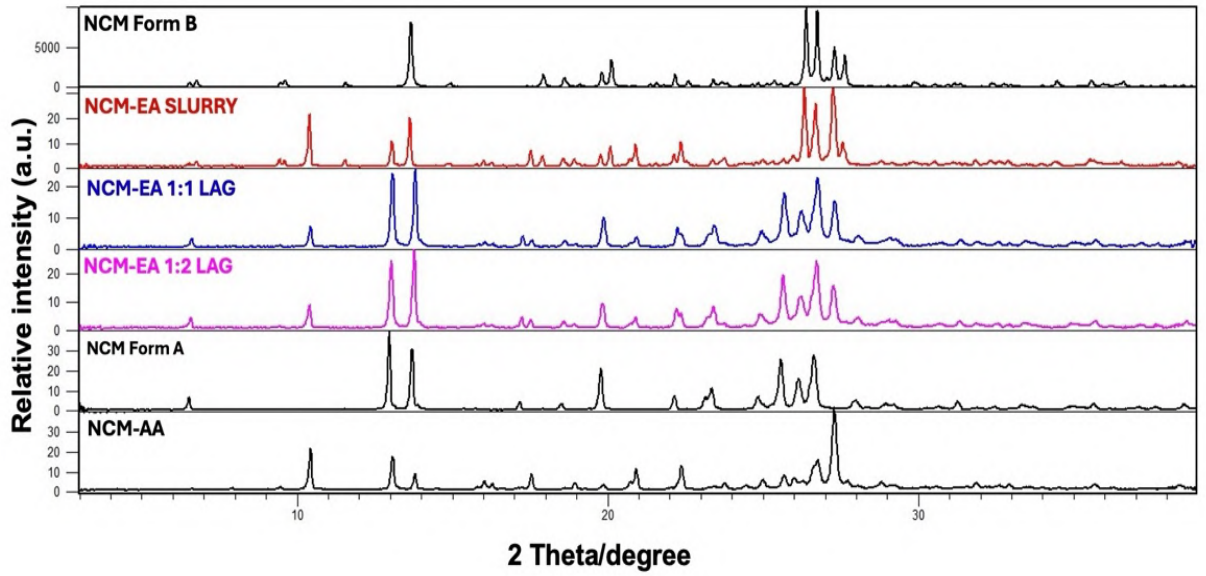

Figure D3. PXRD of NCM Form A, NCM Form B and NCM-AA solvate (black), slurry of NCM-EA (red), LAG of NCM-EA 1:1 (blue) and LAG of NCM-EA 1:2 (pink).

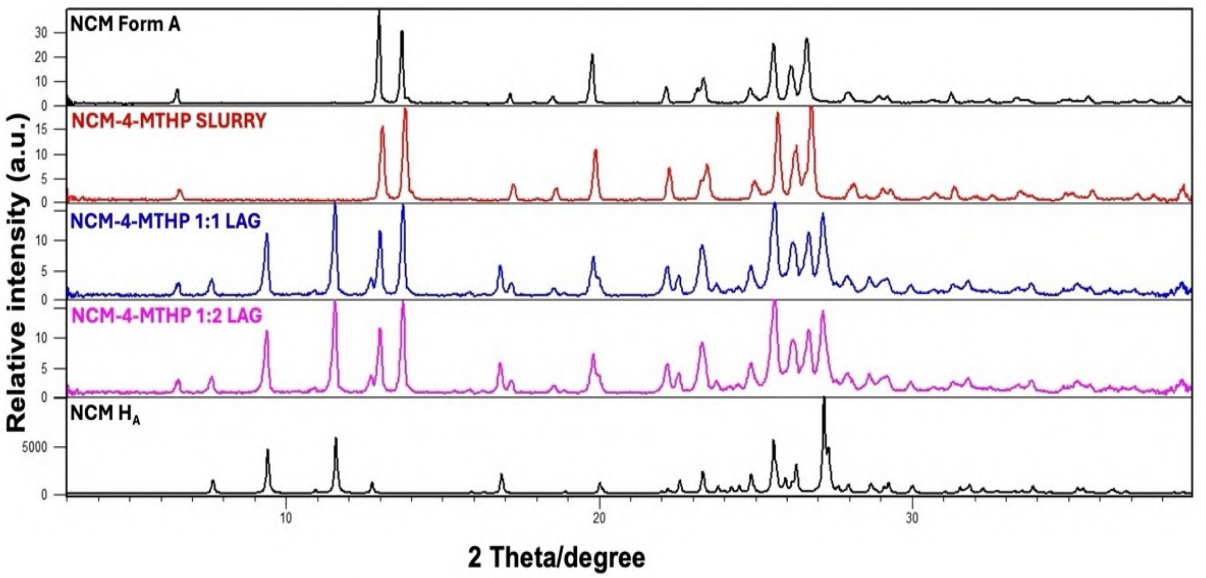

Figure D4. PXRD of NCM Form A, NCM H_A (black), slurry of NCM-4-MTHP (red), LAG of NCM-4-MTHP 1:1 (blue) and LAG of NCM-4-MTHP 1:2 (pink).

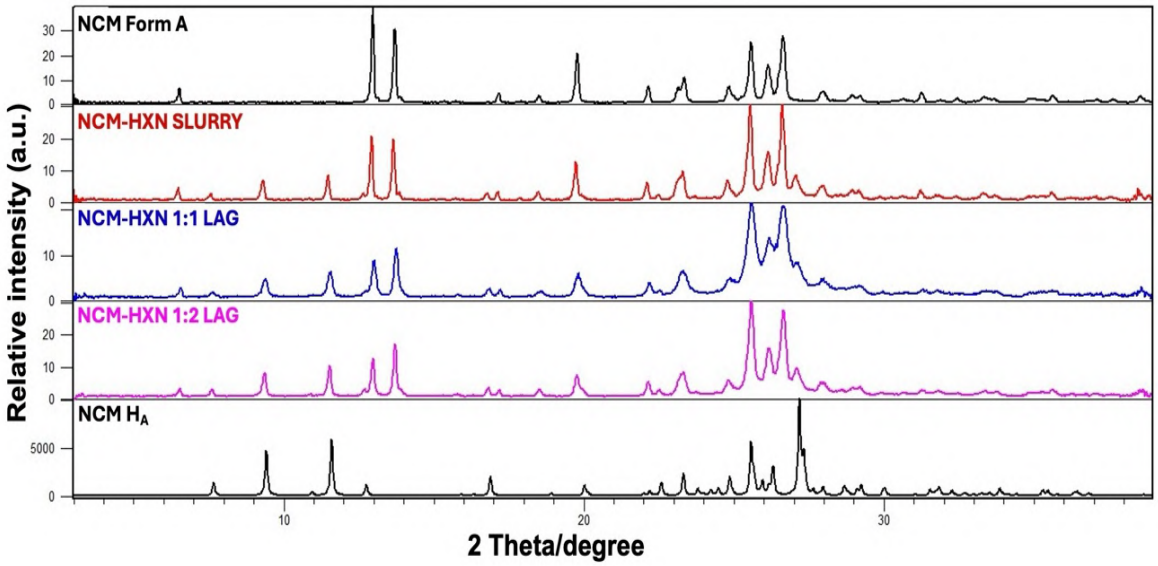

Figure D5. PXRD of NCM Form A, NCM H_A (black), slurry of NCM-HXN (red), LAG of NCM-HXN 1:1 (blue) and LAG of NCM-HXN 1:2 (pink).

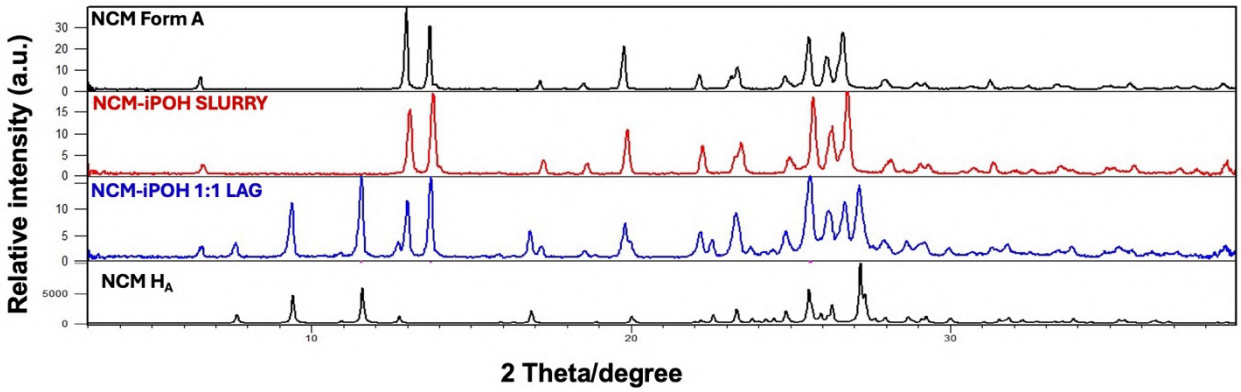

Figure D6. PXRD of NCM Form A, NCM H_A (black), slurry of NCM-iPOH (red) and LAG of NCM-iPOH 1:1 (blue).

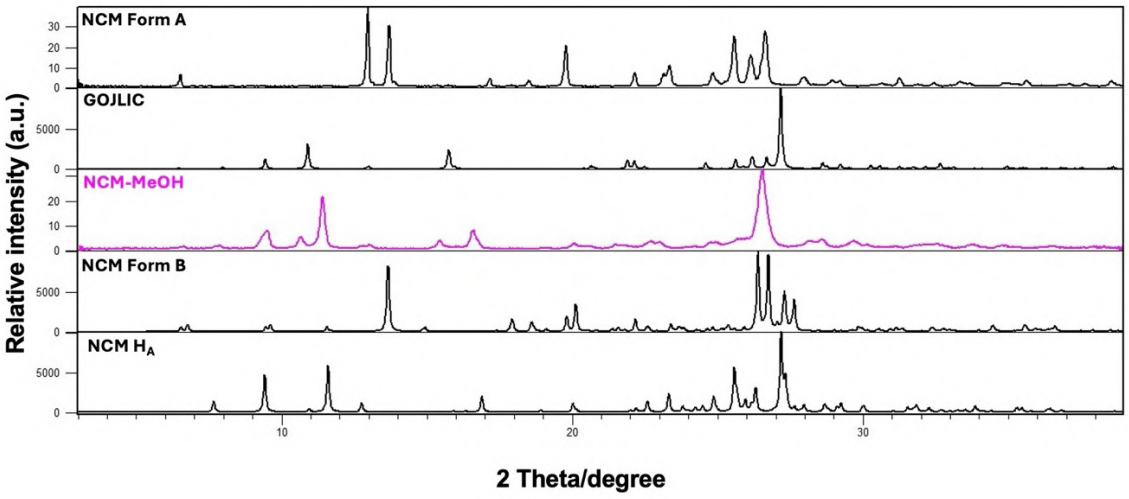

Figure D7. PXRD of NCM Form A, NCM Form B, GOJLIC and NCM H_A (black) and the new phase NCM-MeOH (pink).

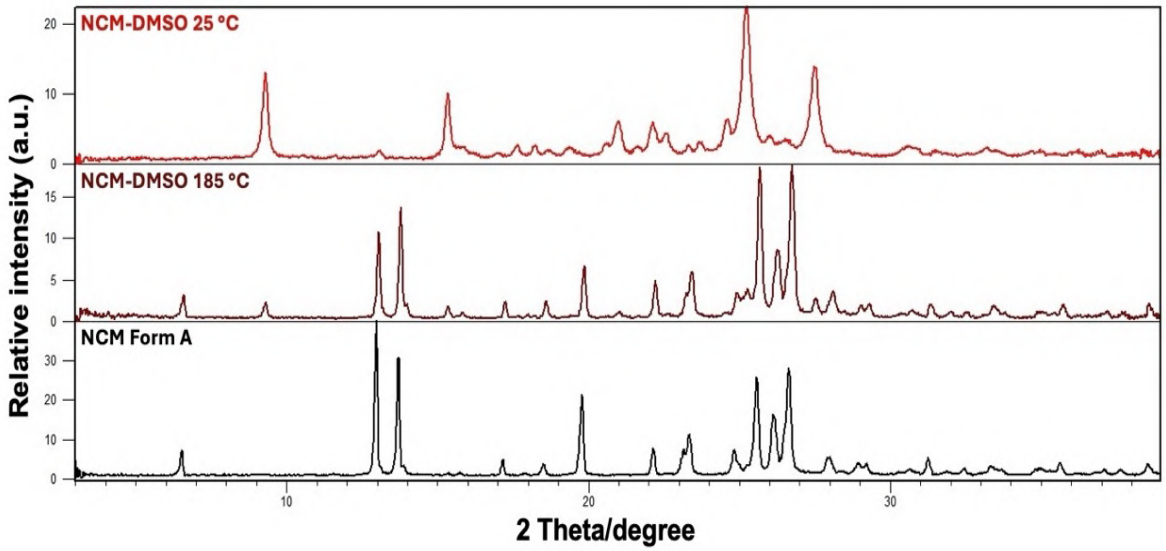

Figure D8. PXRD of NCM-DMSO at room temperature (red), NCM-DMSO after heating/desolvation (brown) and NCM Form A (black).

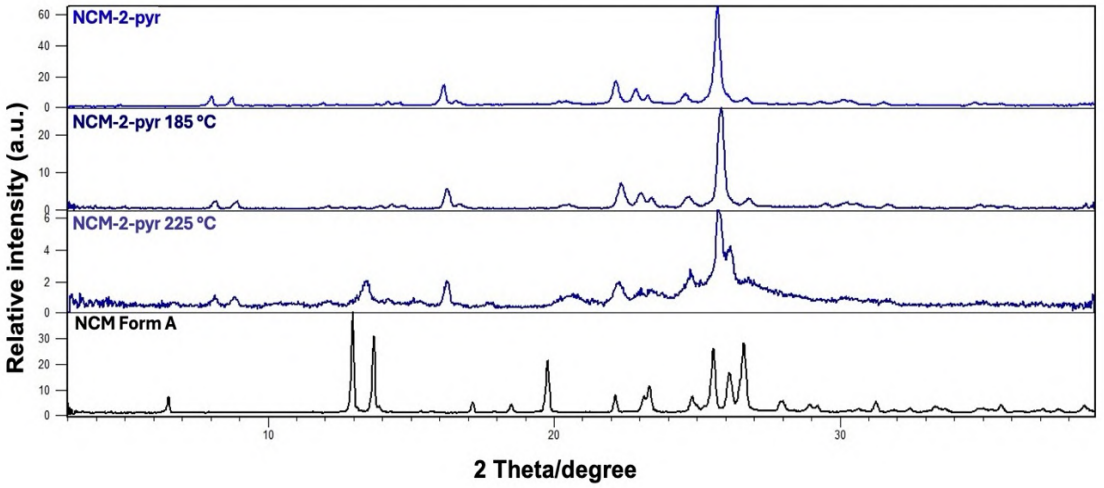

Figure D9. PXRD of NCM-2-pyr at room temperature (blue), NCM-2-pyr after heating to 185 °C (dark blue), NCM-2-pyr after heating to 225 °C (metallic blue) and NCM Form A (black).

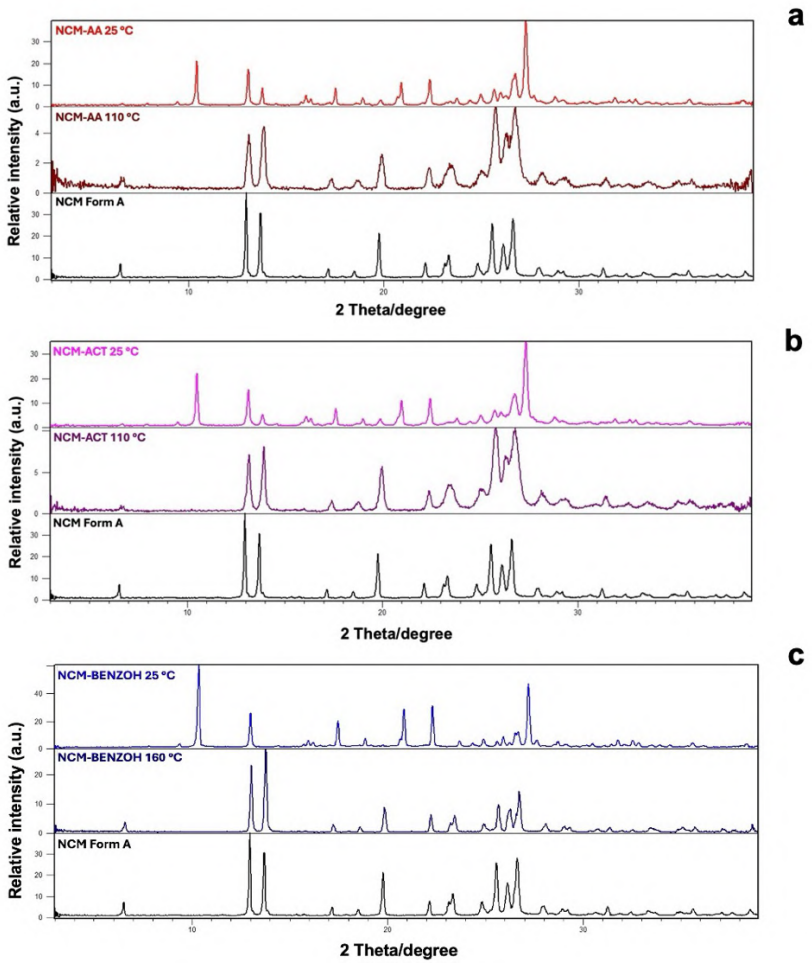

Figure D10. (a) PXRD of NCM-AA at room temperature (red), NCM-AA after heating to 110 °C (brown) and NCM Form A (black). (b) PXRD of NCM-ACT at room temperature (pink), NCM-AA after heating to 110 °C (purple) and NCM Form A (black). (c) PXRD of NCM-BENZOH at room temperature (blue), NCM-BENZOH after heating to 160 °C (dark blue) and NCM Form A (black).

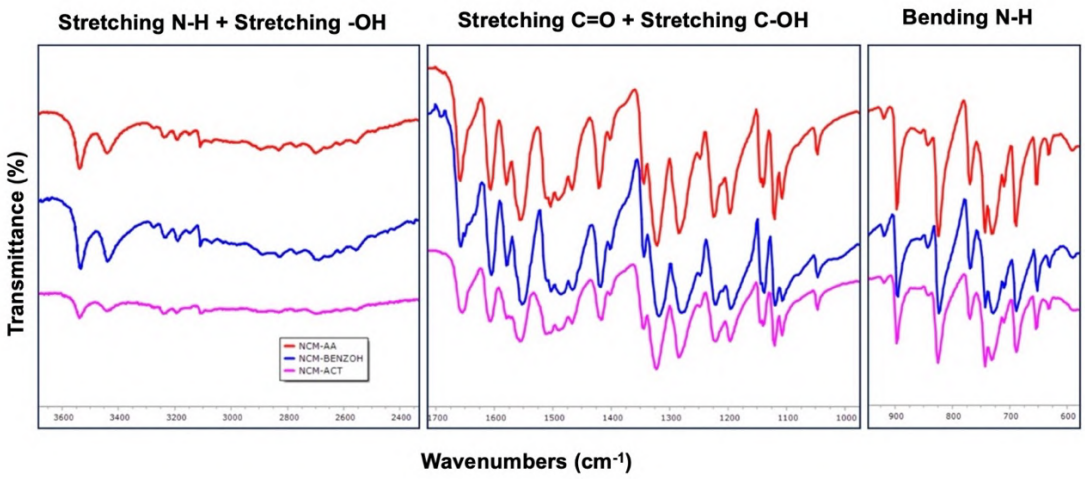

Figure D11. Comparison of (FT-IR)-ATR spectra of NCM-AA solvate (red), NCM-BENZOH solvate (blue) and NCM-ACT solvate (pink).

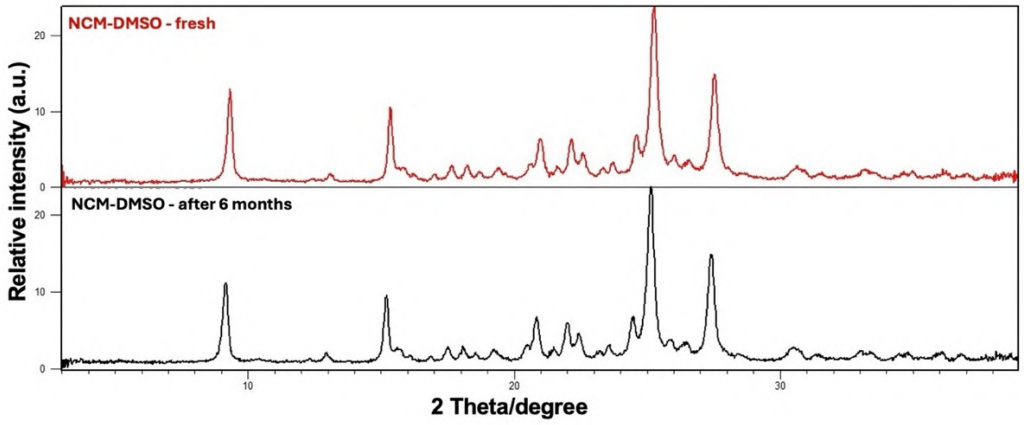

Figure D12. PXRD of NCM-DMSO as fresh product (red) and after 6 months of storage at room temperature (black).

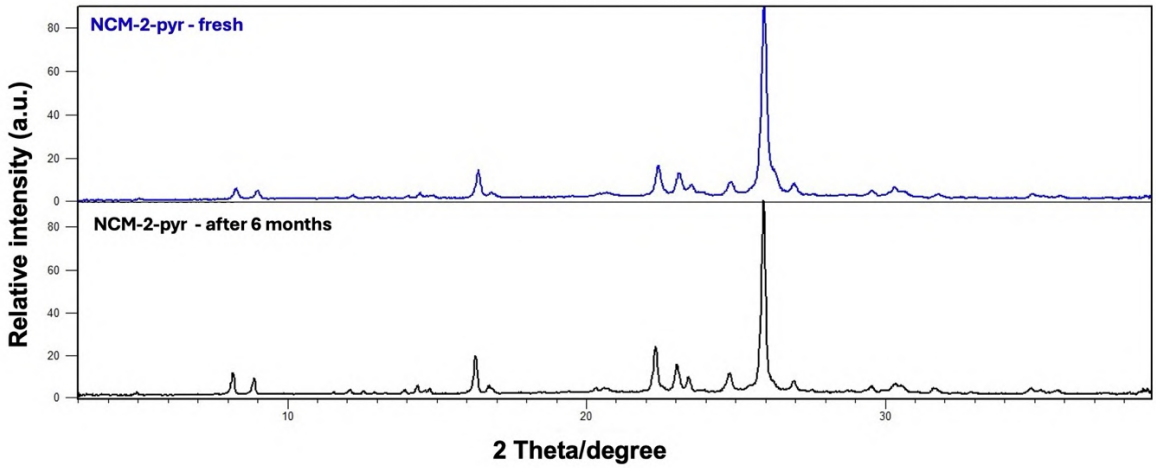

Figure D13. PXRD of NCM-2-pyr as fresh product (blue) and after 6 months of storage at room temperature (black).

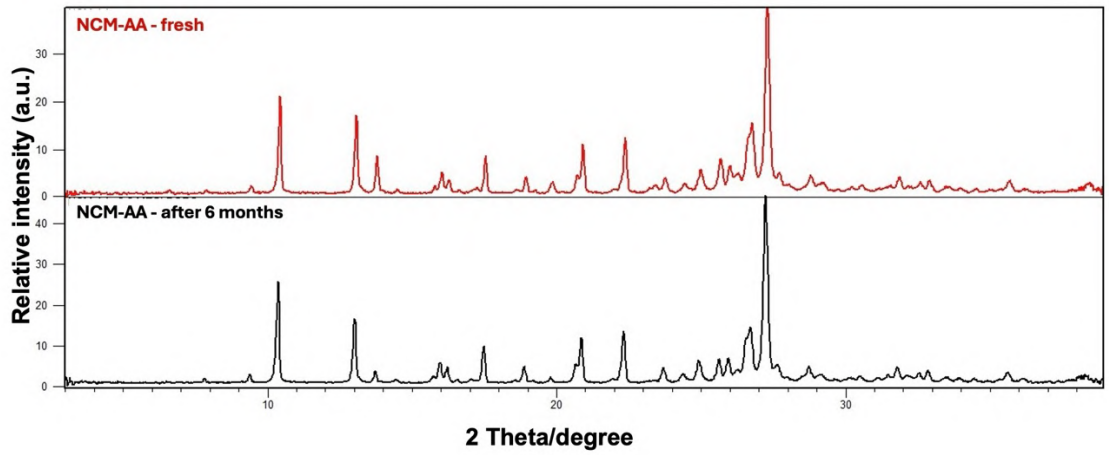

Figure D14. PXRD of NCM-AA as fresh product (red) and after 6 months of storage at room temperature (black).

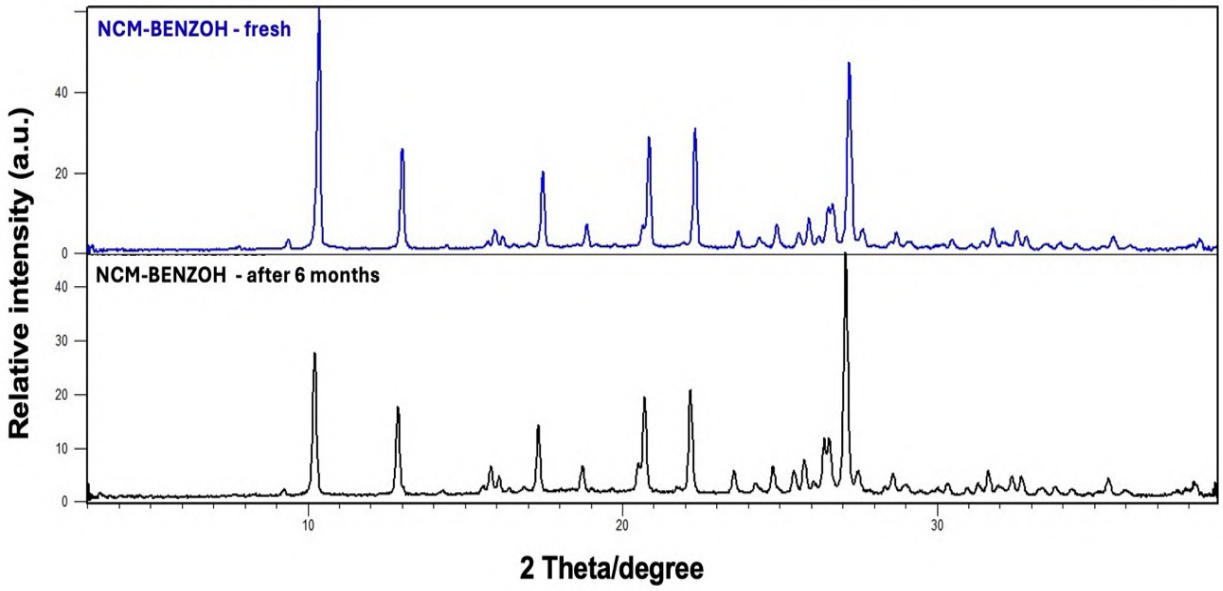

Figure D15. PXRD of NCM-BENZOH as fresh product (blue) and after 6 months of storage at room temperature (black).

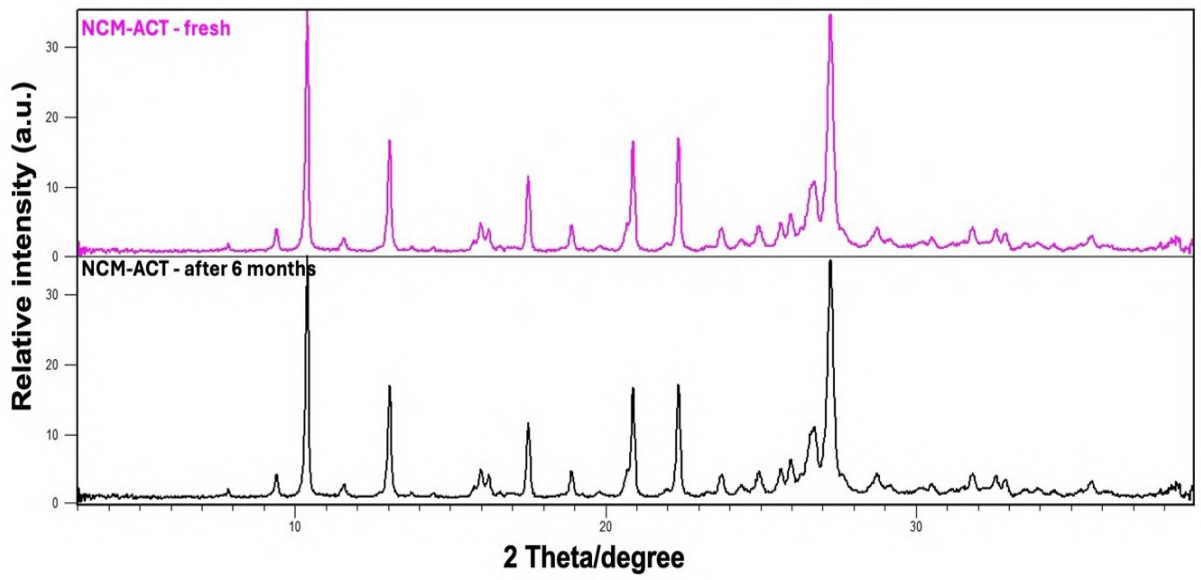

Figure D16. PXRD of NCM-ACT as fresh product (pink) and after 6 months of storage at room temperature (black).

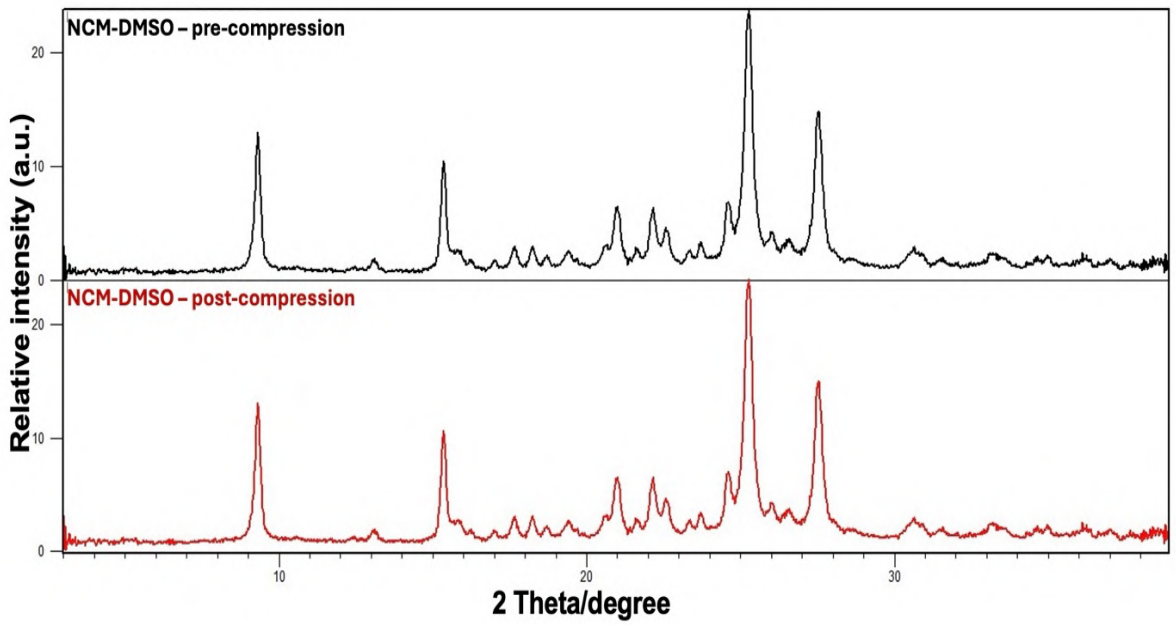

Figure D17. PXRD of NCM-DMSO pre-compression (black) and post-compression (red).

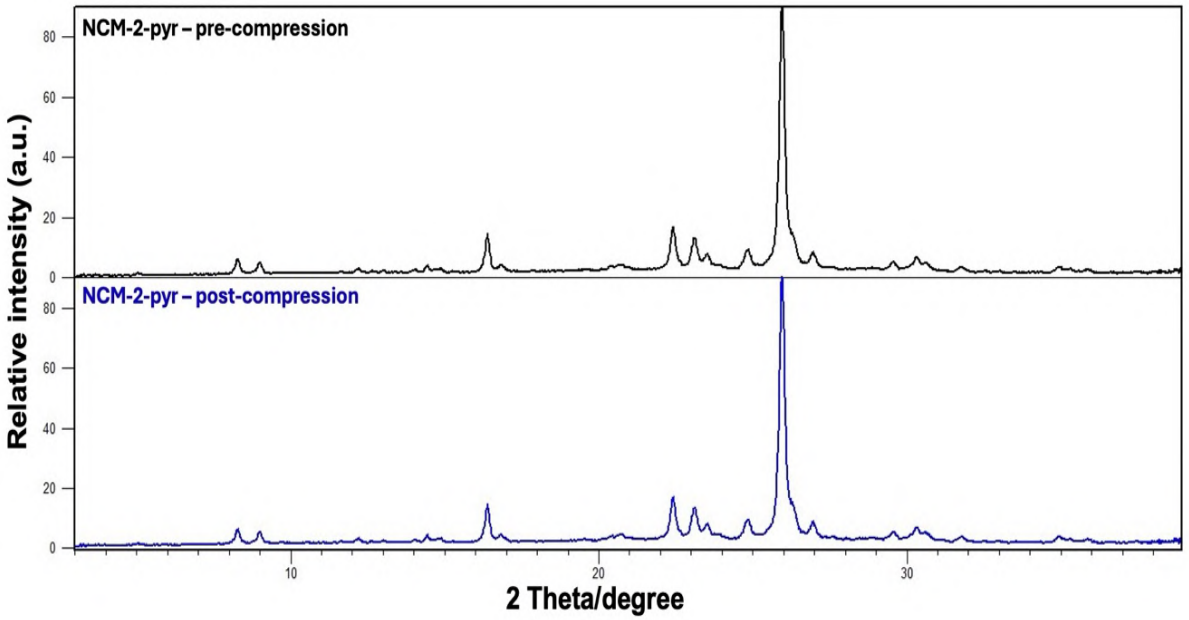

Figure D18. PXRD of NCM-2-pyr pre-compression (black) and post-compression (blue).

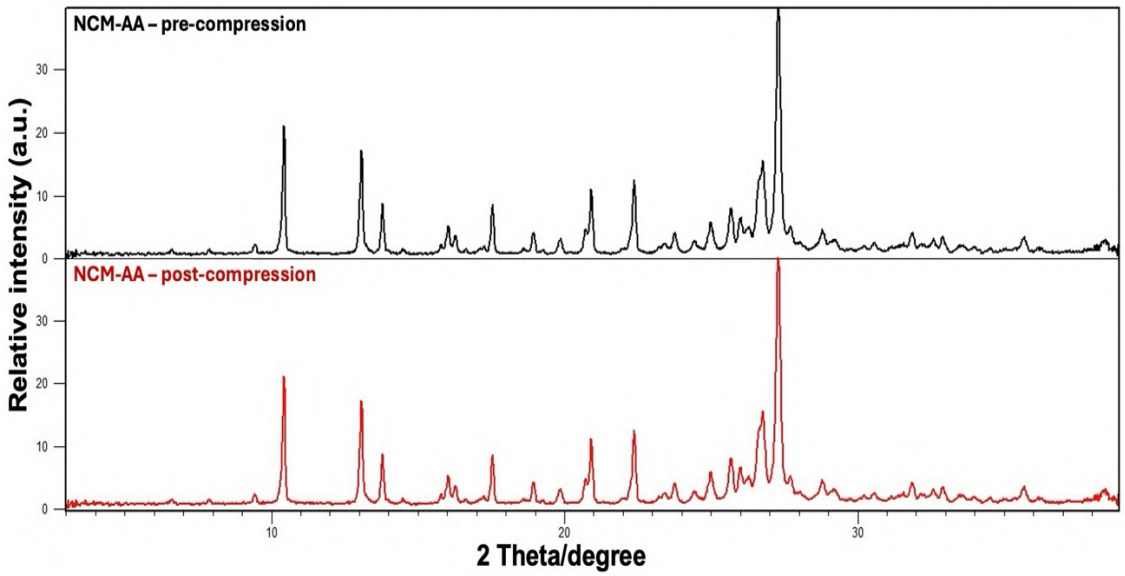

Figure D19. PXRD of NCM-AA pre-compression (black) and post-compression (red).

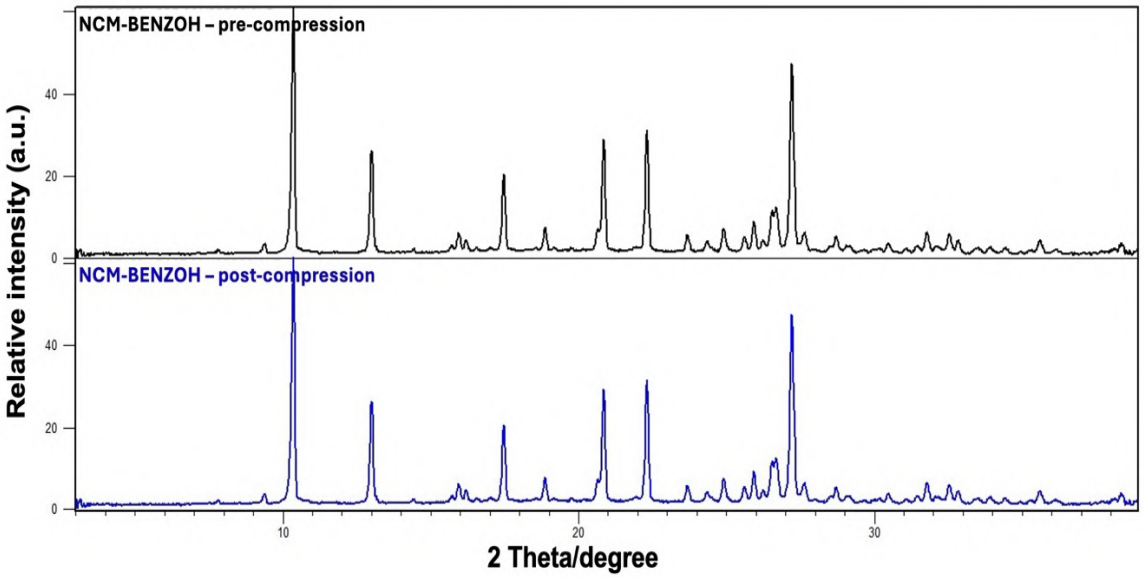

Figure D20. PXRD of NCM-BENZOH pre-compression (black) and post-compression (blue).

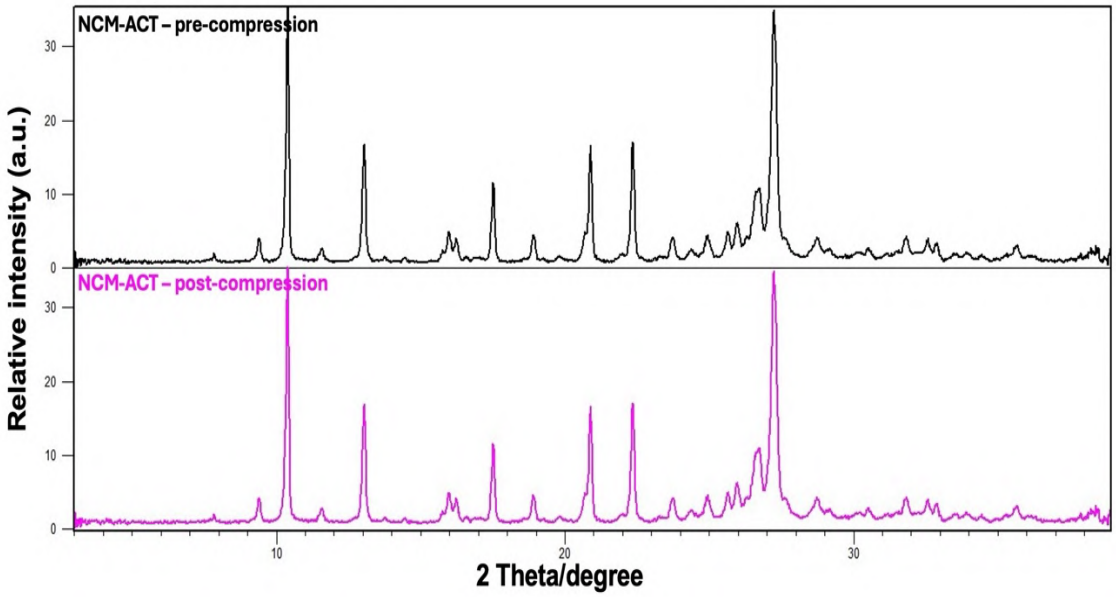

Figure D21. PXRD of NCM-ACT pre-compression (black) and post-compression (pink).

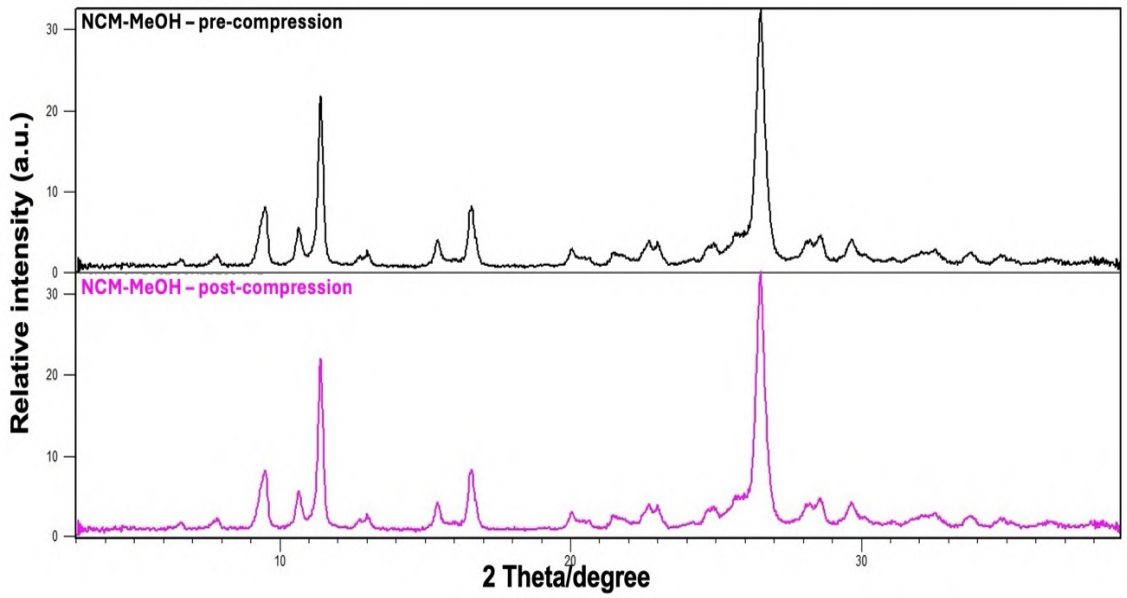

Figure D21. PXRD of NCM-MeOH pre-compression (black) and post-compression (pink).

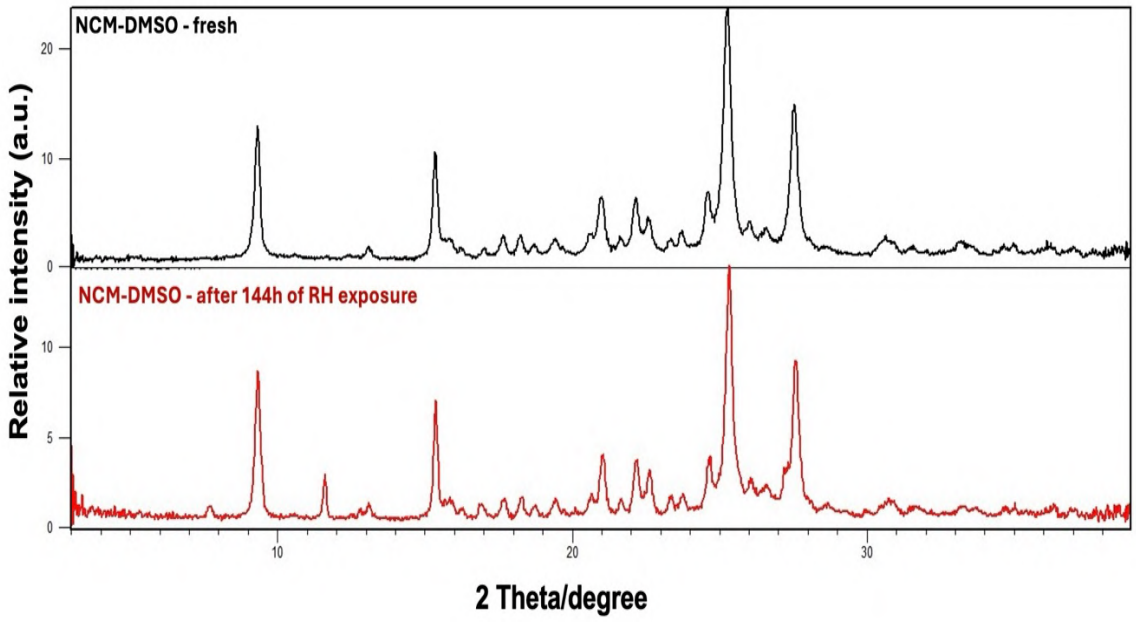

Figure D22. PXRD of NCM-DMSO as fresh product (black) and after 144h of high RH exposure (red).

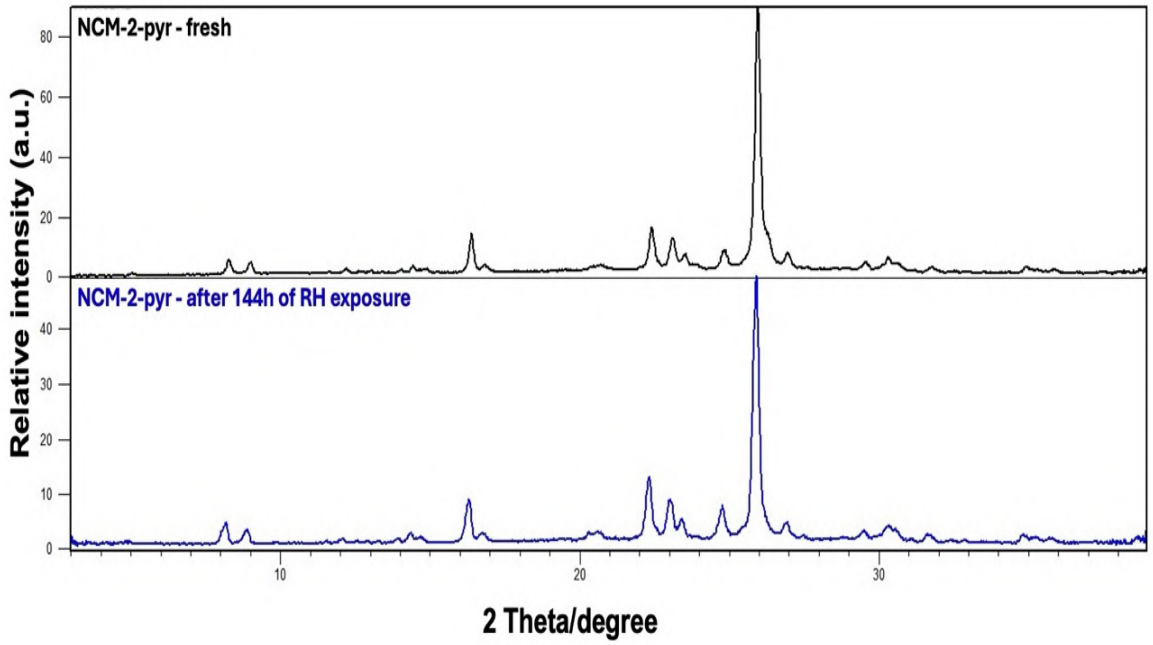

Figure D23. PXRD of NCM-2-pyr as fresh product (black) and after 144h of high RH exposure (blue).

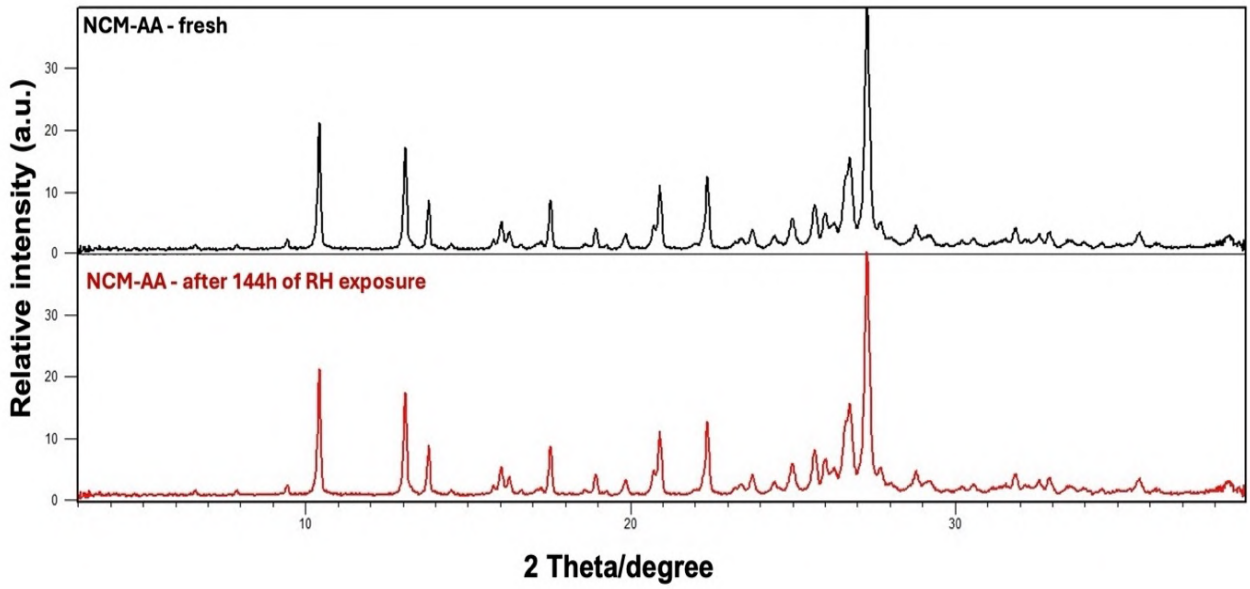

Figure D24. PXRD of NCM-AA as fresh product (black) and after 144h of high RH exposure (red).

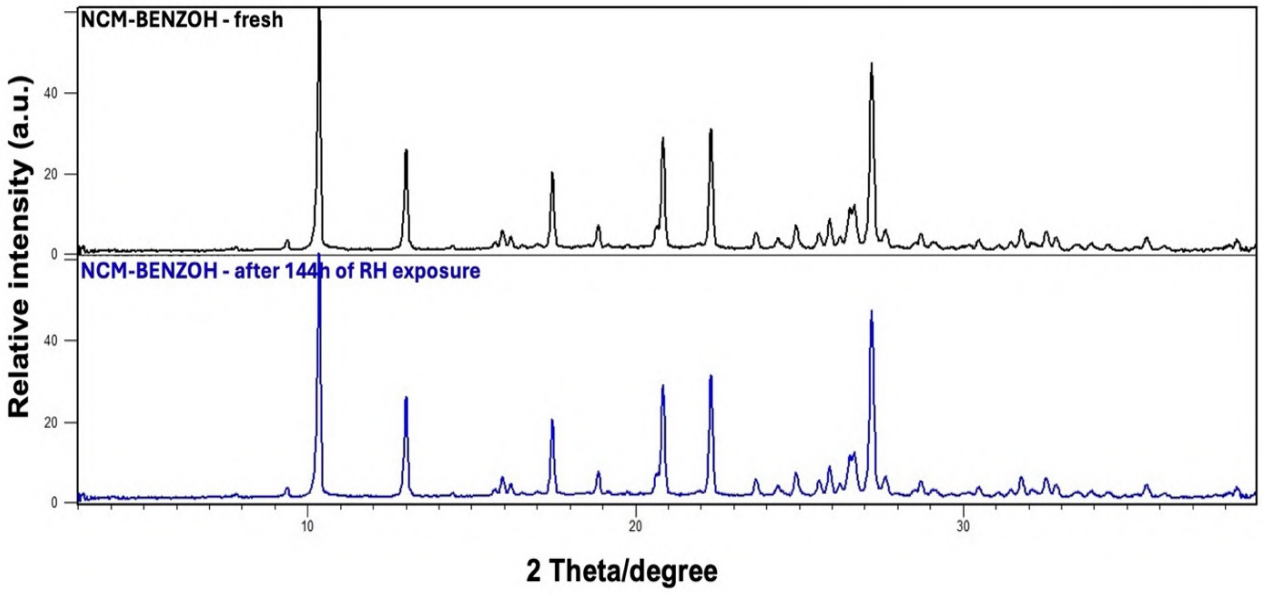

Figure D25. PXRD of NCM-BENZOH as fresh product (black) and after 144h of high RH exposure (blue).

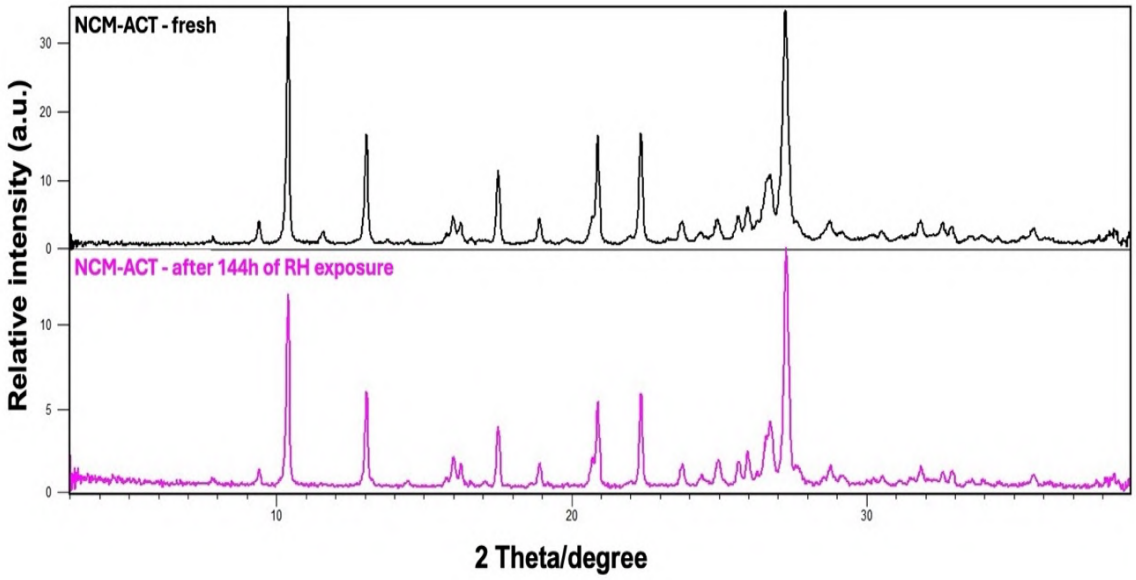

Figure D26. PXRD of NCM-ACT as fresh product (black) and after 144h of high RH exposure (pink).

Summary of Publications and Activities

PhD courses

- "Electron microscopy: an introduction to SEM, TEM and AFM"
  F. Rigoni, University of Venice, Italy
  30 hours, 11/01/2022 - 08/02/2022.

- "Regulatory and Intellectual Property in Drug Development"
  J. Zanon, University of Trieste, Italy
  15 hours, 29/03/2022 - 17/05/2022.

- "Specificity of molecular solids"
  G. Coquerel, Y. Cartigny and J. H. ter Horst, University of Rouen, France
  30 hours, 06/09/2022 - 28/10/2022.

- "Symmetry (+reminder) + fundamental of nucleation and growth"
  G. Coquerel, G. Gbabode and V. Dupray, University of Rouen, France
  30 hours, 08/09/2022 - 29/11/2022.

- "Characterization of molecular crystals"
  G. Coquerel and Y. Cartigny, University of Rouen, France
  15 hours, 20/09/2022 - 18/10/2022.

Cross-disciplinary training courses

- "Business management e gestione delle imprese"
  07/12/2021, University of Trieste, Italy.

- "10 tips for preparing a good manuscript"
  15/02/2022, University of Trieste, Italy.

Publications list

- "Overcoming the Drawbacks of Sulpiride by Means of New Crystal Forms"
  R. Birolo, F. Bravetti, S. Bordignon, **I. D'Abbrunzo**, P. P. Mazzeo, B. Perissutti, A. Bacchi, M. R. Chierotti, R. Gobetto
  Pharmaceutics 2022, 14, 1754. https://doi.org/10.3390/pharmaceutics14091754

- "Praziquantel meets Niclosamide: A dual-drug Antiparasitic Cocrystal"
  I. D'Abbrunzo, E. Bianco, L. Gigli, N. Demitri, R. Birolo, M. R. Chierotti, I. Škorić, J. Keiser, C. Häberli, D. Voinovich, D. Hasa, B. Perissutti
  International Journal of Pharmaceutics 2023, 644, 123315. https://doi.org/10.1016/j.ijpharm.2023.123315

- "Competitive mechanochemical solvate formation of theophylline in the presence of miscible liquid mixtures"
  I. D'Abbrunzo, M. Spadaro, M. Arhanlgelskis, G. Zingone, D. Hasa, B. Perissutti
  Crystal Growth & Design 2023**,** 23(11), 8094-8102. https://doi.org/10.1021/acs.cgd.3c00834

- "Praziquantel Fifty Years on: A Comprehensive Overview of Its Solid State"
  I. D'Abbrunzo, G. Procida, B. Perissutti
  Pharmaceutics 2024**,** 16(1), 27. https://doi.org/10.3390/pharmaceutics16010027

- "Mechanochemical Synthesis of Praziquantel Hemihydrate in the Presence of Five Solvents with Different Water Miscibility"
  I. D'Abbrunzo, D. Voinovich, B. Perissutti
  Crystals 2024**,** 14(4), 374. https://doi.org/10.3390/cryst14040374

- "Enantiospecific crystallisation behaviour of malic acid in mechanochemical reactions with vinpocetine"
  I. D'Abbrunzo, R. Birolo, M. R. Chierotti, D-K. Bučar, D. Voinovich, B. Perissutti, D. Hasa
  European Journal of Pharmaceutics and Biopharmaceutics 2024**,** 114344. https://doi.org/10.1016/j.ejpb.2024.114344

Congress presentations

Poster presentations

- "A new Antiparasitic cocrystal of Praziquantel and Niclosamide" **I. D'Abbrunzo**, E. Bianco, L. Gigli, N. Demitri, R. Birolo, M. R. Chierotti, I. Škorić, J. Keiser, C. Häberli, D. Voinovich, D. Hasa, B. Perissutti; XXIII ADRITELF Symposium, 11-13 September 2023, Savoia Excelsior Palace, Riva del Mandracchio 4, Trieste, 34124, Italy.

- "A Cocrystal Solvate of Praziquantel, Niclosamide and Acetic Acid with anthelminthic properties" **I. D'Abbrunzo**, L. Battaiotto, L. Gigli, N. Demitri, C. Sabena, M. R. Chierotti, S. Bertoni, I. Škorić, J. Keiser, D. Voinovich, D. Hasa, B. Perissutti; 59th ISCoC, 31 May-08 June 2024, Centro per la Cultura Scientifica Ettore Maiorana, Erice (TP), 91016, Italy

Oral presentations

- "Innovative and affordable multidrug solids as a promising strategy for the treatment of tropical diseases" **I. D'Abbrunzo**, D. Hasa, B. Perissutti; XXIII ADRITELF Doctoral School of Pharmaceutical Technology, 13-15 September 2023, Savoia Excelsior Palace, Riva del Mandracchio 4, Trieste, 34124, Italy

Video presentations

- "Role of chirality on the formation of multicomponent crystalline solids containing vinpocetine" **I. D'Abbrunzo**, D. Hasa, B. Perissutti; 13th CESPT, 16-18 September 2021, Gdańsk, Poland.
  Hybrid conference due to Covid-related restrictions.

Auxiliary teaching

- Laboratory Assistant in Pharmaceutical Technology I – Master degree in Pharmacy
  Department of Chemical and Pharmaceutical Sciences, University of Trieste, Italy.
  50 hours per year; Academic years 2021-2022, 2022-2023, 2023-2024.

Periods abroad – Erasmus

- Six-month Erasmus traineeship scholarship at the Laboratoire Sciences et Méthodes Séparatives, University of Rouen, Mont-Saint-Aignan cedex France-Normandie under the supervision of Professor Gerard Coquerel.
  05/09/2022 – 25/02/2023.

Awards

- 1st classified for the PhD scholarship "Prof. Fulvio Rubessa – Dottorato di Ricerca in Chimica", Department of Chemical and Pharmaceutical Sciences, 28 August 2024, University of Trieste, Italy.

Bibliography

1. Štrukil, V.; Fábián, L.; Reid, D.G.; Duer, M.J.; Jackson, G.J.; Eckert-Maksić, M.; Friščić, T. Towards an Environmentally-Friendly Laboratory: Dimensionality and Reactivity in the Mechanosynthesis of Metal–Organic Compounds. *Chemical Communications* **2010**, 46, 9191, doi:10.1039/c0cc03822a.
2. Ardila-Fierro, K.J.; Hernández, J.G. Sustainability Assessment of Mechanochemistry by Using the Twelve Principles of Green Chemistry. *ChemSusChem* **2021**, 14, 2145–2162, doi:10.1002/cssc.202100478.
3. James, S.L.; Adams, C.J.; Bolm, C.; Braga, D.; Collier, P.; Friščić, T.; Grepioni, F.; Harris, K.D.M.; Hyett, G.; Jones, W.; et al. Mechanochemistry: Opportunities for New and Cleaner Synthesis. *Chemical Society Reviews* **2012**, 41, 413–447, doi:10.1039/C1CS15171A.
4. Boldyreva, E. Mechanochemistry of Inorganic and Organic Systems: What Is Similar, What Is Different? *Chemical Society Reviews* **2013**, 42, 7719, doi:10.1039/c3cs60052a.
5. Solares-Briones, M.; Coyote-Dotor, G.; Páez-Franco, J.C.; Zermeño-Ortega, M.R.; de la O Contreras, C.M.; Canseco-González, D.; Avila-Sorrosa, A.; Morales-Morales, D.; Germán-Acacio, J.M. Mechanochemistry: A Green Approach in the Preparation of Pharmaceutical Cocrystals. *Pharmaceutics* **2021**, 13, 790, doi:10.3390/pharmaceutics13060790.
6. Pagola, S. Outstanding Advantages, Current Drawbacks, and Significant Recent Developments in Mechanochemistry: A Perspective View. *Crystals* **2023**, 13, 124, doi:10.3390/cryst13010124.
7. Dong, L.; Li, L.; Chen, H.; Cao, Y.; Lei, H. Mechanochemistry: Fundamental Principles and Applications. *Advanced Science* **2024**, e:2403949, doi:10.1002/advs.202403949.
8. Jones, W.; Eddleston, M.D. Introductory Lecture: Mechanochemistry, a Versatile Synthesis Strategy for New Materials. *Faraday Discussions* **2014**, 170, 9–34, doi:10.1039/C4FD00162A.
9. Shakhtshneider, T.P. Phase Transformations and Stabilization of Metastable States of Molecular Crystals under Mechanical Activation. *Solid State Ion* **1997**, 101–103, 851–856, doi:10.1016/S0167-2738(97)00224-5.
10. Karagianni, A.; Malamatari, M.; Kachrimanis, K. Pharmaceutical Cocrystals: New Solid Phase Modification Approaches for the Formulation of APIs. *Pharmaceutics* **2018**, 10, 18, doi:10.3390/pharmaceutics10010018.
11. Martínez, L.M.; Cruz-Angeles, J.; Vázquez-Dávila, M.; Martínez, E.; Cabada, P.; Navarrete-Bernal, C.; Cortez, F. Mechanical Activation by Ball Milling as a Strategy to Prepare Highly

Soluble Pharmaceutical Formulations in the Form of Co-Amorphous, Co-Crystals, or Polymorphs. *Pharmaceutics* **2022**, 14, 2003, doi:10.3390/pharmaceutics14102003.

12. Howard, J.L.; Cao, Q.; Browne, D.L. Mechanochemistry as an Emerging Tool for Molecular Synthesis: What Can It Offer? *Chemical Science* **2018**, 9, 3080–3094, doi:10.1039/C7SC05371A.
13. Kulla, H.; Becker, C.; Michalchuk, A.A.L.; Linberg, K.; Paulus, B.; Emmerling, F. Tuning the Apparent Stability of Polymorphic Cocrystals through Mechanochemistry. *Crystal Growth & Design* **2019**, 19, 7271–7279, doi:10.1021/acs.cgd.9b01158.
14. Tan, D.; Loots, L.; Friščić, T. Towards Medicinal Mechanochemistry: Evolution of Milling from Pharmaceutical Solid Form Screening to the Synthesis of Active Pharmaceutical Ingredients (APIs). *Chemical Communications* **2016**, 52, 7760–7781, doi:10.1039/C6CC02015A.
15. Do, J.-L.; Friščić, T. Mechanochemistry: A Force of Synthesis. *ACS Central Science* **2017**, 3, 13–19, doi:10.1021/acscentsci.6b00277.
16. Takacs, L. The Historical Development of Mechanochemistry. *Chemical Society Reviews* **2013**, 42, 7649, doi:10.1039/c2cs35442j.
17. Hasa, D.; Jones, W. Screening for New Pharmaceutical Solid Forms Using Mechanochemistry: A Practical Guide. **2017**, 117, 147–161, doi:10.1016/j.addr.2017.05.001.
18. Baláž, P.; Achimovičová, M.; Baláž, M.; Billik, P.; Cherkezova-Zheleva, Z.; Criado, J.M.; Delogu, F.; Dutková, E.; Gaffet, E.; Gotor, F.J.; et al. Hallmarks of Mechanochemistry: From Nanoparticles to Technology. *Chemical Society Reviews* **2013**, 42, 7571, doi:10.1039/c3cs35468g.
19. Friščić, T.; Jones, W. Recent Advances in Understanding the Mechanism of Cocrystal Formation via Grinding. *Crystal Growth & Design* **2009**, 9, 1621–1637, doi:10.1021/cg800764n.
20. Julien, P.A.; Friščić, T. Methods for Monitoring Milling Reactions and Mechanistic Studies of Mechanochemistry: A Primer. *Crystal Growth & Design* **2022**, 22, 5726–5754, doi:10.1021/acs.cgd.2c00587.
21. Užarević, K.; Halasz, I.; Friščić, T. Real-Time and In Situ Monitoring of Mechanochemical Reactions: A New Playground for All Chemists. *Journal of Physical Chemistry Letters* **2015**, 6, 4129–4140, doi:10.1021/acs.jpclett.5b01837.
22. Friščić, T.; Halasz, I.; Beldon, P.J.; Belenguer, A.M.; Adams, F.; Kimber, S.A.J.; Honkimäki, V.; Dinnebier, R.E. Real-Time and in Situ Monitoring of Mechanochemical Milling Reactions. *Nature Chemistry* **2013**, 5, 66–73, doi:10.1038/nchem.1505.

23. Batzdorf, L.; Fischer, F.; Wilke, M.; Wenzel, K.-J.; Emmerling, F. Direct in Situ Investigation of Milling Reactions Using Combined X-Ray Diffraction and Raman Spectroscopy. *Angewandte Chemie Int Ed Engl* **2015**, 54, 1799–1802, doi:10.1002/anie.201409834.
24. Lampronti, G.I.; Michalchuk, A.A.L.; Mazzeo, P.P.; Belenguer, A.M.; Sanders, J.K.M.; Bacchi, A.; Emmerling, F. Changing the Game of Time Resolved X-Ray Diffraction on the Mechanochemistry Playground by Downsizing. *Nature Communications* **2021**, 12, 6134, doi:10.1038/s41467-021-26264-1.
25. Halasz, I.; Puškarić, A.; Kimber, S.A.J.; Beldon, P.J.; Belenguer, A.M.; Adams, F.; Honkimäki, V.; Dinnebier, R.E.; Patel, B.; Jones, W.; et al. Real-Time in Situ Powder X-Ray Diffraction Monitoring of Mechanochemical Synthesis of Pharmaceutical Cocrystals. *Angewandte Chemie Int Ed Engl* **2013**, 52, 11538–11541, doi:10.1002/anie.201305928.
26. Lukin, S.; Germann, L.S.; Friščić, T.; Halasz, I. Toward Mechanistic Understanding of Mechanochemical Reactions Using Real-Time In Situ Monitoring. *Accounts of Chemical Research* **2022**, 55, 1262–1277, doi:10.1021/acs.accounts.2c00062.
27. Beldon, P.J.; Fábián, L.; Stein, R.S.; Thirumurugan, A.; Cheetham, A.K.; Friščić, T. Rapid Room-Temperature Synthesis of Zeolitic Imidazolate Frameworks by Using Mechanochemistry. *Angewandte Chemie Int Ed Engl* **2010**, 49, 9640–9643, doi:10.1002/anie.201005547.
28. Delori, A.; Friščić, T.; Jones, W. The Role of Mechanochemistry and Supramolecular Design in the Development of Pharmaceutical Materials. *CrystEngComm* **2012**, 14, 2350, doi:10.1039/c2ce06582g.
29. Friščić, T.; Jones, W. Benefits of Cocrystallisation in Pharmaceutical Materials Science: An Update. *Journal of Pharmacy and Pharmacology* **2010**, 62, 1547–1559, doi:10.1111/j.2042-7158.2010.01133.x.
30. Sanphui, P.; Kumar, S.S.; Nangia, A. Pharmaceutical Cocrystals of Niclosamide. *Crystal Growth & Design* **2012**, 12, 4588–4599, doi:10.1021/cg300784v.
31. Mazzeo, P.P.; Prencipe, M.; Feiler, T.; Emmerling, F.; Bacchi, A. On the Mechanism of Cocrystal Mechanochemical Reaction via Low Melting Eutectic: A Time-Resolved In Situ Monitoring Investigation. *Crystal Growth & Design* **2022**, 22, 4260–4267, doi:10.1021/acs.cgd.2c00262.
32. Michalchuk, A.A.L.; Hope, K.S.; Kennedy, S.R.; Blanco, M. V.; Boldyreva, E. V.; Pulham, C.R. Ball-Free Mechanochemistry: In Situ Real-Time Monitoring of Pharmaceutical Co-Crystal Formation by Resonant Acoustic Mixing. *Chemical Communications* **2018**, 54, 4033–4036, doi:10.1039/C8CC02187B.

33. Suryanarayana, C. Mechanical Alloying and Milling. *Progress in Materials Science* **2001**, 46, 1–184, doi:10.1016/S0079-6425(99)00010-9.
34. Colombo, I.; Grassi, G.; Grassi, M. Drug Mechanochemical Activation. *Journal of Pharmaceutical Sciences* **2009**, 98, 3961–3986, doi:10.1002/jps.21733.
35. Burmeister, C.F.; Kwade, A. Process Engineering with Planetary Ball Mills. *Chemical Society Reviews* **2013**, 42, 7660, doi:10.1039/c3cs35455e.
36. Hasa, D.; Voinovich, D.; Perissutti, B.; Bonifacio, A.; Grassi, M.; Franceschinis, E.; Dall'Acqua, S.; Speh, M.; Plavec, J.; Invernizzi, S. Multidisciplinary Approach on Characterizing a Mechanochemically Activated Composite of Vinpocetine and Crospovidone. *Journal of Pharmaceutical Sciences* **2011**, 100, 915–932, doi:10.1002/jps.22331.
37. Willart, J.F.; Descamps, M. Solid State Amorphization of Pharmaceuticals. *Molecular Pharmaceutics* **2008**, 5, 905–920, doi:10.1021/mp800092t.
38. Gaffet, E.; Le Caër, G. Mechanical Milling. In: *Nanomaterials and Nanochemistry*; Springer Berlin Heidelberg, **2007**; 455–471, doi:10.1007/978-3-540-72993-8_19
39. André, V.; Duarte, M.T.; Gomes, C.S.B.; Sarraguça, M.C. Mechanochemistry in Portugal—A Step towards Sustainable Chemical Synthesis. *Molecules* **2021**, 27, 241, doi:10.3390/molecules27010241.
40. Shinozaki, M.; Senna, M. Effects of Number and Size of Milling Balls on the Mechanochemical Activation of Fine Crystalline Solids. *Industrial & Engineering Chemistry Fundamentals* **1981**, 20, 59–62, doi:10.1021/i100001a011.
41. Ball Mills - Suitable for Every Application | Retsch Available online: https://www.retsch.com/products/milling/ball-mills/ (accessed on 10 October 2024).
42. Zanolla, D.; Perissutti, B.; Passerini, N.; Invernizzi, S.; Voinovich, D.; Bertoni, S.; Melegari, C.; Millotti, G.; Albertini, B. Milling and Comilling Praziquantel at Cryogenic and Room Temperatures: Assessment of the Process-Induced Effects on Drug Properties. *Journal of Pharmaceutical and Biomedical Analysis* **2018**, 153, 82–89, doi:10.1016/j.jpba.2018.02.018.
43. Zanolla, D.; Perissutti, B.; Passerini, N.; Chierotti, M.R.; Hasa, D.; Voinovich, D.; Gigli, L.; Demitri, N.; Geremia, S.; Keiser, J.; et al. A New Soluble and Bioactive Polymorph of Praziquantel. *European Journal of Pharmaceutics and Biopharmaceutics* **2018**, 127, 19–28, doi:10.1016/j.ejpb.2018.01.018.
44. Karimi-Jafari, M.; Padrela, L.; Walker, G.M.; Croker, D.M. Creating Cocrystals: A Review of Pharmaceutical Cocrystal Preparation Routes and Applications. *Crystal Growth & Design* **2018**, 18, 6370–6387, doi:10.1021/acs.cgd.8b00933.

45. Perissutti, B.; Passerini, N.; Trastullo, R.; Keiser, J.; Zanolla, D.; Zingone, G.; Voinovich, D.; Albertini, B. An Explorative Analysis of Process and Formulation Variables Affecting Comilling in a Vibrational Mill: The Case of Praziquantel. *Internal Journal of Pharmaceutics* **2017**, 533, 402–412, doi:10.1016/j.ijpharm.2017.05.053.
46. Chieng, N.; Aaltonen, J.; Saville, D.; Rades, T. Physical Characterization and Stability of Amorphous Indomethacin and Ranitidine Hydrochloride Binary Systems Prepared by Mechanical Activation. *European Journal of Pharmaceutics and Biopharmaceutics* **2009**, 71, 47–54, doi:10.1016/j.ejpb.2008.06.022.
47. Oliveira, P.F.M.; Willart, J.-F.; Siepmann, J.; Siepmann, F.; Descamps, M. Using Milling To Explore Physical States: The Amorphous and Polymorphic Forms of Dexamethasone. *Crystal Growth & Design* **2018**, 18, 1748–1757, doi:10.1021/acs.cgd.7b01664.
48. Jug, M.; Mura, P.A. Grinding as Solvent-Free Green Chemistry Approach for Cyclodextrin Inclusion Complex Preparation in the Solid State. *Pharmaceutics* **2018**, 10, 189, doi:10.3390/pharmaceutics10040189.
49. Douroumis, D.; Ross, S.A.; Nokhodchi, A. Advanced Methodologies for Cocrystal Synthesis. *Advanced Drug Delivery Reviews* **2017**, 117, 178–195, doi:10.1016/j.addr.2017.07.008.
50. Shan, N.; Toda, F.; Jones, W. Mechanochemistry and Co-Crystal Formation: Effect of Solvent on Reaction Kinetics. *Chemical Communications* **2002**, 2372–2373, doi:10.1039/b207369m.
51. Friščić, T.; Childs, S.L.; Rizvi, S.A.A.; Jones, W. The Role of Solvent in Mechanochemical and Sonochemical Cocrystal Formation: A Solubility-Based Approach for Predicting Cocrystallisation Outcome. *CrystEngComm* **2009**, 11, 418–426, doi:10.1039/B815174A.
52. Hasa, D.; Miniussi, E.; Jones, W. Mechanochemical Synthesis of Multicomponent Crystals: One Liquid for One Polymorph? A Myth to Dispel. *Crystal Growth & Design* **2016**, 16, 4582–4588, doi:10.1021/acs.cgd.6b00682.
53. Arhangelskis, M.; Bučar, D.-K.; Bordignon, S.; Chierotti, M.R.; Stratford, S.A.; Voinovich, D.; Jones, W.; Hasa, D. Mechanochemical Reactivity Inhibited, Prohibited and Reversed by Liquid Additives: Examples from Crystal-Form Screens. *Chemical Science* **2021**, 12, 3264–3269, doi:10.1039/D0SC05071G.
54. Hasa, D.; Schneider Rauber, G.; Voinovich, D.; Jones, W. Cocrystal Formation through Mechanochemistry: From Neat and Liquid-Assisted Grinding to Polymer-Assisted Grinding. *Angewandte Chemie Int Ed Engl* **2015**, 54, 7371–7375, doi:10.1002/anie.201501638.
55. Hasa, D.; Carlino, E.; Jones, W. Polymer-Assisted Grinding, a Versatile Method for Polymorph Control of Cocrystallization. *Crystal Growth & Design* **2016**, 16, 1772–1779, doi:10.1021/acs.cgd.6b00084.

56. Ozaki, S.; Kushida, I.; Yamashita, T.; Hasebe, T.; Shirai, O.; Kano, K. Inhibition of Crystal Nucleation and Growth by Water-Soluble Polymers and Its Impact on the Supersaturation Profiles of Amorphous Drugs. *Journal of Pharmaceutical Sciences* **2013**, 102, 2273–2281, doi:10.1002/jps.23588.
57. Germann, L.S.; Emmerling, S.T.; Wilke, M.; Dinnebier, R.E.; Moneghini, M.; Hasa, D. Monitoring Polymer-Assisted Mechanochemical Cocrystallisation through in Situ X-Ray Powder Diffraction. *Chemical Communications* **2020**, 56, 8743–8746, doi:10.1039/D0CC03460F.
58. Friščić, T.; Mottillo, C.; Titi, H.M. Mechanochemistry for Synthesis. *Angewandte Chemie Int Ed Engl* **2020**, 59, 1018–1029, doi:10.1002/anie.201906755.
59. Scaramuzza, D.; Schneider Rauber, G.; Voinovich, D.; Hasa, D. Dehydration without Heating: Use of Polymer-Assisted Grinding for Understanding the Stability of Hydrates in the Presence of Polymeric Excipients. *Crystal Growth & Design* **2018**, 18, 5245–5253, doi:10.1021/acs.cgd.8b00687.
60. Terban, M.W.; Madhau, L.; Cruz-Cabeza, A.J.; Okeyo, P.O.; Etter, M.; Schulz, A.; Rantanen, J.; Dinnebier, R.E.; Billinge, S.J.L.; Moneghini, M.; et al. Controlling Desolvation through Polymer-Assisted Grinding. *CrystEngComm* **2022**, 24, 2305–2313, doi:10.1039/D2CE00162D.
61. Germann, L.S.; Carlino, E.; Taurino, A.; Magdysyuk, O. V.; Voinovich, D.; Dinnebier, R.E.; Bučar, D.; Hasa, D. Modulating Thermal Properties of Polymers through Crystal Engineering. *Angewandte Chemie Int Ed Engl* **2023**, 62(19), e:202212688, doi:10.1002/anie.202212688.
62. Wong, S.N.; Fu, M.; Li, S.; Kwok, W.T.C.; Chow, S.; Low, K.-H.; Chow, S.F. Discovery of New Cocrystals beyond Serendipity: Lessons Learned from Successes and Failures. *CrystEngComm* **2024**, 26, 1505–1526, doi:10.1039/D4CE00021H.
63. Friščić, T.; Reid, D.G.; Halasz, I.; Stein, R.S.; Dinnebier, R.E.; Duer, M.J. Ion- and Liquid-Assisted Grinding: Improved Mechanochemical Synthesis of Metal–Organic Frameworks Reveals Salt Inclusion and Anion Templating. *Angewandte Chemie Int Ed Engl* **2010**, 49, 712–715, doi:10.1002/anie.200906583.
64. Reichert, W.M.; Holbrey, J.D.; Vigour, K.B.; Morgan, T.D.; Broker, G.A.; Rogers, R.D. Approaches to Crystallization from Ionic Liquids: Complex Solvents–Complex Results, or, a Strategy for Controlled Formation of New Supramolecular Architectures? *Chemical Communications* **2006**, 46, 4767–4779, doi:10.1039/B608496F.

65. Mukherjee, A.; Rogers, R.D.; Myerson, A.S. Cocrystal Formation by Ionic Liquid-Assisted Grinding: Case Study with Cocrystals of Caffeine. *CrystEngComm* **2018**, 20, 3817–3821, doi:10.1039/C8CE00859K.
66. Karadeniz, B.; Žilić, D.; Huskić, I.; Germann, L.S.; Fidelli, A.M.; Muratović, S.; Lončarić, I.; Etter, M.; Dinnebier, R.E.; Barišić, D.; et al. Controlling the Polymorphism and Topology Transformation in Porphyrinic Zirconium Metal–Organic Frameworks via Mechanochemistry. *Journal of the American Chemical Society* **2019**, 141, 19214–19220, doi:10.1021/jacs.9b10251.
67. Agate, S.; Tyagi, P.; Naithani, V.; Lucia, L.; Pal, L. Innovating Generation of Nanocellulose from Industrial Hemp by Dual Asymmetric Centrifugation. *ACS Sustainable Chemistry & Engineering* **2020**, 8, 1850–1858, doi:10.1021/acssuschemeng.9b05992.
68. da Silva, F.F.; Su, B. Dual Asymmetric Centrifugation as a New Tool to Prepare TiO2/S-g-C3N4 Heterojunctions with High Photocatalytic Performance. *Ceramics International* **2023**, 49, 13265–13270, doi:10.1016/j.ceramint.2023.01.109.
69. Massing, U.; Cicko, S.; Ziroli, V. Dual Asymmetric Centrifugation (DAC)—A New Technique for Liposome Preparation. *Journal of Controlled Release* **2008**, 125, 16–24, doi:10.1016/j.jconrel.2007.09.010.
70. Tan, D.; Friščić, T. Mechanochemistry for Organic Chemists: An Update. *European Journal of Organic Chemistry* **2018**, 2018, 18–33, doi:10.1002/ejoc.201700961.
71. Leung, D.H.; Lamberto, D.J.; Liu, L.; Kwong, E.; Nelson, T.; Rhodes, T.; Bak, A. A New and Improved Method for the Preparation of Drug Nanosuspension Formulations Using Acoustic Mixing Technology. *International Journal of Pharmaceutics* **2014**, 473, 10–19, doi:10.1016/j.ijpharm.2014.05.003.
72. Vandenberg, A.; Wille, K. Evaluation of Resonance Acoustic Mixing Technology Using Ultra High Performance Concrete. *Construction and Building Materials* **2018**, 164, 716–730, doi:10.1016/j.conbuildmat.2017.12.217.
73. Osorio, J.G.; Muzzio, F.J. Evaluation of Resonant Acoustic Mixing Performance. *Powder Technology* **2015**, 278, 46–56, doi:10.1016/j.powtec.2015.02.033.
74. Lennox, C.B.; Borchers, T.H.; Gonnet, L.; Barrett, C.J.; Koenig, S.G.; Nagapudi, K.; Friščić, T. Direct Mechanocatalysis by Resonant Acoustic Mixing (RAM). *Chemical Science* **2023**, 14, 7475–7481, doi:10.1039/D3SC01591B.
75. Chen, H.; Lu, Y.; Zhang, H.; Zhou, Y.; Chen, J.; Huang, X.; Tian, B. 20 MS Cm−1 Li-Argyrodite Solid Electrolyte Produced via Facile High-Speed-Mixing. *Chemical Communications* **2023**, 59, 7220–7223, doi:10.1039/D3CC01387A.

76. Gonnet, L.; Borchers, T.H.; Lennox, C.B.; Vainauskas, J.; Teoh, Y.; Titi, H.M.; Barrett, C.J.; Koenig, S.G.; Nagapudi, K.; Friščić, T. The "η-Sweet-Spot" (Hmax) in Liquid-Assisted Mechanochemistry: Polymorph Control and the Role of a Liquid Additive as Either a Catalyst or an Inhibitor in Resonant Acoustic Mixing (RAM). *Faraday Discussions* **2023**, 241, 128–149, doi:10.1039/D2FD00131D.
77. Wright, C.J.; Wilkinson, P.J.; Gaulter, S.E.; Fossey, D.; Burn, A.O.; Gill, P.P. Is ResonantAcoustic Mixing® (RAM) a Game Changer for Manufacturing Solid Composite Rocket Propellants? *Propellants, Explosives, Pyrotechnics* **2022**, 47, doi:10.1002/prep.202100146.
78. Titi, H.M.; Do, J.-L.; Howarth, A.J.; Nagapudi, K.; Friščić, T. Simple, Scalable Mechanosynthesis of Metal–Organic Frameworks Using Liquid-Assisted Resonant Acoustic Mixing (LA-RAM). *Chemical Science* **2020**, 11, 7578–7584, doi:10.1039/D0SC00333F.
79. am Ende, D.J.; Anderson, S.R.; Salan, J.S. Development and Scale-Up of Cocrystals Using Resonant Acoustic Mixing. *Organic Process Research & Development* **2014**, 18(2), 331–341, doi:10.1021/op4003399.
80. Tanaka, R.; Osotprasit, S.; Peerapattana, J.; Ashizawa, K.; Hattori, Y.; Otsuka, M. Complete Cocrystal Formation during Resonant Acoustic Wet Granulation: Effect of Granulation Liquids. *Pharmaceutics* **2021**, 13, 56, doi:10.3390/pharmaceutics13010056.
81. Nagapudi, K.; Umanzor, E.Y.; Masui, C. High-Throughput Screening and Scale-up of Cocrystals Using Resonant Acoustic Mixing. *International Journal of Pharmaceutics* **2017**, 521, 337–345, doi:10.1016/j.ijpharm.2017.02.027.
82. Gonnet, L.; Lennox, C.B.; Do, J.; Malvestiti, I.; Koenig, S.G.; Nagapudi, K.; Friščić, T. Metal-Catalyzed Organic Reactions by Resonant Acoustic Mixing. *Angewandte Chemie Int Ed Engl* **2022**, 61(13), e202115030, doi:10.1002/anie.202115030.
83. Guo, Z.; Boyce, C.; Rhodes, T.; Liu, L.; Salituro, G.M.; Lee, K.; Bak, A.; Leung, D.H. A Novel Method for Preparing Stabilized Amorphous Solid Dispersion Drug Formulations Using Acoustic Fusion. *International Journal of Pharmaceutics* **2021**, 592, 120026, doi:10.1016/j.ijpharm.2020.120026.
84. Hou, H.H.; Rajesh, A.; Pandya, K.M.; Lubach, J.W.; Muliadi, A.; Yost, E.; Jia, W.; Nagapudi, K. Impact of Method of Preparation of Amorphous Solid Dispersions on Mechanical Properties: Comparison of Coprecipitation and Spray Drying. *Journal of Pharmaceutical Science* **2019**, 108, 870–879, doi:10.1016/j.xphs.2018.09.008.

85. Gupta, S.; Pu, Y.E.; Li, M.; Li, Z.; Osorio, J.G. Assessment of Resonant Acoustic Mixing for Low-Dose Pharmaceutical Powder Blends. *AAPS PharmSciTech* **2022**, 23, 126, doi:10.1208/s12249-022-02262-4.
86. Schistosomiasis Available online: https://www.who.int/news-room/fact-sheets/detail/schistosomiasis (accessed on 20 November 2023).
87. Waechtler, A.; Cezanne, B.; Maillard, D.; Sun, R.; Wang, S.; Wang, J.; Harder, A. Praziquantel – 50 Years of Research. *ChemMedChem* **2023**, 18(12), e202300154, doi:10.1002/cmdc.202300154.
88. McManus, D.P.; Dunne, D.W.; Sacko, M.; Utzinger, J.; Vennervald, B.J.; Zhou, X.-N. Schistosomiasis. *Nature Reviews Disease Primers* **2018**, 4, 13, doi:10.1038/s41572-018-0013-8.
89. Quaderni della Società Italiana di Medicina Tropicale e Salute Globale (SIMET) Schistosomiasi: Raccomandazioni per La Gestione Clinica in Italia. In: *Società Italiana di Medicina Tropicale e Salute Globale (SIMET)*, Ed: **2023**, ISBN 978-88-900025-8-8.
90. Colley, D.G.; Bustinduy, A.L.; Secor, W.E.; King, C.H. Human Schistosomiasis. *The Lancet* **2014**, 383, 2253–2264, doi:10.1016/S0140-6736(13)61949-2.
91. Gryseels, B.; Polman, K.; Clerinx, J.; Kestens, L. Human Schistosomiasis. *The Lancet* **2006**, 368, 1106–1118, doi:10.1016/S0140-6736(06)69440-3.
92. Cioli, D.; Pica-Mattoccia, L. Praziquantel. *Parasitology Research* **2003**, 90, S3–S9, doi:10.1007/s00436-002-0751-z.
93. Cioli, D.; Pica-Mattoccia, L.; Basso, A.; Guidi, A. Schistosomiasis Control: Praziquantel Forever? *Molecular and Biochemical Parasitolology* **2014**, 195, 23–29, doi:10.1016/j.molbiopara.2014.06.002.
94. WHO Model List of Essential Medicines - 22nd List, 2021 Available online: https://www.who.int/publications/i/item/WHO-MHP-HPS-EML-2021.02 (accessed on 18 September 2023).
95. WHO Model List of Essential Medicines for Children - 8th List, 2021 Available online: https://www.who.int/publications/i/item/WHO-MHP-HPS-EML-2021.03 (accessed on 18 September 2023).
96. Sousa-Figueiredo, J.C.; Betson, M.; Stothard, J.R. Treatment of Schistosomiasis in African Infants and Preschool-Aged Children: Downward Extension and Biometric Optimization of the Current Praziquantel Dose Pole. *International Health* **2012**, 4, 95–102, doi:10.1016/j.inhe.2012.03.003.

97. Lindenberg, M.; Kopp, S.; Dressman, J.B. Classification of Orally Administered Drugs on the World Health Organization Model List of Essential Medicines According to the Biopharmaceutics Classification System. *European Journal of Pharmaceutics and Biopharmaceutics* **2004**, 58, 265–278, doi:10.1016/j.ejpb.2004.03.001.
98. Hussein I. El-Subbagh; Abdullah A. Al-badr Praziquantel. In: *Analytical profiles of drug substances and excipients*; Brittain Harry, Ed: **1998**; 25, 463–500.
99. Benet, L.Z.; Broccatelli, F.; Oprea, T.I. BDDCS Applied to Over 900 Drugs. *AAPS Journal* **2011**, 13, 519–547, doi:10.1208/s12248-011-9290-9.
100. Dinora, G.-E.; Julio, R.; Nelly, C.; Lilian, Y.-M.; Cook, H.J. In Vitro Characterization of Some Biopharmaceutical Properties of Praziquantel. *International Journal of Pharmaceutics* **2005**, 295, 93–99, doi:10.1016/j.ijpharm.2005.01.033.
101. Jung-Cook, H. Pharmacokinetic Variability of Anthelmintics: Implications for the Treatment of Neurocysticercosis. *Expert Review of Clinical Pharmacology* **2012**, 5, 21–30, doi:10.1586/ecp.11.72.
102. El-Arini, S.K.; Leuenberger, H. Dissolution Properties of Praziquantel–PVP Systems. *Pharmaceutica Acta Helvetiae* **1998**, 73, 89–94, doi:10.1016/S0031-6865(97)00051-4.
103. FDA Biltricide (Praziquantel) Tablets Label Available online: https://www.accessdata.fda.gov/drugsatfda_docs/label/2010/018714s012lbl.pdf (accessed on 4 November 2023).
104. Cedillo-Cruz, A.; Aguilar, M.I.; Flores-Alamo, M.; Palomares-Alonso, F.; Jung-Cook, H. A Straightforward and Efficient Synthesis of Praziquantel Enantiomers and Their 4′-Hydroxy Derivatives. *Tetrahedron Asymmetry* **2014**, 25, 133–140, doi:10.1016/j.tetasy.2013.11.004.
105. Meister, I.; Ingram-Sieber, K.; Cowan, N.; Todd, M.; Robertson, M.N.; Meli, C.; Patra, M.; Gasser, G.; Keiser, J. Activity of Praziquantel Enantiomers and Main Metabolites against Schistosoma Mansoni. *Antimicrobial Agents and Chemotherapy* **2014**, 58, 5466–5472, doi:10.1128/AAC.02741-14.
106. Bagchus, W.M.; Bezuidenhout, D.; Harrison-Moench, E.; Kourany-Lefoll, E.; Wolna, P.; Yalkinoglu, O. Relative Bioavailability of Orally Dispersible Tablet Formulations of Levo- and Racemic Praziquantel: Two Phase I Studies. *Clinical and Translational Science* **2019**, 12, 66–76, doi:10.1111/cts.12601.
107. Kovač, J.; Vargas, M.; Keiser, J. In Vitro and in Vivo Activity of R- and S- Praziquantel Enantiomers and the Main Human Metabolite Trans-4-Hydroxy-Praziquantel against Schistosoma Haematobium. *Parasites & Vectors* **2017**, 10, 365, doi:10.1186/s13071-017-2293-3.

108. Shu-Hua, X.; Catto, B.A. Comparative in Vitro and in Vivo Activity of Racemic Praziquantel and Its Levorotated Isomer on Schistosoma Mansoni. *Journal of Infectious Diseases* **1989**, 159, 589–592, doi:10.1093/infdis/159.3.589.
109. Liu, Y.H.; Qian, M.X.; Wang, X.G.; Quan, Y.Z.; Yan, S.H.; Chen, B.Y.; Li, J.S.; Qiu, Z.Y. Levo-Praziquantel versus Praziquantel in Experimental and Clinical Treatment of Schistosomiasis Japonica. *Chinese Medical Journal* **1993**, 106, 593–596, PMID: 8222907.
110. Liu, Y.; Wang, X.; Wang, J.-K.; Ching, C.B. Investigation of the Phase Diagrams of Chiral Praziquantel. *Chirality* **2006**, 18, 259–264, doi:10.1002/chir.20251.
111. Meyer, T.; Sekljic, H.; Fuchs, S.; Bothe, H.; Schollmeyer, D.; Miculka, C. Taste, A New Incentive to Switch to (R)-Praziquantel in Schistosomiasis Treatment. *PLoS Neglected Tropical Diseases* **2009**, 3, e357, doi:10.1371/journal.pntd.0000357.
112. Olliaro, P.; Delgado-Romero, P.; Keiser, J. The Little We Know about the Pharmacokinetics and Pharmacodynamics of Praziquantel (Racemate and R-Enantiomer). *Journal of Antimicrobial Chemotherapy* **2014**, 69, 863–870, doi:10.1093/jac/dkt491.
113. Yue-han, L.; Ming-xin, Q.; Xiao-gen, W.; Jie, J.; Qi-nan, W.; Yu-fu, J.; Rong-qiu, W.; Yan, S.; Chen, B.; Li, J.; et al. Comparative Efficacy of Praziquantel and Its Optic Isomers in Experimental Therapy of Schistosomiasis Japonica in Rabbits. *Chinese Medical Journal* **1986**, 99, 935–940.
114. De La Torre, P.; Torrado, S.; Torrado, S. Preparation, Dissolution and Characterization of Praziquantel Solid Dispersions. *Chemical and Pharmaceutical Bulletin* **1999**, 47, 1629–1633, doi:10.1248/cpb.47.1629.
115. El-Lakkany, N.; Seif el-Din, S.H.; Heikal, L. Bioavailability and in Vivo Efficacy of a Praziquantel–Polyvinylpyrrolidone Solid Dispersion in Schistosoma Mansoni-Infected Mice. *European Journal of Drug Metabolism and Pharmacokinetics* **2012**, 37, 289–299, doi:10.1007/s13318-012-0089-6.
116. Costa, E.D.; Priotti, J.; Orlandi, S.; Leonardi, D.; Lamas, M.C.; Nunes, T.G.; Diogo, H.P.; Salomon, C.J.; Ferreira, M.J. Unexpected Solvent Impact in the Crystallinity of Praziquantel / Poly(Vinylpyrrolidone) Formulations. A Solubility, DSC and Solid-State NMR Study. *Internation Journal of Pharmaceutics* **2016**, 511, 983–993, doi:10.1016/j.ijpharm.2016.08.009.
117. Chaud, M.; Lima, A.; Vila, M.; Paganelli, M.; Paula, F.; Pedreiro, L.; Gremião, M. Development and Evaluation of Praziquantel Solid Dispersions in Sodium Starch Glycolate. *Tropical Journal of Pharmaceutical Research* **2013**, 12, doi:10.4314/tjpr.v12i2.5.

118. Šagud, I.; Zanolla, D.; Zingone, G.; Perissutti, B.; Škorić, I. Impact of Mesoporous Silica on the Chemical Degradation of Praziquantel upon Grinding. *Comptes Rendus Chimie* **2021**, 24, 233–242, doi:10.5802/crchim.82.
119. Borrego-Sánchez, A.; Carazo, E.; Albertini, B.; Passerini, N.; Perissutti, B.; Cerezo, P.; Viseras, C.; Hernández-Laguna, A.; Aguzzi, C.; Sainz-Díaz, I. Conformational Polymorphic Changes in the Crystal Structure of the Chiral Antiparasitic Drug Praziquantel and Interactions with Calcium Carbonate. *European Journal of Pharmaceutics and Biopharmaceutics* **2018**, 132, 180–191, doi:10.1016/j.ejpb.2018.09.028.
120. Di Marzio, L.; Borrego-Sánchez, A.; Felaco, M.; Pacinelli, M.; Gómez-Morales, J.; d'Avanzo, N.; Sainz-Díaz, C.I.; Celia, C.; Viseras, C. Praziquantel-Loaded Calcite Crystals: Synthesis, Physicochemical Characterization, and Biopharmaceutical Properties of Inorganic Biomaterials for Drug Delivery. *Journal of Drug Delivery Science and Technology* **2022**, 68, 103021, doi:10.1016/j.jddst.2021.103021.
121. Dametto, P.R.; Dametto, A.C.; Polese, L.; Ribeiro, C.A.; Chorilli, M.; de Freitas, O. Development and Physicochemical Characterization of Solid Dispersions Containing Praziquantel for the Treatment of Schistosomiasis. *Journal of Thermal Analysis and Calorimetry* **2017**, 127, 1693–1706, doi:10.1007/s10973-016-5759-1.
122. Borrego-Sánchez, A.; Carazo, E.; Aguzzi, C.; Viseras, C.; Sainz-Díaz, C.I. Biopharmaceutical Improvement of Praziquantel by Interaction with Montmorillonite and Sepiolite. *Applied Clay Science* **2018**, 160, 173–179, doi:10.1016/j.clay.2017.12.024.
123. Becket, G.; Schep, L.J.; Tan, Y. Improvement of the in Vitro Dissolution of Praziquantel by Complexation with A-, b-and g-Cyclodextrins. *International Journal of Pharmaceutics* **1999**, 179, 65–71, doi:10.1016/s0378-5173(98)00382-2.
124. Cugovčan, M.; Jablan, J.; Lovrić, J.; Cinčić, D.; Galić, N.; Jug, M. Biopharmaceutical Characterization of Praziquantel Cocrystals and Cyclodextrin Complexes Prepared by Grinding. *Journal of Pharmaceutical and Biomedical Analysis* **2017**, 137, 42–53, doi:10.1016/j.jpba.2017.01.025.
125. Rodrigues, S.G.; Chaves, I. de S.; Melo, N.F.S.; Jesus, M.B.; Fraceto, L.F.; Fernandes, S.A.; Paula, E.; Freitas, M.P. de; Pinto, L. de M.A. Computational Analysis and Physico-Chemical Characterization of an Inclusion Compound between Praziquantel and Methyl-β-Cyclodextrin for Use as an Alternative in the Treatment of Schistosomiasis. *Journal of Inclusion Phenomena and Macrocyclic Chemistry* **2011**, 70, 19–28, doi:10.1007/s10847-010-9852-y.

126. Maragos, S.; Archontaki, H.; Macheras, P.; Valsami, G. Effect of Cyclodextrin Complexation on the Aqueous Solubility and Solubility/Dose Ratio of Praziquantel. *AAPS PharmSciTech* **2009**, 10, 1444, doi:10.1208/s12249-009-9346-7.

127. Arrúa, E.C.; João, M.; Ferreira, G.; Salomon, C.J.; Nunes, T.G. Elucidating the Guest-Host Interactions and Complex Formation of Praziquantel and Cyclodextrin Derivatives by ^{13}C and ^{15}N Solid-State NMR Spectroscopy. *International Journal of Pharmaceutics* **2015**, 496(2), 812–821, doi:10.1016/j.ijpharm.2015.11.026.

128. de Jesus, M.B.; de Matos Alves Pinto, L.; Fraceto, L.F.; Takahata, Y.; Lino, A.C.S.; Jaime, C.; de Paula, E. Theoretical and Experimental Study of a Praziquantel and -Cyclodextrin Inclusion Complex Using Molecular Mechanic Calculations and -Nuclear Magnetic Resonance. *Journal of Pharmaceutical and Biomedical Analysis* **2006**, 41, 1428–1432, doi:10.1016/j.jpba.2006.03.010.

129. da Silva Mourão, L.C.; Ribeiro Batista, D.R.M.; Honorato, S.B.; Ayala, A.P.; de Alencar Morais, W.; Barbosa, E.G.; Raffin, F.N.; de Lima e Moura, T.F.A. Effect of Hydroxypropyl Methylcellulose on Beta Cyclodextrin Complexation of Praziquantel in Solution and in Solid State. *Journal of Inclusion Phenomena and Macrocyclic Chemistry* **2016**, 85, 151–160, doi:10.1007/s10847-016-0614-3.

130. Mourão, S.C.; Costa, P.I.; Salgado, H.R.N.; Gremião, M.P.D. Improvement of Antischistosomal Activity of Praziquantel by Incorporation into Phosphatidylcholine-Containing Liposomes. *International Journal of Pharmaceutics* **2005**, 295, 157–162, doi:10.1016/j.ijpharm.2005.02.009.

131. Partridge, G.J.; Rao, S.; Woolley, L.D.; Pilmer, L.; Lymbery, A.J.; Prestidge, C.A. Bioavailability and Palatability of Praziquantel Incorporated into Solid-Lipid Nanoparticles Fed to Yellowtail Kingfish Seriola Lalandi. *Comparative Biochemistry and Physiology Part C: Toxicology & Pharmacology* **2019**, 218, 14–20, doi:10.1016/J.CBPC.2018.12.007.

132. Yang, L.; Geng, Y.; Li, H.; Zhang, Y.; You, J.; Chang, Y. Enhancement the Oral Bioavailability of Praziquantel by Incorporation into Solid Lipid Nanoparticles. *Pharmazie* **2009**, 64, 86–89, PMID: 19320279.

133. Mainardes, R.M.; Gremião, M.P.D.; Evangelista, R.C. Thermoanalytical Study of Praziquantel-Loaded PLGA Nanoparticles. *Revista Brasileira de Ciências Farmacêuticas* **2006**, 42, 523–530, doi:10.1590/S1516-93322006000400007.

134. de Souza, A.L.R.; Andreani, T.; Nunes, F.M.; Cassimiro, D.L.; de Almeida, A.E.; Ribeiro, C.A.; Sarmento, V.H.V.; Gremião, M.P.D.; Silva, A.M.; Souto, E.B. Loading of Praziquantel

in the Crystal Lattice of Solid Lipid Nanoparticles. *Journal of Thermal Analysis and Calorimetry* **2012**, 108, 353–360, doi:10.1007/s10973-011-1871-4.

135. Borrego-Sánchez, A.; Sánchez-Espejo, R.; Albertini, B.; Passerini, N.; Cerezo, P.; Viseras, C.; Sainz-Díaz, C.I. Ground Calcium Carbonate as a Low Cost and Biosafety Excipient for Solubility and Dissolution Improvement of Praziquantel. *Pharmaceutics* **2019**, 11, 533, doi:10.3390/pharmaceutics11100533.
136. Gaggero, A.; Jurišić Dukovski, B.; Radić, I.; Šagud, I.; Škorić, I.; Cinčić, D.; Jug, M. Co-Grinding with Surfactants as a New Approach to Enhance in Vitro Dissolution of Praziquantel. *Journal of Pharmaceutical and Biomedical Analysis* **2020**, 189, 113494, doi:10.1016/j.jpba.2020.113494.
137. Trastullo, R.; Dolci, L.S.; Passerini, N.; Albertini, B. Development of Flexible and Dispersible Oral Formulations Containing Praziquantel for Potential Schistosomiasis Treatment of Pre-School Age Children. *International Journal of Pharmaceutics* **2015**, 495, 536–550, doi:10.1016/j.ijpharm.2015.09.019.
138. Passerini, N.; Albertini, B.; Perissutti, B.; Rodriguez, L. Evaluation of Melt Granulation and Ultrasonic Spray Congealing as Techniques to Enhance the Dissolution of Praziquantel. *International Journal of Pharmaceutics* **2006**, 318, 92–102, doi:10.1016/j.ijpharm.2006.03.028.
139. Silva, A.D.A.; Sarcinelli, M.A.; Patricio, B.F. de C.; Chaves, M.H. da C.; Lima, L.M.; Parreiras, P.M.; Pinto, P. de F.; Prado, L.D.; Rocha, H.V.A. Pharmaceutical Development of Micro and Nanocrystals of a Poorly Water-Soluble Drug: Dissolution Rate Enhancement of Praziquantel. *Journal of Drug Delivery Science Technology* **2023**, 81, 104260, doi:10.1016/j.jddst.2023.104260.
140. Yang, R.; Zhang, T.; Yu, J.; Liu, Y.; Wang, Y.; He, Z. In Vitro/Vivo Assessment of Praziquantel Nanocrystals: Formulation, Characterization, and Pharmacokinetics in Beagle Dogs. *Asian Journal of Pharmaceutical Sciences* **2019**, 14, 321–328, doi:10.1016/j.ajps.2018.06.001.
141. Espinosa-Lara, J.C.; Guzman-Villanueva, D.; Arenas-García, J.I.; Herrera-Ruiz, D.; Rivera-Islas, J.; Román-Bravo, P.; Morales-Rojas, H.; Höpfl, H. Cocrystals of Active Pharmaceutical Ingredients - Praziquantel in Combination with Oxalic, Malonic, Succinic, Maleic, Fumaric, Glutaric, Adipic, and Pimelic Acids. *Cryst Growth & Design* **2013**, 13, 169–185, doi:10.1021/cg301314w.
142. Zanolla, D.; Perissutti, B.; Vioglio, P.C.; Chierotti, M.R.; Gigli, L.; Demitri, N.; Passerini, N.; Albertini, B.; Franceschinis, E.; Keiser, J.; et al. Exploring Mechanochemical Parameters

Using a DoE Approach: Crystal Structure Solution from Synchrotron XRPD and Characterization of a New Praziquantel Polymorph. *European Journal of Pharmaceutical Sciences* **2019**, 140, 105084, doi:10.1016/j.ejps.2019.105084.

143. Saikia, B.; Seidel-Morgenstern, A.; Lorenz, H. Role of Mechanochemistry in Solid Form Selection and Identification of the Drug Praziquantel. *Crystal Growth & Design* **2021**, 21, 5854–5861, doi:10.1021/acs.cgd.1c00736.
144. Guedes Fernandes de Moraes, M.; Gomes Barreto Jr., A.; Resende Secchi, A.; B. de Souza Jr., M.; Laranjeira da Cunha Lage, P.; S. Myerson, A. Polymorphism of Praziquantel: Role of Cooling Crystallization in Access to Solid Forms and Discovery of New Polymorphs. *Crystal Growth & Design* **2023**, 23, 1247–1258, doi:10.1021/acs.cgd.2c01381.
145. Salazar-Rojas, D.; Maggio, R.M.; Kaufman, T.S. Preparation and Characterization of a New Solid Form of Praziquantel, an Essential Anthelmintic Drug. Praziquantel Racemic Monohydrate. *European Journal of Pharmaceutical Sciences* **2020**, 146, 105267, doi:10.1016/j.ejps.2020.105267.
146. Zanolla, D.; Hasa, D.; Arhangelskis, M.; Schneider-Rauber, G.; Chierotti, M.R.; Keiser, J.; Voinovich, D.; Jones, W.; Perissutti, B. Mechanochemical Formation of Racemic Praziquantel Hemihydrate with Improved Biopharmaceutical Properties. *Pharmaceutics* **2020**, 12, doi:10.3390/pharmaceutics12030289.
147. MacEachern, L.; Kermanshahi-pour, A.; Mirmehrabi, M. Transformation under Pressure: Discovery of a Novel Crystalline Form of Anthelmintic Drug Praziquantel Using High-Pressure Supercritical Carbon Dioxide. *International Journal of Pharmaceutics* **2022**, 619, 121723, doi:10.1016/J.IJPHARM.2022.121723.
148. Zanolla, D.; Gigli, L.; Hasa, D.; Chierotti, M.R.; Arhangelskis, M.; Demitri, N.; Jones, W.; Voinovich, D.; Perissutti, B. Mechanochemical Synthesis and Physicochemical Characterization of Previously Unreported Praziquantel Solvates with 2-Pyrrolidone and Acetic Acid. *Pharmaceutics* **2021**, 13, 1606, doi:10.3390/pharmaceutics13101606.
149. MacEachern, L.A.; O'Connor, G.; Shojaeiarani, J.; Mirmehrabi, M.; Kermanshahi-pour, A. Influence of Solvent Selection and RESS Processing Conditions on Formation of a Praziquantel-Malonic Acid Cocrystal in Supercritical CO2. *Journal of Supercritical Fluids* **2025**, 215, 106417, doi:10.1016/j.supflu.2024.106417.
150. Wang, L.; Xie, Q.; Shi, X.; Zhu, Y.; Li, S.; Ji, F.; Yu, J.; Li, D.; Zhang, H. Polymorphs of Praziquantel–Succinic Acid Cocrystal: Crystal Structure, Thermodynamic Relationship, and Improved Pharmaceutical Performance. *Journal of Molecular Structure* **2024**, 1308, 138124, doi:10.1016/J.MOLSTRUC.2024.138124.

151. Rodríguez-Ruiz, C.; Salas-Zúñiga, R.; Obdulia Sánchez-Guadarrama, M.; Delgado-Díaz, A.; Herrera-Ruiz, D.; Morales-Rojas, H.; Höpfl, H. Structural, Physicochemical, and Biopharmaceutical Properties of Cocrystals with RS- and R-Praziquantel─Generation and Prolongation of the Supersaturation State in the Presence of Cellulosic Polymers. *Crystal Growth & Design* **2022**, 22, 6023–6038, doi:10.1021/acs.cgd.2c00661.

152. Sánchez-Guadarrama, O.; Mendoza-Navarro, F.; Cedillo-Cruz, A.; Jung-Cook, H.; I. Arenas-García, J.; Delgado-Díaz, A.; Herrera-Ruiz, D.; Morales-Rojas, H.; Höpfl, H. Chiral Resolution of RS-Praziquantel via Diastereomeric Co-Crystal Pair Formation with l-Malic Acid. *Crystal Growth & Design* **2015**, 16, 307–314, doi:10.1021/acs.cgd.5b01254.

153. Yang, D.; Cao, J.; Heng, T.; Xing, C.; Yang, S.; Zhang, L.; Lu, Y.; Du, G. Theoretical Calculation and Structural Analysis of the Cocrystals of Three Flavonols with Praziquantel. *Crystal Growth & Design* **2021**, 21, 2292–2300, doi:10.1021/acs.cgd.0c01706.

154. Devogelaer, J.J.; Charpentier, M.D.; Tijink, A.; Dupray, V.; Coquerel, G.; Johnston, K.; Meekes, H.; Tinnemans, P.; Vlieg, E.; Ter Horst, J.H.; et al. Cocrystals of Praziquantel: Discovery by Network-Based Link Prediction. *Crystal Growth & Design* **2021**, 21, 3428–3437, doi:10.1021/acs.cgd.1c00211.

155. Gerard, C.J.J.; Pinetre, C.; Cercel, H.; Charpentier, M.D.; Sanselme, M.; Couvrat, N.; Brandel, C.; Cartigny, Y.; Dupray, V.; Ter Horst, J.H. Phase Diagrams of Praziquantel and Vanillic Acid Cocrystals: Racemic Compound and Conglomerate System. *Crystal Growth & Design* **2024**, 24, 3378–3387, doi:10.1021/acs.cgd.4c00114.

156. Liu, Q.; Yang, D.; Chen, T.; Zhang, B.; Xing, C.; Zhang, L.; Lu, Y.; Du, G. Insights into the Solubility and Structural Features of Four Praziquantel Cocrystals. *Crystal Growth & Design* **2021**, 21, 6321–6331, doi:10.1021/acs.cgd.1c00785.

157. Yang, S.; Liu, Q.; Ji, W.; An, Q.; Song, J.; Xing, C.; Yang, D.; Zhang, L.; Lu, Y.; Du, G. Cocrystals of Praziquantel with Phenolic Acids: Discovery, Characterization, and Evaluation. *Molecules* **2022**, 27, 2022, doi:10.3390/molecules27062022.

158. Cappuccino, C.; Spoletti, E.; Renni, F.; Muntoni, E.; Keiser, J.; Voinovich, D.; Perissutti, B.; Lusi, M. Co-Crystalline Solid Solution Affords a High-Soluble and Fast-Absorbing Form of Praziquantel. *Molecular Pharmaceutics* **2022**, 20(4), 2009–2016, doi:10.1021/acs.molpharmaceut.2c00984.

159. Rapeenun, P.; Gerard, C.J.J.; Cartigny, Y.; Tinnemans, P.; De Gelder, R.; Flood, A.E.; Ter Horst, J.H. Searching for Conglomerate Cocrystals of the Racemic Compound Praziquantel. *Crystal Growth & Design* **2024**, 24, 490, doi:10.1021/acs.cgd.3c01158.

160. Caro Garrido, C.; Vandooren, M.; Robeyns, K.; Debecker, D.P.; Luis, P.; Leyssens, T. Combining a Drug and a Nutraceutical: A New Cocrystal of Praziquantel and Curcumin. *Crystals* **2024**, 14, 181, doi:10.3390/cryst14020181.
161. Mureşan-Pop, M.; Simon, S.; Bodoki, E.; Simon, V.; Turza, A.; Todea, M.; Vulpoi, A.; Magyari, K.; Iacob, B.C.; Bărăian, A.I.; et al. Mechanochemical Synthesis of New Praziquantel Cocrystals: Solid-State Characterization and Solubility. *Crystal Growth & Design* **2024**, 24(11), 4668–4681, doi:10.1021/acs.cgd.4c00296.
162. De Vries, T.E.; Van Eert, E.; Weevers, L.; Tinnemans, P.; Vlieg, E.; Meekes, H.; De Gelder, R. Optimizing Link Prediction for the CSD Cocrystal Network: A Demonstration Using Praziquantel. *Crystal Growth & Design* **2024**, 24, 5210, doi:10.1021/acs.cgd.4c00438.
163. European Pharmacopoeia 11.5 Available online: https://pheur.edqm.eu/app/11-5/search/ (accessed on 25 October 2024).
164. Persson, L.C.; Porter, C.J.H.; Charman, W.N.; Bergström, C.A.S. Computational Prediction of Drug Solubility in Lipid Based Formulation Excipients. *Pharmaceutical Research* **2013**, 30, 3225–3237, doi:10.1007/s11095-013-1083-7.
165. El-Arini, S.K.; Giron, D.; Leuenberger, H. Solubility Properties of Racemic Praziquantel and Its Enantiomers. *Pharmaceutical Development and Technology* **1998**, 3, 557–564, doi:10.3109/10837459809028638.
166. Liu, Y.; Zhang, X.; Wang, M.; Ma, Y.; Tang, W. Uncovering the Effect of Solvents on Solid-Liquid Phase Equilibrium of Praziquantel. *Journal of Molecular Liquids* **2020**, 297, 111917, doi:10.1016/j.molliq.2019.111917.
167. Li, R.; Chen, X.; He, G.; Wu, C.; Gan, Z.; He, Z.; Zhao, J.; Han, D. The Dissolution Behaviour and Thermodynamic Properties Calculation of Praziquantel in Pure and Mixed Organic Solvents. *Journal of Chemical Thermodynamics* **2020**, 144, 106062, doi:10.1016/j.jct.2020.106062.
168. Groom, C.R.; Bruno, I.J.; Lightfoot, M.P.; Ward, S.C. The Cambridge Structural Database. *Acta Crystallographica Section B: Structural Science, Crystal Engineering and Materials* **2016**, 72, 171–179, doi:10.1107/S2052520616003954.
169. Borrego-Sánchez, A.; Hernández-Laguna, A.; Sainz-Díaz, C.I. Molecular Modeling and Infrared and Raman Spectroscopy of the Crystal Structure of the Chiral Antiparasitic Drug Praziquantel. *Journal of Molecular Modeling* **2017**, 23, 106, doi:10.1007/s00894-017-3266-3.
170. Borrego-Sánchez, A.; Viseras, C.; Aguzzi, C.; Sainz-Díaz, C.I. Molecular and Crystal Structure of Praziquantel. Spectroscopic Properties and Crystal Polymorphism. *European Journal of Pharmaceutical Sciences* **2016**, 92, 266–275, doi:10.1016/j.ejps.2016.04.023.

171. Schepers, H.; Brasseur, R.; Goormaghtigh, E.; Duquenoy, P.; Ruysschaert, J.-M. Mode of Insertion of Praziquantel and Derivatives into Lipid Membranes. *Biochemical Pharmacolology* **1988**, 37, 1615–1623, doi:10.1016/0006-2952(88)90026-3.
172. Liu, Y.; Wang, X.; Wang, J.; Ching, C.B. Structural Characterization and Enantioseparation of the Chiral Compound Praziquantel. *Journal of Pharmaceutical Sciences* **2004**, 93, 3039–3046, doi:10.1002/jps.20211.
173. da Silva, V.B.R.; Campos, B.R.K.L.; de Oliveira, J.F.; Decout, J.-L.; do Carmo Alves de Lima, M. Medicinal Chemistry of Antischistosomal Drugs: Praziquantel and Oxamniquine. *Bioorganic & Medicinal Chemistry* **2017**, 25, 3259–3277, doi:10.1016/j.bmc.2017.04.031.
174. Cedillo-Cruz, A.; Aguilar, M.I.; Jung-Cook, H. (S)-(+)-Cis-4′-Benzyloxypraziquantel. *Acta Crystallographica Section E: Crystallographic Communications* **2013**, 69, o1835–o1836, doi:10.1107/S1600536813031735.
175. Valenti, G.; Tinnemans, P.; Baglai, I.; Noorduin, W.L.; Kaptein, B.; Leeman, M.; ter Horst, J.H.; Kellogg, R.M. Combining Incompatible Processes for Deracemization of a Praziquantel Derivative under Flow Conditions. *Angewandte Chemie Int Ed Engl* **2021**, 60, 5279–5282, doi:10.1002/anie.202013502.
176. McNaught A. D.; Wilkinson A. *The IUPAC Compendium of Chemical Terminology*; Gold, V., Ed: 2nd; International Union of Pure and Applied Chemistry (IUPAC): Research Triangle Park, NC, **1997**; Available online: https://publications.iupac.org/compendium/index.html (accessed on 25 October 2024).
177. Raza, K. Polymorphism: The Phenomenon Affecting the Performance of Drugs. *SOJ Pharmacy and Pharmaceutical Sciences* **2014**, doi:10.15226/2374-6866/1/2/00111.
178. Brittain, H.G. Polymorphism and Solvatomorphism 2010. *Journal of Pharmaceutical Sciences* **2012**, 101, 464–484, doi:10.1002/jps.22788.
179. Singhal, D. Drug Polymorphism and Dosage Form Design: A Practical Perspective. *Advanced Drug Delivery Reviews* **2004**, 56, 335–347, doi:10.1016/j.addr.2003.10.008.
180. Leopold, G.; Ungethum, W.; Groll, E.; Diekmann, H.W.; Nowak, H.; Wegner, D.H.G. Clinical Pharmacology in Normal Volunteers of Praziquantel, a New Drug against Schistosomes and Cestodes. *European Journal of Clinical Pharmacolology* **1978**, 14, 281–291, doi:10.1007/BF00560463.
181. Bylund, G.; Bång, B.; Wikgren, K. Tests with a New Compound (Praziquantel) against Diphyllobothrium Latum. *Journal of Helminthology* **1977**, 51, 115–119, doi:10.1017/S0022149X00007343.

182. Toro R.; Kaduk J.; Delgado M.; de D G.D. Structural Characterization of Praziquantel: A Broad Spectrum Anthelmintic, in Powder Diffraction. *ICDD Annual Spring Meetings, Powder Diffraction.* **2014**, 29(2), 206–207.
183. Lombardo, F.C.; Perissutti, B.; Keiser, J. Activity and Pharmacokinetics of a Praziquantel Crystalline Polymorph in the Schistosoma Mansoni Mouse Model. *European Journal of Pharmaceutics and Biopharmaceutics* **2019**, 142, 240–246, doi:10.1016/j.ejpb.2019.06.029.
184. Doehlert, D.H. Uniform Shell Designs. *Journal of Applied Statistics* **1970**, 19, 231, doi:10.2307/2346327.
185. Mayoka, G.; Keiser, J.; Häberli, C.; Chibale, K. Structure–Activity Relationship and in Vitro Absorption, Distribution, Metabolism, Excretion, and Toxicity (ADMET) Studies of N-Aryl 3-Trifluoromethyl Pyrido[1,2-A]Benzimidazoles That Are Efficacious in a Mouse Model of Schistosomiasis. *ACS Infectious Diseases* **2019**, 5, 418–429, doi:10.1021/acsinfecdis.8b00313.
186. Salas-Zúñiga, R.; Mondragón-Vásquez, K.; Alcalá-Alcalá, S.; Lima, E.; Höpfl, H.; Herrera-Ruiz, D.; Morales-Rojas, H. Nanoconfinement of a Pharmaceutical Cocrystal with Praziquantel in Mesoporous Silica: The Influence of the Solid Form on Dissolution Enhancement. *Molecular Pharmaceutics* **2022**, 19, 414–431, doi:10.1021/acs.molpharmaceut.1c00606.
187. Zanolla, D.; Bertoni, S.; Passerini, N.; Albertini, B.; Zingone, G.; Perissutti, B. From Bitter to Sweet: A Preliminary Study towards a Patient-Friendly Praziquantel Dosage Form. *Comptes Rendus Chimie* **2022**, 25, 179–188, doi:10.5802/crchim.188.
188. Alzghoul, A.; Alhalaweh, A.; Mahlin, D.; A. S. Bergström, C. Experimental and Computational Prediction of Glass Transition Temperature of Drugs. *Journal of Chemical Information and Modeling* **2014**, 54, 3396–3403, doi:10.1021/ci5004834.
189. Khankari, R.K.; Grant, D.J.W. Pharmaceutical Hydrates. *Thermochimica Acta* **1995**, 248, 61–79, doi:10.1016/0040-6031(94)01952-D.
190. Salazar-Rojas, D.; Kaufman, T.S.; Maggio, R.M. A Study of the Heat-Mediated Phase Transformations of Praziquantel Hydrates. Evaluation of Their Impact on the Dissolution Rate. *Heliyon* **2022**, 8, e11317, doi:10.1016/j.heliyon.2022.e11317.
191. Griesser, U.J. The Importance of Solvates. In: *Polymorphism*; Wiley, **2006**, 211–233.
192. Essen, C. von; Luedeker, D. In Silico Co-Crystal Design: Assessment of the Latest Advances. *Drug Discovery Today* **2023**, 28, 103763, doi:10.1016/j.drudis.2023.103763.

193. Shaikh, R.; Singh, R.; Walker, G.M.; Croker, D.M. Pharmaceutical Cocrystal Drug Products: An Outlook on Product Development. *Trends in Pharmacological Sciences* **2018**, 39, 1033–1048, doi:10.1016/j.tips.2018.10.006.

194. Sun, L.; Wang, Y.; Yang, F.; Zhang, X.; Hu, W. Cocrystal Engineering: A Collaborative Strategy toward Functional Materials. *Advanced Materials* **2019**, 31, doi:10.1002/adma.201902328.

195. Taylor, C.R.; Day, G.M. Evaluating the Energetic Driving Force for Cocrystal Formation. *Crystal Growth & Design* **2018**, 18, 892–904, doi:10.1021/acs.cgd.7b01375.

196. Urbanus, J.; Roelands, C.P.M.; Verdoes, D.; Jansens, P.J.; ter Horst, J.H. Co-Crystallization as a Separation Technology: Controlling Product Concentrations by Co-Crystals. *Crystal Growth & Design* **2010**, 10, 1171–1179, doi:10.1021/cg9010778.

197. Schultheiss, N.; Newman, A. Pharmaceutical Cocrystals and Their Physicochemical Properties. *Crystal Growth & Design* **2009**, 9, 2950–2967, doi:10.1021/cg900129f.

198. Thakuria, R.; Delori, A.; Jones, W.; Lipert, M.P.; Roy, L.; Rodríguez-Hornedo, N. Pharmaceutical Cocrystals and Poorly Soluble Drugs. *International Journal of Pharmaceutics* **2013**, 453, 101–125, doi:10.1016/j.ijpharm.2012.10.043.

199. Wasim, M.; Abdul Mannan, A.M.; Azim, T.; Ali Khan, R.; Alotaibi, G.; Amer, M.; Shafique, M.; Asghar Khan, M.; Gul, S.; Hussain, I. Physicochemical and Pharmacokinetic Evaluation of Praziquantel Co-Crystals by Varying the Spacer Group of Co-Crystal Formers. *Sains Malays* **2022**, 51, 3271–3284, doi:10.17576/jsm-2022-5110-13.

200. Nartowski, K.P.; Malhotra, D.; Hawarden, L.E.; Fábián, L.; Khimyak, Y.Z. Nanocrystallization of Rare Tolbutamide Form V in Mesoporous MCM-41 Silica. *Molecular Pharmaceutics* **2018**, 15, 4926–4932, doi:10.1021/acs.molpharmaceut.8b00575.

201. Nartowski, K.P.; Tedder, J.; Braun, D.E.; Fábián, L.; Khimyak, Y.Z. Building Solids inside Nano-Space: From Confined Amorphous through Confined Solvate to Confined 'Metastable' Polymorph. *Physical Chemistry Chemical Physics* **2015**, 17, 24761–24773, doi:10.1039/C5CP03880D.

202. Hamilton, B.D.; Ha, J.-M.; Hillmyer, M.A.; Ward, M.D. Manipulating Crystal Growth and Polymorphism by Confinement in Nanoscale Crystallization Chambers. *Accounts of Chemical Research* **2012**, 45, 414–423, doi:10.1021/ar200147v.

203. Reddy, L.S.; Bethune, S.J.; Kampf, J.W.; Rodríguez-Hornedo, N. Cocrystals and Salts of Gabapentin: PH Dependent Cocrystal Stability and Solubility. *Crystal Growth & Design* **2009**, 9, 378–385, doi:10.1021/cg800587y.

204. Adachi, M.; Hinatsu, Y.; Kusamori, K.; Katsumi, H.; Sakane, T.; Nakatani, M.; Wada, K.; Yamamoto, A. Improved Dissolution and Absorption of Ketoconazole in the Presence of Organic Acids as PH-Modifiers. *European Journal of Pharmaceutical Sciences* **2015**, 76, 225–230, doi:10.1016/j.ejps.2015.05.015.
205. Musumeci, D.; Hunter, C.A.; Prohens, R.; Scuderi, S.; McCabe, J.F. Virtual Cocrystal Screening. *Chemical Sciences* **2011**, 2, 883, doi:10.1039/c0sc00555j.
206. D'Abbrunzo, I.; Bianco, E.; Gigli, L.; Demitri, N.; Birolo, R.; Chierotti, M.R.; Škoríc, I.; Keiser, J.; Häberli, C.; Voinovich, D.; et al. Praziquantel Meets Niclosamide: A Dual-Drug Antiparasitic Cocrystal. *International Journal of Pharmaceutics* **2023**, 644, 123315, doi:10.1016/j.ijpharm.2023.123315.
207. Scientific Image and Illustration Software | BioRender Available online: https://www.biorender.com/ (accessed on 16 October 2024).
208. Devogelaer, J.-J.; Meekes, H.; Vlieg, E.; de Gelder, R. Cocrystals in the Cambridge Structural Database: A Network Approach. *Acta Crystallographica Section B: Structural Science, Crystal Engineering and Materials* **2019**, 75, 371–383, doi:10.1107/S2052520619004694.
209. Devogelaer, J.-J.; Brugman, S.J.T.; Meekes, H.; Tinnemans, P.; Vlieg, E.; de Gelder, R. Cocrystal Design by Network-Based Link Prediction. *CrystEngComm* **2019**, 21, 6875–6885, doi:10.1039/C9CE01110B.
210. Charpentier, M.D.; Devogelaer, J.-J.; Tijink, A.; Meekes, H.; Tinnemans, P.; Vlieg, E.; De Gelder, R.; Johnston, K.; Ter Horst, J.H. Comparing and Quantifying the Efficiency of Cocrystal Screening Methods for Praziquantel. *Crystal Growth & Design* **2022**, 22, 5525, doi:10.1021/acs.cgd.2c00615.
211. Yang, D.; Wang, L.; Yuan, P.; An, Q.; Su, B.; Yu, M.; Chen, T.; Hu, K.; Zhang, L.; Lu, Y.; et al. Cocrystal Virtual Screening Based on the XGBoost Machine Learning Model. *Chinese Chemical Letters* **2023**, 34, 107964, doi:10.1016/J.CCLET.2022.107964.
212. Dong, J.; Cao, D.-S.; Miao, H.-Y.; Liu, S.; Deng, B.-C.; Yun, Y.-H.; Wang, N.-N.; Lu, A.-P.; Zeng, W.-B.; Chen, A.F. ChemDes: An Integrated Web-Based Platform for Molecular Descriptor and Fingerprint Computation. *Journal of Cheminformatics* **2015**, 7, 60, doi:10.1186/s13321-015-0109-z.
213. Galland, A.; Dupray, V.; Berton, B.; Morin-Grognet, S.; Sanselme, M.; Atmani, H.; Coquerel, G. Spotting Conglomerates by Second Harmonic Generation. *Crystal Growth & Design* **2009**, 9, 2713–2718, doi:10.1021/cg801356m.
214. Chen, W.; Mook, R.A.; Premont, R.T.; Wang, J. Niclosamide: Beyond an Antihelminthic Drug. *Cellular Signalling* **2018**, 41, 89–96, doi:10.1016/j.cellsig.2017.04.001.

215. Clinical Treatment of Taeniasis | Human Tapeworm (Taeniasis) | CDC Available online: https://www.cdc.gov/taeniasis/hcp/clinical-care/index.html (accessed on 25 October 2024).
216. Xu, J.; Shi, P.Y.; Li, H.; Zhou, J. Broad Spectrum Antiviral Agent Niclosamide and Its Therapeutic Potential. *ACS Infectious Diseases* **2020**, 6, 909–915, doi:10.1021/ACSINFECDIS.0C00052/ASSET/IMAGES/LARGE/ID0C00052_0002.JPEG.
217. Jara, M.O.; Williams III, R.O. The Challenge of Repurposing Niclosamide: Considering Pharmacokinetic Parameters, Routes of Administration, and Drug Metabolism. *Journal of Drug Delivery Science Technology* **2023**, 81, 104187, doi:10.1016/j.jddst.2023.104187.
218. Van Tonder, E.C.; Maleka, T.S.P.; Liebenberg, W.; Song, M.; Wurster, D.E.; De Villiers, M.M. Preparation and Physicochemical Properties of Niclosamide Anhydrate and Two Monohydrates. *International Journal of Pharmaceutics* **2004**, 269, 417–432, doi:10.1016/j.ijpharm.2003.09.035.
219. Al-Hadiya, B.M.H. Niclosamide: Comprehensive Profile. In: *Profiles of Drug Substances, Excipients and Related Methodology*, **2005**; 67–96.
220. Frayha, G.J.; Smyth, J.D.; Gobert, J.G.; Savel, J. The Mechanisms of Action of Antiprotozoal and Anthelmintic Drugs in Man. *General Pharmacology: The Vascular System* **1997**, 28, 273–299, doi:10.1016/S0306-3623(96)00149-8.
221. Sovago, I.; Bond, A.D. Expanding the Structural Landscape of Niclosamide: A High Z′ Polymorph, Two New Solvates and Monohydrate HA. *Acta Crystallographica C Structural Chemistry* **2015**, 71, 394–401, doi:10.1107/S2053229615005847.
222. Grifasi, F.; Chierotti, M.R.; Gaglioti, K.; Gobetto, R.; Maini, L.; Braga, D.; Dichiarante, E.; Curzi, M. Using Salt Cocrystals to Improve the Solubility of Niclosamide. *Crystal Growth & Design* **2015**, 15, 1939–1948, doi:10.1021/acs.cgd.5b00106.
223. Mann, J.E.; Gao, R.; Swift, J.A. Dehydration of Niclosamide Monohydrate Polymorphs: Different Mechanistic Pathways to the Same Product. *Crystal Growth & Design* **2023**, 23, 5102–5111, doi:10.1021/acs.cgd.3c00322.
224. Luedeker, D.; Gossmann, R.; Langer, K.; Brunklaus, G. Crystal Engineering of Pharmaceutical Co-Crystals: “NMR Crystallography” of Niclosamide Co-Crystals. *Crystal Growth & Design* **2016**, 16, 3087–3100, doi:10.1021/acs.cgd.5b01619.
225. Yamauchi, M.; Lee, E.H.; Otte, A.; Byrn, S.R.; Carvajal, M.T. Contrasting the Surface and Bulk Properties of Anhydrate and Dehydrated Hydrate Materials. *Crystal Growth & Design* **2011**, 11, 692–698, doi:10.1021/cg101098v.

226. Healy, A.M.; Ayenew Worku, Z.; Kumar, D.; Madi, A.M. Pharmaceutical Solvates, Hydrates and Amorphous Forms: A Special Emphasis on Cocrystals. *Advanced Drug Delivery Reviews* **2017**, 117, 25-46, doi:10.1016/j.addr.2017.03.002.
227. Braun, D.E.; Gelbrich, T.; Kahlenberg, V.; Tessadri, R.; Wieser, J.; Griesser, U.J. Stability of Solvates and Packing Systematics of Nine Crystal Forms of the Antipsychotic Drug Aripiprazole. *Crystal Growth & Design* **2009**, 9, 1054–1065, doi:10.1021/cg8008909.
228. Tian, F.; Qu, H.; Louhi-Kultanen, M.; Rantanen, J. Insight into Crystallization Mechanisms of Polymorphic Hydrate Systems. *Chemical Engineering & Technology* **2010**, 33, 833–838, doi:10.1002/ceat.200900572.
229. Caira, M.R.; Van Tonder, E.C.; De Villiers, M.M.; Lötter, A.P. Diverse Modes of Solvent Inclusion in Crystalline Pseudopolymorphs of the Anthelmintic Drug Niclosamide. *Journal of Inclusion Phenomena and Molecular Recognition in Chemistry* **1998**, 31, 1–16, doi:10.1023/A:1007931314609.
230. Harriss, B.I.; Wilson, C.; Radosavljevic Evans, I. Niclosamide Methanol Solvate and Niclosamide Hydrate: Structure, Solvent Inclusion Mode and Implications for Properties. *Acta Crystallographica C Structural Chemistry* **2014**, 70, 758–763, doi:10.1107/S2053229614015496.
231. Van Tonder, E.C.; Mahlatji, M.D.; Malan, S.F.; Liebenberg, W.; Caira, M.R.; Song, M.; De Villiers, M.M. Preparation and Physicochemical Characterization of 5 Niclosamide Solvates and 1 Hemisolvate. *AAPS PharmSchiTech* **2004**, 5(1), e12, doi:10.1208/pt050112.
232. Kuri, P.; Nanubolu, J.B. Why Does the Niclosamide Drug Form Solvates or Hydrates? *CrystEngComm* **2024**, 26, 4313–4328, doi:10.1039/D4CE00463A.
233. Tao, H.; Zhang, Y.; Zeng, X.; Shulman, G.I.; Jin, S. Niclosamide Ethanolamine–Induced Mild Mitochondrial Uncoupling Improves Diabetic Symptoms in Mice. *Nature Medicine* **2014**, 20, 1263–1269, doi:10.1038/nm.3699.
234. Alasadi, A.; Chen, M.; Swapna, G.V.T.; Tao, H.; Guo, J.; Collantes, J.; Fadhil, N.; Montelione, G.T.; Jin, S. Effect of Mitochondrial Uncouplers Niclosamide Ethanolamine (NEN) and Oxyclozanide on Hepatic Metastasis of Colon Cancer. *Cell Death & Disease* **2018**, 9, 215, doi:10.1038/s41419-017-0092-6.
235. Kapale, S.S.; Chaudhari, H.K. Niclosamide & Challenges in Chemical Modifications: A Broad Review on Enhancement of Solubility. *Journal of the Indian Chemical Society* **2021**, 98, 100262, doi:10.1016/j.jics.2021.100262.
236. MacEachern, L.; Kermanshahi-pour, A.; Mirmehrabi, M.; Ajiboye, L.; Trivedi, V.; Rohani, S.; He, Q. Cocrystal Formation of Niclosamide and Urea in Supercritical CO_2 and Impact of

Cosolvent. *Journal of Supercrital Fluids* **2023**, 201, 106029, doi:10.1016/j.supflu.2023.106029.

237. MacEachern, L.A.; Walwyn-Venugopal, R.; Kermanshahi-pour, A.; Mirmehrabi, M. Ternary Phase Diagram Development and Production of Niclosamide-Urea Co-Crystal by Spray Drying. *Journal of Pharmaceutical Sciences* **2021**, 110, 2063–2073, doi:10.1016/j.xphs.2020.11.036.
238. Bhanushali, J.S.; Bharate, S.S. Estimating Thermodynamic Equilibrium Solubility and Solute–Solvent Interactions of Niclosamide in Eight Mono-Solvents at Different Temperatures. *Journal of Molecular Liquids* **2022**, 367, 120359, doi:10.1016/j.molliq.2022.120359.
239. European Pharmacopoeia 11.0 – Niclosamide Available online: https://pheur.edqm.eu/app/11-5/search?q=niclosamide (accessed on 25 October 2024)
240. Vuai, S.A.H.; Sahini, M.G.; Onoka, I.; Kiruri, L.W.; Shadrack, D.M. Cation–π Interactions Drive Hydrophobic Self-Assembly and Aggregation of Niclosamide in Water. *RSC Advances* **2021**, 11, 33136–33147, doi:10.1039/D1RA05358B.
241. Bhushan, B.; Dubey, P.; Kumar, S.U.; Sachdev, A.; Matai, I.; Gopinath, P. Bionanotherapeutics: Niclosamide Encapsulated Albumin Nanoparticles as a Novel Drug Delivery System for Cancer Therapy. *RSC Advances* **2015**, 5, 12078–12086, doi:10.1039/c4ra15233f.
242. Xie, Y.; Yao, Y. Octenylsuccinate Hydroxypropyl Phytoglycogen Enhances the Solubility and In-Vitro Antitumor Efficacy of Niclosamide. *International Journal of Pharmaceutics* **2018**, 535, 157–163, doi:10.1016/j.ijpharm.2017.11.004.
243. Jara, M.O.; Warnken, Z.N.; Sahakijpijarn, S.; Thakkar, R.; Kulkarni, V.R.; Christensen, D.J.; Koleng, J.J.; Williams, R.O. Oral Delivery of Niclosamide as an Amorphous Solid Dispersion That Generates Amorphous Nanoparticles during Dissolution. *Pharmaceutics* **2022**, 14, 2568, doi:10.3390/pharmaceutics14122568.
244. Bhanushali, J.S.; Dhiman, S.; Nandi, U.; Bharate, S.S. Molecular Interactions of Niclosamide with Hydroxyethyl Cellulose in Binary and Ternary Amorphous Solid Dispersions for Synergistic Enhancement of Water Solubility and Oral Pharmacokinetics in Rats. *International Journal of Pharmaceutics* **2022**, 626, 122144, doi:10.1016/j.ijpharm.2022.122144.
245. International Union of Pure and Applied Chemistry Available online: https://old.iupac.org/publications/compendium/index.html (accessed on 18 October 2024).
246. Serajuddin, A.T.M. Salt Formation to Improve Drug Solubility. *Advanced Drug Delivery Reviews* **2007**, 59, 603–616, doi:10.1016/j.addr.2007.05.010.

247. Elder, D.P.; Holm, R.; Diego, H.L. de Use of Pharmaceutical Salts and Cocrystals to Address the Issue of Poor Solubility. *International Journal of Pharmaceutics* **2013**, 453, 88–100, doi:10.1016/j.ijpharm.2012.11.028.
248. MacRae, C.F.; Sovago, I.; Cottrell, S.J.; Galek, P.T.A.; McCabe, P.; Pidcock, E.; Platings, M.; Shields, G.P.; Stevens, J.S.; Towler, M.; et al. Mercury 4.0: From Visualization to Analysis, Design and Prediction. *Journal of Applied Crystallography* **2020**, 53, 226–235, doi:10.1107/S1600576719014092.
249. Brittain, H.G. Pharmaceutical Cocrystals: The Coming Wave of New Drug Substances. *Journal of Pharmaceutical Sciences* **2013**, 102, 311–317, doi:10.1002/jps.23402.
250. Manek, R. V; Kolling, W.M. Influence of Moisture on the Crystal Forms of Niclosamide Obtained from Acetone and Ethyl Acetate. *AAPS PharmSciTech* **2004**, 5, E14, doi:10.1208/pt050114.
251. Mann, J.E.; Gao, R.; London, S.S.; Swift, J.A. Desolvation Processes in Channel Solvates of Niclosamide. *Molecular Pharmaceutics* **2023**, 20, 5554–5562, doi:10.1021/acs.molpharmaceut.3c00481.
252. Smallwood, I.McN. In: *Handbook of Organic Solvent Properties*; Arnold, **1996**; ISBN: 0340645784.
253. Lausi, A.; Polentarutti, M.; Onesti, S.; Plaisier, J.R.; Busetto, E.; Bais, G.; Barba, L.; Cassetta, A.; Campi, G.; Lamba, D.; et al. Status of the Crystallography Beamlines at Elettra. *The European Physical Journal Plus* **2015**, 130, 43, doi:10.1140/epjp/i2015-15043-3.
254. Kabsch, W. *XDS*. *Acta Crystallographica Section D: Biological Crystallography* **2010**, 66, 125–132, doi:10.1107/S0907444909047337.
255. Sheldrick, G.M. SHELXT - Integrated Space-Group and Crystal-Structure Determination. *Acta Crystallographica Section A: Foundations and Advances* **2015**, 71, 3–8, doi:10.1107/S2053273314026370.
256. Sheldrick, G.M. Crystal Structure Refinement with SHELXL. *Acta Crystallographica Section C: Structural Chemistry* **2015**, 71, 3–8, doi:10.1107/S2053229614024218.
257. Emsley, P.; Lohkamp, B.; Scott, W.G.; Cowtan, K. Features and Development of Coot. *Acta Crystallographica Section D: Biological Crystallography* **2010**, 66, 486–501, doi:10.1107/S0907444910007493.
258. Farrugia, L.J. WinGX and ORTEP for Windows: An Update. *Journal of Applied Crystallography* **2012**, 45, 849–854, doi:10.1107/S0021889812029111.
259. Schrodinger L The PyMOL Molecular Graphics System Available online: http://www.pymol.org (accessed on 4 April 2023).

260. Lombardo, F.C.; Pasche, V.; Panic, G.; Endriss, Y.; Keiser, J. Life Cycle Maintenance and Drug-Sensitivity Assays for Early Drug Discovery in Schistosoma Mansoni. *Nature Protocols* **2019**, 14, 461–481, doi:10.1038/s41596-018-0101-y.

261. Wang, L.; Li, S.; Xu, X.; Xu, X.; Wang, Q.; Li, D.; Zhang, H. Drug-Drug Cocrystals of Theophylline with Quercetin. *Journal of Drug Delivery Science and Technology* **2022**, 70, 103228, doi:10.1016/J.JDDST.2022.103228.

262. de Villiers, M.M.; Mahlatji, M.D.; Malan, S.F.; van Tonder, E.C.; Liebenberg, W.; de Villiers, M.M. Physical Transformation of Niclosamide Solvates in Pharmaceutical Suspensions Determined by DSC and TG Analysis. *Pharmazie* **2004**, 59(7), 534–540. PMID: 1529609.

263. Schindelin, J.; Arganda-Carreras, I.; Frise, E.; Kaynig, V.; Longair, M.; Pietzsch, T.; Preibisch, S.; Rueden, C.; Saalfeld, S.; Schmid, B.; et al. Fiji: An Open-Source Platform for Biological-Image Analysis. *Nature Methods* **2012**, 9, 676–682, doi:10.1038/nmeth.2019.

264. Šagud, I.; Zanolla, D.; Perissutti, B.; Passerini, N.; Škorić, I. Identification of Degradation Products of Praziquantel during the Mechanochemical Activation. *Journal of Pharmaceutical and Biomedical Analysis* **2018**, 159, 291–295, doi:10.1016/j.jpba.2018.07.002.

265. Eddleston, M.D.; Thakuria, R.; Aldous, B.J.; Jones, W. An Investigation of the Causes of Cocrystal Dissociation at High Humidity. *Journal of Pharmaceutical Sciences* **2014**, 103, 2859–2864, doi:10.1002/jps.23865.

266. Thakuria, R.; Arhangelskis, M.; Eddleston, M.D.; Chow, E.H.H.; Sarmah, K.K.; Aldous, B.J.; Krzyzaniak, J.F.; Jones, W. Cocrystal Dissociation under Controlled Humidity: A Case Study of Caffeine–Glutaric Acid Cocrystal Polymorphs. *Organic Process Research & Development* **2019**, 23, 845–851, doi:10.1021/acs.oprd.8b00422.

267. Port, A.; Almansa, C.; Enrech, R.; Bordas, M.; Plata-Salamán, C.R. Differential Solution Behavior of the New API-API Co-Crystal of Tramadol-Celecoxib (CTC) versus Its Constituents and Their Combination. *Crystal Growth & Design* **2019**, 19, 3172–3182, doi:10.1021/acs.cgd.9b00008.

268. D'Abbrunzo, I.; Spadaro, M.; Arhangelskis, M.; Zingone, G.; Hasa, D.; Perissutti, B. Competitive Mechanochemical Solvate Formation of Theophylline in the Presence of Miscible Liquid Mixtures. *Crystal Growth & Design* **2023**, 23, 8094–8102, doi:10.1021/acs.cgd.3c00834.

269. Hammersley, A.P.; Svensson, S.O.; Hanfland, M.; Fitch, A.N.; Hausermann, D. Two-Dimensional Detector Software: From Real Detector to Idealised Image or Two-Theta Scan. *High Pressure Research* **1996**, 14, 235–248, doi:10.1080/08957959608201408.

270. THE FIT2D - HOME PAGE Available online: https://www.esrf.fr/computing/scientific/FIT2D/ (accessed on 10 September 2024).
271. Altomare, A.; Cuocci, C.; Giacovazzo, C.; Moliterni, A.; Rizzi, R.; Corriero, N.; Falcicchio, A. EXPO2013: A Kit of Tools for Phasing Crystal Structures from Powder Data. *Journal of Applied Crystallography* **2013**, 46, 1231–1235, doi:10.1107/S0021889813013113.
272. CCDC - Access Structures Available online: https://www.ccdc.cam.ac.uk/structures/Search?Ccdcid=896766&DatabaseToSearch=Published (accessed on 10 September 2024).
273. BIOVIA Materials Studio | Dassault Systèmes Available online: https://www.3ds.com/products/biovia/materials-studio (accessed on 10 September 2024).
274. Giannozzi, P.; Baroni, S.; Bonini, N.; Calandra, M.; Car, R.; Cavazzoni, C.; Ceresoli, D.; Chiarotti, G.L.; Cococcioni, M.; Dabo, I.; et al. QUANTUM ESPRESSO: A Modular and Open-Source Software Project for Quantum Simulations of Materials. *Journal of Physics: Condensed Matter* **2009**, 21, 395502, doi:10.1088/0953-8984/21/39/395502.
275. Lee, K.; Murray, É.D.; Kong, L.; Lundqvist, B.I.; Langreth, D.C. Higher-Accuracy van Der Waals Density Functional. *Physical Review B* **2010**, 82, 081101, doi:10.1103/PhysRevB.82.081101.
276. Hamada, I. Van Der Waals Density Functional Made Accurate. *Physical Review B* **2014**, 89, 121103, doi:10.1103/PhysRevB.89.121103.
277. Prandini, G.; Marrazzo, A.; Castelli, I.E.; Mounet, N.; Marzari, N. Precision and Efficiency in Solid-State Pseudopotential Calculations. *NPJ Computational Materials* **2018**, 4, 72, doi:10.1038/s41524-018-0127-2.
278. Lejaeghere, K.; Bihlmayer, G.; Björkman, T.; Blaha, P.; Blügel, S.; Blum, V.; Caliste, D.; Castelli, I.E.; Clark, S.J.; Dal Corso, A.; et al. Reproducibility in Density Functional Theory Calculations of Solids. *Science* **2016**, 351, doi:10.1126/science.aad3000.
279. Charpentier, T. The PAW/GIPAW Approach for Computing NMR Parameters: A New Dimension Added to NMR Study of Solids. *Solid State Nuclear Magnetic Resonance* **2011**, 40, 1–20, doi:10.1016/j.ssnmr.2011.04.006.
280. Dal Corso, A. Pseudopotentials Periodic Table: From H to Pu. *Computational Materials Science* **2014**, 95, 337–350, doi:10.1016/j.commatsci.2014.07.043.
281. Franco, F.; Baricco, M.; Chierotti, M.R.; Gobetto, R.; Nervi, C. Coupling Solid-State NMR with GIPAW Ab Initio Calculations in Metal Hydrides and Borohydrides. *Journal of Physical Chemistry C* **2013**, 117, 9991–9998, doi:10.1021/jp3126895.

282. Harris, R.K.; Hodgkinson, P.; Pickard, C.J.; Yates, J.R.; Zorin, V. Chemical Shift Computations on a Crystallographic Basis: Some Reflections and Comments. *Magnetic Resonance in Chemistry* **2007**, 45, S174–S186, doi:10.1002/mrc.2132.
283. Reddy, G.N.M.; Huqi, A.; Iuga, D.; Sakurai, S.; Marsh, A.; Davis, J.T.; Masiero, S.; Brown, S.P. Co-existence of Distinct Supramolecular Assemblies in Solution and in the Solid State. *Chemistry – A European Journal* **2017**, 23, 2315–2322, doi:10.1002/chem.201604832.
284. Nimmo, J.K.; Lucas, B.W. Solid-State Phase Transition in Triethylenediamine, $N(CH_2CH_2)_3N$. I. The Crystal Structure of Phase II at 298 K. *Acta Crystallographica Section B*: *Structural Science, Crystal Engineering and Materials* **1976**, 32, 348–353, doi:10.1107/S0567740876003038.
285. Greenspan, L. Humidity Fixed Points of Binary Saturated Aqueous Solutions. *Journal of Research of the National Bureau of Standards-A. Physics and Chemistry* **1976**, 81, 89–96, doi:10.6028/jres.081A.011.
286. Xiao, S.-H.; Keiser, J.; Chollet, J.; Utzinger, J.; Dong, Y.; Endriss, Y.; Vennerstrom, J.L.; Tanner, M. In Vitro and In Vivo Activities of Synthetic Trioxolanes against Major Human Schistosome Species. *Antimicrobial Agents Chemotherapy* **2007**, 51, 1440–1445, doi:10.1128/AAC.01537-06.
287. Tan, X.; Yan, Y.; Zhang, G.; Li, P.; Ling, F.; Liu, T.; Wang, G. Target Epidermal Damage of Gyrodactylus Kobayashii to Obtain the Effective Anthelmintic Compound Glacial Acetic Acid. *Aquaculture* **2023**, 577, 739993, doi:10.1016/j.aquaculture.2023.739993.
288. SCOGS (Select Committee on GRAS Substances) Available online: https://www.cfsanappsexternal.fda.gov/scripts/fdcc/?set=SCOGS&sort=Sortsubstance&order=ASC&startrow=1&type=basic&search=ACETIC%20ACID (accessed on 20 June 2024).
289. Substances Added to Food (Formerly EAFUS) Available online: https://www.cfsanappsexternal.fda.gov/scripts/fdcc/?set=FoodSubstances (accessed on 20 June 2024).
290. ICH Q3C (R8) Residual Solvents - Scientific Guideline | European Medicines Agency Available online: https://www.ema.europa.eu/en/ich-q3c-r8-residual-solvents-scientific-guideline (accessed on 29 February 2024).
291. Madanayake, S.N.; Manipura, A.; Thakuria, R.; Adassooriya, N.M. Opportunities and Challenges in Mechanochemical Cocrystallization toward Scaled-Up Pharmaceutical Manufacturing. *Organic Process Research & Development* **2023**, 27, 409–422, doi:10.1021/acs.oprd.2c00314.

292. Dengale, S.J.; Grohganz, H.; Rades, T.; Löbmann, K. Recent Advances in Co-Amorphous Drug Formulations. *Advanced Drug Delivery Reviews* **2016**, 100, 116–125, doi:10.1016/j.addr.2015.12.009.
293. Acetic Acid Available online: https://webbook.nist.gov/cgi/cbook.cgi?ID=C64197&Units=SI&Mask=80#IR-Spec (accessed on 16 July 2024).
294. D'Abbrunzo, I.; Procida, G.; Perissutti, B. Praziquantel Fifty Years on: A Comprehensive Overview of Its Solid State. *Pharmaceutics* **2023**, 16, 27, doi:10.3390/pharmaceutics16010027.
295. Rosenberger, L.; Jenniches, J.; von Essen, C.; Khutia, A.; Kühn, C.; Marx, A.; Georgi, K.; Hirsch, A.K.H.; Hartmann, R.W.; Badolo, L. Metabolic Profiling of S-Praziquantel: Structure Elucidation Using the Crystalline Sponge Method in Combination with Mass Spectrometry and Nuclear Magnetic Resonance. *Drug Metabolism and Disposition* **2022**, 50, 320–326, doi:10.1124/dmd.121.000663.
296. Schlesinger, C.; Fitterer, A.; Buchsbaum, C.; Habermehl, S.; Chierotti, M.R.; Nervi, C.; Schmidt, M.U. Ambiguous Structure Determination from Powder Data: Four Different Structural Models of 4,11-Difluoroquinacridone with Similar X-Ray Powder Patterns, Fit to the PDF, SSNMR and DFT-D. *IUCrJ* **2022**, 9, 406–424, doi:10.1107/S2052252522004237.
297. Wolczyk, A.; Paik, B.; Sato, T.; Nervi, C.; Brighi, M.; GharibDoust, S.P.; Chierotti, M.; Matsuo, M.; Li, G.; Gobetto, R.; et al. Li5(BH4)3NH: Lithium-Rich Mixed Anion Complex Hydride. *Journal of Physical Chemistry C* **2017**, 121, 11069–11075, doi:10.1021/acs.jpcc.7b00821.
298. van de Streek, J.; Neumann, M.A. Validation of Experimental Molecular Crystal Structures with Dispersion-Corrected Density Functional Theory Calculations. *Acta Crystallographica Section B: Structural Science, Crystal Engineering and Materials* **2010**, 66, 544–558, doi:10.1107/S0108768110031873.
299. Douillet, J.; Stevenson, N.; Lee, M.; Mallet, F.; Ward, R.; Aspin, P.; Dennehy, D.R.; Camus, L. Development of a Solvate as an Active Pharmaceutical Ingredient: Developability, Crystallisation and Isolation Challenges. *Journal of Crystal Growth* **2012**, 342, 2–8, doi:10.1016/j.jcrysgro.2011.05.023.
300. Zhang, C.; Kersten, K.M.; Kampf, J.W.; Matzger, A.J. Solid-State Insight Into the Action of a Pharmaceutical Solvate: Structural, Thermal, and Dissolution Analysis of Indinavir Sulfate Ethanolate. *Journal of Pharmaceutical Sciences* **2018**, 107, 2731–2734, doi:10.1016/j.xphs.2018.06.020.

301. Praziquantel EP Impurity B | CymitQuimica Available online: https://cymitquimica.com/products/4Z-P-634/125273-86-1/praziquantel-ep-impurity-b/%20(accessed%20on%204%20June%202024). (accessed on 20 July 2024).
302. Wang, K.; Sun, C.C. Direct Compression Tablet Formulation of Celecoxib Enabled with a Pharmaceutical Solvate. *International Journal of Pharmaceutics* **2021**, 596, 120239, doi:10.1016/j.ijpharm.2021.120239.
303. Tabanez, A.M.; Nogueira, B.A.; Milani, A.; Eusébio, M.E.S.; Paixão, J.A.; Nur Kabuk, H.; Jajuga, M.; Ildiz, G.O.; Fausto, R. Thiabendazole and Thiabendazole-Formic Acid Solvate: A Computational, Crystallographic, Spectroscopic and Thermal Study. *Molecules* **2020**, 25, 3083, doi:10.3390/molecules25133083.
304. Heinz, A.; Strachan, C.J.; Gordon, K.C.; Rades, T. Analysis of Solid-State Transformations of Pharmaceutical Compounds Using Vibrational Spectroscopy. *Journal of Pharmacy and Pharmacology* **2009**, 61, 971–988, doi:10.1211/jpp/61.08.0001.
305. Dhondale, M.R.; Thakor, P.; Nambiar, A.G.; Singh, M.; Agrawal, A.K.; Shastri, N.R.; Kumar, D. Co-Crystallization Approach to Enhance the Stability of Moisture-Sensitive Drugs. *Pharmaceutics* **2023**, 15, 189, doi:10.3390/pharmaceutics15010189.
306. PRALEN Gocce per Gatti, Cani Cuccioli e Di Piccola Taglia | UPD Available online: https://medicines.health.europa.eu/veterinary/it/600000094039 (accessed on 26 September 2024).
307. Zou, Z.; Huang, Q.; Li, X.; Liu, X.; Yin, L.; Zhao, Y.; Liang, G.; Wu, W. Dissolution Changes in Drug-Amino Acid/Biotin Co-Amorphous Systems: Decreased/Increased Dissolution during Storage without Recrystallization. *European Journal of Pharmaceutical Sciences* **2023**, 188, 106526, doi:10.1016/j.ejps.2023.106526.
308. Barbosa, E.J.; Andrade, M.A.B.; Gubitoso, M.R.; Bezzon, V.D.N.; Smith, P.A.; Byrn, S.R.; Bou-Chacra, N.A.; Carvalho, F.M.S.; de Araujo, G.L.B. Acoustic Levitation and High-Resolution Synchrotron X-Ray Powder Diffraction: A Fast Screening Approach of Niclosamide Amorphous Solid Dispersions. *International Journal of Pharmaceutics* **2021**, 602, 120611, doi:10.1016/j.ijpharm.2021.120611.
309. Chen, J.-M.; Wang, Z.-Z.; Wu, C.-B.; Li, S.; Lu, T.-B. Crystal Engineering Approach to Improve the Solubility of Mebendazole. *CrystEngComm* **2012**, 14, 6221, doi:10.1039/c2ce25724f.
310. Voinovich, D.; Campisi, B.; Phan-Tan-Luu, R. Experimental Design for Mixture Studies. *Comprehensive Chemometrics* **2020**, 1, 391–452, doi:10.1016/B978-044452701-1.00084-3.

311. Qui Sommes-Nous ? | NemrodW Available online: https://www.nemrodw.com/fr/whoweare#intro%20(accessed%20on%2030%20August%202024). (accessed on 21 September 2024).
312. Hsu, W.-P.; Yeh, C.-F. Phase Behavior of Ternary Blends of Tactic Poly(Methyl Methacrylate)s and Poly(Styrene-Co-Acrylonitrile). *Polymer Journal* **1999**, 31, 574–578, doi:10.1295/polymj.31.574.
313. Tobyn, M.; Brown, J.; Dennis, A.B.; Fakes, M.; gao, Q.; Gamble, J.; Khimyak, Y.Z.; Mcgeorge, G.; Patel, C.; Sinclair, W.; et al. Amorphous Drug-PVP Dispersions: Application of Theoretical, Thermal and Spectroscopic Analytical Techniques to the Study of a Molecule With Intermolecular Bonds in Both the Crystalline and Pure Amorphous State. *Journal of Pharmaceutical Sciences* **2009**, 98, 3456–3468, doi:10.1002/jps.21738.
314. Skrdla, P.J.; Floyd, P.D.; Dell'Orco, P.C. Predicting the Solubility Enhancement of Amorphous Drugs and Related Phenomena Using Basic Thermodynamic Principles and Semi-Empirical Kinetic Models. *International Journal of Pharmaceutics* **2019**, 567, 118465, doi:10.1016/j.ijpharm.2019.118465.
315. Xie, T.; Taylor, L.S. Effect of Temperature and Moisture on the Physical Stability of Binary and Ternary Amorphous Solid Dispersions of Celecoxib. *Journal of Pharmaceutical Sciences* **2017**, 106, 100–110, doi:10.1016/j.xphs.2016.06.017.
316. Babu, N.J.; Nangia, A. Solubility Advantage of Amorphous Drugs and Pharmaceutical Cocrystals. *Crystal Growth & Design* **2011**, 11, 2662–2679, doi:10.1021/cg200492w.
317. Shi, Q.; Moinuddin, S.M.; Cai, T. Advances in Coamorphous Drug Delivery Systems. *Acta Pharmaceutica Sinica B* **2019**, 9, 19–35, doi:10.1016/j.apsb.2018.08.002.
318. Newman, A.; Knipp, G.; Zografi, G. Assessing the Performance of Amorphous Solid Dispersions. *Journal of Pharmaceutical Sciences* **2012**, 101, 1355–1377, doi:10.1002/jps.23031.
319. Laitinen, R.; Löbmann, K.; Strachan, C.J.; Grohganz, H.; Rades, T. Emerging Trends in the Stabilization of Amorphous Drugs. *International Journal of Pharmaceutics* **2013**, 453, 65–79, doi:10.1016/j.ijpharm.2012.04.066.
320. Kaminska, E.; Adrjanowicz, K.; Zakowiecki, D.; Milanowski, B.; Tarnacka, M.; Hawelek, L.; Dulski, M.; Pilch, J.; Smolka, W.; Kaczmarczyk-Sedlak, I.; et al. Enhancement of the Physical Stability of Amorphous Indomethacin by Mixing It with Octaacetylmaltose. Inter and Intra Molecular Studies. *Pharmaceutical Research* **2014**, 31, 2887–2903, doi:10.1007/s11095-014-1385-4.

321. Li, J.; Duggirala, N.K.; Kumar, N.S.K.; Su, Y.; Suryanarayanan, R. Design of Ternary Amorphous Solid Dispersions for Enhanced Dissolution of Drug Combinations. *Molecular Pharmaceutics* **2022**, 19, 2950–2961, doi:10.1021/acs.molpharmaceut.2c00307.
322. Heng, W.; Song, Y.; Luo, M.; Hu, E.; Wei, Y.; Gao, Y.; Pang, Z.; Zhang, J.; Qian, S. Mechanistic Insights into the Crystallization of Coamorphous Drug Systems. *Journal of Controlled Release* **2023**, 354, 489–502, doi:10.1016/j.jconrel.2023.01.019.
323. Lodagekar, A.; Chavan, R.B.; Mannava, M.K.C.; Yadav, B.; Chella, N.; Nangia, A.K.; Shastri, N.R. Co Amorphous Valsartan Nifedipine System: Preparation, Characterization, in Vitro and in Vivo Evaluation. *European Journal of Pharmaceutical Sciences* **2019**, 139, 105048, doi:10.1016/j.ejps.2019.105048.
324. D'angelo, A.; Edgar, B.; Hurt, A.P.; Antonijević, M.D. Physico-Chemical Characterisation of Three-Component Co-Amorphous Systems Generated by a Melt-Quench Method. *Journal of Thermal Analysis and Calorimetry* **2018**, 134, 381–390, doi:10.1007/s10973-018-7291-y.
325. Narala, S.; Nyavanandi, D.; Srinivasan, P.; Mandati, P.; Bandari, S.; Repka, M.A. Pharmaceutical Co-Crystals, Salts, and Co-Amorphous Systems: A Novel Opportunity of Hot-Melt Extrusion. *Journal of Drug Delivery Sciences and Technology* **2021**, 61, 102209, doi:10.1016/j.jddst.2020.102209.
326. Silva, J.F.C.; Rosado, M.T.S.; Maria, T.M.R.; Pereira Silva, P.S.; Silva, M.R.; Eusébio, M.E.S. Introduction to Pharmaceutical Co-Amorphous Systems Using a Green Co-Milling Technique. *Journal of Chemical Education* **2023**, 100, 1627–1632, doi:10.1021/acs.jchemed.3c00036.
327. Murthy, N.S.; Minor, H. General Procedure for Evaluating Amorphous Scattering and Crystallinity from X-Ray Diffraction Scans of Semicrystalline Polymers. *Polymer (Guildf)* **1990**, 31, 996–1002, doi:10.1016/0032-3861(90)90243-R.
328. Fatema, K.; Sajeeb, B.; Sikdar, K.Y.K.; Hossain, A.M. Al; Bachar, S.C. Evaluation of the Formulation of Combined Dosage Form of Albendazole and Mebendazole through In Vitro Physicochemical and Anthelmintic Study. *Dhaka University Journal of Pharmaceutical Sciences* **2022**, 21, 153–163, doi:10.3329/dujps.v21i2.63116.
329. A. Q. P. Garbuio; T. Hanashiro; B. Markman; F. Fonseca; F. Perazzo; P. Rosa Evaluation and Study of Mebendazole Polymorphs Present in Raw Materials and Tablets Available in the Brazilian Pharmaceutical Market. *Journal of Applied Pharmaceutical Sciences* **2014**, 4, 1–7, doi:10.7324/JAPS.2014.4111.
330. Kasten, G.; Löbmann, K.; Grohganz, H.; Rades, T. Co-Former Selection for Co-Amorphous Drug-Amino Acid Formulations. *International Journal of Pharmaceutics* **2019**, 557, 366–373, doi:10.1016/j.ijpharm.2018.12.036.

331. Lu, Q.; Zografi, G. Phase Behavior of Binary and Ternary Amorphous Mixtures Containing Indomethacin, Citric Acid and PVP. *Pharmaceutical Research* **1998**, 15, 1202–1206, doi:10.1023/A:1011983606606.
332. Tajber, L.; Corrigan, O.I.; Healy, A.M. Physicochemical Evaluation of PVP–Thiazide Diuretic Interactions in Co-Spray-Dried Composites—Analysis of Glass Transition Composition Relationships. *European Journal of Pharmaceutical Sciences* **2005**, 24, 553–563, doi:10.1016/j.ejps.2005.01.007.
333. Skrdla, P.J.; Floyd, P.D.; Dell'Orco, P.C. The Amorphous State: First-Principles Derivation of the Gordon–Taylor Equation for Direct Prediction of the Glass Transition Temperature of Mixtures; Estimation of the Crossover Temperature of Fragile Glass Formers; Physical Basis of the "Rule of 2/3." *Physical Chemistry Chemical Physics* **2017**, 19, 20523–20532, doi:10.1039/C7CP04124A.
334. Feng, T.; Bates, S.; Carvajal, M.T. Toward Understanding the Evolution of Griseofulvin Crystal Structure to a Mesophase after Cryogenic Milling. *International Journal of Pharmaceutics* **2009**, 367, 16–19, doi:10.1016/j.ijpharm.2008.10.011.
335. Hancock, B.C.; Shamblin, S.L.; Zografi, G. Molecular Mobility of Amorphous Pharmaceutical Solids Below Their Glass Transition Temperatures. *Pharmaceutical Research* **1995**, 12, 799–806, doi:10.1023/A:1016292416526.
336. Van den Mooter, G. The Use of Amorphous Solid Dispersions: A Formulation Strategy to Overcome Poor Solubility and Dissolution Rate. *Drug Discovery Today Technology* **2012**, 9, e79–e85, doi:10.1016/j.ddtec.2011.10.002.
337. Yoshioka, M.; Hancock, B.C.; Zografi, G. Crystallization of Indomethacin from the Amorphous State below and above Its Glass Transition Temperature. *Journal of Pharmaceutical Sciences* **1994**, 83, 1700–1705, doi:10.1002/jps.2600831211.
338. Sheokand, S.; Modi, S.R.; Bansal, A.K. Dynamic Vapor Sorption as a Tool for Characterization and Quantification of Amorphous Content in Predominantly Crystalline Materials. *Journal of Pharmaceutical Sciences* **2014**, 103, 3364–3376, doi:10.1002/jps.24160.
339. Wu, W.; Wang, Y.; Löbmann, K.; Grohganz, H.; Rades, T. Transformations between Co-Amorphous and Co-Crystal Systems and Their Influence on the Formation and Physical Stability of Co-Amorphous Systems. *Molecular Pharmaceutics* **2019**, 16, 1294–1304, doi:10.1021/acs.molpharmaceut.8b01229.
340. Sovago, I.; Wang, W.; Qiu, D.; Raijada, D.; Rantanen, J.; Grohganz, H.; Rades, T.; Bond, A.; Löbmann, K. Properties of the Sodium Naproxen-Lactose-Tetrahydrate Co-Crystal upon Processing and Storage. *Molecules* **2016**, 21, 509, doi:10.3390/molecules21040509.

341. Kilpeläinen, T.; Pajula, K.; Ervasti, T.; Uurasjärvi, E.; Koistinen, A.; Korhonen, O. Raman Imaging of Amorphous-Amorphous Phase Separation in Small Molecule Co-Amorphous Systems. *European Journal of Pharmaceutics and Biopharmaceutics* **2020**, 155, 49–54, doi:10.1016/j.ejpb.2020.08.007.
342. Vazquez-Rodriguez, J.A.; Shaqour, B.; Guarch-Pérez, C.; Choińska, E.; Riool, M.; Verleije, B.; Beyers, K.; Costantini, V.J.A.; Święszkowski, W.; Zaat, S.A.J.; et al. A Niclosamide-Releasing Hot-Melt Extruded Catheter Prevents Staphylococcus Aureus Experimental Biomaterial-Associated Infection. *Scientific Reports* **2022**, 12, 12329, doi:10.1038/s41598-022-16107-4.
343. Dimethyl Sulfoxide Available online: https://webbook.nist.gov/cgi/cbook.cgi?ID=C67685&Mask=80#IR-Spec (accessed on 3 September 2024).
344. Yu, L.; Reutzel, S.M.; Stephenson, G.A. Physical Characterization of Polymorphic Drugs: An Integrated Characterization Strategy. *Pharmaceutical Science & Technology Today* **1998**, 1, 118–127, doi:10.1016/S1461-5347(98)00031-5.
345. Kumar Bandaru, R.; Rout, S.R.; Kenguva, G.; Gorain, B.; Alhakamy, N.A.; Kesharwani, P.; Dandela, R. Recent Advances in Pharmaceutical Cocrystals: From Bench to Market. *Frontiers in Pharmacology* **2021**, 12, 780582, doi:10.3389/fphar.2021.780582.
346. Lehn, J.-M. Supramolecular Chemistry: From Molecular Information towards Self-Organization and Complex Matter. *Reports on Progress in Physics* **2004**, 67, 249–265, doi:10.1088/0034-4885/67/3/R02.
347. Wang, X.; Du, S.; Zhang, R.; Jia, X.; Yang, T.; Zhang, X. Drug-Drug Cocrystals: Opportunities and Challenges. *Asian Journal of Pharmaceutical Sciences* **2021**, 16, 307–317, doi:10.1016/j.ajps.2020.06.004.

Acknowledgements

At this point in my academic journey, it is essential to express my gratitude to the many individuals and collaborators who have supported me and contributed to the realization of this thesis.
In particular, I am deeply thankful to:

- **M. R. Chierotti** and collaborators of the Department of Chemistry, University of Turin (Italy), for SSNMR, ^{1}H-NMR analyses and DFT calculations.

- **L. Gigli** and **N. Demitri**, crystallographers in Elettra-Sincrotrone in Area Science Park, Basovizza–Trieste (Italy), for crystal structures' solutions.

- **J. Keiser** and collaborators of the Department of Medical Pharmacology, Swiss Tropical and Public Health Institute (Switzerland), for *in vitro* and *in vivo* tests.

- **I. Škorić** of the Department of Organic Chemistry, University of Zagreb (Croatia), for drug recovery analyses.

- **S. Bertoni** and collaborators of the Department of Pharmacy and Biotechnology, University of Bologna, (Italy), for TGA analyses.

- **F. Selmin** of the Department of Pharmaceutical Sciences, University of Milan (Italy), for modulated DSC analyses.

- **E. Bernardo** of Department of Industrial Engineering, University of Padova (Italy), for powders' true density determinations.

- **G. Coquerel** of Laboratoire Sciences et Méthodes Séparatives, University of Rouen, Mont-Saint-Aignan cedex (France-Normandie), for DVS analyses and Eramsus traineeship.